

**COUPLED ELECTROMAGNETIC/THERMAL MACHINE DESIGN**  
**OPTIMIZATION BASED ON FINITE ELEMENT ANALYSIS**  
**USING HIGH-THROUGHPUT COMPUTING**

By

Wenying Jiang

A dissertation submitted in partial fulfillment of the  
requirements for the degree of

Doctor of Philosophy

(Electrical and Computer Engineering)

at the

**UNIVERSITY OF WISCONSIN-MADISON**

**2014**

Date of final oral examination: 06/27/2014

The dissertation is approved by the following members of the Final Oral Committee:

Jahns, Thomas M., Professor, Electrical and Computer Engineering

Lorenz, Robert D., Professor, Mechanical Engineering

Nellis, Gregory F., Professor, Mechanical Engineering

Sarlioglu, Bulent, Assistant Professor, Electrical and Computer Engineering

Lipo, Thomas A., Professor Emeritus, Electrical and Computer Engineering

Liang, Feng, Industry, Ford Motor Company

## Abstract

The torque production capability of an electrical machine depends on how high the winding current density can be raised before reaching a maximum temperature threshold. Therefore, determining the maximum current density limit is crucial for optimizing a machine's performance. Today's machine design optimization is typically accomplished by using a maximum limit on the stator current density as an inadequate surrogate for the underlying maximum temperature constraints that cannot be directly incorporated into electromagnetic (EM) finite element (FE) analysis. To overcome this limitation, a coupled EM/thermal model is necessary for a more accurate prediction of the machine's performance limits. Such a model has been developed for a surface permanent magnet (SPM) machine that is capable of efficiently identifying its maximum current density. This coupled EM/thermal model can be readily incorporated into the machine design optimization process.

FE analysis is often the preferred analytical tool for electric machines because of the highly-nonlinear nature of the machine's EM, thermal, and structural characteristics. Unfortunately, the adoption of FE analysis in multi-dimensional search programs to find optimal designs has generally been impractical because of the intensive computational load imposed by FE analysis of such large numbers of candidate designs. An approach for overcoming this obstacle has been proposed using a high-throughput computing (HTC) environment that harnesses the parallel processing capabilities of large numbers of computers to evaluate many candidate designs simultaneously. The HTC technique along with fast FE solvers offers opportunities for significantly reducing the total computational time for iterative optimization of electric machines, making FE analysis much more attractive for this task.

In addition, artificial neural networks (ANN) have been successfully applied to many system identification problems in order to take advantage of their noted ability to efficiently map nonlinear relationships between inputs and outputs. The ANN technique has been adopted for this machine design optimization initiative to further reduce the computational effort and time.

A machine design optimization algorithm has been implemented based on the coupled EM/thermal FE-based model combined with artificial neural network that is capable of efficiently identifying the maximum current density for a given machine design during static operation. The software is applied to optimize a 30 kW (continuous) surface PM machine for achieving maximum torque density. Comparison of the optimal designs found with the coupled EM/thermal model versus the baseline EM-only model highlights the advantages of the coupled EM/thermal optimization. This exercise has also confirmed that the introduction of the ANN technique into the machine optimization process leads to a significant reduction in the total computation time.

For demanding applications such as traction motors, the electric machine is frequently required to run at peak torque conditions for short periods of time, causing large thermal swings. A modified version of the coupled EM/thermal model has been developed that is suitable for applications with large transient torque requirements. This makes it significantly easier for machine designers to maximize the winding current density to achieve the highest possible torque/power ratings within thermal limits set by the winding insulation or demagnetization threshold requirements. This transient model has been integrated into the optimization program to give it the capability of optimizing the machine designs for both steady-state and short-duration transient operating conditions.

## Acknowledgement

I wish to express my deepest thanks to my advisor, Professor Thomas M. Jahns, for his expert guidance throughout my graduate study. His constructive skepticism constantly led me to a deeper understanding of electric machines. His profound knowledge, enthusiasm in teaching, extensive professional experience, as well as his energetic work attitude, encouraged me to reach the place where I am today. I owe him both professionally and personally a large debt of gratitude.

My sincere thanks go to Professor Thomas A. Lipo who taught me how to design electric machines at the early stage of my graduate study. His invaluable advice and encouragement provided the strong motivation of this research.

Special acknowledgements must be made to Professor Ming Cheng and Professor Heyun Lin from Southeast University, China. They introduced me to the wonderful world of electric machines, and recommended me to join WEMEPC, which makes my dream come true.

I am very grateful to Ford Motor Company and WEMPEC for providing gift financial support for this research, and to Dr. Feng Liang and Dr. Michael Degner from Ford Motor Company for their technical guidance. I would also like to thank Dr. Yamada for supplying us with plenty of JMAG licenses, and Hiroyuki Sano, Yusaku Suzuki, Tetsuo Ogawa, David Farnia for their technical assistance. Additionally, thanks to the Center for High Throughput Computing at UW-Madison for access to their facilities and technical support.

Many thanks to the entire WEMPEC faculty team for their passionate teaching that prepared me with the background knowledge on machines, drives, power electronics, and controls. I would also like to extend my thanks to all the WEMPEC administrative staff for their assistance

and support. There is a lengthy list of people within the WEMPEC graduate student community whose inspiring discussions and constructive comments pulled me out of confusion at times. I am deeply indebted to the WEMPEC faculty, staff, and fellow students for making my stay in Madison an enjoyable and unforgettable experience.

Although it is impossible to mention everyone who helped me, I would like to thank all the people who have taught, guided, and assisted me during these past few years.

Last but not least, I am forever grateful to my parents for the love and care they put into my life, and the support and encouragement they gave me through my difficult times. I could not have done this without you always being there for me.

## Table of Contents

Abstract .....	i
Acknowledgement .....	iii
Table of Contents .....	v
List of Figures .....	x
List of Tables .....	xiv
Chapter 1: Introduction and Literature Review .....	1
1.1 Problem Background and Solution Approach.....	1
1.2 Thesis Objectives .....	3
1.3 State-of-the-Art Review .....	4
1.3.1 Electromagnetic Machine Design Optimization.....	5
1.3.2 Coupled Electromagnetic and Thermal Machine Modeling.....	14
1.3.3 Coupled Electromagnetic/Thermal Machine Design Optimization .....	19
1.4 Thesis Layout .....	26
Chapter 2: Electromagnetic Machine Design Optimization.....	29
2.1 Target Application and Machine Configuration .....	29
2.2 Optimization Algorithm: Differential Evolution (DE).....	31
2.3 Implementation of FE Analysis Based Machine Design Optimization .....	33
2.3.1 Machine Design Optimization Routine .....	33
2.3.2 Preliminary Optimization Test Results.....	34
2.4.1 Tuning Tol & NP, Keeping Cr & F Constant.....	39
2.4.1 Tuning Cr & F, Keeping Tol & NP Constant.....	41
2.5 Adding One More Degree of Freedom: Airgap Radius $R_g$ Set as Variable.....	42
2.6 Objective Function Tuning.....	44
2.6.1 Tuning the Objective Function for Various Evaluation Criteria .....	44
2.6.2 Tuning the Objective Function for Various Operating Points.....	46

2.7 Conclusions .....	49
<b>Chapter 3: Machine Design Optimization Using High-Throughput Computing ....</b>	<b>51</b>
3.1 High-Throughput Computing (HTC) Environment: Project Condor.....	51
3.2 FE Analysis Based Machine Design Optimization in Condor .....	52
3.3 Comparison between HTC and Single Computer Optimization Results .....	56
3.3.1 Comparison Test Conditions & Optimization Parameters .....	56
3.3.2 Optimized Design .....	57
3.3.3 Comparison of Computational Time .....	59
3.4 Computation Time Breakdown and Acceleration Factor Improvements.....	64
3.5 Conclusions .....	67
<b>Chapter 4: Coupled Electromagnetic/Thermal Model for Electric Machines .....</b>	<b>68</b>
4.1 2D vs. 3D Electromagnetic Model.....	68
4.2 Thermal FE Model .....	70
4.2.1 Building the FE Model .....	71
4.2.2 Selecting Active Cooling Methods.....	74
4.3 Temperature Dependent Material Properties .....	80
4.3.1 Permanent Magnet .....	80
4.3.2 Copper .....	83
4.3.3 Coolant.....	83
4.3.4 Lamination Steel.....	84
4.4 Tests of Coupled EM/Thermal Analysis .....	86
4.5 Key Observations of the Coupled EM/Thermal Models.....	88
4.5.1 Convergence Property of Coupled EM/Thermal Model .....	88
4.5.2 Maximum Winding Temperature Limit .....	89
4.5.3 Demagnetization Constraint .....	91
4.5.4 EM Model vs. Coupled EM/Thermal Model.....	94
4.6 Conclusions .....	96

Chapter 5: Coupled Electromagnetic/Thermal Machine Design Optimization for Steady-State Operation .....	97
5.1 Finding the Maximum Current Density for Winding Insulation Limit.....	97
5.1.1 Problem Identification .....	97
5.1.2 Finding the Maximum Current Density Using Numerical Methods .....	98
5.2 Estimating the Maximum Current Density While Avoiding Irreversible Demagnetization .....	104
5.3 Procedure for Efficiently Obtaining Maximum Current Density for Steady-State Operation .....	106
5.4 Coupled EM/Thermal Machine Design Optimization for Steady-State Operation .....	107
5.4.1 Implementation of Coupled EM/Thermal Machine Design Optimization.....	108
5.4.2 Optimized Design.....	109
5.4.3 Computational Time .....	111
5.5 Coupled EM/Thermal Machine Design Optimization for Steady-State Operation with Application of Artificial Neural Network .....	111
5.5.1 Construct the Artificial Neural Network .....	112
5.5.2 Validation of the Trained Neural Network.....	115
5.6 Conclusion.....	117
Chapter 6: Coupled EM/Thermal Machine Design Optimization Including Transient Operation with Application of Artificial Neural Network .....	118
6.1 Valid Initial Current Density Region for Machine Transient Operation .....	118
6.2 Coupling EM and Transient Thermal FE Analysis.....	120
6.2.1 Initial Loss Profile Assumption.....	120
6.2.2 Loss Profile Update .....	122
6.3 Maximum Transient Current Density Identification.....	127
6.4 Optimization of Machine Operation with a Given Peak/Continuous Power Ratio.....	130
6.5 Coupled EM/Thermal Machine Design Optimization for a Given Peak/Continuous Power Ratio with Application of ANN Technique .....	134



6.6 Conclusions .....	139
<b>Chapter 7: Generalization of Machine Design Optimization Techniques.....</b>	<b>141</b>
7.1 Interior Permanent Magnet Machine Design Optimization .....	141
7.1.1 Target IPM Machine Configuration .....	141
7.1.2 Implementation of IPM Machine Design Optimization .....	143
7.1.3 Optimized Design .....	147
7.2 Constrained Optimization Routine for the U.S. DRIVE Specifications .....	151
7.2.1 U.S. DRIVE (FreedomCAR) Advanced Traction Motor Specifications .....	152
7.2.2 Constrained Optimization of a Given Machine Cross-Section Design Based on U.S. DRIVE Specifications .....	153
7.2.3 Application of the Constrained Optimization Routine to the Target Machines .....	156
7.3 Conclusion.....	160
<b>Chapter 8: Parameter Sensitivity .....</b>	<b>162</b>
8.1 Investigation of Mesh Size of the EM FE Model.....	162
8.2 Thermal Coefficient Sensitivity for a Given Machine Design.....	164
8.3 Sensitivity Analysis of Machine Design Parameters and Thermal Coefficients .....	164
8.3.1 Data Collection: Parametric Study Using the Monte Carlo Method .....	165
8.3.2 Sensitivity Analysis with Scatter Plots Method .....	167
8.3.3 Evaluation of Parameter Sensitivity Using Regression Analysis.....	169
8.4 Experimental Thermal Coefficient Estimation .....	174
8.5 Conclusion.....	177
<b>Chapter 9: Conclusions, Contributions and Future Work .....</b>	<b>179</b>
9.1 Conclusions .....	179
9.1.1 Electromagnetic Machine Design Optimization Using High-Throughput Computing .....	179
9.1.2 Coupled Electromagnetic/Thermal Machine Model .....	181
9.1.3 Coupled EM/Thermal Machine Design Optimization for Steady-State Operation....	182

9.1.4 Coupled EM/Thermal Machine Design Optimization for Operation with Transient Power Pulse Intervals .....	183
9.2 Contributions .....	185
9.2.1 Electromagnetic Machine Design Optimization Based on FE Analysis in a High-Throughput Computing Environment .....	185
9.2.2 Coupled Electromagnetic/ Thermal Machine Model .....	185
9.2.3 Coupled EM/Thermal Machine Design Optimization for Steady-State Operation....	186
9.2.4 Coupled EM/Thermal Machine Design Optimization for Operation with Transient Peak Power Intervals .....	188
9.2.5 Generalization of Machine Design Optimization Techniques .....	189
9.2.6 Parameter Sensitivity .....	191
9.3 Suggestions for Future Work .....	192
<b>Bibliography</b> .....	<b>195</b>
<b>Appendix</b> .....	<b>207</b>
A.1 EM-Thermal Coupled Tests for TD Design under Static Operation.....	207
A.2 EM-Thermal Coupled Tests for TPD Design under Static Operation .....	211
A.3 EM-Thermal Coupled Tests for Eff. Design under Static Operation.....	214
A.4 EM-Thermal Coupled Tests for TD Design under Transient Operation.....	220
A.5 EM-Thermal Coupled Tests for TPD Design under Transient Operation .....	221
A.6 EM-Thermal Coupled Tests for Eff. Design under Transient Operation.....	223

## List of Figures

Fig. 2 - 1 :FE model cross-section compared with the prototype machine.....	31
Fig. 2 - 2: Machine design Optimization Routine.....	34
Fig. 2 - 3: FSCW-SPM machine design variables (initially proposed) .....	35
Fig. 2 - 4: Objective function values of designs in Gen. #1, #11, #21, #31, and #41.....	37
Fig. 2 - 5: Lowest objective function value in each generation .....	38
Fig. 2 - 6: Minimum objective function value vs. NP with various Tol values.....	40
Fig. 2 - 7: Number of total designs vs. NP with Tol $\leq 10^{-4}$ .....	40
Fig. 2 - 8: Number of generations vs. NP with Tol $\leq 10^{-4}$ .....	40
Fig. 2 - 9: Minimum objective function value vs. F with various Cr values .....	41
Fig. 2 - 10: Number of total designs vs. F at Cr = 0.8 .....	41
Fig. 2 - 11: Number of generations vs. F at Cr = 0.8.....	41
Fig. 2 - 12: Cross-sections of the optimal machine designs with fixed $R_g$ and varied $R_g$ .....	44
Fig. 2 - 13: Cross-section comparison among TD Design, TPD Design, and Eff. Design.....	46
Fig. 2 - 14: Cross-section comparison among TD_560, TD_2800, and TD_14000.....	48
Fig. 2 - 15: Specified envelopes for continuous torque and output power vs. rotor speed [103].	49
Fig. 3 - 1: Flow chart of machine design optimization algorithm in HTC environment. ....	53
Fig. 3 - 2: Data flow in the Project Condor HTC environment .....	54
Fig. 3 - 3: FSCW-SPM machine design variables .....	54
Fig. 3 - 4: Plots showing magnet mass, machine efficiency, torque ripple, and power factor, (all for rated power operation) vs. machine electromagnetic mass for all of the machine designs evaluated during the DE optimization. Points for initial design (green square) and final design (red triangle) are highlighted in each plot.....	58
Fig. 3 - 5: Time duration between “Execute” and “Terminate” for each design in Generation #25 (Condor).....	61
Fig. 3 - 6: Time duration for each design in Generation #25 (Single Computer).....	61
Fig. 3 - 7: Time duration of each generation over the 50 generations (Condor) .....	63
Fig. 3 - 8: Time duration of each generation over the total 50 generations (Single Computer) ...	63
Fig. 3 - 9: Total time duration between “Start” and “Terminate” for each design in Generation #29 (Condor).....	66
Fig. 3 - 10: Acceleration factor vs. number of machine designs in each generation .....	66
Fig. 4 - 1: TD Design 2D and 3D FE Models.....	70
Fig. 4 - 2: TD Design thermal model with all nature convection .....	74
Fig. 4 - 3: TD Design thermal model with water jacket cooling .....	75
Fig. 4 - 4: TD Design average component temperatures vs. water jacket coolant temperature ...	75
Fig. 4 - 5: TD Design thermal model with forced convection at machine ends .....	76
Fig. 4 - 6: TD Design average component temperatures vs. machine end air speed.....	77
Fig. 4 - 7: TD Design thermal model with forced convection on machine axial surface .....	79

Fig. 4 - 8: TD Design average component temperatures vs. air speed on machine axial surface	79
Fig. 4 - 9: TD Design final thermal model with active cooling	80
Fig. 4 - 10: BH curve of neodymium magnet NMX-39EH from JMAG library	82
Fig. 4 - 11: Neodymium magnet resistivity vs. temperature	82
Fig. 4 - 12: Air thermal conductivity vs. temperature	84
Fig. 4 - 13: Air density vs. temperature	84
Fig. 4 - 14: Air viscosity vs. temperature	84
Fig. 4 - 15: Correction coefficient for steel permeability vs. temperature [118]	85
Fig. 4 - 16: Preliminary coupled EM/thermal FE analysis flow diagram	86
Fig. 4 - 17: Front view and side view of the three candidate designs' 3D thermal model	88
Fig. 4 - 18: TD Design maximum winding temperature vs. current density	90
Fig. 4 - 19: TPD Design maximum winding temperature vs. current density	91
Fig. 4 - 20: Eff. Design maximum winding temperature vs. current density	91
Fig. 4 - 21: Demagnetization curve at different temperature of Neodymium magnet [119]	92
Fig. 4 - 22: TD Design demagnetization ratio vs. current density	93
Fig. 4 - 23: TPD Design demagnetization ratio vs. current density	93
Fig. 4 - 24: Eff. Design demagnetization ratio vs. current density	93
Fig. 4 - 25: TD Design EM model and EM/Thermal model comparison	95
Fig. 4 - 26: TPD Design EM model and EM/Thermal model comparison	95
Fig. 4 - 27: Eff. Design EM model and EM/Thermal model comparison	95
Fig. 5 - 1: TD Design maximum winding temperature from 1st EM/Thermal iteration	97
Fig. 5 - 2: Finding TD Design max. current density for insulation limit using Bisection method	99
Fig. 5 - 3: Finding TD Design max. current density for insulation limit using the bisection method	100
Fig. 5 - 4: Finding TD Design max. current density for insulation limit using secant method	102
Fig. 5 - 5: Finding TD Design max. current density for insulation limit using Müller's method	104
Fig. 5 - 6: Finding TPD Design max. current density for demag. constraint using linear extrapolation method	105
Fig. 5 - 7: Flow chart of proposed procedure for finding the maximum current density for machine steady-state operation	107
Fig. 5 - 8: EM-only optimal machine design	110
Fig. 5 - 9: Coupled EM/thermal optimal machine design	110
Fig. 5 - 10: Artificial neural network [124]	113
Fig. 5 - 11: Configuration of the neural network	113
Fig. 5 - 12: Performance plot when training the neural network	114
Fig. 5 - 13: Error histogram for the trained neural network	114
Fig. 5 - 14: Max. current density found with coupled EM/thermal model (blue) and predicted by ANN (red)	115

Fig. 5 - 15: Optimal machine design w/o ANN .....	116
Fig. 5 - 16: Optimal machine design w/ ANN .....	116
Fig. 6 - 1: TD Design valid initial current density region.....	119
Fig. 6 - 2: TPD Design valid initial current density region .....	119
Fig. 6 - 3: Eff. Design valid initial current density region.....	119
Fig. 6 - 4: Initial Loss Profile Assumption .....	121
Fig. 6 - 5: Predicted temperature transient based on initial loss profile assumption .....	122
Fig. 6 - 6: Loss components estimation at time = 18 sec.....	124
Fig. 6 - 7: Linear relationship between loss components and their corresponding temperatures	125
Fig. 6 - 8: Loss profile update.....	126
Fig. 6 - 9: Predicted temperature transient based on updated loss profile .....	127
Fig. 6 - 10: Maximum winding temperature vs. current density under transient operation condition .....	128
Fig. 6 - 11: Demagnetization ratio vs. current density under transient operation condition.....	130
Fig. 6 - 12: TD Design initial max. winding temperature vs. peak/continuous ratio.....	132
Fig. 6 - 13: TPD Design initial max. winding temperature vs. peak/continuous ratio .....	132
Fig. 6 - 14: Eff. Design initial max. winding temperature vs. peak/continuous ratio.....	132
Fig. 6 - 15: TD Design peak/continuous ratio vs. initial current density.....	133
Fig. 6 - 16: TPD Design peak/continuous ratio vs. initial current density.....	133
Fig. 6 - 17: Eff. Design peak/continuous ratio vs. initial current density .....	133
Fig. 6 - 18: Flow chart of procedure for finding the initial current density for optimizing machine operation with a given peak/continuous power ratio .....	134
Fig. 6 - 19: Actual peak/continuous power ratio of the first 300 evaluated designs.....	136
Fig. 6 - 20: Maximum initial steady-state (continuous) current density found with coupled EM/thermal model (blue) and predicted by ANN (red).....	137
Fig. 6 - 21: Static version of coupled EM/thermal optimal machine design .....	138
Fig. 6 - 22: Transient version of coupled EM/thermal optimal machine design .....	138
Fig. 7 - 1: Target IPM machine configuration .....	142
Fig. 7 - 2: IPM machine design variables .....	144
Fig. 7 - 3: Torque vs. current angle for a candidate IPM machine .....	146
Fig. 7 - 4: Flow chart for finding the MTPA angle of the IPM machine with step search method .....	147
Fig. 7 - 5: Optimal SPM machine design.....	148
Fig. 7 - 6: Optimal IPM machine design w/ MTPA .....	148
Fig. 7 - 7: Optimal IPM machine design w/ MTPA .....	151
Fig. 7 - 8: Optimal IPM machine design w/o MTPA .....	151
Fig. 7 - 9: Procedures of applying the optimization routine on TD Design, TPD Design, and Eff. Design .....	157
Fig. 8 - 1: TD Design FE model with coarse mesh.....	163

Fig. 8 - 2: TD Design FE model with medium mesh.....	163
Fig. 8 - 3: TD Design FE model with fine mesh.....	163
Fig. 8 - 4: TD machine component temperatures vs. water jacket coolant temperature.....	165
Fig. 8 - 5: TD machine component temperatures vs. contact resistance between water jacket and stator lamination core.....	165
Fig. 8 - 6: TD machine component temperatures vs. heat transfer coefficient in the airgap.....	165
Fig. 8 - 7: TD machine component temperatures vs. heat transfer coefficient at machine ends	165
Fig. 8 - 8: Scatter plot (red dots) of average torque vs. water jacket coolant temperature with regression (blue line).....	167
Fig. 8 - 9: Scatter plot (red dots) of average torque vs. contact resistance between water jacket and stator core with regression (blue line).....	167
Fig. 8 - 10: Scatter plot (red dots) of average torque vs. heat transfer coefficient in the airgap with regression (blue line) .....	168
Fig. 8 - 11: Scatter plot (red dots) of average torque vs. heat transfer coefficient at machine ends with regression (blue line) .....	168
Fig. 8 - 12: Scatter plot (red dots) of average torque vs. tooth width to slot pitch ratio with regression (blue line).....	168
Fig. 8 - 13: Scatter plot (red dots) of average torque vs. stator yoke thickness to tooth width ratio with regression (blue line) .....	168
Fig. 8 - 14: Scatter plot (red dots) of average torque vs. magnet span to rotor pole pitch ratio with regression (blue line).....	168
Fig. 8 - 15: Scatter plot (red dots) of average torque vs. rotor yoke thickness to rotor pole pitch ratio with regression (blue line) .....	168
Fig. 8 - 16: Scatter plot (red dots) of average torque vs. magnet thickness to airgap thickness ratio with regression (blue line) .....	169
Fig. 8 - 17: Scatter plot (red dots) of average torque vs. airgap radius to stator outer radius ratio with regression (blue line) .....	169
Fig. 8 - 18: Coefficients $\beta$ estimated with regression analysis .....	171
Fig. 8 - 19: Residual plots for average torque $T_{avg}$ .....	171
Fig. 8 - 20: Parameter sensitivities for the TD Design, TPD Design, and Eff. Design .....	173
Fig. 8 - 21: Prototype FSCW surface PM machine mounted on a water jacket .....	175
Fig. 8 - 22: Measured temperatures with fan cooling on machine ends .....	176

## List of Tables

Table 2 - 1: FreedomCAR Specifications [103] .....	30
Table 2 - 2: Prototype FSCW-SPM Traction Machine Key Dimensions and Material Characteristics .....	30
Table 2 - 3: FSCW-SPM Variable Definitions and Ranges (Initially Proposed) .....	35
Table 2 - 4: Details of FSCW-SPM Machine Optimized with Fixed $R_g$ Using Static FE Analysis .....	36
Table 2 - 5: Computation Cost and Min. OF Value Comparison between $R_g$ Fixed & $R_g$ Varied Optimizations .....	43
Table 2 - 6: Comparisons of FSCW-SPM Machines Optimized with $R_g$ Fixed and $R_g$ Varied ...	43
Table 2 - 7: Key Dimension and Performance Comparisons among TD Design, TPD Design, and Eff. Design .....	46
Table 2 - 8: Key Dimension and Performance Comparisons among TD_560, TD_2800, and TD_14000 .....	48
Table 3 - 1: FSCW-SPM Variable Definitions and Ranges .....	54
Table 3 - 2: Optimal FSCW-SPM Machine Details .....	57
Table 4 - 1: Comparison in Loss Estimation between TD Design 2D and 3D FE Models .....	70
Table 4 - 2: Average Temperature Summary for TD Design with Natural Convection.....	73
Table 4 - 3: Average Temperature Summary for TD Design with Water Jacket Cooling (Coolant@65 °C) .....	76
Table 4 - 4: Average Component Temperatures Comparison between Initial Model and Final Model .....	80
Table 4 - 5: Iteration No. Summary with  Current Iteration Temp. (all) - Final Iteration Temp. (all)  $\leq 1$ °C.....	89
Table 4 - 6: Maximum Current Density for Winding Insulation Constraint .....	91
Table 4 - 7: Maximum Current Density for Demagnetization.....	94
Table 5 - 1: Finding TD Design Max. Current Density for Insulation Limit Using Bisection Method .....	99
Table 5 - 2: Finding TD Design Max. Current Density for Insulation Limit Using the False-Position Method.....	101
Table 5 - 3: Finding TD Design Max. Current Density for Insulation Limit Using Secant Method .....	101
Table 5 - 4: Finding TD Design Max. Current Density for Insulation Limit Using Müller's Method .....	103
Table 5 - 5: Required Iterations to Calculate Maximum Current Density for Winding Insulation Limit.....	104
Table 5 - 6: Finding TPD Design Max. Current Density for Demagnetization Constraint Using Linear Extrapolation Method.....	106

Table 5 - 7: Comparison of Optimal Machines with EM-Only and Coupled EM/Thermal Models .....	110
Table 5 - 8: Comparison of Optimal Machines w/ and w/o ANN .....	116
Table 6 - 1: Component Temperatures Based on Initial Loss Profile Assumption .....	122
Table 6 - 2: Component Temperatures Based on Updated Loss Profile.....	126
Table 6 - 3: Comparison of Optimal Machines with Static and Transient Coupled EM/Thermal Models.....	138
Table 7 - 1: Target IPM Traction Machine Key Dimensions and Material Characteristics .....	142
Table 7 - 2: IPM Variable Definitions and Ranges.....	144
Table 7 - 3: Comparison of Optimal SPM and IPM Machines .....	149
Table 7 - 4: Comparison of Optimal IPM Machines w/ and w/o MTPA .....	151
Table 7 - 5: U.S. DRIVE (FreedomCAR) Advanced Traction Motor Specifications [125] .....	153
Table 8 - 1: Comparison of EM FE Models with Different Mesh Sizes .....	163
Table 8 - 2: FSCW-SPM Variable Definitions and Ranges .....	166
Table 8 - 3: Comparison of Thermal Coefficient Predicted from Analytical Model and Experimental Test .....	177



## Nomenclature

<i>Symbols</i>	<i>Definition</i>
FE	Finite element
HTC	High-throughput computing
FSCW	Fractional slot concentrated winding
SPM	Surface permanent magnet
EM	Electromagnetic
AM	Analytical model
PM	Permanent magnet
PSO	Particle swarm optimization
BDFM	Brushless doubly-fed machine
ANN	Artificial neural network
GA	Genetic algorithm
SRM	Switched reluctance machine
NEDC	New European Driving Cycle
DE	Differential evolution
DOE	Design of experiment
CE-FEA	Computationally efficient finite element analysis
IM	Induction machine
CFD	Computational fluid dynamics
HEV	Hybrid electric vehicle
$n$	Rotor mechanical speed

<i>P</i>	Power
<i>T</i>	Torque
<i>F</i>	Scale factor
<i>Cr</i>	Crossover probability
OF	Objective function
VB	Visual basic
<i>Tol</i>	Convergence tolerance
<i>GenMax</i>	Maximum Generation Number
<i>NP</i>	Number of designs in each generation
$R_g$	Machine airgap radius
TD Design	Machine optimized for maximum torque density
TPD Design	Machine optimized for minimum cost
Eff. Design	Machine optimized for maximum efficiency
CPSR	Constant power speed ratio
CHTC	Center for High Throughput Computing
VM	Virtual machine
FFT	Fast Fourier transform

## **Chapter 1: Introduction and Literature Review**

### **1.1 Problem Background and Solution Approach**

#### *Electrical Machine Torque Production Limit*

The maximum torque production capability of an electrical machine typically depends on how high the winding current density can be raised before reaching a maximum temperature threshold [12]. As a result, determining the maximum current density limit is crucial for optimizing a machine's performance. Techniques for determining the maximum current density include the selection of values based on past experience with other similar machines, or calculations using closed-form equations derived from analytical models [13]. An alternative approach uses the current density as a variable during a multi-dimensional search process that requires checking the predicted maximum machine temperatures after every iteration [14]. However, the use of winding current density as a means of determining the thermal performance limits of electrical machines is indirect, inaccurate in many cases, and time consuming, especially for applications with significant transient operation. Instead, calculation of the maximum machine temperature for a selected value of current density is highly preferred when determining a machine's maximum torque production capabilities.

The problem becomes further complicated when the application involves sudden increases in the torque production requirements for short periods of time, such as electrical machines used for starting internal combustion engines. The calculation of the maximum machine temperature under such conditions must take account of the transient nature of these high torque requirements.

The availability of thermal FE solvers makes it possible to accurately predict a machine's thermal response in demanding applications, including the detection of nonlinear phenomena such as hot spot winding temperatures [8-10]. As a result, FE analysis is often the preferred analysis tool for electric machines because of the highly nonlinear nature of the machine electromagnetic (EM), thermal, and structural characteristics. Versions of these FE solvers are available that are designed to handle transient thermal conditions.

### *Electrical Machine Design Optimization*

Today's machine design optimization is typically accomplished by using a maximum limit on the stator current density as an inadequate surrogate for the underlying maximum temperature constraints that cannot be directly incorporated into electromagnetic (EM) finite element (FE) analysis. A coupled EM/thermal model is necessary in order to more accurately predict the machine's performance limits. The EM and thermal models are directly linked because of the temperature-dependent properties of the machine materials including copper, lamination steel, magnets, and coolant. Due to the multiple nonlinearities of the coupled EM/thermal problem, an iterative procedure is required for the EM and thermal FE analyses to converge into a self-consistent solution [11].

Unfortunately, the adoption of FE analysis in multi-dimensional search programs to find optimal designs has generally been impractical because of the intensive computational load imposed by FE analysis of such large numbers of candidate designs. As a result, only a few researchers have reported efforts to pursue this approach [1-3], despite the fact that the idea of applying distributed computing techniques to finite element analysis and optimization of electric machines has been recognized for many years [4].

### *Solution Approach*

A high-throughput computing (HTC) environment is available at UW-Madison; it is known as Project Condor, and it harnesses the parallel processing capabilities of more than 10,000 cores [5]. The availability of these distributed parallel computing resources offers opportunities for significantly reducing the total computational time for iterative optimization of electric machines, making FE analysis much more attractive for this task. Mathematical techniques are available for accelerating the rate of convergence for iterative solutions involving both steady-state and transient thermal operating conditions.

In addition, artificial neural networks (ANN) have been successfully applied to many system identification problems [6,7] in order to take advantage of their noted ability to efficiently map nonlinear relationships between inputs and outputs. The ANN technique can be adopted for machine design optimization to further reduce computational effort and time.

## **1.2 Thesis Objectives**

The objective of this thesis is to address several of the major challenges associated with coupled EM/thermal machine design optimization. More specifically, these objectives include the following:

1. Develop software that can efficiently optimize the design of various types of machines using FE analysis in an HTC environment in order to achieve the best performance results in the least amount of computing time.
2. Couple the EM and thermal analyses inside the machine using temperature-dependent material properties, so that temperatures inside the machine can be predicted simultaneously with the EM performance.

3. For a given machine design operating under steady-state conditions, develop a method for using the coupled EM/thermal model to rapidly determine the machine's maximum current density for operation within the specified thermal limit.
4. For a given machine design operating under transient conditions that include intervals of high torque/current demand, develop a method for using the coupled EM/thermal model to efficiently locate the machine's maximum current density that will keep the maximum winding temperature within a preset limit and avoid demagnetization of the rotor magnets.
5. Implement the machine design optimization algorithm based on the coupled EM/thermal FE-based models summarized in #3 and #4 above for a meaningful surface PM machine design example. In addition, apply some mathematical techniques to reduce the computation time.
6. Extend the coupled analysis and optimization to other machine configurations, such as interior permanent magnet (IPM) machines. Explore the possibility of applying these techniques to the optimization of an electric machine for the challenging case of the U.S. DRIVE Specifications.
7. Conduct a sensitivity analysis to determine the key heat transfer coefficients that affect a machine's performance. Estimate these coefficients based on corresponding experimental results.

### **1.3 State-of-the-Art Review**

This section provides a review of state-of-the-art published research literature that is relevant to the work discussed in this thesis. A large portion of the literature review will focus on the key

topics of electromagnetic (EM) machine design optimization, coupled EM/thermal machine modeling, and coupled EM/thermal machine design optimization.

### **1.3.1 Electromagnetic Machine Design Optimization**

Published research shows considerable progress in the area of electromagnetic machine design optimization, including various modeling approaches, optimization algorithms, simulation environment, etc. This section presents some of the publications that are most relevant to this thesis topic.

Sari et al. [15] use a multi-objective particle swarm optimization algorithm for designing a PM synchronous machine for proton exchange membrane fuel cell air circuit compressor, where the analytical model is applied in order to evaluate machine performance. The results from the analytical model are comparable to those obtained through FE analysis, while the simulation time for the analytical model is significantly reduced.

Duan et al. [1] develop analytical design models for surface mounted PM machines with good accuracy and consideration for the nonlinearity in the material. Their analytical models are incorporated into a machine design optimization program using the particle swarm optimization (PSO) algorithm. The program is capable of finding the optimal solution of the design with respect to certain user-defined objective functions, while the computing time is almost negligible since the analytical machine models are adopted.

Chedot et al. [16] apply optimization techniques to the design and control of a highly constrained PM integrated starter generator. First, a classic uncoupled d, q reluctant circuit model is used to find the optimal design. Then the optimal currents for control on the whole torque-

speed plane are determined based on the FE model. The optimization algorithm adopted for both of the steps is sequential quadratic programming.

Wijenayake et al. [17] derive simplified parametric equations and a design procedure with optimization capabilities using software package QPRO for the design of the axial gap machine. The procedure obtains the optimum design parameters with respect to machine efficiency and specific power, using Quasi-Newton Quadratic extrapolation method. However, the authors indicate that FE analysis is still required for determining the fine dimensions of slot and other parameters.

Huang et al. [18] introduce a general approach to summarizing and interpreting an equation for radial, axial and transverse motors. They present the application of this equation to optimizing a slotless TORUS machine to achieve maximum power density and maximum efficiency. The generalized sizing equations are also used to compare six different slotted and non-slotted radial and axial flux SPM machines in terms of torque/power density, efficiency, utilization, heat dissipation, and weight.

Cosovic et al, [19] apply the genetic algorithm to minimize a weighted sum of five normalized objectives for a four-phase switched reluctance machine: minimal torque ripple, maximal torque factor, torque quality factor, torque density, and losses factor. The calculation of machine designs' static characteristics and the implementation of the optimization are done by a combination of 2D FEM software Maxwell and the MATLAB programming language.

Hong et al. [20] introduce an optimum design process for designing PM type transverse flux linear motors with weight reduction and improvement in thrust force, while maintaining the



detent force of the initially designed machine. The response surface method is adopted to help reduce the number of iteration of experiments in the optimization.

Messine et al. [21] propose a deterministic Branch and Bound algorithm associated with internal arithmetic, which is then applied to the dimensioning of a slotless PM machine. The results show that the algorithm is capable of locating the global optimum within a relatively short lapse of time.

Omekada [22] applies the Taguchi two-step optimization method as well as the zero point proportional dynamic response in order to optimize the torque and the torque-per-inertia for switched reluctance motors. Finite element analysis is used to compute the performance of the motor designs generated by the Taguchi experiment design method.

Sulaiman et al. [23] apply a deterministic optimization method to design the wound field flux switching machine with non-rare-earth magnets for hybrid electric vehicle drive applications. This achieves maximum torque and power under the designated restriction. 2D finite element analysis is used to evaluate machine performance.

Tapia et al. [24] use an optimization procedure based on the Lagrange multiplier to maximize the airgap apparent power under tangential stress constraints for large PM generators. The authors develop a correction procedure for the analytical model to take into account both the non-ideal condition established by the slots-teeth group as well as iron characteristics, in order to improve the torque capacity of the designed lamination.

Wang et al. [25] present an iterative method for the stator design optimization of the brushless doubly-fed machine (BDFM) based on a per-phase equivalent circuit model and a tabu search

method. Maximum power output from a frame size 180 BDFM is obtained by optimally dividing the overall electric and magnetic loadings between the stator windings.

Liu et al. [26] adapt an advanced mathematical method, the filled function method (FFM), in order to seek the global minimum of the multi-modal model of electrical machines. The configuration of the FFM in a constrained environment, the construction of the optimization algorithm, and the implementation of the software are discussed in details.

Sharifian et al. [27] implement the multi-objective optimization of induction motor design by employing the weighting method and a combination of finite element analysis and the conjugate direction search algorithm. A high efficiency induction motor design is found using this optimization program.

Idir et al. [6] adopt the artificial neural networks (ANNs) techniques in order to optimize a set of design parameters for induction motors within a given set of specification and desired constraints. It is pointed out that the training patterns for the ANNs can be generated by the FE method, an expert system, or an experienced design engineer. This technique is capable of finding the optimal design in a relatively reduced computational time by avoiding intensive use of the FE method.

Idir et al. [28] introduce a new optimization approach for designing electric machines, which uses an error function between the actual objective function, at a given computational step, and its limit value to search for the global minimum. The method has been effectively utilized to improve the performance of induction machines.

Dabrowski et al. [29] demonstrate the application of optimization techniques on induction machines using non-linear programming with the turn number and wire diameters of windings

treated as independent discrete variables.  $(\mu+\lambda)$ -ES,  $(\mu\lambda)$ -ES and the modified genetic algorithm (GA) are tested for effectiveness. By comparison,  $(\mu+\lambda)$ -ES is found to be the best algorithm.

Fodorean et al. [30] optimize the power density and the energetic performance of permanent magnet (PM) machines with fractional slot configuration by using a hybrid optimization algorithm that combines simulated annealing and particle swarm optimization techniques.

Ilea et al. [31] apply particle swarm optimization in order to find the best compromise between torque and torque ripple for a switched reluctance machine (SRM), accounting for its switching strategy. The permeance network analysis is adopted for the modeling of the SRM. It considers both the magnetic phenomena and the control scheme accurately, and in addition, it helps to reduce the computation time.

Oh et al. [32] develop a new algorithm, consisting of the genetic algorithm in conjunction with the direct search method, for optimizing DC motor designs. The genetic algorithm is used for locating the global optimum region while the direct search method is applied to achieve objective function convergence. The field and torque characteristics of the DC motor are computed using the FE method.

Mohammed [33] discusses several issues for the practical implementation of the genetic algorithm (GA) to optimization problems, and examines the possibility of premature convergence in the implementation of GA in some applications.

Sakthivel et al. [34] propose a modified particle swarm optimization (MPSO) algorithm for optimizing the design of a three-phase squirrel cage induction motor with active power loss effects. The proposed algorithm employs the modified inertia weight and acceleration factors to

enhance the performance of general PSO. In addition, an efficient constraint treatment approach is adopted.

Kan et al. [35] propose an improved particle swarm optimization algorithm for solving the parameter design optimization of brushless doubly-fed machine (BDFM) based on the equivalent circuit method. It is demonstrated that electric loadings and magnetic loadings can be optimally divided between the stator windings to maximize the torque output from a prototype BDFM.

Deihimi [36] demonstrates a systematic approach for optimizing switched reluctance machines under a voltage PWM control strategy. In the optimization process, all operating points of the machine are taken into account in order to evaluate the global machine-drive efficiency using a fuzzy decision machine technique.

Nguyen et al. [37] present a simplified analytical model of a brushless DC machine as well as a discretized travel time computing method. Three optimization algorithms of MATLAB (SQP, direct search, and genetic algorithm) are applied to optimize the time it takes for the machine to drive a variable load to fulfill its trajectory. The advantages and drawbacks of the three algorithms are compared.

Chen et al. [38] adopt a sequential surrogate optimizer, the default method for optimization with finite element analysis in Got-It, to maximize the energy efficiency of a traction machine over the New European Driving Cycle (NEDC). 12-point representation of the energy distribution of the NEDC for the given vehicle parameters has been utilized for the optimization process.

Duan et al. [39] optimize the design of a surface mounted PM machine with PSO and GA respectively, where an analytical model is used to evaluate machine performance. The

performances of PSO and GA are compared in terms of accuracy, robustness to population size, and algorithm coefficients. It is demonstrated that PSO has advantages over GA in these aspects and is preferred when computation time is a constraint.

Wen et al. [40] optimize two interior PM machines by directly coupling finite element analysis with the machine design guidelines embedded in the optimization process. Multivariable optimization methods based on Monte Carlo and differential evolution (DE) algorithms are applied respectively. Comparison results indicate that DE is a reliable method for machine design optimization problems.

Zarko et al. [41] propose a multi-objective optimization procedure for the design of interior PM motors based on the differential evolution algorithm in order to minimize the active volume of the motor and maximize its characteristic current.

Duan et al. [42] demonstrate the efficient use of a design of experiment (DOE)-based sensitivity analysis for reducing the number of independent variables to be used in a electric machine design optimization program. Additionally, an improvement in the differential evolution algorithm is represented by a newly proposed stopping criteria combining information provided both by the design and the solution space.

Duan et al. [43] review the developments of the last decade in the area of machine design optimization, including surrogate modeling of electrical machines, and direct and stochastic search algorithms for both single - and multi - objective design optimization problems. Response surface and differential evolution (DE) algorithms are compared on a bi-objective optimization benchmark represented by a PM synchronous motor. The numerical results indicate the superiority of the DE algorithm.

Sizov et al. [44, 45] present the computationally efficient finite element analysis (CE-FEA) method and apply it to a parametric design study of an interior permanent magnet machine. Significant reduction of simulation times is achieved (approximately two orders of magnitude) by using this method, permitting a comprehensive search of large design spaces for optimization purposes.

Lee et al. [46] propose a new type of memetic algorithm implemented with the genetic algorithm and a guided mesh adaptive direct search method, which contributes to fast convergence and search reliability. An optimal interior PM machine design is found effectively using this optimization algorithm.

Yamazaki et al. [47] introduce the adaptive finite element method for minor shape modification in the optimization process, which provides the mesh of the new shape with the least modification from the old one in order to reduce the calculation time and improve the quality of the optimized results.

Ma et al. [48] propose the reduced-basis finite element method (RBFEM), where the order of the reduced-basis matrix is much smaller than the number of nodes, and its sets of data values cover the entire regime, including all FEM solutions. As a result, the computational effort can be cut down without significantly affecting the accuracy of the FEM solution using this approach.

Okamoto et al. [49] present the 3-D topological optimization method based on utilization of the genetic algorithm, which is able to obtain a practical solution and improve the convergence by reducing the design space. Moreover, the elapsed time of the 3D optimization can be further reduced to a quarter of the conventional analysis through the nonconforming mesh connection.

Lahteenmaki [50] applies a genetic optimization algorithm to minimize the losses for high-speed motors using finite element analysis. The optimization takes over 200 hours of computation with 50 to 60 designs per population and over 150 generations in total. 6 to 12 parallel CPU-processors are applied during the process.

Schoning [9] introduces an automated design process using the differential evolution optimization algorithm with the FE simulations performed on a high-performance cluster. During this process, the time consuming iterative design optimization is done autonomously. The developer's knowledge is included in the form of weighting factors in the objective function.

In the development of machine design optimization algorithms, high accuracy is desired throughout the entire solution space along with fast computational speed. FE analysis is often the preferred analysis tool for electric machines because of the highly nonlinear nature of the machines' electromagnetic characteristics. Unfortunately, the adoption of FE analysis in multi-dimensional search programs to find optimal designs has generally been impractical because of the intensive computational load imposed by conducting FE analysis of such a large number of candidate designs. As a result, only a few researchers have reported efforts to pursue this approach [2, 3], despite the fact that the potential benefit of applying distributed computing techniques to finite element analysis and optimization of electric machines has been recognized for many years [4].

A high-throughput computing (HTC) environment is available at UW-Madison that harnesses the parallel processing capabilities of more than 10,000 cores; it is known as Project Condor [5]. The availability of these distributed parallel computing resources offers opportunities for

significantly reducing the total computational time for the iterative optimization of electric machines, making FE analysis much more attractive for this task.

There are many different optimization algorithms used in machine design optimization. Differential evolution (DE), particle swarm optimization (PSO), and genetic algorithm (GA) are the three optimization algorithms discussed most widely in publications [51-56]. DE, PSO, and GA all fall into the class of population-based, stochastic function minimizers. As such, they are all well-suited for machine design optimization, which is a nonlinear and constrained problem involving both continuous and discrete variables. One recent study compares DE and many other optimization algorithms[57]. The results show that DE may not always be the fastest method, but it is usually the one that produces the best results, and there are frequent cases in which it is the fastest algorithm as well. Since DE is a population-based algorithm, it is suitable for adoption in a distributed parallel computing environment.

Considering the two most important aspects of electrical machine optimization—model accuracy and simulation time—this work focuses on the implementation of a machine design optimization algorithm based on FE analysis in a high-throughput computing environment. Differential evolution is selected as the optimization algorithm in order to help efficiently locate the optimal design.

### **1.3.2 Coupled Electromagnetic and Thermal Machine Modeling**

There is a fair amount of literature on the topic of coupled electromagnetic and thermal modeling of electric machines, including mono-directional coupling and bi-directional coupling that takes temperature-dependent material properties into account. The publications most relevant to this thesis topic are presented in this section.



Barcaro et al. [58] design a surface PM motor for a submersed catamaran propeller with an accurate coupled magnetic and thermal analysis, where the FE method is used for magnetic analysis while the lumped parameter network is used for thermal analysis. The mono-directional coupling is adopted, which suggests that the thermal analysis is used to check if any temperature constraint is violated.

Hafner et al. [59] couple an electromagnetic dimensioning model parameterized by FE analysis with its associated thermal lumped-parameter model to estimate the magnet and winding temperature. Although it is only unidirectional coupling, this process helps to prevent irreversible material damage and keep the machine parts below their maximum temperature limits.

Lateb et al. [60] develop a coupled model to estimate the main performances of induction machines (IMs) for ship propulsion systems, taking into account saturation, thermal constraint and space harmonics. A combination of the FE model and the multi-harmonic equivalent circuit is applied in order to establish the electromagnetic model of a squirrel cage IM, while the thermal model used for checking temperature constraints is based on an equivalent thermal network.

Hruska et al. [61] design an air self-cooled hub-wheel PM synchronous machine from an electromagnetic point of view using finite element analysis, while the thermal analysis is performed to evaluate whether any kind of forced cooling is required for the designed machine in its nominal state.

Bo et al. [62] present an algorithm for mapping the element loss calculated in 2D FE electromagnetic analysis into its corresponding 3D FE thermal model to calculate transient

temperature field. This method takes the stator core loss distribution as the heat source for thermal analysis rather than the loss as a whole, resulting in more accurate results.

Huang et al. [63] link the core loss calculated from 3-D FE electromagnetic analysis directly into its associated thermal calculation by keeping the same hexahedral mesh structure between magnetic field analysis and thermal analysis. Therefore, the accurate temperature distribution of the stator core can be obtained.

Schoning et al. [8] introduce a thermal FE solver using boundary conditions to take slot insulation and air gap into account, which results in a significant reduction in the computation time. The values for the heat flow coefficients used for setting up the boundary conditions are determined by measurements.

Ahn et al. [64] deal with the prediction of temperature rise for a power transformer through coupled electromagnetic-thermal-fluid field analysis. The FE method is adopted for both the electromagnetic and thermal analysis, and the temperature-dependent material property of coil windings is taken into account during the iterative process to increase accuracy.

Alberti et al [65] apply an object-oriented programming-based thermal network to work in conjunction with the electromagnetic FE model of electrical machines, where temperature-dependent material properties are taken into account during the iterative coupled analysis. The magnetic analysis and thermal simulation are carried out separately with different time steps, different intervals and different modes (steady state vs. transient).

Bracikowski et al. [66, 67] build a design model for a PM synchronous machine for traction applications, taking into account different physical aspects, such as electromagnetics, thermics, mechanics, and acoustics, each of which is represented by its associated lumped parameter

network. The coupling between electromagnetic and thermal analysis is bidirectional, which takes temperature-dependent stator resistance and magnet coercive field into account.

Chun et al. [68] introduce a new model for the optimal design of a surface PM machine, which corrects stator resistance and magnet residual flux density through an iterative process combining the characteristic analysis with the thermal analysis. The characteristic analysis is made by the FE method, while the thermal analysis is done through the heat equivalent network.

Driesen et al. [69] propose algorithms to perform coupled thermal-electromagnetic FE calculations using an iteration loop involving a single FE magnetic model and one or two thermal FE models. The thermal anisotropy of the opposing slot/tooth combinations is handled by radial averaging of temperature.

Khliissa et al. [6] develop a multi-physical modeling approach for a PM machine used as an integrated starter generator. FE analyses are applied for evaluating electromagnetic behavior, while temperature distributions are computed by equivalent lumped parameter networks. Bidirectional electromagnetic-thermal coupling is adopted, where the temperature-dependent electrical resistances and magnet properties are taken into account.

Traxler et al. [70] introduce a computation method where the power loss, airflow, and temperature calculations for a large air-cooled synchronous machine are coupled in an iterative process. Electrical losses are calculated by an analytical model, while the thermal model is based on a nodal network that can identify hot spots on the windings. The critical parameters are derived from model tests, literature, and computational fluid dynamics (CFD) analysis.

Yan et al. [71] analyze the 3-D temperature field of an air core power reactor, whose heat sources are losses calculated from 3-D magnetic field analysis. An iterative method is adopted

for predicting the temperature distribution, since losses are changing corresponding to the variation in temperature.

Driesen et al. [72] discuss ways of handling the large difference in time scales encountered in the simulation of a coupled electromagnetic-thermal field problem. It is indicated that the high ratio between the largest and smallest time constants associated with the two types of analyses yields numerical stiffness, making it possible to separate some of the dynamic phenomena at different time scales.

Fireteanu et al. [73] introduce a coupled magnetic and thermal transient FE model for studying the heating of the squirrel-cage rotor of induction machines during motor startup, where temperature-dependent material properties are taken into account. The thermal time step is specified to be equal to an integer number of semiperiods of the electromagnetic field, and the heating source is set up by the mean value of the instantaneous volume density of the Joule power over the thermal time step.

Rothe et al. [74] present a method allowing for the calculation of motor life expectancies with regard to variable periodic motor temperature. The temperature is derived from assumed periodic driving cycles and is calculated with the powertrain simulation tool ADVISOR, where the thermal motor model is simple and based on a single heat capacity.

Vong et al. [75] introduce an FE modeling of coupled electromagnetic/thermal problems, where the coupling is weak between the two physical aspects due to the fact that thermal time constants are relatively very long. The time-harmonic and time-transient thermal methods including non-linear surface convection and radiation terms are adopted.

Today's machine design optimization is typically accomplished using a maximum limit on the stator current density as a surrogate for the underlying maximum temperature constraints that cannot be directly incorporated into electromagnetic (EM) finite element (FE) analysis. A coupled EM/thermal model is needed for more accurate prediction of the machine's performance limits. The availability of fast thermal FE solvers and high-throughput computing environments makes it possible to rapidly and accurately predict a machine's thermal response in demanding applications, including the detection of nonlinear phenomena such as hot spot winding temperatures [8-10].

The EM and thermal models are directly linked because of the temperature-dependent properties of the machine materials including copper, lamination steel, magnets, and coolant. Due to the multiple nonlinearities of the coupled EM/thermal problem, an iterative procedure is required in order for the EM and thermal FE analyses to converge into a self-consistent solution [11].

In this research, a 3D thermal FE model is adopted for the thermal part of the coupled analysis. The thermal model is linked to its associated 2D electromagnetic FE model in an iterative fashion by taking temperature-dependent material properties into account, which can significantly help to improve the accuracy of the results from this coupled analysis. In addition, although the electromagnetic and thermal analyses are linked, they are performed separately due to the large difference between the electrical and thermal time constants [76].

### **1.3.3 Coupled Electromagnetic/Thermal Machine Design Optimization**

The thermal aspects have been incorporated into the machine design optimization process by either evaluating the temperature constraints or optimizing the utilization of electrical loading.

The goal of this section is to present a review of coupled electromagnetic/thermal machine design optimization.

Cao et al. [10] present an overview of electric motor technologies used for electric aircraft, with a comparison of the relative merits and disadvantages of caged induction, SR, and PM motor drives using analytical methods. The thermal robustness of these candidate machines is also discussed.

Ganev [77] analyzes and optimizes electric machines for high performance electric drives using those aspects of Six Sigma theory that relate to critical-to-quality subjects. Thermal limitations are considered as part of the machine evaluation criteria.

Zhu et al. [78] present a software platform that has the optimization capacity to seek optimized solutions for any single subject at will, in order to conceptually design a hydraulic generator. It is pointed out that the system level's optimization should be completed through multi-disciplinary analysis.

Cho et al. [79] propose optimal design of an induction motor for an electric vehicle using a niching method that adopts restricted competition selection. The thermal equivalent circuit method is used to analyze transient winding temperature rise, which is part of the evaluation criteria.

Debusschere et al. [80, 81] propose a suitable model for heavily saturated single-phase permanent capacitor induction machines used in a very specific context, where the machine operations are purely transient. The thermal constraints are checked while optimizing the machine over its life cycle in order to minimize energy cost.

Drouen et al. [82] couple electromagnetic (EM) and thermal models of the PM generator and hydrodynamics models of the turbine blades to optimize the global efficiency for a rim-driven marine turbine generator for a sail boat. An analytical model is used for EM analysis, while a lumped parameter model is adopted for thermal analysis. The results from the thermal analysis help to evaluate whether the winding temperature exceeds the thermal constraint.

El-Refaie et al. [83] present a lumped-parameter thermal model for a multi-barrier interior PM synchronous machine, which is used in an iterative Monte Carlo design optimization algorithm. During the optimization process, the thermal model is used to predict the winding and magnet temperature to determine whether they exceed the thermal limits, and any candidate design that does not meet the thermal requirements is rejected.

Encica et al. [84] optimize a slotted tubular PM actuator for minimum mass using the output polynomial space mapping technique, when both electromagnetic and thermal aspects of the machine are considered. A lumped parameter thermal model is applied for checking temperature constraints.

Gilson et al. [85] optimize both electromagnetic and thermal designs for a PM synchronous machine for aerospace actuation systems. This goal is achieved by linking up the electromagnetic design process and the motor housing design process and searching for a design with overall minimum mass, where the thermal analysis is used for evaluating temperature constraints.

Jannot et al. [86] optimize an interior PM machine for high efficiency and low weight using a multi-physics model. Analytical models are adopted for both the electromagnetic and the thermal parts of the analysis. The coupling between electromagnetic and thermal phenomena is obtained by solving the depending equations of losses, thermal field, and physical properties using a

fixed-point method. GA is chosen as the optimization algorithm, and thermal constraints are taken into account during the optimization process.

Keysan et al. [87] apply GA to optimize a PM machine for a tidal current turbine in order to achieve maximum annual electricity generation and minimum generator cost, using an electromagnetic, structural and thermal coupled analytical design tool. The thermal model used to evaluate thermal constraints during the optimization process requires an iterative process to take temperature-dependent winding resistance into account.

Khliissa et al. [88] adopt space-mapping techniques to optimize a PM machine used as an integrated starter generator with a coupled electromagnetic and thermal modeling approach. The thermal constraints are evaluated during the optimization process, and temperature-dependent material properties are taken into account.

Legranger et al. [89] integrate a coupled electromagnetic and thermal model into a sequential simplex optimizer for the interior PM machine, where temperature-dependent material properties are taken into account. For the electromagnetic part of the analysis, a magnetic model including dq transformation is adopted along with the finite element method (FEM). For the thermal part of the analysis, a 3-D transient lumped parameter network is applied to predict the temperatures of key points inside the machine.

Legranger et al. [90] apply a sequential quadratic programming method to optimize a rotary transformer for a highly constrained application using a multi-physics model. The magnetic model is based on the reluctance network, while the thermal model is built by forming a thermal resistance network. These two models are linked to SimPowerSystem, a simulation software for electrical circuits.



Makni et al. [91] propose a multi-physics design methodology for PM synchronous motors in two stages. In the first stage, the combination of a coupled electromagnetic-thermal analytical model and a gradient optimization algorithm provides a quick initial solution. In the second stage, the initial solution is further optimized based on a simplex algorithm using an FE model.

Ragot et al. [92] optimize a brushless DC motor for a solar airplane using the commercial optimization software Pro@Design. A multi-physics model that considers electromagnetic and thermal aspects of the machine and includes propeller modeling, is adopted in the software. The thermal part of the model helps to evaluate temperature constraints.

Rossi et al. [93] apply a mixed-variable constrained non-dominating sorting GA to optimize inductors or transformers for railway applications with coupled electromagnetic and thermal models. A 3-D nodal thermal network, allowing the observation of local phenomena as hot spots, is used to check temperature constraints.

Rosu et al. [94] present a complete modeling approach for the analysis of a radial field multipole NdFeB PM cylinder. Electromagnetically equivalent state space variables are first extracted from 3D FE parametric study and then transferred to a circuit simulator to optimize the circuit parameters using GA. Finally, the temperature distribution and structural deformation are predicted using 3D transient FE thermal analysis and 3D FE stress analysis, respectively.

Wrobel et al. [12] present a detailed analysis of the impact of initial design decisions on the final performance of a brushless PM hub-motor. It shows that the initial choice of current density has a much more significant impact on the machine thermal performance than the initial choice of flux density in the core.

Gerada et al. [95] use a multi-domain design environment to find the optimal split ratio of a machine's electrical and magnetic loadings in order to achieve the highest power density and ensure mechanical robustness in the meantime. During this process, equivalent weight is placed on electromagnetic, mechanical, and thermal aspects. It is pointed out that the optimal split ratio is usually found when materials are operated closer to their thermal and mechanical limits.

Bianchi et al. [96] present the design of a 1kW PM brushless motor operating at 20-40 krpm using coupled electromagnetic and thermal analysis. The torque is maximized by adopting the maximum stator current density estimated by thermal limits and possible PM demagnetization.

Marquez-Fernandez et al. [97] present the optimization of an electric motor for a hybrid passenger car using a coupled electromagnetic and thermal model. At first, static thermal analyses are performed to iteratively determine the maximum current density loading of the windings, according to given temperature limits and cooling conditions. Then the electromagnetic characteristics of the machine are evaluated at different operating points by a set of static electromagnetic FE analyses.

Meessen et al. [98] couple a semi-analytical magnetic field description with thermal models to create a tubular actuator design that can achieve a translator acceleration of 20 g. It is pointed out that the current density can be determined based on the temperature difference between the armature and the ambient, as the electrical performance of the actuator is mainly restricted by thermal constraints.

Momen et al. [99] present a design methodology for an optimal switched reluctance machine incorporating the thermal response, where the current density is selected considering optimal

utilization of magnetic and electrical loading. A lumped parameter thermal model is used to estimate machine temperature rise.

Reinap et al. [100] develop a machine design environment for the numeric modeling and analysis of radial flux machines. During the optimization process, the maximum current density of the windings is analytically determined by the cooling conditions and the maximum allowed temperature rise.

Semidey et al. [14] present a novel integrated electromagnetic-thermo-mechanical design method for designing a surface mount PM machine, where particle swarm optimization is chosen as the optimization algorithm. The current density is defined as a variable parameter during the optimization process. Since all analytical models are applied, the proposed approach has the merit of good computational efficiency.

Wang et al. [13] establish analytical formulas for predicting the parameters and performance of radially magnetized, iron-cored, tubular PM machines and drive systems. The machine can be optimized by taking thermal constraint into account; in other words, the permissible current density can be defined by the allowable temperature rise for a specific cooling arrangement.

Wu et al. [101] present the design optimization of SRMs for HEV applications, using a combination of 2D electromagnetic FE analysis, experience from previous designs, 3D correction factors, simple lumped parameter thermal models, and computer search techniques. During the optimization process, the peak current density at peak power and continuous power operations are set as variables.

The maximum torque production capability of an electrical machine typically depends on how high the winding current density can be raised before reaching a maximum temperature threshold

[12]. As a result, determining the maximum current density limit is crucial for optimizing a machine's performance. Techniques for determining the maximum current density include selection of values based on past experience with other similar machines, as well as calculations using closed-form equations derived from analytical models [13]. An alternative approaches uses the current density as a variable during a multi-dimensional search process that requires checking the predicted maximum machine temperatures after every iteration [14]. However, the use of winding current density as a means of determining the thermal performance limits of electrical machines is indirect, inaccurate in many cases, and time consuming, especially for applications with significant transient operation.

In this study, procedures to quickly find the maximum current density using the coupled EM/thermal model are proposed for machine operating at both static and transient operation conditions. In addition, a new approach for optimizing a machine design with a specified peak/continuous power ratio requirement is also developed, which is valuable for designing machines that operate regularly with high transient loading.

## **1.4 Thesis Layout**

This thesis is organized as follows:

- Chapter Two presents the target application and candidate machine configuration selected for this study. The implementation of this FE analysis-based machine design optimization program is demonstrated, along with a description of the applied optimization algorithm—differential evolution. The tuning of the optimizer control parameters and objective function is discussed as well.

- Chapter Three introduces Project Condor, a high-throughput computing (HTC) environment used in this study, in which the FE analysis-based machine design optimization is implemented to facilitate a major reduction in computation time. Comparison of the test results delivered by the Condor HTC resources and a single computer is demonstrated, followed by a discussion about improving the acceleration factor.
- Chapter Four presents the development of efficient coupled EM/thermal models of electric machines based on FE analysis. The EM and thermal analyses are linked by temperature-dependent material properties. Test cases for this coupled-model analysis have been carried out on three 30 kW (continuous) surface PM machines that are optimized for maximum torque density, minimum cost, and maximum efficiency, respectively, under various current density conditions.
- Chapter Five demonstrates the procedure for quickly finding the maximum current density using the coupled EM/thermal model for machine steady-state operation, and the integration of this procedure into an iterative machine design optimization program. The artificial neural network (ANN) technique is also introduced, which can help to significantly reduce the computation time.
- Chapter Six presents an extension of the FE-based EM/thermal coupled modeling technique for electrical machines that includes the impact of high form-factor operation with large thermal transients. This coupled EM/thermal model, which is capable of efficiently identifying the maximum current density for a given machine design during transient operation is also integrated into the optimization program with the application of ANN techniques.

- Chapter Seven discusses the generalization of the optimization techniques for a different machine configuration—the interior permanent magnet (IPM) machine. The procedure to optimize an IPM machine for the U.S. Drive specification is also introduced with the application of the coupled EM/thermal model.
- Chapter Eight uses regression analysis to evaluate the sensitivities of the machine design parameters and the coefficients used in the thermal model. The key thermal coefficients are estimated by analyzing the experimental results.
- Chapter Nine concludes this thesis with a summary of the work presented in previous chapters, identifying the new technical contributions that provide the basis for this Ph.D. research program. A proposal is presented for future work to extend this research topic.

## **Chapter 2: Electromagnetic Machine Design Optimization**

### **2.1 Target Application and Machine Configuration**

These days, electric traction drives have been the target of major design initiatives. In order to achieve high fuel economy, the electric machine, as one of the key components of the power train, must fulfill a long list of requirements, such as high power density, high efficiency, wide constant power speed ratio, and low ripple torque. Therefore, optimization techniques are desired for designing a satisfactory electric machine for this type of demanding application. Moreover, the machine should be optimized not just for one single operating point but also for an entire torque-speed envelope, indicating that a large amount of computation efforts are required. These features associated with the electric vehicle application can help to distinguish the significance of this work. Therefore, it was chosen as the target application to conduct this research.

The candidate machine selected for this study is a 30 kW (continuous) fractional-slot concentrated winding (FSCW) surface PM machine, configured with 10 poles and 12 stator slots. This machine configuration has been developed as part of an investigation of FSCW-SPM machines for high-performance traction machine applications [102]. A prototype FSCW machine was designed and built for this application with an active mass of 27.8 kg that includes the stator and rotor electromagnetic assemblies [103].

The prototype machine was designed for the FreedomCAR (now renamed U.S. DRIVE) advanced traction motor specifications (Table 2-1), while the specifications used for this study are shown in Table 2-2. The specifications for this study differ from the FreedomCAR specs

primarily by concentrating their focus on machine performance at the corner point operating conditions, i.e.,  $n = 2800$  r/min,  $P = 30$  kW (continuous).

**Table 2 - 1: FreedomCAR Specifications [103]**

Parameter/Metric	Value
Peak Power @ 2800 r/min	55 kW
Maximum Speed	14,000 r/min
Continuous Power	30 kW
Mass Power Density for Total Machine	>1.6 kW/kg
Volume Power Density for Total Machine	>5.67 kW/l
Constant Power Speed Ratio	5:1
Maximum Phase Current	400 Arms
Peak Line-Line Back-EMF @ 2800 r/min	600 V
Efficiency at 20% Rated Torque up to the Max. Speed	> 95%

**Table 2 - 2: Prototype FSCW-SPM Traction Machine Key Dimensions and Material Characteristics**

Parameter/Metric	Value
Continuous Power Rating [kW]	30
Rated Speed [r/min]	2800
Stator Outer Diameter [mm]	274.2
Airgap Thickness [mm]	1
Banding Thickness [mm]	1.5
Current Density [ $A/mm^2$ ]	4.6
Copper Fill Factor [%]	50%
Copper Resistivity [nOhm-m]	25 @ 150 °C
Steel Lamination Material, Packing Factor	M19, 95%
Remanent Flux Density [T]	1.1 @ 150 °C
Magnet Coercive Force [kA/m]	800
Hysteresis Loss Coeff. [ $W/m^3/Hz$ ]	256
Eddy Current Loss Coeff. [ $W/m^3/Hz^2$ ]	0.37
Copper Density [ $kg/m^3$ ]	8940
Steel Density [ $kg/m^3$ ]	7850
Magnet Density [ $kg/m^3$ ]	7450
Copper Price [\$/kg]	5
Steel Price [\$/kg]	1
Magnet Price [\$/kg]	55

An electromagnetic FE model has been built based on the parameters provided in [103], and its cross-section is compared with that of the prototype machine in Fig. 2-1. Based on the operating condition specified in Table 2-2, the rated torque is  $T = 102.3$  Nm. The FE model of



the prototype PM machine predicts an average torque of 100.7 Nm for corner point operation, while the experimental test results show that the prototype machine is able to deliver an output torque of 99.7 Nm under these conditions [102]. As a result of this good agreement, there is confidence that the FE model can be adopted for this study to accurately evaluate the torque production characteristics of candidate FSCW-SPM machine designs.

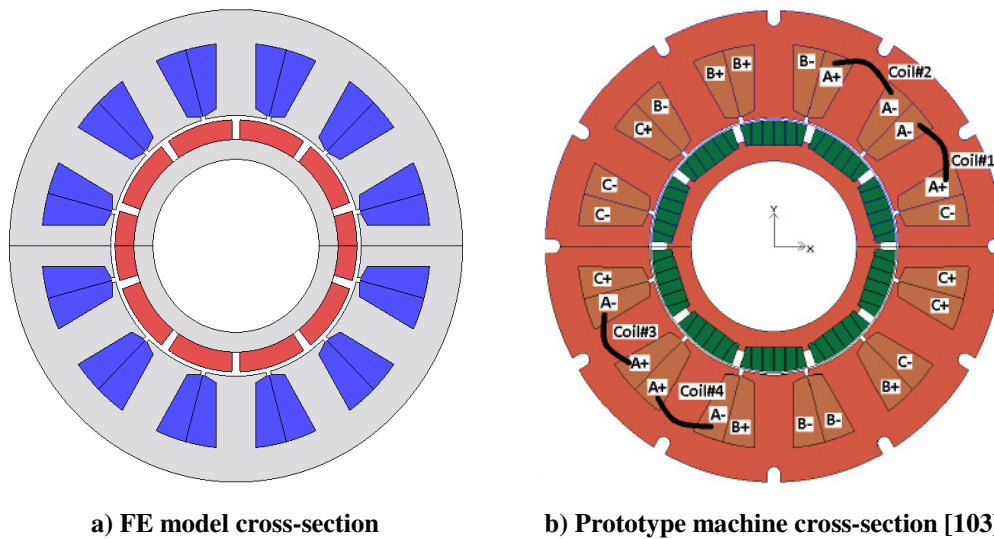


Fig. 2 - 1 :FE model cross-section compared with the prototype machine

## 2.2 Optimization Algorithm: Differential Evolution (DE)

Machine design optimization is a nonlinear and constrained problem involving both continuous and discrete variables. The dependency of the objective function and its gradients on the design parameters is unknown, when the FE analysis method is used for evaluating machine performance. DE is a very simple population based, stochastic function minimizer, which fulfills all the requirements for machine design optimization. In particular, it provides the opportunity for parallel analysis of all designs within each generation. This unique combination of characteristics are why DE was selected for this study. Through initialization, mutation,

crossover and selection, DE is able to explore the entire design space and locate the global optimum with high confidence [57, 104]. Each is described briefly as follows:

### 1. Initialization

$$x_{j,i,0} = rand_j(0,1) * (b_{j,U} - b_{j,L}) + b_{j,L} \quad (1)$$

where  $\mathbf{x}$  represents the vector of adjustable machine design variables. The subscript 0 represents the initial generation (i.e.  $g = 0$ ),  $j$  and  $i$  represent the  $j^{th}$  parameter of the  $i^{th}$  vector in the initial generation of variable vectors,  $rand$  is a scalar random number between 0 and 1, and  $\mathbf{b}_L$ ,  $\mathbf{b}_U$  are initialization lower- and upper-bound vectors, respectively.

### 2. Mutation

$$\mathbf{v}_{i,g} = \mathbf{x}_{r0,g} + F * (\mathbf{x}_{r1,g} - \mathbf{x}_{r2,g}) \quad (2)$$

In the  $g^{th}$  generation,  $\mathbf{x}_{r0,g}$ ,  $\mathbf{x}_{r1,g}$  and  $\mathbf{x}_{r2,g}$  are three randomly selected vectors of machine design variables. The mutant vector  $\mathbf{v}_{i,g}$  is created by adding a scaled vector difference to the third vector. The scale factor,  $F \in (0, 1+)$ , is an adjustable user-defined scalar variable that controls the rate at which the population evolves.

### 3. Crossover

$$\mathbf{u}_{i,g} = u_{j,i,g} = \begin{cases} v_{j,i,g} & \text{if } (rand_j(0,1) \leq Cr) \\ x_{j,i,g} & \text{otherwise.} \end{cases} \quad (3)$$

The trial vector  $\mathbf{u}_{i,g}$  is assembled from parameter values that have been copied from two different source vectors: the mutant vector  $\mathbf{v}_{i,g}$  and the current vector  $\mathbf{x}_{i,g}$ . The crossover

probability,  $Cr \in [0, 1]$ , is a user-defined value that controls the fraction of parameter values that are selected from the mutant vector.

#### 4. Selection

$$\mathbf{x}_{i,g+1} = \begin{cases} \mathbf{u}_{i,g} & \text{if } f(\mathbf{u}_{i,g}) \leq f(\mathbf{x}_{i,g}) \\ \mathbf{x}_{i,g} & \text{otherwise.} \end{cases} \quad (4)$$

A user-defined objective function (OF)  $f$  is used to evaluate the performance metrics of all candidate designs. DE uses objective function results to formulate choices for the next generation of designs, and the design performance improves with each generation. Once the pre-specified termination criterion is satisfied, the iterative optimization process ends.

## 2.3 Implementation of FE Analysis Based Machine Design Optimization

### 2.3.1 Machine Design Optimization Routine

The machine design optimization routine is described in Fig. 2-2. DE, the optimization algorithm discussed in the previous section, is written in MATLAB to provide the outer shell for this algorithm. Each unique electric machine FE model can be described by an array of parameters, both fixed and varied. A set of varied parameters is assigned by the DE optimizer and fed into a template visual basic (VB) script, which contains information on machine configuration, material properties, excitation and the fixed parameters for generating an FE model, in order to create a specific script for one candidate machine design. Then this script is executed in JMAG, an FE analysis package, to estimate the performance of this design. After this step, the FE analysis results are written in an Excel file and used by the main DE code to evaluate the objective function. If the evaluated objective function value fulfills the convergence

criteria, the optimization run will terminate, otherwise, the whole process will be repeated until the optimum is found.

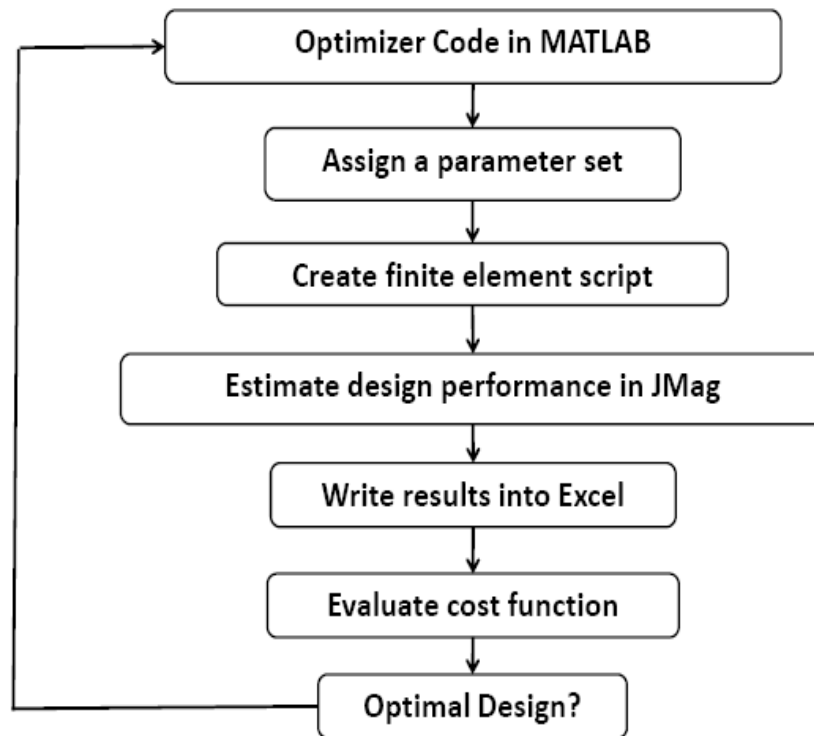


**Fig. 2 - 2: Machine design Optimization Routine**

### 2.3.2 Preliminary Optimization Test Results

The machine design optimization routine has been implemented with the candidate design, i.e. the 30 kW (continuous) FSCW-SPM machine with a 10-poles/12-slots configuration. The fixed parameters are determined by the specifications shown in Table 2-2. The initially proposed variable parameters are shown in Fig. 2-3. These are tooth width, stator yoke thickness, magnet span ratio, rotor yoke thickness, and magnet thickness. The ranges for these variables, shown in Table 2-3, are defined in ratios rather than in absolute values, in order to make sure that each design is within all geometric constraints [104]. Further, they are chosen to be wide enough to

make sure the optimum is inside the searching pool. It is important to note that the airgap radius  $R_g$  is kept at 75.15 mm, the same as the prototype machine [102], at this stage.

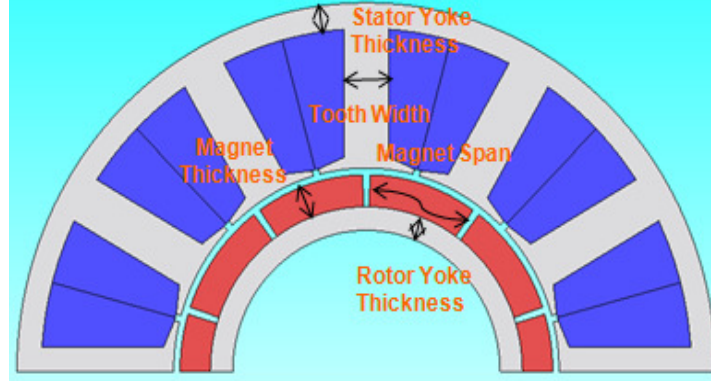


Fig. 2 - 3: FSCW-SPM machine design variables (initially proposed)

Table 2 - 3: FSCW-SPM Variable Definitions and Ranges (Initially Proposed)

Variable Parameters	Range
Tooth Width to Slot Pitch Ratio	[0.1, 0.8]
Stator Yoke Thickness to Tooth Width Ratio	[0.1, 0.8]
Magnet Span to Rotor Pole Pitch Ratio	[0.5, 0.95]
Rotor Yoke Thickness to Rotor Pole Pitch Ratio	[0.1, 0.6]
Magnet Thickness to Airgap Thickness Ratio	[1, 7]

In order to test how this software behaves, it is used to optimize the candidate machine's torque density under the rated operating condition, i.e.,  $n = 2800$  rpm,  $P = 30$  kW,  $T = 102.3$  N\*m, where  $n$ ,  $P$ , and  $T$  represent the rotor speed, power, and torque, respectively. The objective function is then defined as

$$OF_{TD} = \frac{\text{Calculated Active Mass to Produce Required Torque}}{\text{Baseline Machine Active Mass}} \quad (5)$$

where the baseline machine is the one studied previously in [102], with an active mass of 27.8 kg that includes the stator and rotor electromagnetic assemblies. The control parameters for the DE optimizer are chosen as convergence tolerance  $Tol = 10^{-6}$ , number of designs in each

generation  $NP = 25$ , crossover probability  $Cr = 0.8$ , and scale factor  $F = 0.8$ . The reason for choosing these control parameters will be discussed in next section. Since the torque production is the only evaluation criterion for this optimization case, the fast static FE analysis is adopted.

Then this optimization routine is launched. It converges at the 47th iteration, with a total number of 1,175 designs evaluated. The best design is found with a cost function value of 0.785, i.e., a total mass of 21.82 kg. The optimized machine has a mass reduction of 21.5% compared to the baseline machine, which is a significant improvement in torque density. The key dimensions and performance metrics of the optimal design are summarized in Table 2-4. Only copper loss and iron loss are considered for efficiency calculation, since a method for segmenting the magnet has not been determined at this point.

**Table 2 - 4: Details of FSCW-SPM Machine Optimized with Fixed  $R_g$  Using Static FE Analysis**

Parameter/Dimension	Value
Airgap Diameter [mm]	150.3
Active Stack Length [mm]	53.00
Magnet Height [mm]	11.86
Magnet Span [deg. elec.]	32.85
Volume [m <sup>3</sup> ]	0.0027
Copper Mass [kg]	10.97
Magnet Mass [kg]	1.85
Total Active Mass [kg]	21.83
Active Material Cost [\$]	165.49
Torque Ripple [pk-pk/ $T_{rated}$ ]	0.028
Power Factor	0.75
Core Loss [W]	411.69
Copper Loss [W]	774.88
Efficiency	0.96

During the optimization, the objective function value of each evaluated design is recorded. Fig. 2-4 shows the objective function values of designs in Generations #1, #11, #21, #31, and #41. The designs in each of these generations are marked from #1 to #25 in sequence. It can be

seen that the objective function values of the designs in each generation are getting smaller and smaller as the generation number increases. The objective function values of designs in Generation #41, which is close to the final generation (Generation #47), are all about the same—that is, around the final minimum value.

The goal of this optimization is to find the lowest objective function value after evaluating generations of various machine designs. Fig. 2-5 shows the lowest objective function values of each generation as a function of the generation number. It can be observed that the lowest objective function value of each generation decreases across the generations, and it finally converges on the minimum value (i.e. the optimum). There are a few bumps in between, such as Generations #5, #9, and #13, indicating that DE explores the areas outside of previous regions to avoid the chance of being trapped in a local minimum.

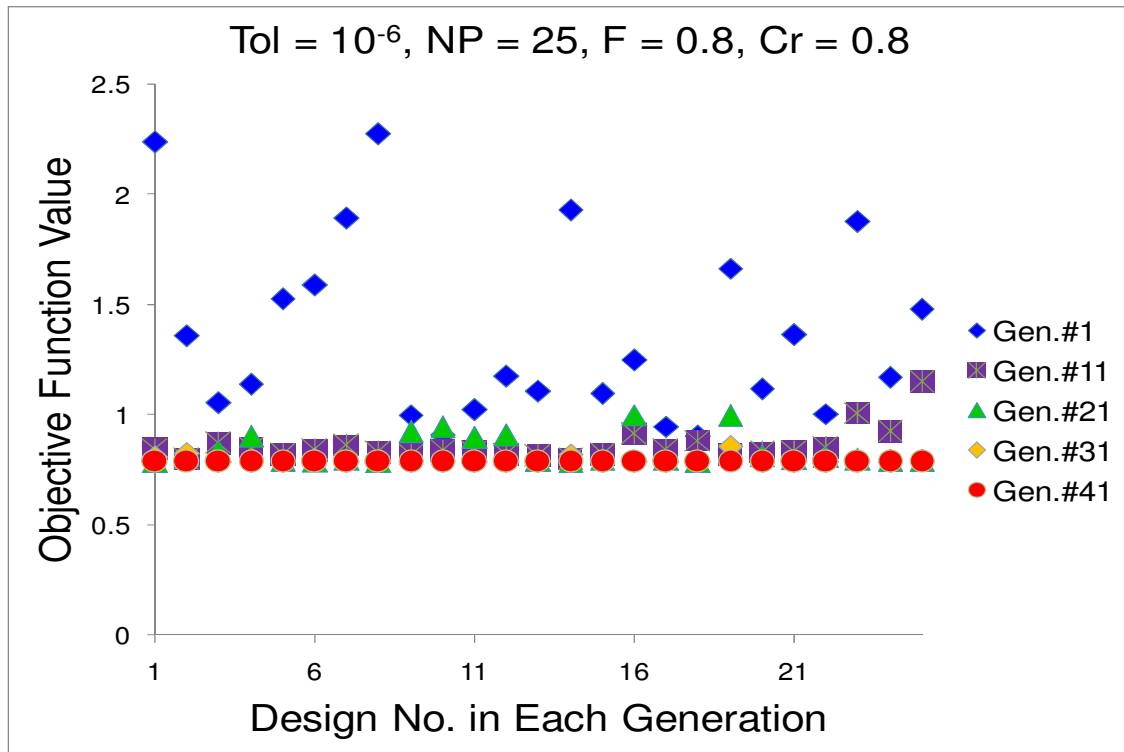


Fig. 2 - 4: Objective function values of designs in Gen. #1, #11, #21, #31, and #41

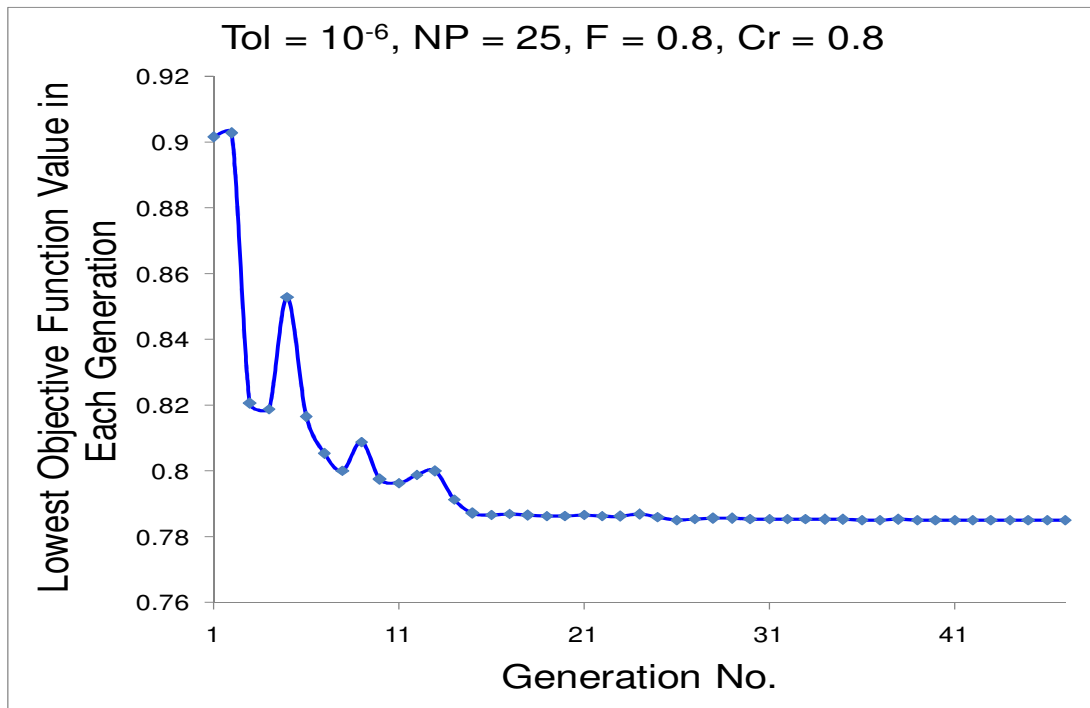


Fig. 2 - 5: Lowest objective function value in each generation

## 2.4 Tuning DE Control Parameters

There are five control parameters of the differential evolution algorithm that need to be determined before beginning an optimization, which are:

1. **Convergence Tolerance (Tol):** This is defined as the difference between minimum objective function values between adjacent generations, which can be used to serve as the thresholds for terminating optimization.
2. **Number of Population Members (NP):** This indicates the number of parallel designs per generation. The minimum value for NP is 5 according to the rules specified for DE, while the maximum value is set at 95 based on the number of JMAG licenses available for this investigation.
3. **Crossover Probability (Cr):** This determines the mutation aggressiveness, and its value falls in the region  $[0, 1]$ .



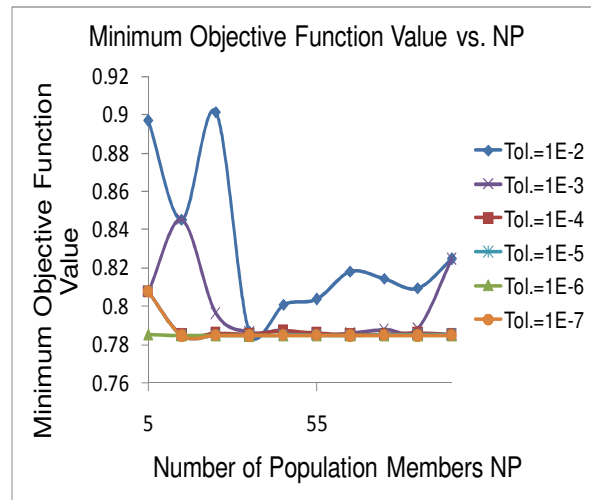
4. **Scale Factor (F):** This controls the rate of evolution. Its value is chosen from the region  $[0, 2]$ .
5. **Maximum Generation Number (MaxGen):** This is defined as the maximum number of generations an optimization goes through, which can either be used alone to terminate the optimization, or in combination with the convergence tolerance **Tol**.

#### 2.4.1 Tuning Tol & NP, Keeping Cr & F Constant

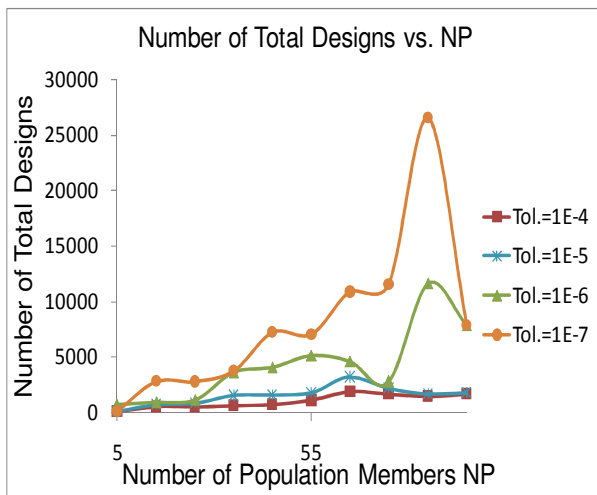
In order to find out the most suitable combination of the four control parameters, parametric tests are conducted in groups. At first, the values of Tol and NP are varied, while maintaining  $Cr = 0.8$  and  $F = 0.8$ . The variation range of the Tol value is from  $10^{-2}$  to  $10^{-7}$  with logarithmic spacing. For each Tol value, the value of NP changes from 5 to 95, with a step of 5. Fig. 2-6 shows the minimum objective function value as a function of NP for each of the Tol values. It can be observed that the smaller the Tol value, the better the result that can be achieved as the minimum objective function value becomes lower. When Tol is set to be less than or equal to  $10^{-4}$ , the accuracy of the results is deemed acceptable. It can also be noticed that the minimum objective function value can be reached regardless of what NP value is used when  $Tol = 10^{-6}$ .

Figure 2-7 shows the total number of evaluated designs in one optimization as a function of NP when  $Tol \leq 10^{-4}$ . It can be observed that the computation cost is higher when the Tol value is smaller, assuming a single computer is used, i.e., each design is evaluated consecutively. For a given Tol value, the total number of designs tends to be lower when the NP value is smaller, which implies that a relatively small NP value is preferred when the optimization is performed on a single computer. Fig. 2-8 shows the number of generations required to reach the convergence of an optimization as a function of NP when  $Tol \leq 10^{-4}$ . It indicates that the

computation cost is higher when the Tol value is smaller, assuming a parallel computing approach is adopted—that is, designs in each generation are evaluated simultaneously. Unfortunately, these test results do not show a clear relationship between the total number of generations and the NP values for each Tol value. Therefore, the best choice of NP value to save computation time can not be determined using parallel computing.



**Fig. 2 - 6: Minimum objective function value vs. NP with various Tol values**



**Fig. 2 - 7: Number of total designs vs. NP with Tol  $\leq 10^{-4}$**

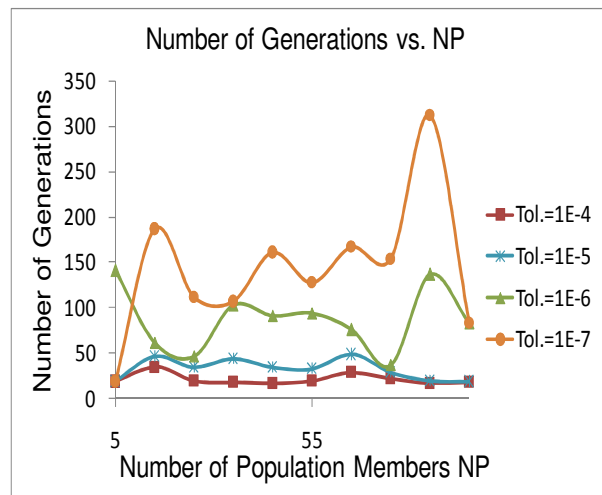


**Fig. 2 - 8: Number of generations vs. NP with Tol  $\leq 10^{-4}$**

### 2.4.1 Tuning Cr & F, Keeping Tol & NP Constant

According to previous test results, the values for Tol and NP are chosen to be  $Tol = 10^{-6}$ , with  $NP = 25$ , for running the optimization in a single computer. In this test, the value of Cr varies from 0 to 1 with a step of 0.2. For each Cr value, the value of F changes from 0 to 2 in a step of 0.2. Fig. 2-9 shows the minimum objective function value as a function of scale factor F for each of the Cr values, indicating that the optimization can always achieve its best value when Cr = 0.8 and F is between 0.4 and 2. As a result, the value of Cr is determined to be 0.8.

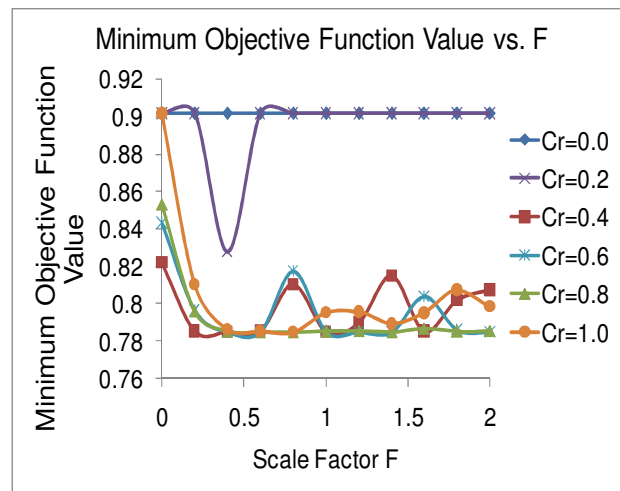


Fig. 2 - 9: Minimum objective function value vs. F with various Cr values

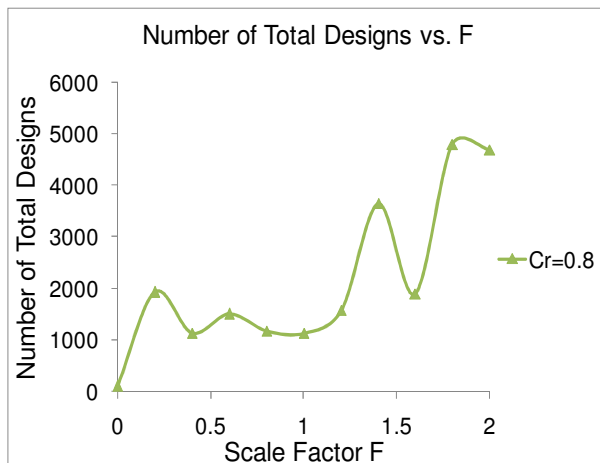


Fig. 2 - 10: Number of total designs vs. F at Cr = 0.8

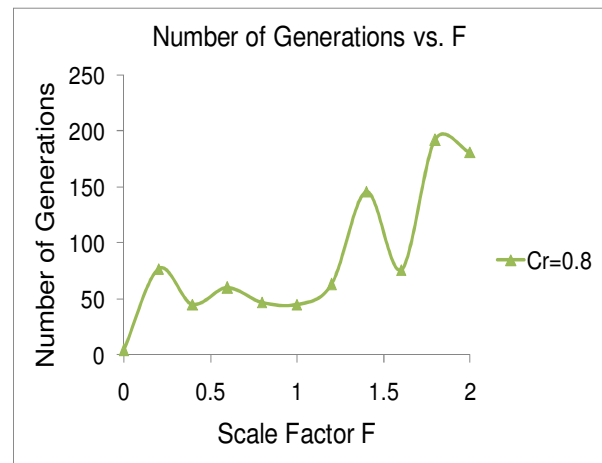


Fig. 2 - 11: Number of generations vs. F at Cr = 0.8

Fig. 2-10 shows the total number of evaluated designs in one optimization as a function of  $F$  when  $Cr = 0.8$ . It can be seen that the computation cost is relatively low when the  $F$  value falls between 0.4 and 1, assuming a single computer is used, i.e., each design is evaluated consecutively. Fig. 2-11 shows the number of generations required to reach the convergence of an optimization as a function of  $F$  when  $Cr = 0.8$ . This suggests that the computation cost is minimized when  $F$  is between 0.4 and 1, assuming a parallel computing approach is adopted—that is, designs in each generation are evaluated simultaneously. To summarize, a suitable combination of the DE control parameters for this study is chosen to be  $Tol = 10^{-6}$ ,  $NP = 25$ ,  $Cr = 0.8$ , and  $F = 0.8$ , for use with a single computer.

## **2.5 Adding One More Degree of Freedom: Airgap Radius $R_g$ Set as Variable**

Previously, the airgap radius  $R_g$  was held constant at 75.15 mm, which is the same as that of the baseline machine [102]. At this stage of the study, the airgap radius is defined as a variable with the ratio of airgap radius to stator outer radius ranging from 0.3 to 0.75, in order to explore the impact of  $R_g$  on the optimization result. Keeping all the settings the same as those mentioned in 2.3.2 but varying  $R_g$ , the optimization is performed again. Table 2-5 shows that this new optimization converges at Generation #180, with a total number of 4,500 designs evaluated with static EM analysis. This optimization ends with a minimum objective function value of 0.7405, which is smaller than that of the optimization with a fixed airgap radius. Hence, setting  $R_g$  as a variable parameter in the optimization helps produce an optimal design with higher torque density. However, the cost of computation also goes up as this additional degree of freedom is added to the optimization.

**Table 2 - 5: Computation Cost and Min. OF Value Comparison between  $R_g$  Fixed &  $R_g$  Varied Optimizations**

	$R_g$ Fixed	$R_g$ Varied
Total Number of Designs	1175	4500
Number of Generations	47	180
Minimum Objective Function Value	0.7850	0.7405

The cross-sections of the optimal machine design with fixed  $R_g$  and the one with varied  $R_g$  are shown in Fig. 2-12, and their key dimensions and metrics are compared in Table 2-6. Only copper loss and iron loss are considered for efficiency calculation, since the method of segmenting the magnet is not specified at this point. It can be seen that the airgap radius and the rotor inner radius of the optimal design with varying  $R_g$  are larger, and its magnet thickness is thinner, while the total amount of magnet is about the same as that of the optimal machine with fixed  $R_g$ . In addition, the optimal machine with varying  $R_g$  has the desirable feature of a high power factor, although its torque ripple (peak to peak ripple/average torque) is a bit higher than that of the design with fixed  $R_g$ . Consequently, the airgap radius is treated as a variable parameter for all of the following optimizations.

**Table 2 - 6: Comparisons of FSCW-SPM Machines Optimized with  $R_g$  Fixed and  $R_g$  Varied**

Parameter/Dimension	$R_g$ Fixed	$R_g$ Varied
Airgap Diameter [mm]	150.3	179.52
Active Stack Length [mm]	53.00	56.20
Magnet Height [mm]	11.86	9.98
Magnet Span [deg. elec.]	32.85	33.09
Volume [m <sup>3</sup> ]	0.0027	0.0025
Copper Mass [kg]	10.97	10.31
Magnet Mass [kg]	1.85	1.99
Total Active Mass [kg]	21.83	20.59
Active Material Cost [\$]	165.49	169.10
Torque Ripple [pk-pk/ $T_{rated}$ ]	0.028	0.043
Power Factor	0.75	0.90
Core Loss [W]	411.69	445.93
Copper Loss [W]	774.88	698.28
Efficiency	0.96	0.96

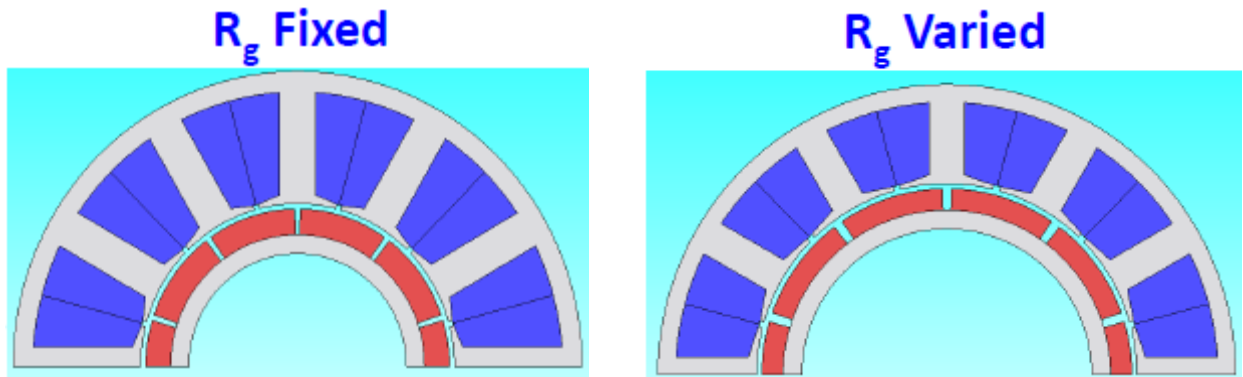


Fig. 2 - 12: Cross-sections of the optimal machine designs with fixed  $R_g$  and varied  $R_g$

## 2.6 Objective Function Tuning

### 2.6.1 Tuning the Objective Function for Various Evaluation Criteria

“Optimal electrical machine” is hard to quantify precisely, and the nature of the optimum depends on the application and objective function priorities, due to tradeoffs between different design metrics. The previous optimization for maximizing a machine’s corner point torque density (with objective function  $OF_{TD}$ ) is run again with transient electromagnetic FE analysis, in order to evaluate each candidate machine’s efficiency, torque ripple, and power factor performance, as well as to estimate its objective function value. The resulting design from this optimization is labeled TD Design. Under the same testing conditions, two additional optimization runs are launched with objective function  $OF_{TPD}$  and  $OF_{Eff}$ . (defined below) to minimize machine cost and maximize machine efficiency, respectively. The machine optimized for low cost is named TPD Design, while the one optimized for high efficiency is called Eff. Design.

$$OF_{TPD} = \frac{\text{Calculated Material Cost}}{\text{Baseline Machine Material Cost}} \quad (6)$$

$$OF_{Eff.} = \frac{\text{Baseline Machine Efficiency}}{\text{Calculated Efficiency}} \quad (7)$$

where the baseline machine cost is estimated to be \$198.2, according to the active material price listed in Table 2-2. The efficiency of the baseline machine is assumed to be 0.95.

The cross-sections of the three optimal machine designs are shown in Fig. 2-13, and the key dimensions and performance metrics for the three optimized machine designs are summarized in Table 2-7. It can be observed that the optimized TD Design machine has the largest slot area and the shortest stack length. The TPD design machine, optimized for minimum cost, has the thinnest magnets. The optimized high-efficiency machine design (Eff. Design) has the thickest magnet, the smallest slot area, and the longest stack length.

Table 2-7 also shows that optimizing the torque density helps to simultaneously reduce the magnet mass, improve the efficiency, and increase the power factor, even though these other metrics are not part of the objective function. However, the optimization does not have much impact on the predicted torque ripple. Taken together, these results suggest that torque density is a good choice for the target for the objective function and that it results in improvements for several important performance metrics of the machine. When the increase in any material price is significant, cost minimization can be added as part of the objective function, although it may lead to a drop in power factor, and vulnerability to demagnetization. Additionally, the objective function should not emphasize purely on achieving high efficiency as it may end up with large and expensive designs.

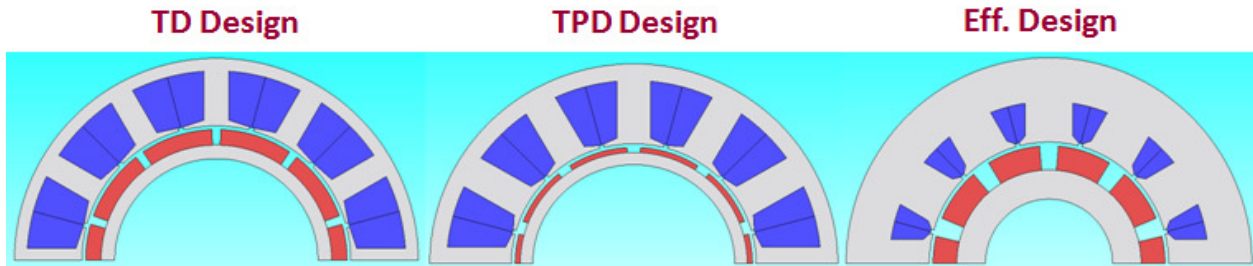


Fig. 2 - 13: Cross-section comparison among TD Design, TPD Design, and Eff. Design

Table 2 - 7: Key Dimension and Performance Comparisons among TD Design, TPD Design, and Eff. Design

Parameter/Dimension	TD Design	TPD Design	Eff. Design
Airgap Diameter [mm]	181.48	163.43	160.67
Active Stack Length [mm]	57.01	82.18	174.66
Magnet Height [mm]	10.46	3.42	16.02
Magnet Span [deg. elec.]	32.14	29.34	26.68
Volume [m <sup>3</sup> ]	0.0025	0.0037	0.0093
Copper Mass [kg]	10.11	10.58	5.60
Magnet Mass [kg]	2.07	0.83	6.56
Total Active Mass [kg]	20.65	27.16	63.76
Active Material Cost [\$]	172.63	114.43	440.19
Torque Ripple [pk-pk/ $T_{rated}$ ]	0.052	0.048	0.032
Power Factor	0.91	0.61	0.96
Core Loss [W]	241.69	399.37	286.93
Copper Loss [W]	598.11	625.77	331.39
Efficiency	0.97	0.96	0.98

## 2.6.2 Tuning the Objective Function for Various Operating Points

For certain applications, the machine is designed for a mix of various operating conditions, rather than one single operating point. Take the traction motor application, for example: the motor has to be designed to achieve a very high constant power speed ratio (CPSR) with the required maximum speed of 14000 rpm, according to U.S. DRIVE specifications [105, 106]. It is important to understand how the resulting designs vary from optimizations focusing on different operating conditions. Therefore, the objective function  $OF_{TD}$  has been applied to find the machine design with highest torque density at two additional operating conditions besides the



corner point ( $n = 2800$  rpm,  $P = 30$  kW,  $T = 102.3$  N\*m). These two cases are: (1)  $n = 560$  rpm,  $P = 6$  kW,  $T = 102.3$  N\*m (constant torque region); (2).  $n = 14000$  rpm,  $P = 30$  kW,  $T = 20.5$  N\*m (constant power region). Since the previous discussed TD Design was optimized for high torque density at the corner point with a speed of 2800 rpm, it is referred to as TD\_2800 here. Accordingly, the two new optimal designs are named TD\_560 and TD\_14000, respectively.

The cross-sections of the machine designs optimized for high torque density under these three operating points are shown in Fig. 2-14, and their key dimensions and performance metrics are compared in Table 2-8. It can be observed that TD\_560 and TD\_2800 look almost identical, and their performance results are similar except that TD\_560's efficiency is lower than that of TD\_2800, indicating that high output power (high machine speed) leads to high efficiency in the constant torque region.

Figure 2-14 shows that TD\_14000 has a larger airgap radius, smaller slot area, and much shorter stack length, as compared to TD\_2800. The required torque production for TD\_14000 is only one fifth of that required for TD\_2800, since both of the operating points are within a constant power region. The machine size is determined by the torque requirement rather than the power requirement [107]. Therefore, the size of TD\_14000 should be smaller than TD\_2800, which is verified by the results shown in Table 2-8. In traction motor applications, the corner point is required to deliver both maximum torque and maximum power according to the torque-speed envelope (Fig. 2-15), which implies that the machine designed for the corner point operating condition should be able to satisfy the torque and power requirements at any other operating points. Therefore, the objective function of the optimization can be purely focused on the corner point operating condition in a conservative fashion.

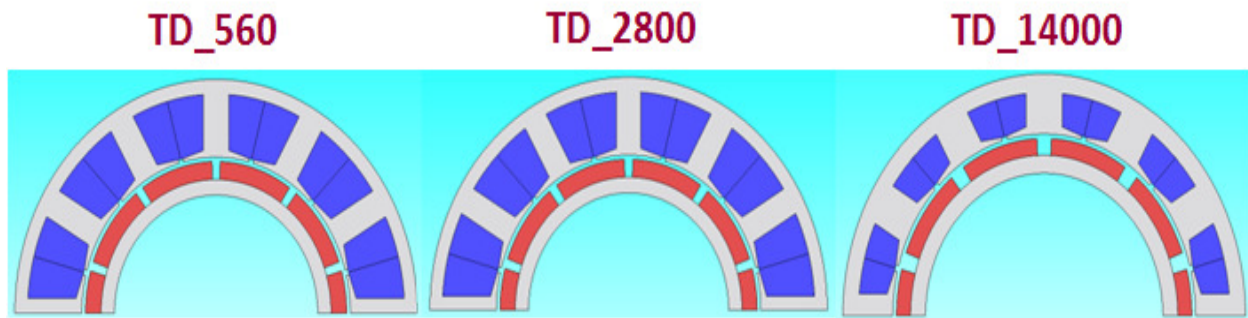


Fig. 2 - 14: Cross-section comparison among TD\_560, TD\_2800, and TD\_14000

Table 2 - 8: Key Dimension and Performance Comparisons among TD\_560, TD\_2800, and TD\_14000

Parameter/Dimension	TD_560	TD_2800	TD_14000
Airgap Diameter [mm]	181.90	181.48	205.11
Active Stack Length [mm]	57.43	57.01	17.62
Magnet Height [mm]	10.57	10.46	9.53
Magnet Span [deg. elec.]	32.4	32.14	30.35
Volume [m <sup>3</sup> ]	0.0025	0.0025	0.0007
Copper Mass [kg]	9.92	10.11	4.08
Magnet Mass [kg]	2.12	2.07	0.63
Total Active Mass [kg]	20.67	20.65	7.62
Active Material Cost [\$]	175.06	172.63	57.90
Torque Ripple [pk-pk/ $T_{rated}$ ]	0.053	0.052	0.034
Power Factor	0.92	0.91	0.98
Core Loss [W]	36.01	241.69	748.79
Copper Loss [W]	586.78	598.11	241.41
Efficiency	0.91	0.97	0.97

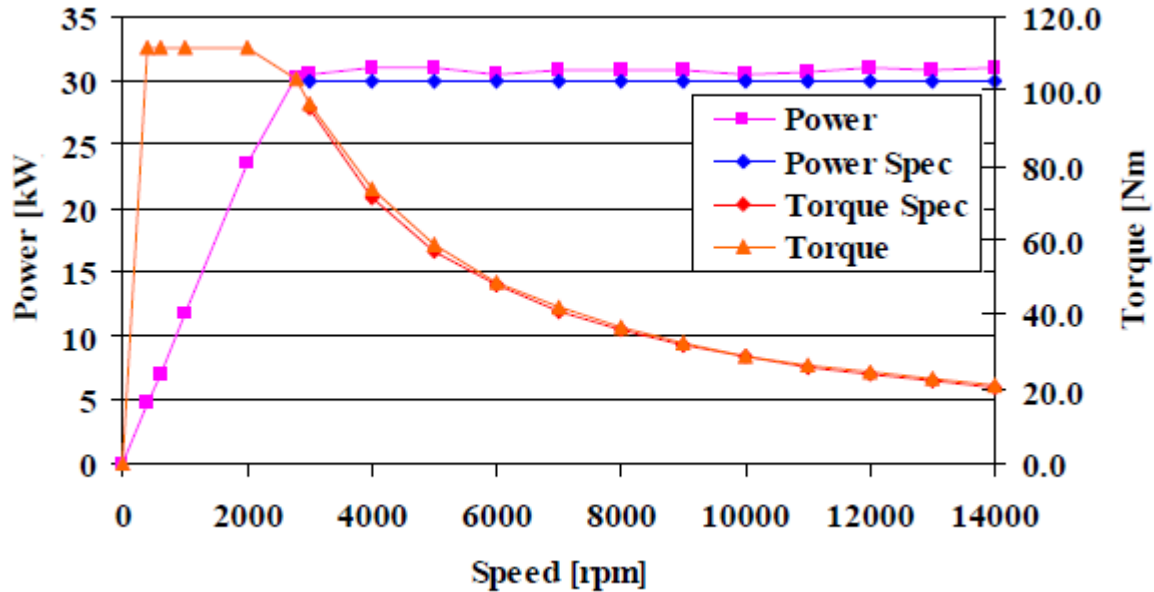


Fig. 2 - 15: Specified envelopes for continuous torque and output power vs. rotor speed [103]

## 2.7 Conclusions

This chapter has presented the implementation of an iterative FE-based machine design optimization algorithm based on differential evolution in a single desktop computing environment. The algorithm has been applied to optimize a 30 kW (continuous) FSCW-SPM machine for high torque density, and the performance of each candidate machine was evaluated with a commercially available FE analysis package. The optimization run converges at a design with a total active mass of 21.82 kg, which exhibits a mass reduction of 21.5% compared to the baseline machine design.

Trade-offs between the accuracy of the optimization results and the computation cost were studied through parametric tests of the four DE control parameters, based on both a single computer and the HTC computing environment. A suitable combination of the control parameters was found for this machine design optimization, which guarantees accurate results

and helps to save computation time. One more degree of freedom, the airgap radius  $R_g$ , is added to the optimization program, leading to an optimal machine design with further improvement in torque density.

The optimization has been applied to minimize the material cost (TPD Design), and maximize the efficiency (Eff. Design) in addition to optimizing the torque density of the target machine (TD Design), all in the interest of exploring the effects of different definitions of the objective function. Comparison results among the three optimal designs suggest that the choice of torque density as the target for the objective function is a good one, which helps to enhance several important performance metrics for the machine. The operating point at which the machine design is optimized is chosen to be the corner point, since it guarantees that the optimal machine will be capable of delivering the required torque/power at any condition along the torque-speed envelope.

## **Chapter 3: Machine Design Optimization Using High-Throughput Computing**

### **3.1 High-Throughput Computing (HTC) Environment: Project Condor**

Condor is a specialized workload management system for computation-intensive jobs. It can be used to manage a cluster of dedicated compute nodes or to harness CPU power from otherwise idle desktop workstations [5]. Condor utilizes open-source software developed by the UW Condor Team that can be run on Linux, Macintosh, and Windows machines. It matches jobs to available computers, and transfers required data to and from remote resources. Moreover, Condor enables workflow execution that allows its users to utilize many resources while maintaining the complex job inter-dependencies and dataflow.

In the Condor pool, all the computers are classified into two major types: Submit Machines and Execute Machines. Users send their jobs to the Submit Machine and specify which kind of Execute Machines they want their jobs to be run on. After job initiation, the Submit Machine begins searching the pool for Execute Machines. Condor plays the critical role of “Matchmaker” that efficiently matches submitted job requests with appropriate Execute Machines. Once it detects any suitable Execute Machine that becomes available, Condor automatically builds the links between the Submit Machine and the Execute Machines, sends the required input data to the Execute Machines, runs the analyses, and collects the results.

There are over 10,000 cores available for use by HTC users through the Center for High Throughput Computing (CHTC) at UW-Madison. Approximately one-third of the cores were purchased and are maintained by the center. The other two-thirds are owned by its users, who contribute their cores to make up the system and become part of the shared resource.

Condor used to be a very specialized research facility that was utilized by a small group of scientists. Today, it is open to a much wider community of users. The opportunity to install commercial software in this environment makes Condor an attractive environment for running FE analysis.

### **3.2 FE Analysis Based Machine Design Optimization in Condor**

The implementation of the FE analysis in Condor is based on the machine design optimization flow diagram presented in Fig. 3-1, which is similar to the machine design optimization routine discussed in previous chapter. The highlighted circle in Fig. 3-1 is the key to this optimization, identifying the site of the major of this work from conventional methods. More specifically, the Condor HTC environment provides the opportunity for parallel analysis that reduces the required computational time by simultaneously analyzing the  $N$  designs in each generation.

The data flow in the Project Condor HTC environment is illustrated in Fig. 3-2. Each electric machine FE model can be defined by a set of parameters, including both fixed and variable types. The fixed parameters are defined by the machine specifications listed in Table 2-2. The six variable parameters for the FSCW-SPM machine are identified in Fig. 3-3, consisting of the stator tooth width, stator yoke thickness, magnet span ratio, rotor yoke thickness, magnet thickness, and airgap radius. The numerical ranges for these variables, shown in Table 3-1 for this example, are defined as ratios rather than absolute values in order to help ensure that each candidate design meets all of the geometric constraints. The range boundary values are chosen to ensure that the optimum values fall within the variable ranges.

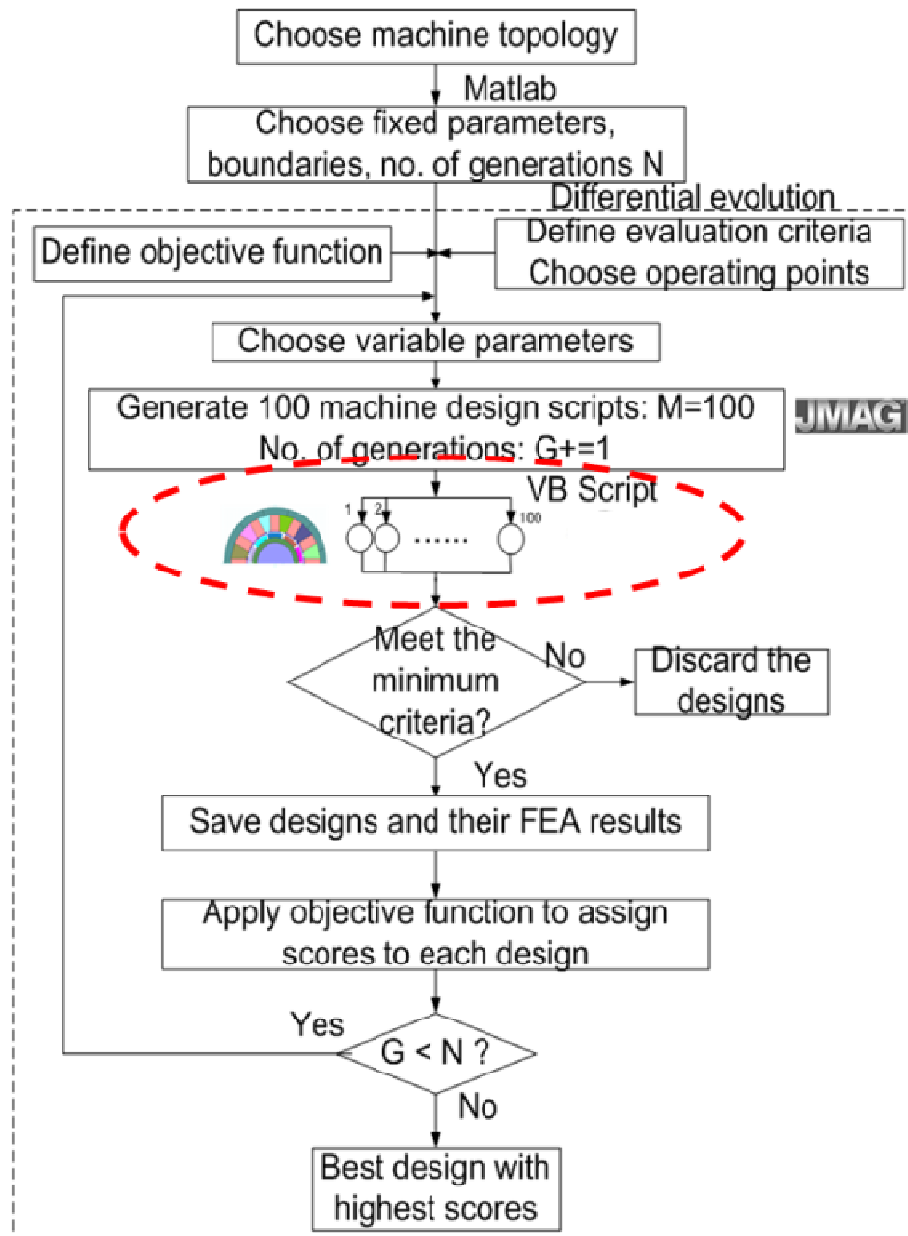


Fig. 3 - 1: Flow chart of machine design optimization algorithm in HTC environment.

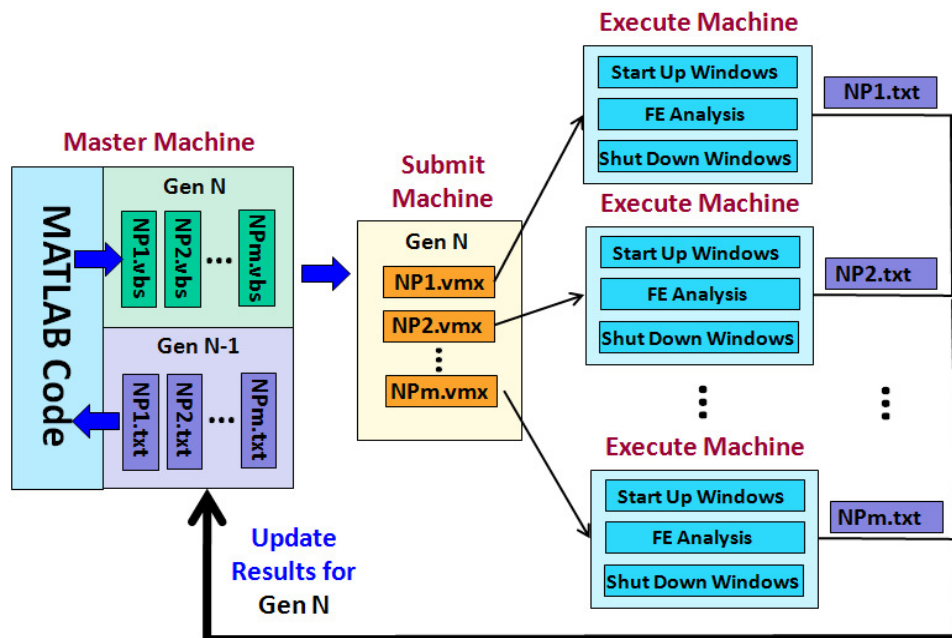


Fig. 3 - 2: Data flow in the Project Condor HTC environment

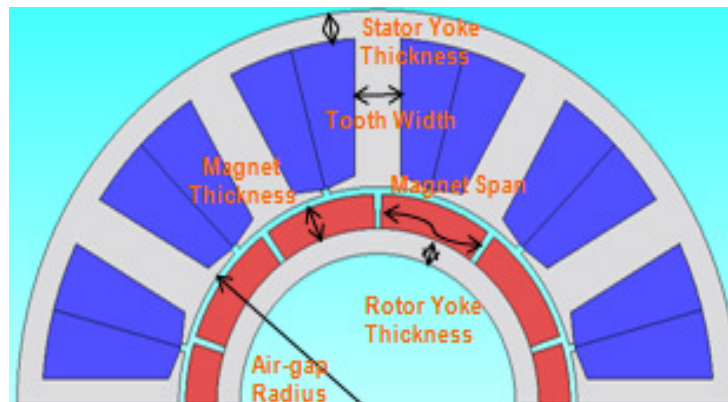


Fig. 3 - 3: FSCW-SPM machine design variables

Table 3 - 1: FSCW-SPM Variable Definitions and Ranges

Variable Parameters	Range
Tooth Width to Slot Pitch Ratio	[0.1, 0.8]
Stator Yoke Thickness to Tooth Width Ratio	[0.1, 0.8]
Magnet Span to Rotor Pole Pitch Ratio	[0.5, 0.95]
Rotor Yoke Thickness to Rotor Pole Pitch Ratio	[0.1, 0.6]
Magnet Thickness to Airgap Thickness Ratio	[1, 7]
Airgap Radius to Stator Outer Radius Ratio	[0.3, 0.75]



Next, all of the parameters in the parameter set are fed into the template Visual Basic(VB) script for FE analysis that contains information on the machine configuration, material, and excitation to create a specific script for each candidate design. All of these FE analysis conditions are set up in the same way as described for the FE model in Section 2.1.

When all of the VB scripts in one generation (iteration) of the DE optimization are written, each VB script is mounted in Virtual Machine (VM) format, which corresponds to a CD-ROM image. The Virtual Machine approach is necessary because JMAG, the commercial FE analysis package used for the study, can only run in a Windows computer, while Condor is a Linux-based environment. The VM method helps to solve this problem since it allows Windows jobs to be run on a Linux machine.

Next, all of the VM images for each generation are sent to the Submit Machine (see Fig. 3-2). Every VM image will be mapped from the Submit Machine to an Execute Machine where each candidate machine design is analyzed by JMAG immediately after starting up Windows. When each FE analysis is completed, Windows is automatically shut down. Then the FE results for the candidate machine, which is written in a text file, is extracted from the VM image and transferred back to the Submit Machine for the main DE code to evaluate the objective (cost) function for the candidate machine. If the evaluated cost function value fulfills the convergence criteria, the optimization run will terminate. Otherwise, the whole process described in Figs. 3-1 and 3-2 will be repeated again until the optimal design is found.

### 3.3 Comparison between HTC and Single Computer Optimization Results

In order to quantify the reduction in computation time that can be achieved using the Condor HTC environment compared to using a single computer, a comparison test was launched. The same machine design optimization software has been applied to optimize the torque density for the FSPM-SPM machine using either the Condor HTC resources or a single computer that was chosen from the Condor pool in order to provide a fair comparison.

#### 3.3.1 Comparison Test Conditions & Optimization Parameters

The candidate machine was designed for rated operating conditions, i.e.  $n = 2800$  r/min,  $P = 30$  kW,  $T = 102.3$  Nm, where  $n$ ,  $P$  and  $T$  represent the rotor speed, output mechanical power, and torque, respectively. The objective function  $OF$  has been defined as

$$OF = \frac{\text{CalculatedActiveMasstoProduceRequiredTorque}}{\text{BaseMachineActiveMass}} \quad (8)$$

where the base machine is the one studied previously in [103] with an active mass of 27.8 kg that includes the stator and rotor electromagnetic assemblies.

Based on previous experience, the control parameters for the DE optimizer were chosen to be: convergence tolerance  $Tol = 10^{-6}$ ; crossover probability  $Cr = 0.8$ ; and scale factor  $F = 0.8$ . The number of designs in each generation is chosen to be  $NP = 85$ , in order to demonstrate the power of parallel computing.

### 3.3.2 Optimized Design

The two optimizations were then run and both converge to the same optimal design at the 50th generation, with a total number of 4,250 designs evaluated in each case. The best design is found to have an objective function value of 0.7426 for both cases, i.e., a total mass of 20.65 kg.

Key dimensions and metrics for the optimal machine are summarized in Table 3-2. Plots of four machine metrics evaluated at the corner operating point – torque, efficiency, torque ripple, and power factor – are plotted in Fig. 3-4 as a function of machine mass for all of the candidate machine designs that were evaluated during the optimization (i.e., the Pareto-optimal set). That is, each of the >4,000 machine designs is represented by a point in each plot. Two data points are highlighted in each plot that identifies the metrics of the original machine and the final optimal machine.

**Table 3 - 2: Optimal FSCW-SPM Machine Details**

<b>Parameter/Dimension</b>	<b>Value</b>
Airgap Diameter [mm]	181.48
Active Stack Length [mm]	57.01
Magnet Height [mm]	10.46
Magnet Span [deg. elec.]	32.14
Volume [m <sup>3</sup> ]	0.0025
Copper Mass [kg]	10.11
Magnet Mass [kg]	2.07
Total Active Mass [kg]	20.65
Torque Ripple [pk-pk/ $T_{rated}$ ]	0.05
Power Factor	0.91
Magnet Loss [W]	59.44
Core Loss [W]	282.39
Copper Loss [W]	609.64
Efficiency	0.97

It can be observed that optimizing the torque density helps to simultaneously reduce the magnet mass, improve the efficiency, and increase the power factor even though these other metrics are not part of the objective function. However, the optimization does not have much impact on the predicted torque ripple. Taken together, these results suggest the choice of torque density as the target for the objective function is a good one that results in improvements for several important performance metrics of the machine.

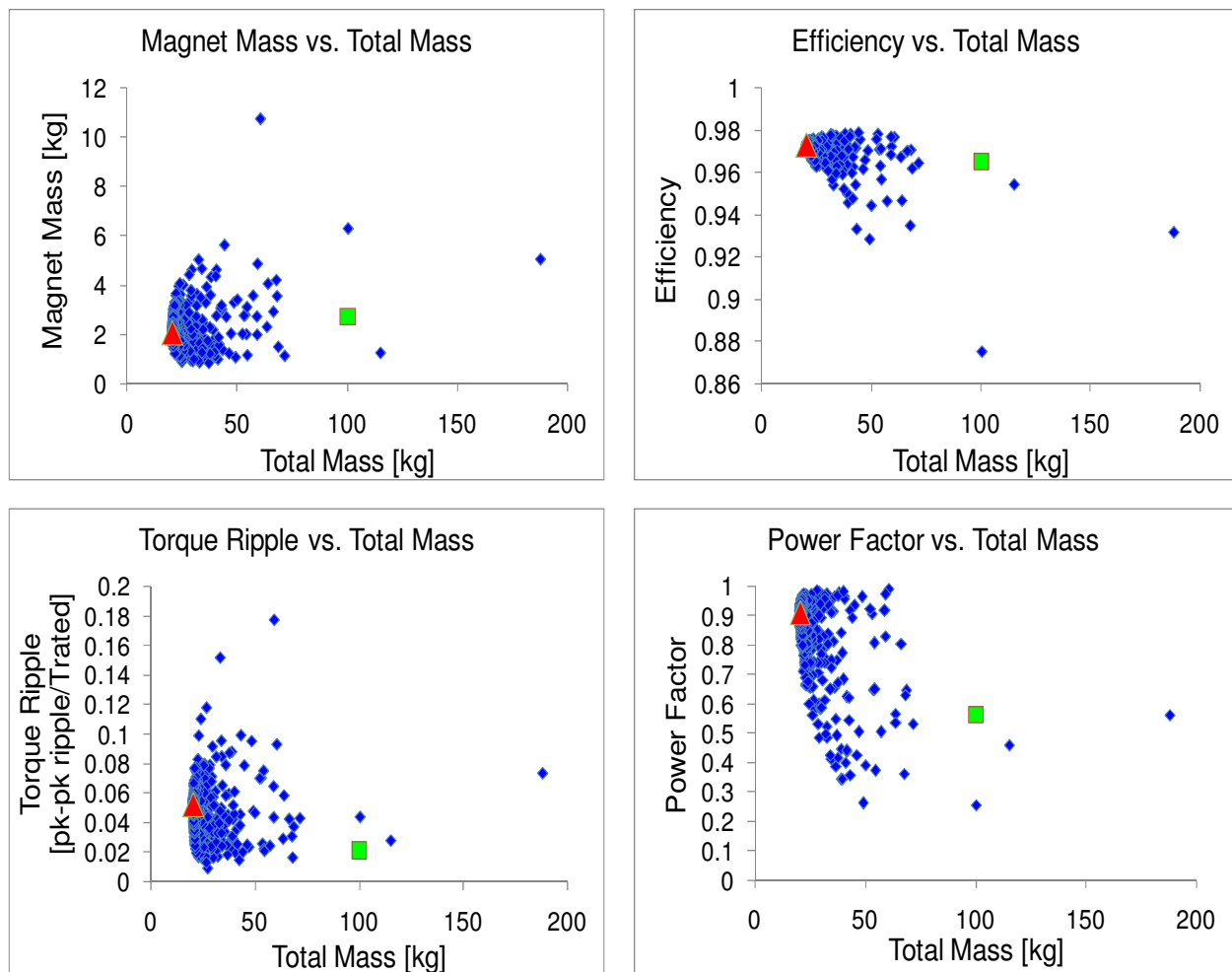


**Fig. 3 - 4:** Plots showing magnet mass, machine efficiency, torque ripple, and power factor, (all for rated power operation) vs. machine electromagnetic mass for all of the machine designs evaluated during the DE optimization. Points for initial design (green square) and final design (red triangle) are highlighted in each plot.

The optimized machine has a mass reduction of 25.7% compared to the base machine, representing a significant improvement in torque density. Although appealing, the significance of this improvement must be tempered by the fact that the specifications for this new design and the earlier prototype machine are not identical. Nevertheless, the fact that both optimization runs converged to the same optimal design in the same number of generations helps to build confidence in the fairness of the computation time comparison that is presented in the next section.

### **3.3.3 Comparison of Computational Time**

Log files have been captured to record each step during the optimization runs for both the HTC and single computer cases. In Condor, there are three time stamps collected for each design, i.e., “submit”, “execute” and “terminate”. “Submit” refers to the time when the VM image is submitted to the Submit Machine. “Execute” refers to the time when the VM image is mapped from the Submit Machine to the Execute Machine. “Terminate” refers to the time when Windows has been shut down in the Execute Machine.

Figure 3-5 shows the time duration between “Execute” and “Terminate” for each of the 85 designs evaluated in one of the 50 DE design generations, Generation #25. This time duration represents the time that is required for each design in an Execute Machine, including Windows start-up, FE analysis time, and Windows shutdown. The shortest time is 9 min 19 sec, while the longest one is 18 min 51 sec, indicating a range that exceeds 2:1. Because Condor is a shared computational environment, every computer in the Condor pool can be assigned to multiple users at the same time. If a machine design is submitted to a heavily loaded Execute Machine, it takes longer to analyze. Since this delay slows the overall computation time, efforts are under way to

improve the assignment algorithm so that the designs are preferentially matched with lightly-loaded Execute Machines to reduce this overhead time.

Unfortunately, the total time required to complete each generation of design evaluations in the Condor HTC environment is determined by the slowest of the computational periods for the 85 designs in the generation. For Generation #25, this total consist of the maximum “Execute” to “Terminate” value shown in Fig. 3-5 (18 min 51 sec) plus 1 min 9 sec to distribute the design parameters to all of the Execute Machines, plus 1 min 30 sec for processing the VM format conversions. Thus, the total time required for completing the computations for Generation #25 in the Condor HTC environment is 21 min 30 sec.

In the single computer optimization run, there are no overhead or delay time components such as those encountered in the Condor HTC environment with shared parallel computers. One of the impacts of this difference can be observed in Fig. 3-6 showing the total time required for evaluating each of the 85 designs in Generation #25 with the single computer. This bar chart shows that the shortest time is 8 min 19 sec, while the longest one is 10 min 46 sec. The differences in computation times among the designs using a single computer are significantly smaller than those encountered in the Condor HTC environment, and the longest computation time for any of the 85 designs using a single computer is approx. 50% of the longest time for the Condor case.

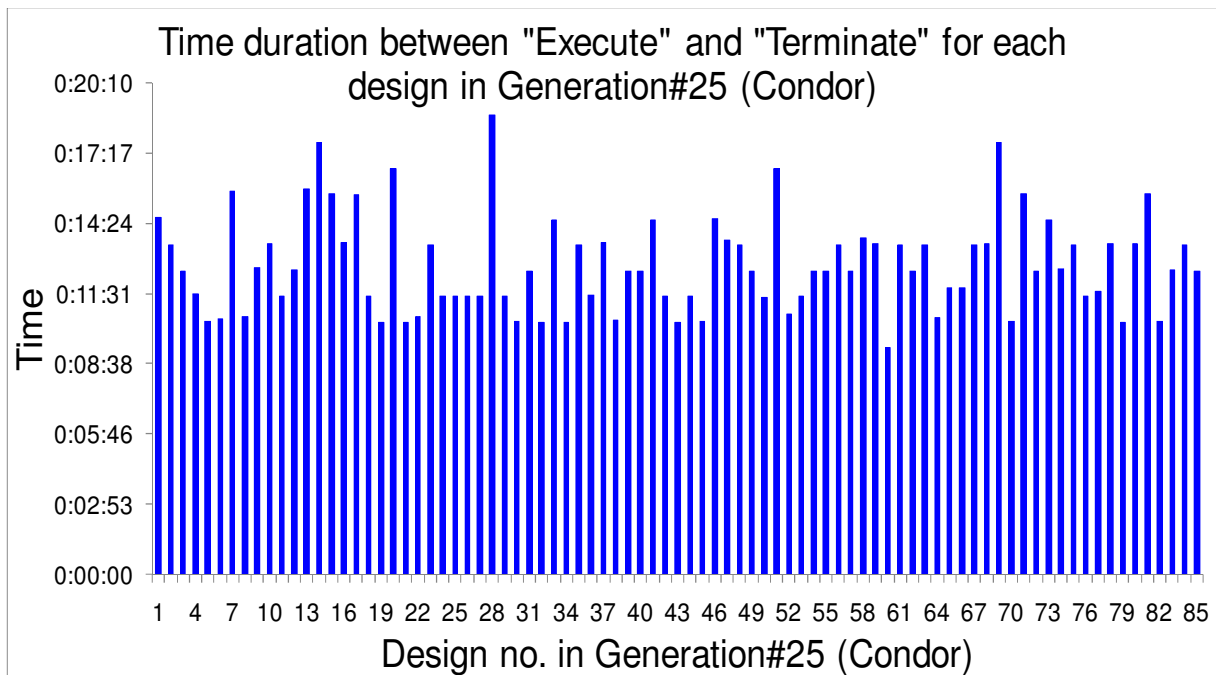


Fig. 3 - 5: Time duration between "Execute" and "Terminate" for each design in Generation #25 (Condor)

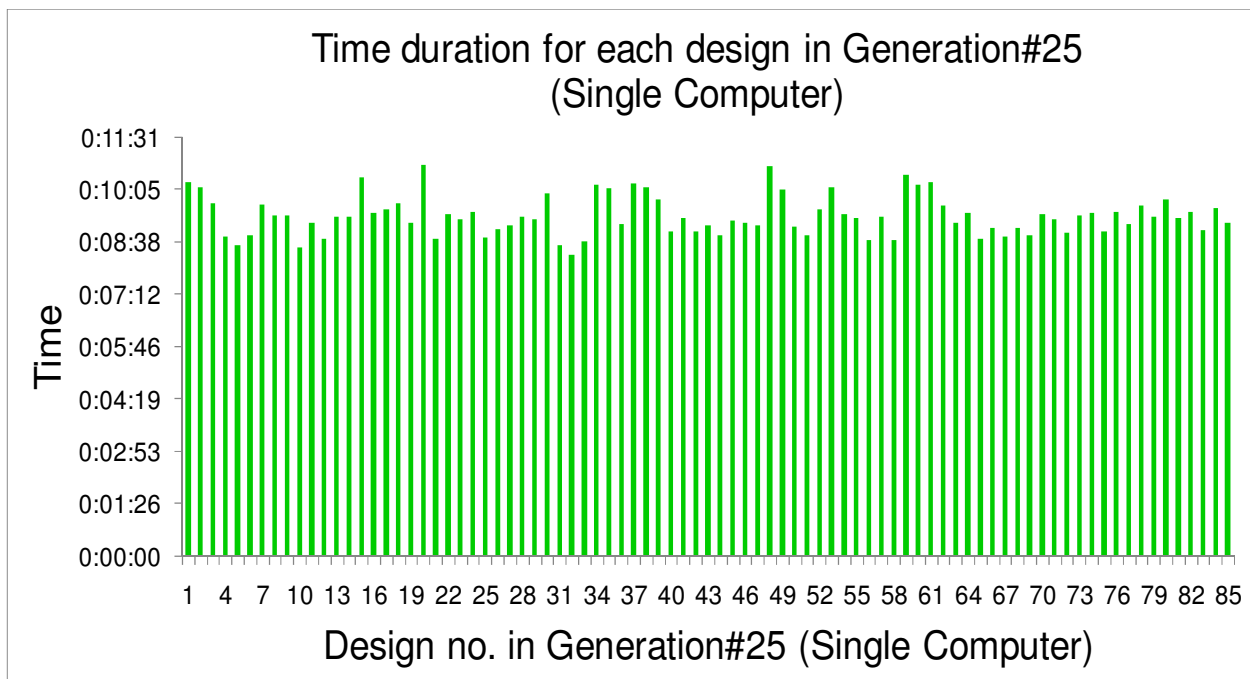


Fig. 3 - 6: Time duration for each design in Generation #25 (Single Computer)

Despite this advantage for the single computer case, the total time for each generation is calculated by summing up all of the computation times for the 85 designs when using a single computer since the designs must be evaluated serially. As a result, the total computation time for Generation #25 in the single computer run is 13 hr 16 min 52 sec, which is approx. 37 times longer than the corresponding time period for the Condor run.

Figure 3-7 shows the computation time required by each of the 50 design generations in the Condor HTC environment. There are variations in the computation time required for the generations ranging from 19 min 32 sec for Generation #15 to 1 hr 4 min 34 sec for Generation #1. By adding these individual generation times together, the total time required for the optimization to converge in the Condor HTC environment is 25 hr 0 min 26 sec, or 1.04 days.

The corresponding computation time for each generation in the single computer case is shown in Fig. 3-8. Although the variation in the computation times among the 50 generations in the single computer case are small, the total computation time required for the optimization to converge in a single computer environment is 29 d 22 hr 17 min 8 sec, or 29.93 days. Thus, the time acceleration factor for completing the optimization using the Condor HTC environment instead of a single computer is 28.7, representing a very significant improvement in computational speed.



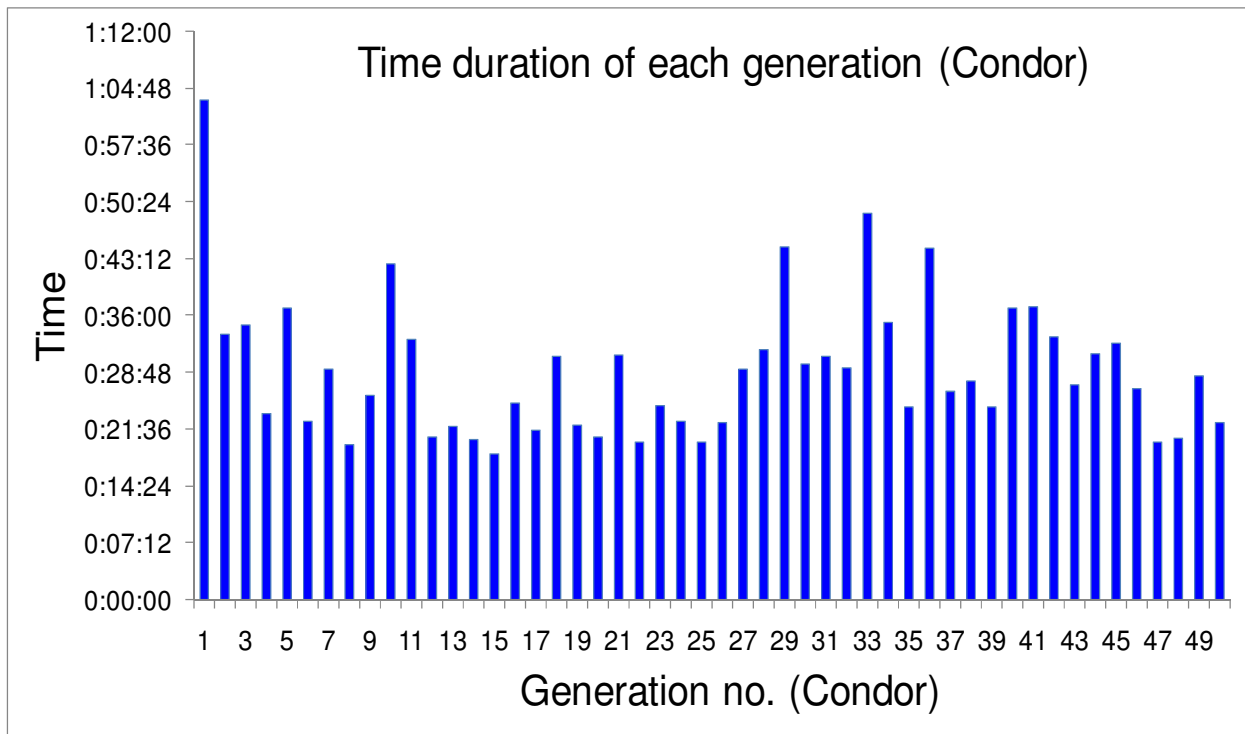


Fig. 3 - 7: Time duration of each generation over the 50 generations (Condor)

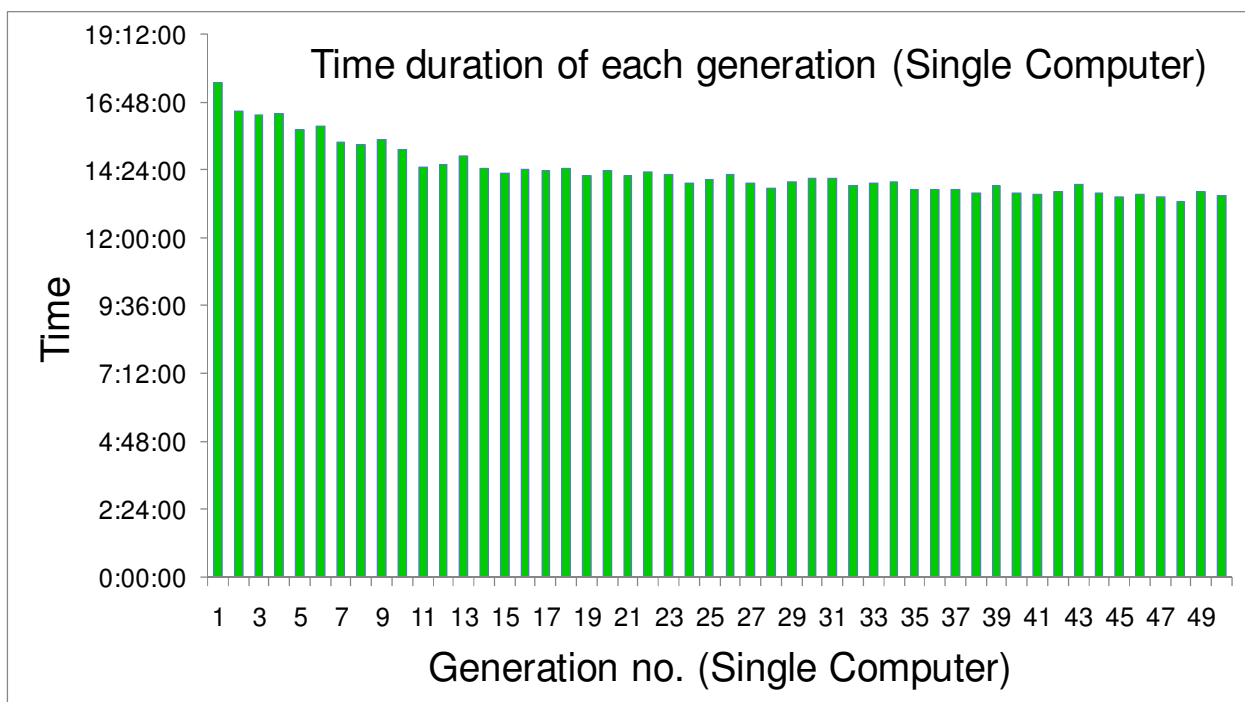


Fig. 3 - 8: Time duration of each generation over the total 50 generations (Single Computer)

### 3.4 Computation Time Breakdown and Acceleration Factor Improvements

The computation time acceleration factor of 28.7 that was achieved in the demonstration case using the Condor HTC environment is only approx. one-third of the ideal upper limit value of 85 that this project seeks to approach when using 85 computers performing computations in parallel. After breaking down of all the time components during the optimization, one finds that the required computation time for the DE main code performing most of the operations in Fig. 3-1 is negligible compared to the FE analysis times. A second important observation is that the variations in the FE analysis times among all of the 4,250 designs that were evaluated during the optimization run using the single computer are small.

Using these numbers from the demonstration case, it is estimated that the acceleration factor could be significantly increased if a dedicated HTC network would be completely allocated to solving this same optimization problem. Much of this improvement comes from eliminating the overhead and delay times that are present in the shared Condor HTC environment.

There is clearly a large gap between the demonstrated acceleration factor and the estimated achievable value for a dedicated HTC environment. Some promising opportunities have been identified to improve the acceleration factor in the current Condor HTC environment. For example, Fig. 3-9 shows the total time duration between “Start” and “Terminate” for each of the 85 designs in Generation #29 for the HTC case. This figure indicates that 46 min 2 sec was required for completing this generation in the Condor HTC environment. This completion time is considerably longer than many of the other generations (see Fig. 3-5) because of 3 outlier designs that required much longer times to complete than the rest of the designs in the same generation. Alternative approaches to significantly reduce the number of these outliers cases are

under investigation, including modifications of the DE algorithm and improvements of the machine assignment software in the Condor HTC environment.

Figure 3-10 provides simplified estimates of the acceleration factor that can be achieved as a function of the number of designs in each DE generation for different HTC computing environments. The steepest line is for the unattainable ideal case for which the acceleration factor simply equals the number of designs that are being analyzed in parallel. A dedicated HTC environment is estimated to be capable of achieving approx. 90 to 95% of the ideal value, raising the acceleration factor to approx. 80 for the considered case with 85 designs in each generation.

As discussed in preceding sections, the current shared Condor HTC environment achieves only approx. 34% of the ideal acceleration factor value. It is currently estimated that efforts to reduce the accumulated overhead time in the Condor HTC environment can increase the acceleration factor to >50 for the case with 85 designs in each generation, corresponding to approx. 60% of the ideal value.

One of the implicit assumptions for Fig. 3-10 is that the number of generations required by the DE algorithm to find an optimum design is fixed (50) independent of the number of designs per generation. While this topic extends beyond the scope of this paper, it is acknowledged that this assumption does not hold for all numbers of designs per generation. Nevertheless, it is interesting to note that the acceleration factor is largely independent of the number of generations because it is a ratio of computation times for two cases that each requires the same number of generations, even if that number varies. As a result, the key conclusions reached in this section about the acceleration factor are insensitive to the number of required DE generations.

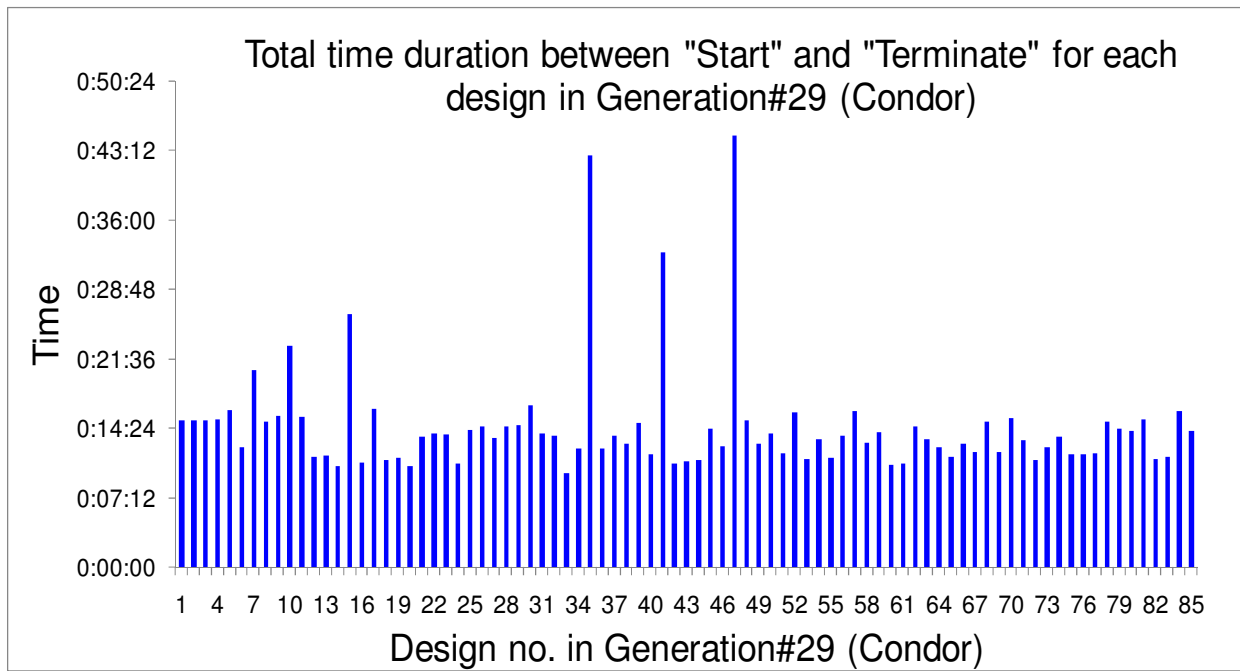


Fig. 3 - 9: Total time duration between "Start" and "Terminate" for each design in Generation #29 (Condor)

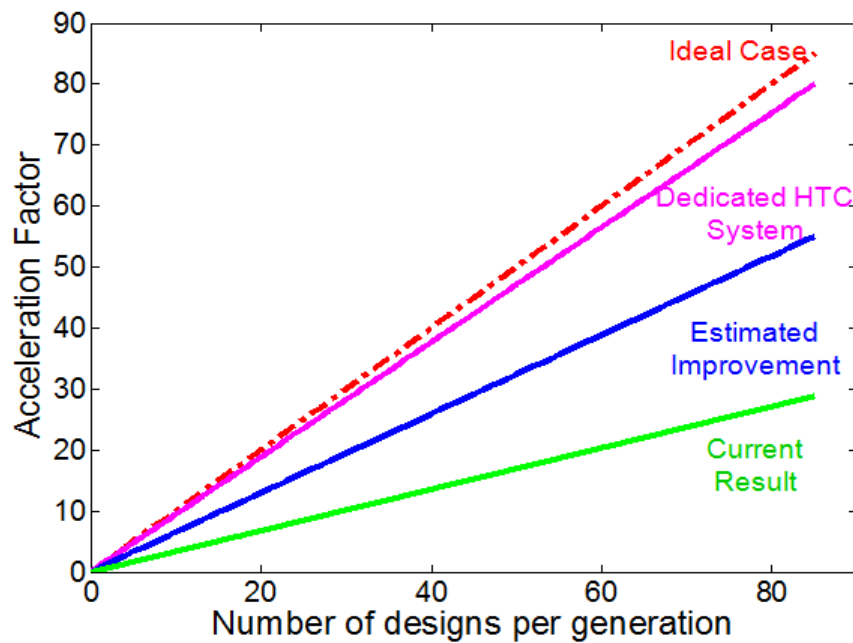


Fig. 3 - 10: Acceleration factor vs. number of machine designs in each generation

### 3.5 Conclusions

This chapter presents the implementation of an iterative FE-based machine design optimization algorithm based on differential evolution in a high-throughput computing (HTC) environment. The software has been applied to optimize a 30 kW (continuous) FSCW-SPM machine for high torque density using both an available HTC environment (Project Condor) and a single computer of the same type used in the HTC system. Commercially-available FE analysis software is used for these calculations.

The two optimization runs converge at the same optimal design, which exhibits a mass reduction of 25.7% compared to the baseline machine design. The comparison shows that the parallel HTC environment achieves a reduction in the computational time by a factor of 28.7 compared to the single computer. This result highlights the significant reductions in computational time of FE-based machine design optimization problems that can be achieved using currently-available HTC resources. Moreover, a dedicated HTC environment is estimated to be capable of raising the acceleration factor to approx. 80 for the considered case with 85 designs in each generation, after breaking down of all the time components during the optimization.

## **Chapter 4: Coupled Electromagnetic/Thermal Model for Electric Machines**

The focus of this study in previous chapters has been on electromagnetic design. However, an electrical machine is also heavily constrained by thermal limits. Moreover, if the machine is operated at elevated speeds, the structural limits need to be taken into account as well. As a result, comprehensive optimization of an electrical machine design requires that its electromagnetic, thermal, and structural performance be analyzed and optimized simultaneously. With researchers' increasing ability to access powerful HTC environments, there are new opportunities to extend the optimization to include these critical multi-physics dimensions. In the current study, efforts have been made to expand the investigation by focusing initially on the integration of the electromagnetic and thermal machine design optimizations, which will be discussed in the following sections.

### **4.1 2D vs. 3D Electromagnetic Model**

The three-dimensional (3D) electromagnetic FE model is generally thought to be more accurate in estimating machine loss components compared to the two-dimensional (2D) model. However, adoption of the 3D model typically means days of simulation time, which is considerably longer than the time required for the 2D model. As a result, the 2D FE model is used for the EM component of the analysis.

A comparison test between the 2D and 3D EM FE model is carried out to estimate the loss of accuracy in machine performance predictions associated with the 2D model. The TD Design mentioned in Chapter 2 is selected as the target machine, and its 2D cross-section and 3D side view are shown in Fig. 4-1. Three-phase sinusoidal current is applied to excite the machine. Only dc resistance is considered in the copper loss calculation. The core and magnet losses are

estimated using JMAG, a commercial FE analysis package used in this study. The lamination steel has been selected to be 29 Gauge M19 material. The detailed loss profile for this steel (i.e., core loss as a function of both frequency and magnetic flux density) is used to calculate the core losses. The hysteresis core loss is evaluated using the apply-loop method, while the eddy current core loss is calculated with the Fast Fourier Transfer (FFT) approach. Both of these core loss calculation techniques are built-in function blocks in JMAG. The electric resistivity for the neodymium magnet used in this test is  $1.6 \mu\Omega\text{-m}$  for calculating the magnet loss. Each magnet is circumferentially segmented into 6 pieces, resulting in an approx. 90% reduction in magnet loss.

For both machine models, the predicted torque values are nearly equal and their predictions for machine loss components are compared in Table 4-1. The 2D and 3D EM FE models show good agreement for magnet loss and hysteresis core loss. However, there is a 10-15% discrepancy in the calculated eddy current core loss between the two models, which is mainly due to the end winding effect. The difference in total core loss is 11.18% as the eddy current core loss represents a large portion of the total core loss. Taken all together, the 2D EM FE model is a better choice for this study because it can predict machine performance with an acceptable level of accuracy in a reasonable amount of time.

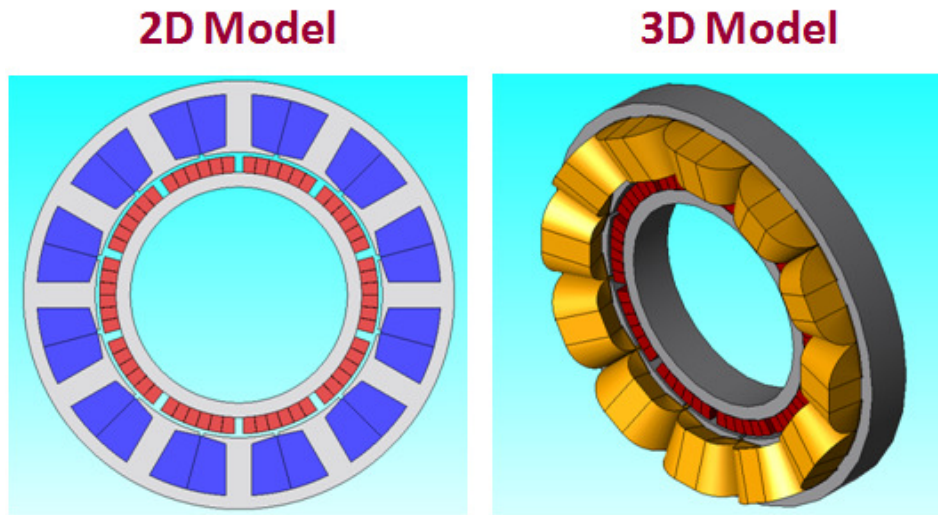


Fig. 4 - 1: TD Design 2D and 3D FE Models

Table 4 - 1: Comparison in Loss Estimation between TD Design 2D and 3D FE Models

Loss Components	2D Model	3D Model	(2D - 3D) / 3D
Magnet Loss [W]	59.44	57.35	3.64%
Stator Hysteresis Loss [W]	74.51	74.58	-0.09%
Stator Eddy Current Loss [W]	197.63	231.97	-14.8%
Rotor Hysteresis Loss [W]	0.37	0.37	0%
Rotor Eddy Current Loss [W]	9.87	11.02	-10.44%
Total Core Loss	282.39	317.95	-11.18%

## 4.2 Thermal FE Model

There are three modeling approaches widely used for estimating the thermal behavior of electrical machines: 1) computational fluid dynamics (CFD) model, 2) FE model, and the 3) analytical model. The CFD model is the most computation-intensive, although it usually delivers the most accurate results due to being able to describe and simulate fluid dynamic phenomena in detail. The FE thermal solver can easily calculate conduction heat transfer after the thermal conductivity values of the machine components are specified. If the boundary conditions can be specified with precise heat transfer coefficient estimations, the FE model is capable of accounting for convection and radiation as well. The analytical method always provides the



fastest and least computationally intensive solution. However, it is the method with the least accuracy, as the complex machine geometry is not considered in the modeling process. Therefore, the FE modeling approach is used for evaluating machine thermal performance in this study.

A 3D thermal FE model is regarded as more accurate than a 2D model because the 2D model cannot calculate the heat transfer in the axial direction. Additionally, the simulation time for a 3D model is comparable with that for a 2D model if the computing workstation has sufficient memory available. As a result, a 3D thermal FE model is adopted for the thermal component of the analysis.

#### 4.2.1 Building the FE Model

The thermal conductivity [ $\text{Wm}^{-1}\text{K}^{-1}$ ] of the system winding impregnation and insulation  $k_{cu,ir}$  is calculated using (9) according to [108, 109]. Next, the winding thermal conductivity  $k_{wind}$  can be defined as a combination of  $k_{cu,ir}$  and copper thermal conductivity  $k_{Cu}$ , expressed in (10).

$$k_{cu,ir} = 0.2749[(1 - k_f)A_{slot}L_{core}]^{-0.4471} \quad (9)$$

$$k_{wind} = k_f * k_{Cu} + (1 - k_f) * k_{cu,ir} \quad (10)$$

where  $k_f$  is the slot fill factor,  $A_{slot}$  represents the slot area [ $\text{m}^2$ ], and  $L_{core}$  is the axial core length [m].

The three materials are assigned to their corresponding parts on the 3D drawing of the machine. Once the material properties are defined the windings, magnets, stator core, and rotor core are assigned as the heat sources for the copper loss, magnet loss, stator core loss, and rotor core loss, respectively. The spatial loss distributions are mapped from the EM analysis results

and used as inputs for the thermal analysis. For the component surfaces that are in direct physical contact with each other (e.g., the inner winding surface and the stator teeth surface, and the magnet bottom surface and rotor core upper surface), contact thermal resistances are specified using typical values that are provided in a JMAG application note [110].

Heat transfer coefficients, defined by evaluating empirical equations found in the literature for the given cooling conditions, are used to apply boundary conditions that account for convection and radiation.

The important heat transfer between the machine stator and rotor is modeled as convection in the airgap area. The spinning rotor forces the air into tangential motion and this tangential flow is known as Taylor-vortex flow. This effect enhances the heat transfer characteristics of the airgap. The Taylor vortices are described by the Taylor number as follows according to [111, 112].

$$T_a = \frac{\rho^2 \omega_r^2 \gamma_m \delta^3}{\mu^2} \quad (11)$$

where  $\rho$  and  $\mu$  are the density [ $\text{kg}/\text{m}^3$ ] and dynamic viscosity [ $\text{kg}\cdot\text{m}^{-1}\text{s}^{-1}$ ] of the air, respectively,  $\omega_r$  is the angular velocity of the rotor [ $\text{rad}/\text{s}$ ],  $\delta$  is the radial air-gap length [ $\text{m}$ ], and  $\gamma_m$  is the average of the stator and rotor radius values [ $\text{m}$ ]. The Taylor number determines the Nusselt number in three different regimes:

$$\begin{aligned} Nu &= 2 & (T_a < 1700) \\ Nu &= 0.128T_a^{0.367} & (1700 < T_a < 10^4) \\ Nu &= 0.409T_a^{0.241} & (10^4 < T_a < 10^7) \end{aligned} \quad (12)$$

When the Nusselt number is determined, the heat transfer convection coefficient for the rotor and stator surfaces in the airgap [ $\text{W}/(\text{m}^2\text{K})$ ] can be calculated using the following equation:

$$h_{ag} = \frac{Nuk_{air}}{\delta} \quad (13)$$

where  $k_{air}$  is the thermal conductivity of the air. In the thermal model, the stator-to-airgap heat transfer boundary condition must be connected with the corresponding rotor-to-airgap boundary condition since they share the same airgap.

It is assumed that there is no active cooling applied to the candidate machine, in other words, natural convection boundary condition is specified on all machine surface areas, and the combined natural convection and radiation heat transfer coefficient lies in the range 12-14 W/(m<sup>2</sup>K) [108]. Boundary condition settings related to applying active cooling methods will be discussed in the following section.

The TD Design is used as an example to demonstrate the procedure for building a 3D thermal FE model. The model's 3D drawing is created by extruding its corresponding 2D cross-section and linking end windings. A natural convection boundary condition is initially specified on all machine surface areas, as described in Fig. 4-2. 2D EM FE analysis is performed on this design with 1 p.u. (4.6 A/mm<sup>2</sup>) current density applied to excite the winding. The resulting 2D loss profile is mapped onto the 3D thermal model as a heat source, assuming uniform distribution in the axial direction. The thermal analysis is performed, and the average temperature of the machine parts are summarized in Table 4-2.

**Table 4 - 2: Average Temperature Summary for TD Design with Natural Convection**

Stator Core Temp. [°C]	Rotor Core Temp. [°C]	Winding Temp. [°C]	PM Temp. [°C]	Airgap Temp. [°C]
164.09	144.28	159.45	150.67	164.26

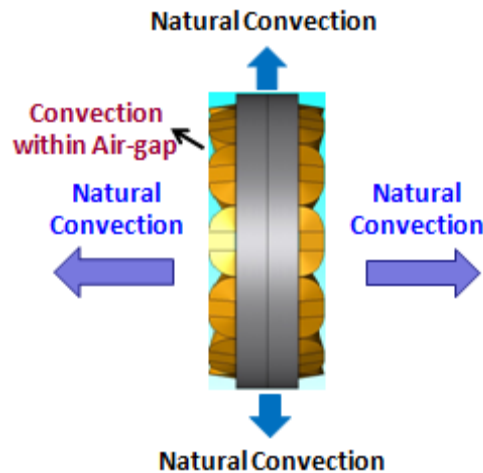


Fig. 4 - 2: TD Design thermal model with all nature convection

#### 4.2.2 Selecting Active Cooling Methods

Parametric analyses on various kinds of active cooling methods are carried out in order to make a reasonable assumption about the machine cooling condition used in this study. The first cooling scenario is for the case of the candidate machines mounted in water jackets (Fig. 4-3), which can be modeled as a coolant temperature boundary condition and a thermal contact resistance according to [113]. The temperature for each part of the TD Design as a function of the coolant temperature is shown in Fig. 4-4. All machine component temperatures increase as the coolant temperature goes up. The stator core temperature (the blue curve) has the steepest increasing slope, since it is closest to the water jacket and therefore responds very quickly to the temperature change in the coolant.

The coolant temperature is maintained at 65 °C for the motor used in the 2007 Camry [114], so the coolant temperature for this study is also set to 65 °C. The average temperature for each part of the TD Design under the condition of water jacket cooling is summarized in Table 4-3. Following the application of the water cooling jacket, the average winding temperature dropped

from 159.45 °C (Table 4-2) to 97.64 °C, which suggests that mounting an electric machines in a water jacket is a very effective cooling technique.

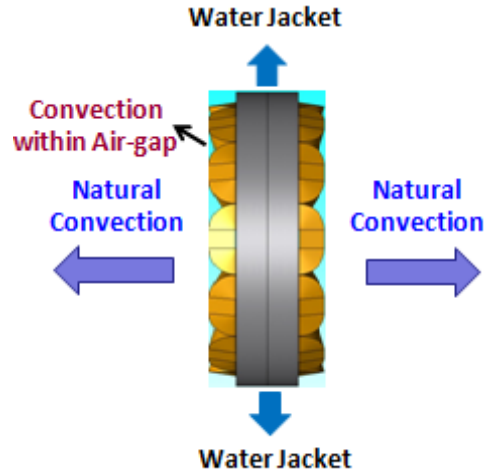


Fig. 4 - 3: TD Design thermal model with water jacket cooling

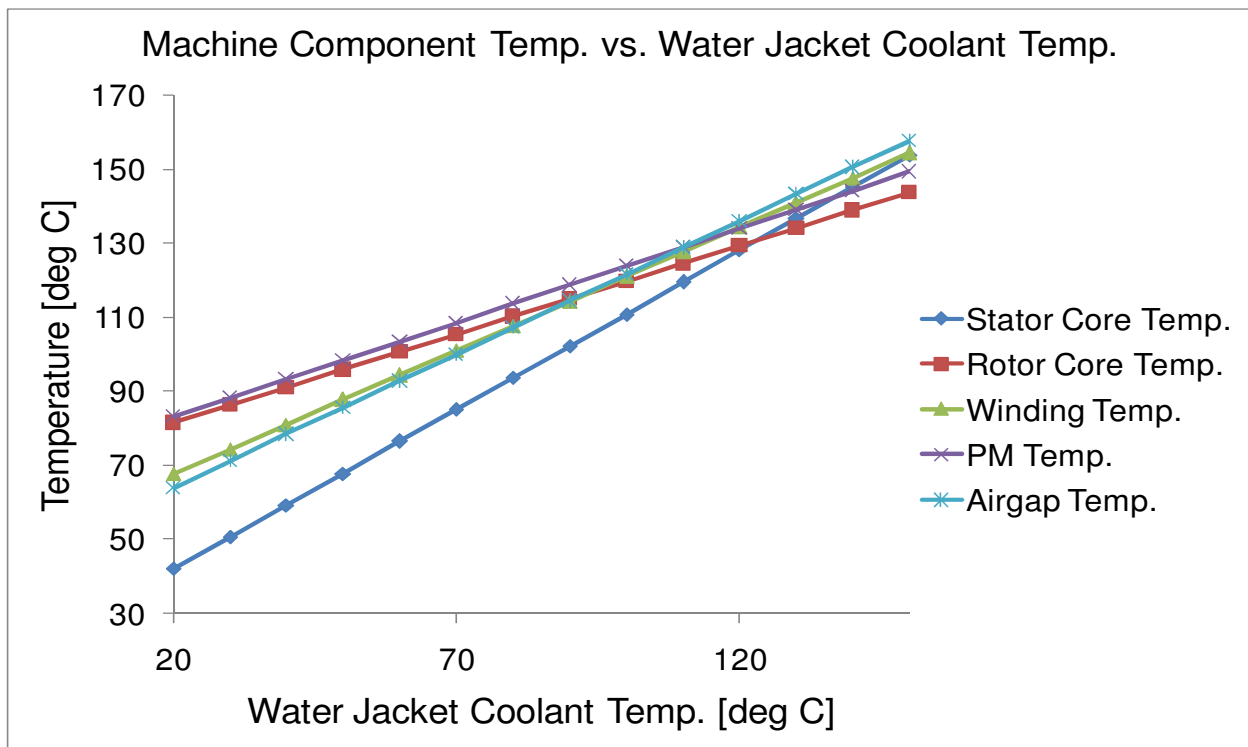


Fig. 4 - 4: TD Design average component temperatures vs. water jacket coolant temperature

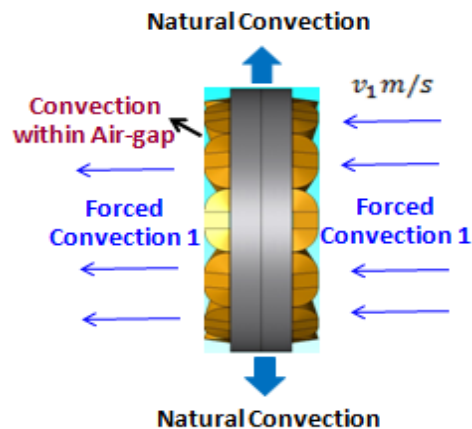
**Table 4 - 3: Average Temperature Summary for TD Design with Water Jacket Cooling (Coolant@65 °C)**

Stator Core Temp. [°C]	Rotor Core Temp. [°C]	Winding Temp. [°C]	PM Temp. [°C]	Airgap Temp. [°C]
80.75	102.95	97.64	105.99	96.35

The second cooling scenario is for the candidate machines to be air-cooled by an external blower (Fig. 4-5). The heat transfer coefficient of the forced convection for both of the machine ends can be modeled as increasing linearly with the air speed, expressed in (14) according to [108, 109], as follows:

$$h = 41.4 + 6.22v_1 \quad (14)$$

where  $v_1$  is the air speed at machine ends [m/s]. The temperature for each part of the TD Design is shown as a function of the air speed in Fig. 4-6. All machine component temperatures decrease simultaneously as the air velocity increases. An air speed value of 2 m/sec has been used for this investigation, for which the average winding temperature drops to 139.12 °C from 159.45 °C in the original model (without active cooling).

**Fig. 4 - 5: TD Design thermal model with forced convection at machine ends**

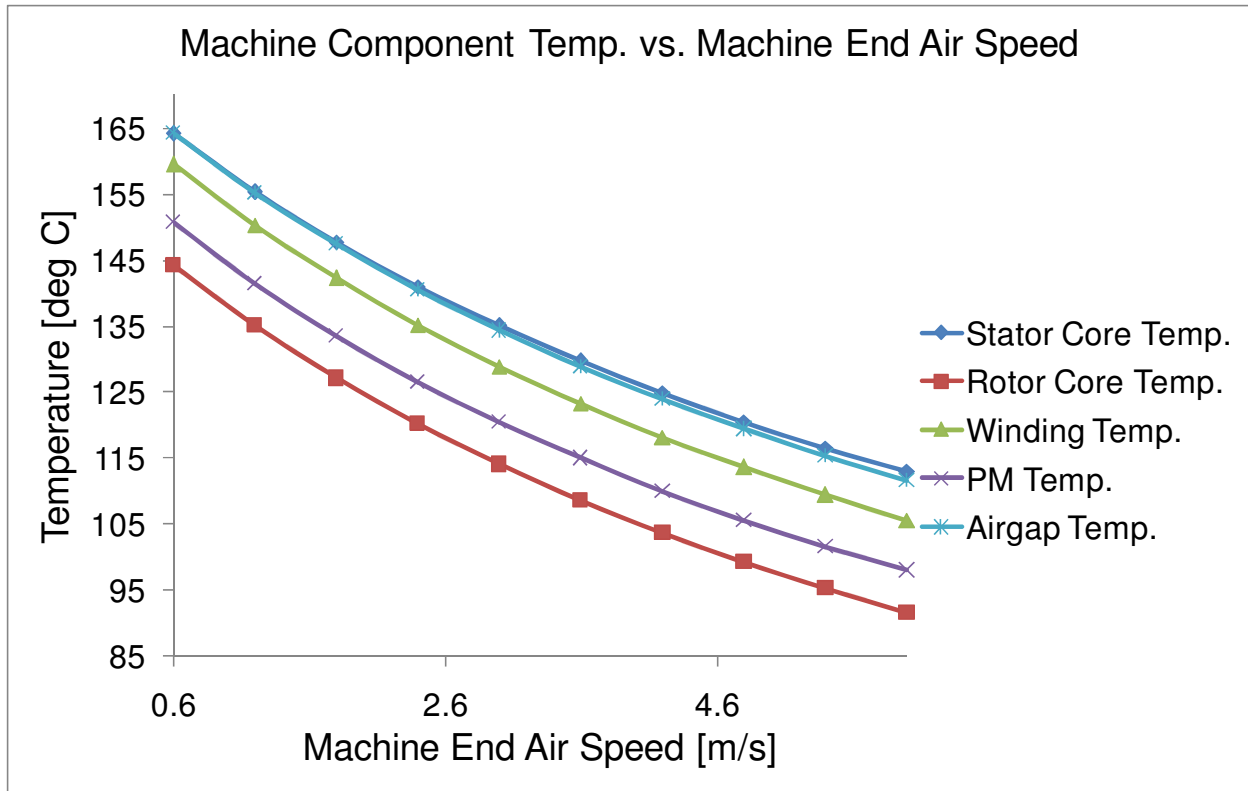


Fig. 4 - 6: TD Design average component temperatures vs. machine end air speed

In the third cooling scenario, the cylindrical outer surface of the candidate machine is assumed to be air-cooled (Fig.4-7). The heat transfer coefficient of the forced convection for this area can be modeled by following equations according to [115]:

$$Nu = 0.664(Re)^{0.5}(Pr)^{0.33} \quad (15)$$

$$Re = \frac{\rho v_2 L}{\mu} \quad (16)$$

$$Pr = \frac{c_p \mu}{k_{air}} \quad (17)$$

$$h = \frac{Nu k}{L} \quad (18)$$

where  $Re$  is the dimensionless Reynolds number,  $Pr$  is the dimensionless Prandtl number,  $L$  represents the characteristics of the surface [m], which is the machine axial length in the case, and  $c_p$  is the fluid specific heat capacity [J/(kgK)]. The temperature for each part of the TD Design as a function of the air speed on the cylindrical surface is shown in Fig. 4-8. All machine component temperatures drop as the air velocity increases, and the stator core temperature (the blue curve) decreases faster than others, as it is closest to the cooling air. For an air speed equal to 2 m/sec, the average winding temperature drops to 148.76 °C from 159.45 °C in the original model (without active cooling). Compared to the temperature drop achieved by using water jackets, this cooling method is less effective.

Based on the results from this parametric analysis, the subsequent candidate machines are assumed to be mounted in water jackets with a coolant temperature of 65°C, and both of the machine ends are air-cooled by an external blower with an average air velocity of 2 m/sec, as illustrated in Fig. 4-9. The temperature for each part of the TD Design under the cooling condition is compared to that of the original model (without active cooling) in Table 4-4, where the average winding temperature has dropped to 90.58 by applying these active cooling techniques.



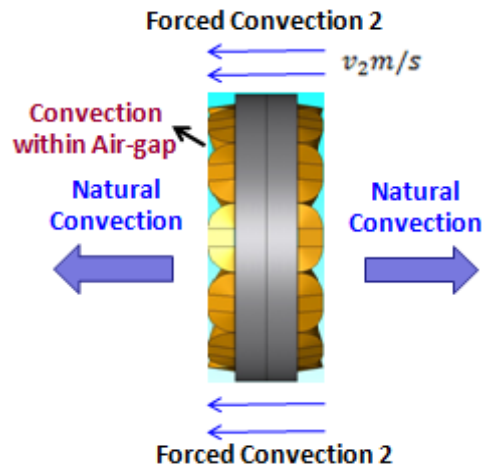


Fig. 4 - 7: TD Design thermal model with forced convection on machine axial surface

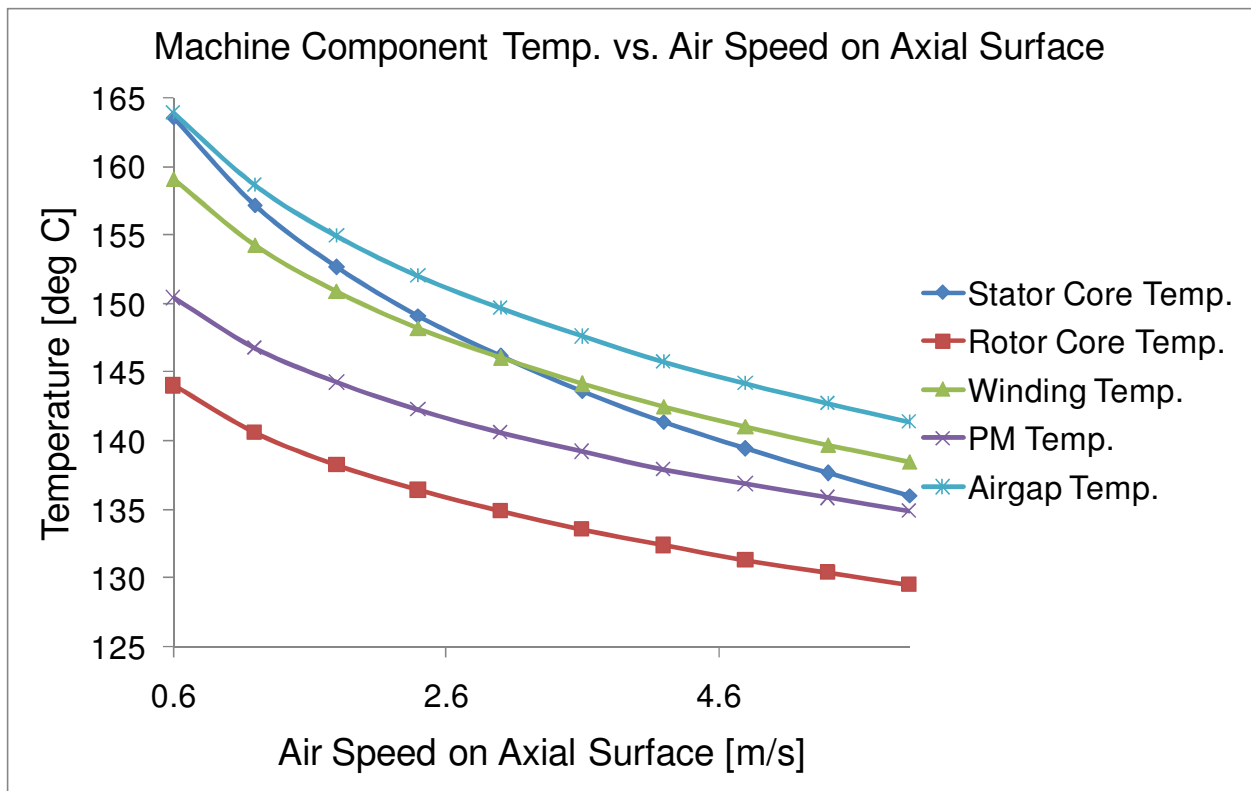


Fig. 4 - 8: TD Design average component temperatures vs. air speed on machine axial surface

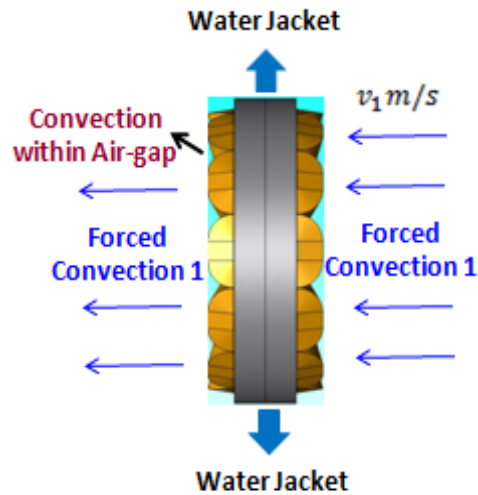


Fig. 4 - 9: TD Design final thermal model with active cooling

Table 4 - 4: Average Component Temperatures Comparison between Initial Model and Final Model

	Stator Core Temp. [°C]	Rotor Core Temp. [°C]	Winding Temp. [°C]	PM Temp. [°C]	Airgap Temp. [°C]
Initial Model	164.09	144.28	159.45	150.67	164.26
Final Model	77.76	91.88	90.58	95.54	90.35

### 4.3 Temperature Dependent Material Properties

The EM and thermal analysis components are coupled with the temperature-dependent material properties of the copper, magnets, coolant, and lamination steel. Understanding these material attributes as functions of temperature is essential for establishing the coupled EM/thermal model.

#### 4.3.1 Permanent Magnet

This study uses neodymium magnets, a rare-earth magnet material widely used in traction motor applications. This material is well known to be sensitive to operating temperature, as shown in Fig. 4-10; both the magnet remanent flux density and coercive force decrease when the

temperature increases. The irreversible temperature-dependent characteristics of the magnets are incorporated into the EM FE model. As a result, the magnet's B-H curve is automatically updated according to the input magnet temperature, and demagnetization thresholds are detected during the analysis.

The electric resistivity of the magnet material is also dependent on operating temperature. In addition, the resistivity value along the magnetization (normal) direction differs from the value in the tangential direction [114]. Magnet resistivity values are shown in Fig. 4-11 as a function of the temperature in both normal and tangential directions. The magnet resistivity in the normal direction can be expressed by a second order polynomial:

$$\rho_{m_n}(T) = c_n * T^2 + b_n * T + a_n \quad (19)$$

where the coefficients  $c_n = -5.468 * 10^{-6}$ ,  $b_n = 1.765 * 10^{-3}$ , and  $a_n = 1.52$ . The resistivity in the tangential direction has a linear relationship with temperature and can be defined as

$$\rho_{m_t}(T) = b_t * T + a_t \quad (20)$$

where the coefficients  $b_t = 0.884 * 10^{-3}$  and  $a_t = 1.258$ . The temperature-dependent magnet resistivity in the tangential direction is adopted in this investigation, since a 2D FE model is used for the EM component of the coupled analysis.

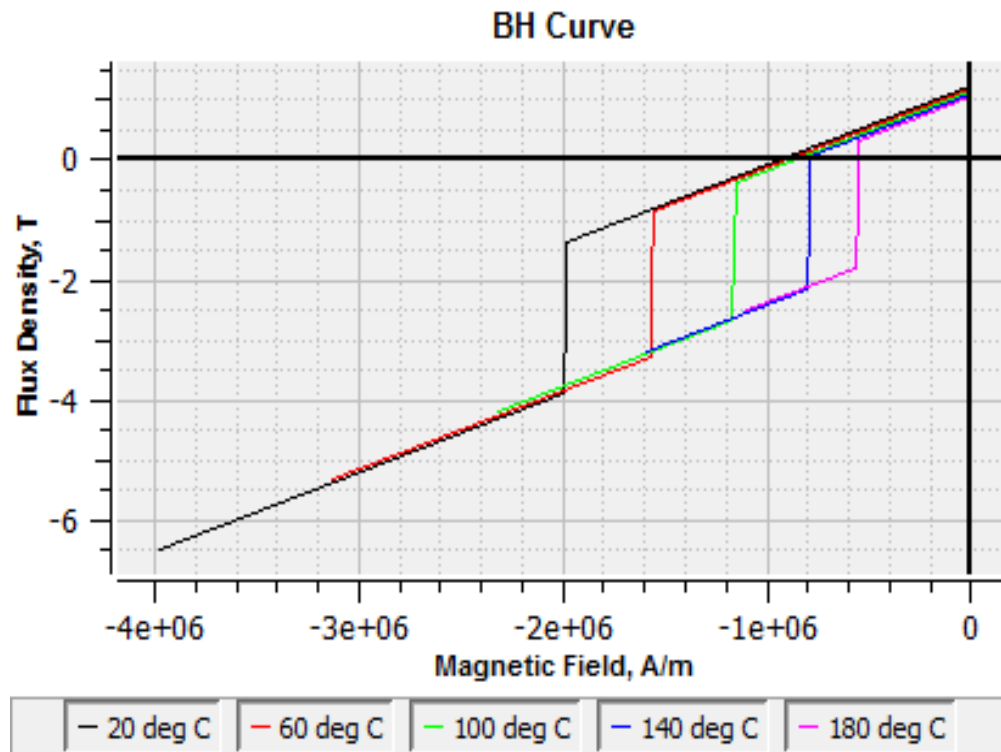


Fig. 4 - 10: BH curve of neodymium magnet NMX-39EH from JMAG library

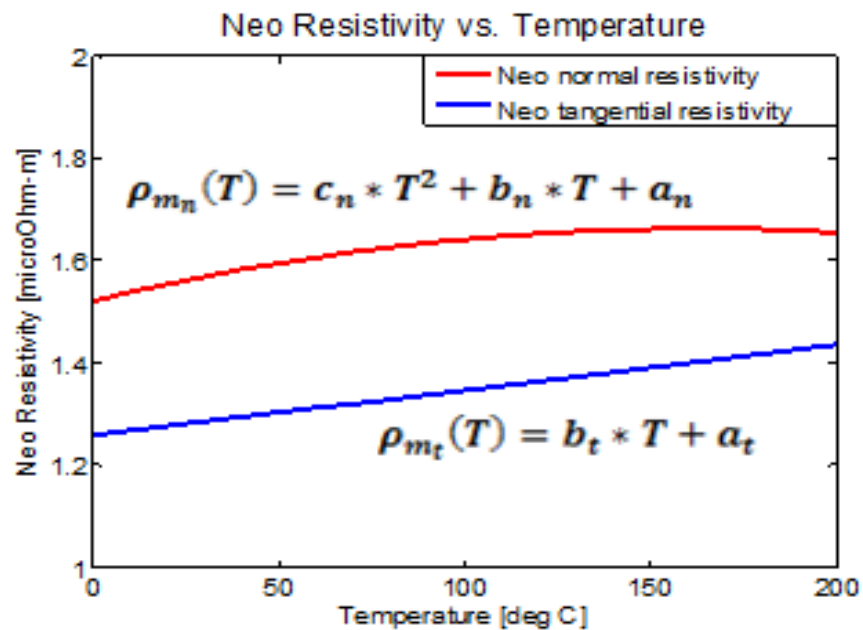


Fig. 4 - 11: Neodymium magnet resistivity vs. temperature

### 4.3.2 Copper

Copper loss can be calculated using the following equation, where only dc resistance is considered:

$$P_c = 3I^2R \quad (21)$$

$$R = \frac{\rho_c L}{A} \quad (22)$$

where  $I$  is phase rms current [A],  $R$  represents the winding dc electric resistance [ $\Omega$ ], and  $L$  and  $A$  are the length [m] and cross-section area [m<sup>2</sup>] of the windings, respectively.  $\rho_c$  is the copper electric resistivity [ $\Omega$  m], which varies with temperature, expressed in (23) as follows:

$$\rho_c(T) = \rho_{c0}[1 + \alpha_c(T - T_0)] \quad (23)$$

where  $\rho_{c0}$  is the copper electric resistivity at 20 °C, and  $\alpha_c$  is the copper temperature coefficient [1/K].  $T_0$  is the base temperature (20 °C).

### 4.3.3 Coolant

The 2007 Camry Report [114] indicates that the coolant loop for the motor consists of a standard 50% ethylene glycol and 50% water mixture flowing at 10 L per minute, and has an average operating temperature of 65 °C. The same coolant condition is assumed for the water jacket employed in this study.

In addition to the water jacket cooling, both the airgap area and machine ends are air-cooled. In order to accurately estimate the heat transfer coefficient, the correlation between the air density, air viscosity, air thermal conductivity and the temperature is found according to [117].

Figs. 4-12 to 4-14 show the density, viscosity, and thermal conductivity of air as a function of temperature, and they can be well approximated with straight line fitting.

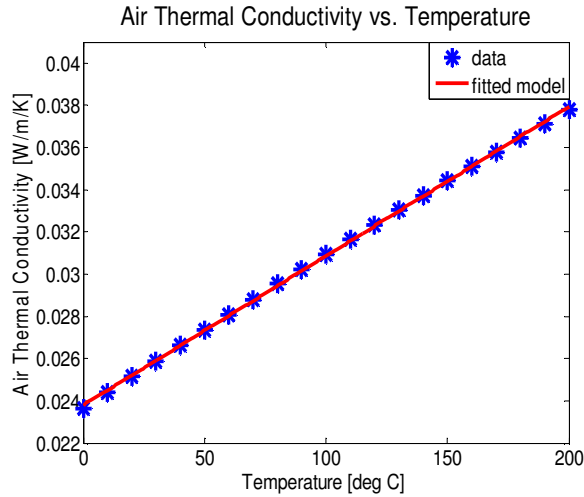


**Fig. 4 - 12: Air thermal conductivity vs. temperature**

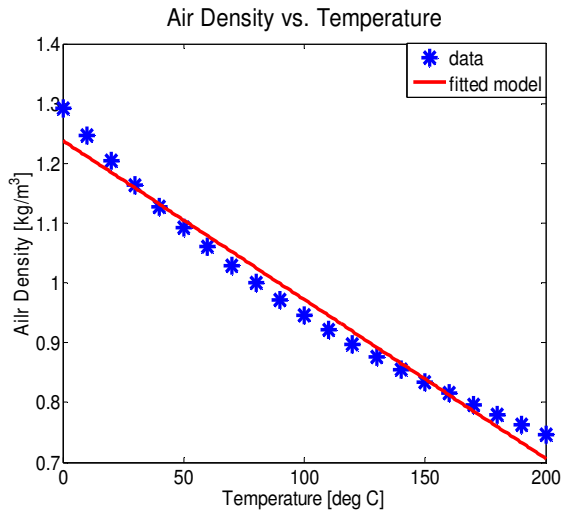


**Fig. 4 - 13: Air density vs. temperature**

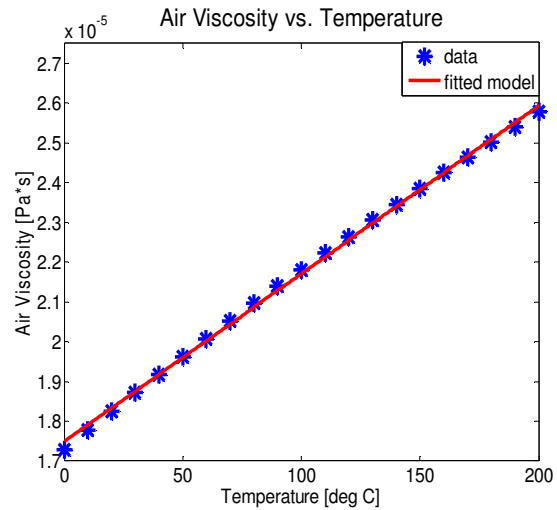


**Fig. 4 - 14: Air viscosity vs. temperature**

### 4.3.4 Lamination Steel

The M19 lamination steel with a gauge number of 29 is used as the stator core and rotor core material. Its permeability is expressed in (24) according to [118], as follows:

$$\mu_R(T) = (\mu_{20} - 1) * C + 1 \quad (24)$$

where  $\mu_{20}$  is the steel permeability at 20 °C, and C is the correction factor, which is temperature dependent as shown in Fig. 4-15. This correction factor equals one below 300 °C, indicating the steel permeability does not change under the normal operating condition for this traction motor application (max. temp < 300 °C). Therefore, the steel permeability in this coupled model is assumed to remain constant as temperature varies.

The core loss is estimated using JMAG, a commercial FE analysis package used in this study. The lamination steel has been selected to be 29 Gauge M19 material. The detailed loss profile for this steel (i.e., core loss as a function of both frequency and magnetic flux density) is used to calculate the core losses. There is currently no information available about the impact of temperature on the loss profile of lamination steels in either the technical literature or the manufacturer-supplied information. As a result, it is assumed that the temperature variation does not affect the core loss estimation in the coupled analysis.

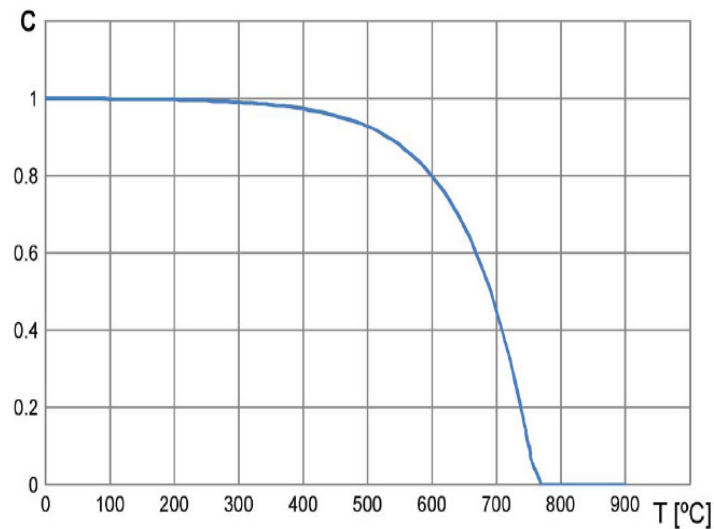


**Fig. 4 - 15: Correction coefficient for steel permeability vs. temperature [118]**

#### 4.4 Tests of Coupled EM/Thermal Analysis

A flow chart of the coupled EM/thermal FE analysis is proposed in Fig.4-16 to illustrate the organization of this coupled analysis. An initial temperature (150 °C) is assumed for all machine components at the beginning of the analysis. Temperature-dependent material parameters are updated according to updated machine component temperatures after each iteration. Following this update, the machine's EM performance is evaluated using 2D transient FE analysis and the resulting loss values become inputs for the 3D thermal FE static analysis. Next, the convergence criterion is checked. If the convergence criterion is not satisfied, the process repeats until the requirement is met. At this point the loop iteration terminates, and the final machine performance results are delivered.

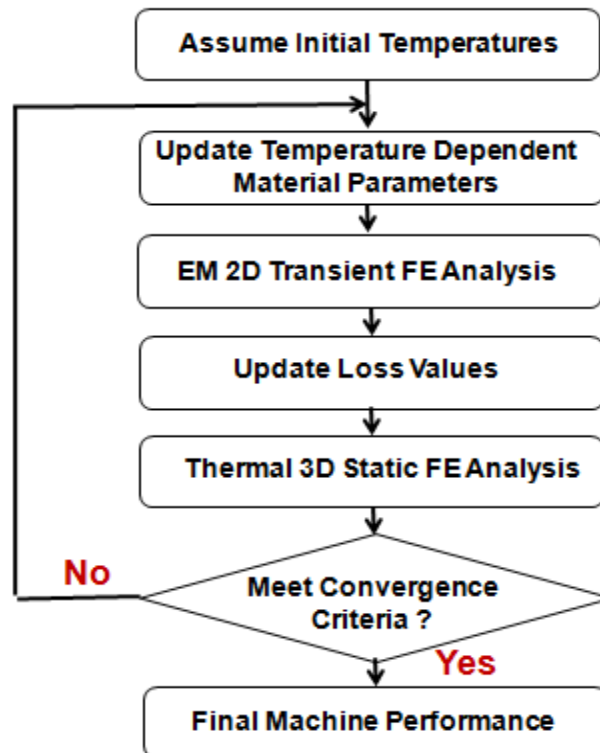


Fig. 4 - 16: Preliminary coupled EM/thermal FE analysis flow diagram



In order to understand the convergence properties of the coupled EM and thermal FE analysis and to explore the characteristics of the EM/thermal coupled model, tests have been carried out with several current density values. Key conditions include:

- Ambient temperature: 20°C
- Base current density: 4.6 A/mm<sup>2</sup> (i.e., 1 p.u.)
- Initial temperature: 150 °C for all machine components
- Convergence criterion: the iterative loop terminates when the temperature differences of all machine components are less than 0.5°C between the current and preceding iteration.

This criterion guarantees that self-consistent results are attained.

The target machines selected for study are 30 kW 10-pole, 12-slot fractional-slot concentrated winding (FSCW) surface PM machines optimized for maximum torque density (TD Design), minimum cost (TPD Design), and maximum efficiency (Eff. Design), as outlined in Section 2.6.1. Front views and side views of the machine 3D thermal models are shown in Fig. 4-17 and the key dimensions and metrics for the three optimal machines are summarized in Table 2-7. It can be observed that the TD Design has the largest slot area and the shortest stack length. The TPD Design, optimized for minimum cost, has the thinnest magnets. The high-efficiency design (Eff. Design) has the thickest magnets, the smallest slot area, and the longest stack length. Although none of the three machines represents a practical design for fabrication, the significant differences between the 3 machines makes them useful for exploring the effectiveness of the coupled-model approach over a wide range of different motor designs.

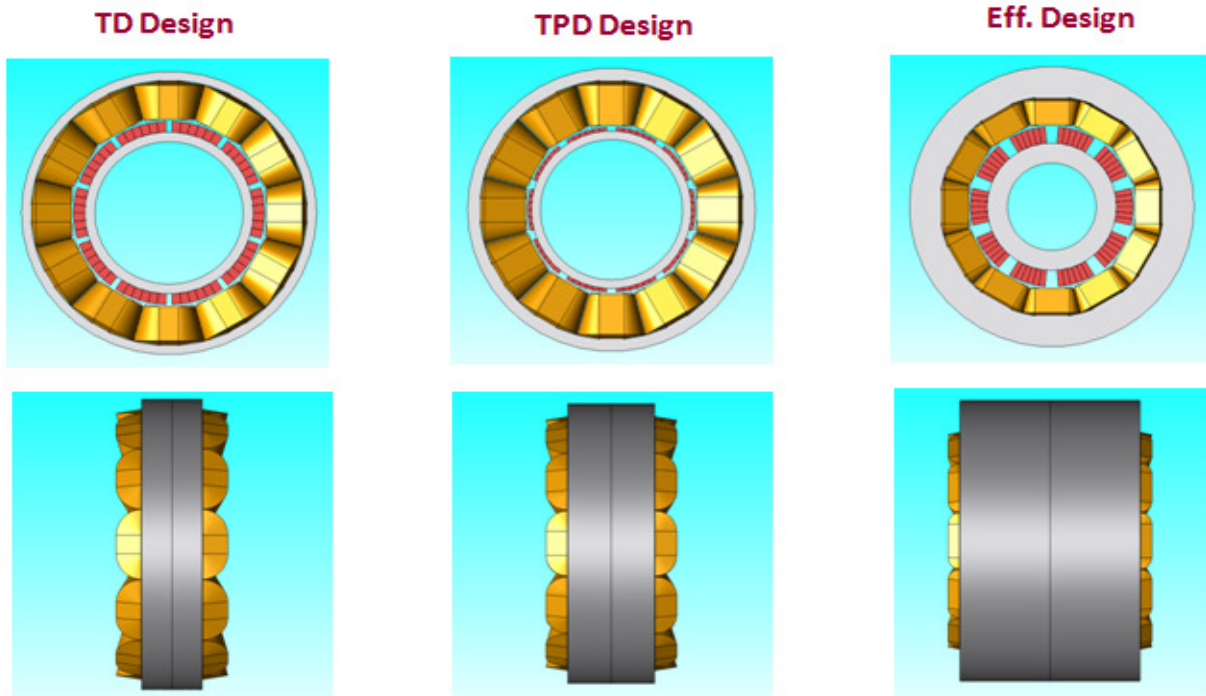


Fig. 4 - 17: Front view and side view of the three candidate designs' 3D thermal model

## 4.5 Key Observations of the Coupled EM/Thermal Models

The three candidate machine designs are subject to the coupling tests under various current density conditions, with the above-mentioned EM/thermal analyses coupling routine, test settings, and convergence criterion. The detailed testing results are attached in the Appendix.

### 4.5.1 Convergence Property of Coupled EM/Thermal Model

The coupled model analysis converges in 2 to 6 iterations using the  $0.5^{\circ}\text{C}$  convergence criterion for the three candidate machines for the full range of current density values. The iteration count can be reduced to increase the solution speed with a trade-off cost of a small amount of accuracy. For example, by increasing the maximum allowable temperature difference between iterations to  $1.0^{\circ}\text{C}$ , the candidate designs converge within 2 EM/thermal iterations for almost all current density cases, as described in Table 4-5. There are few cases wherein the

iteration number exceeds 2. In these cases, either the winding temperature has surpassed the insulation limit or demagnetization has occurred, which are both beyond the scope of interest for this investigation. As a result, 2 EM/thermal iterations are considered sufficiently accurate for attaining machine performance.

**Table 4 - 5: Iteration No. Summary with  $|\text{Current Iteration Temp. (all)} - \text{Final Iteration Temp. (all)}| \leq 1 \text{ }^\circ\text{C}$**

<b>Current Density [p.u.]</b>	<b>TD Design Iteration no.</b>	<b>TPD Design Iteration no.</b>	<b>Eff. Design Iteration no.</b>
<b>0.25</b>	2	2	1
<b>0.50</b>	2	2	1
<b>0.75</b>	2	2	1
<b>1.00</b>	2	2	2
<b>1.25</b>	2	2	2
<b>1.50</b>	2	2	2
<b>1.75</b>	3	2	2
<b>2.00</b>	5	4	2
<b>2.25</b>			2
<b>2.50</b>			2
<b>2.75</b>			1
<b>3.00</b>			3
<b>3.25</b>			4
<b>3.50</b>			5

#### **4.5.2 Maximum Winding Temperature Limit**

Figures 4-18 to 4-20 show the calculated maximum (hot spot) winding temperature as a function of current density for the TD Design, TPD Design, and Eff. Design, respectively. The blue curve represents the final maximum winding temperature; the green curve is the result from the second EM/thermal iteration; and the red curve is the maximum winding temperature with only one EM/thermal iteration. The blue and green curves are nearly equal, which again confirms that two EM/thermal iterations are sufficient for attaining relatively accurate results.

It can be noted that the red curves in Figs. 4-18 to 4-20, which plot the results from the first iteration, are very close to the final results in the region near the insulation temperature limit

(155°C for F Class insulation). The reason for this behavior is that the initial temperature for the winding is assumed to be 150°C for these analyses. As a result, one EM/thermal iteration is sufficient to find the maximum winding temperature when the final temperature is close to the initial assumed value.

Additionally, Table 4-6 shows the current densities at which the maximum winding temperatures in the three candidate designs reach the insulation limit. These maximum current densities vary considerably among the three designs, even though all three are exposed to the same cooling environment. These results are consistent with the observation at the beginning of the paper that current density alone is a poor surrogate for more rigorous maximum winding temperature limits.

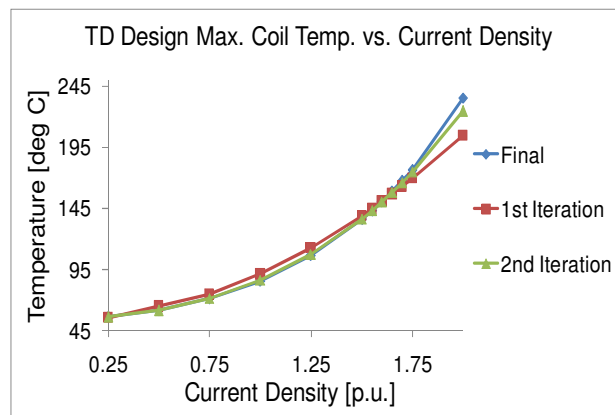


**Fig. 4 - 18: TD Design maximum winding temperature vs. current density**

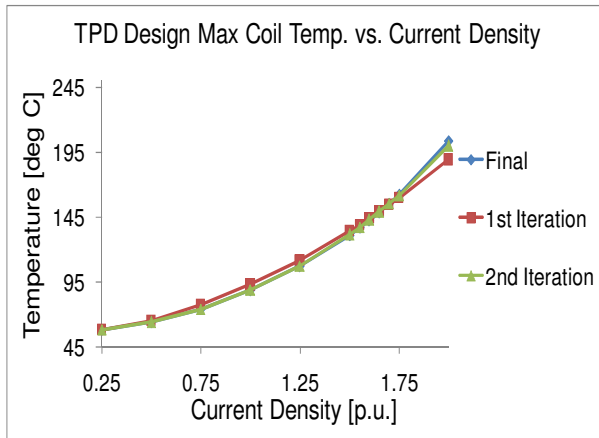


**Fig. 4 - 19: TPD Design maximum winding temperature vs. current density**

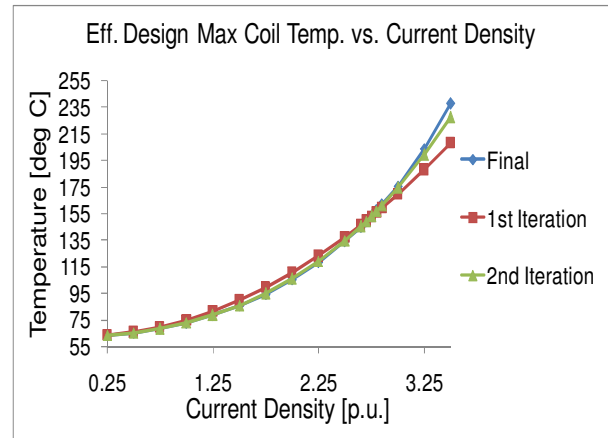


**Fig. 4 - 20: Eff. Design maximum winding temperature vs. current density**

Finally, it can be observed in Figs. 4-18 to 4-20 that the three curves in each figure diverge at the upper end of the current density range. In this regime, the positive feedback between the winding ohmic losses, higher winding temperatures, and the resulting higher winding resistivity becomes increasingly apparent as the current density increases, which ultimately requires additional EM/thermal iterations to achieve convergence. It should be noted that this curve divergence becomes apparent for current density values above the maximum safe value, listed in Table 4-6, for each of the three machine designs.

**Table 4 - 6: Maximum Current Density for Winding Insulation Constraint**

	<b>TD Design</b>	<b>TPD Design</b>	<b>Eff. Design</b>
Max. Winding Temperature [°C]	155	155	155
Magnet Thickness [mm]	10.46	3.42	16.02
Airgap Radius $R_g$ [mm]	90.74	81.72	80.34
Current Density [p.u.]	1.63	1.7	2.78
Current RMS Value $I_{rms}$ [A]	267.48	257.31	138.42
Electrical Loading [A/m]	112596	120271	65811

### 4.5.3 Demagnetization Constraint

Armature reaction in PM machines can cause partial or total demagnetization of the magnets if the stator currents are too high. For a machine that is properly designed, the intersection of the

machine's B-H load line and the magnet's demagnetization curve should be higher than the knee point at the magnet's working temperature, as described in Fig. 4-21. However, if the intersection of the load line and the demagnetization curve occurs beyond the knee point due to excessive currents, then the magnet suffers partial or total demagnetization [119].

Since temperature-dependent magnet material is applied in the electromagnetic FE model, the “health” of the magnet can be checked at every mesh node inside the magnets, but this check requires two EM/thermal iterations. More specifically, the magnet temperature is calculated during the first iteration and the possible onset of demagnetization is checked during the second iteration when the magnet temperature has been updated.

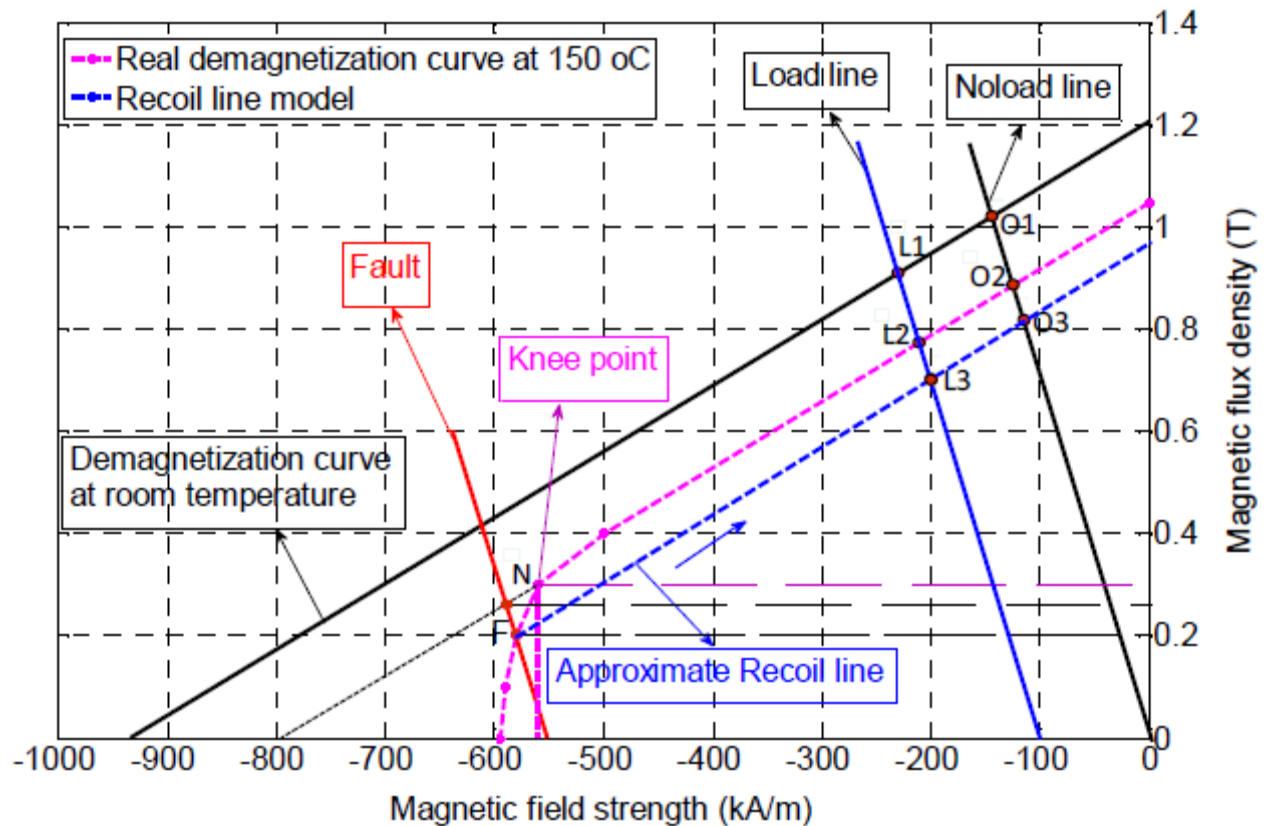


Fig. 4 - 21: Demagnetization curve at different temperature of Neodymium magnet [119]

Figures 4-22 to 4-24 show the demagnetization ratio vs. current density for the TD Design, TPD Design, and Eff. Design, respectively – where the demagnetization ratio is defined as the sum of surface areas of the magnet FE cells that experience irreversible demagnetization divided by the total magnet surface area. It can be seen that there is a near-linear relationship between the demagnetization ratio and the current density, once the demagnetization ratio diverges from zero.

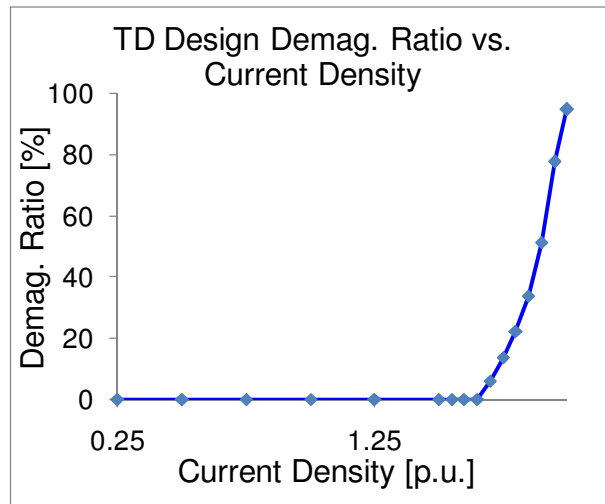


Fig. 4 - 22: TD Design demagnetization ratio vs. current density

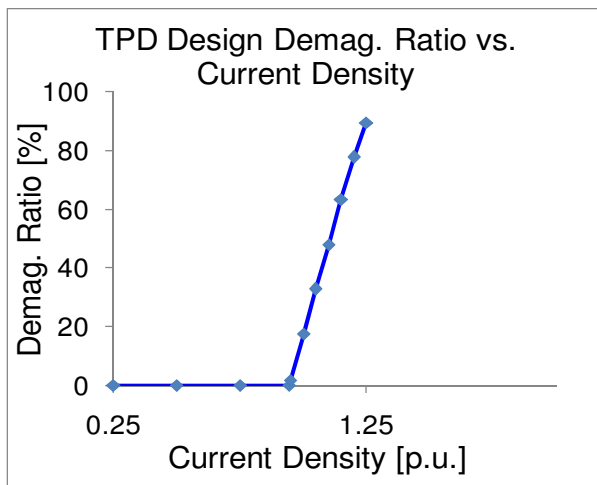


Fig. 4 - 23: TPD Design demagnetization ratio vs. current density

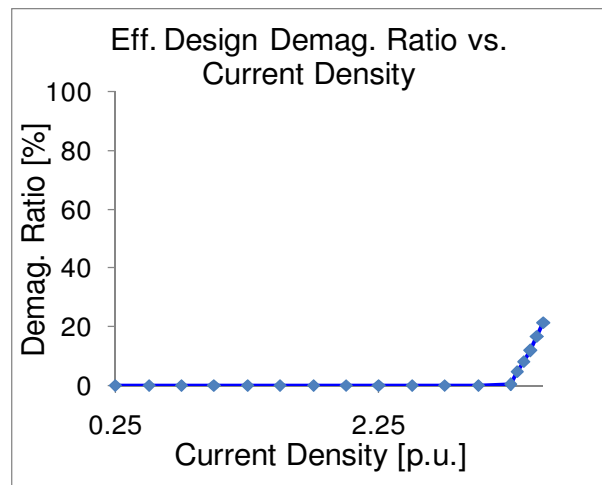


Fig. 4 - 24: Eff. Design demagnetization ratio vs. current density

Magnet temperature and current density when demagnetization begins, for the three candidate designs, is summarized in Table 4-7, along with the magnet's thickness. Referenced to current density values, the TPD Design is the first to show signs of demagnetization, the TD Design is second, and the Eff. Design is third. This order of demagnetization onset is the same as that for the magnet thicknesses of the three designs; that is to say, the design with the thinnest magnets (TPD Design) also has the lowest current density threshold for demagnetization. This result suggests that increasing the magnet thickness will help to reduce the machine's vulnerability to demagnetization. However, there are inevitable trade-offs between demagnetization vulnerability, machine cost, and torque density that must be appropriately balanced in order to optimize the machine design.

**Table 4 - 7: Maximum Current Density for Demagnetization**

	<b>TD Design</b>	<b>TPD Design</b>	<b>Eff. Design</b>
Magnet Temperature [°C]	172.37	156.19	201.07
Magnet Thickness [mm]	10.46	3.42	16.02
Airgap Radius $R_g$ [mm]	90.74	81.72	80.34
Current Density [p.u.]	1.65	0.95	3.25
Current RMS Value $I_{rms}$ [A]	270.77	143.79	161.82
Electrical Loading [A/m]	113981	67210	76938

#### **4.5.4 EM Model vs. Coupled EM/Thermal Model**

The torque vs. current density curves for the TD Design, TPD Design, and Eff. Design machines are shown in Figs. 4-25, 4-26, and 4-27, respectively. The blue curves are the results from the EM models alone with a fixed temperature (150°C), while the red curves are the results from the coupled EM/thermal model. These results show that when only the EM model is used, there is a risk of selecting a current density that results in temperatures beyond the threshold of magnet demagnetization or the maximum thermal limit of the winding insulation. By applying



the coupled EM/thermal model, these physical constraints can be recognized during the design stage. The availability of this coupled model makes it much easier to identify the maximum current density for a given machine design that respects both the winding insulation limit and the magnet demagnetization constraints during steady-state operation.

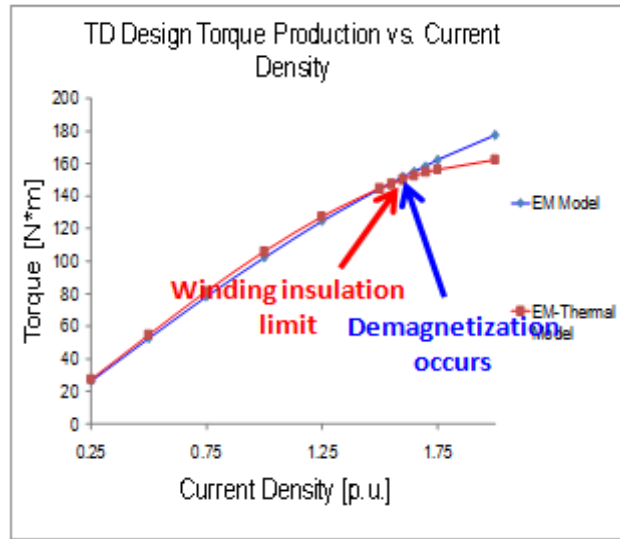


Fig. 4 - 25: TD Design EM model and EM/Thermal model comparison

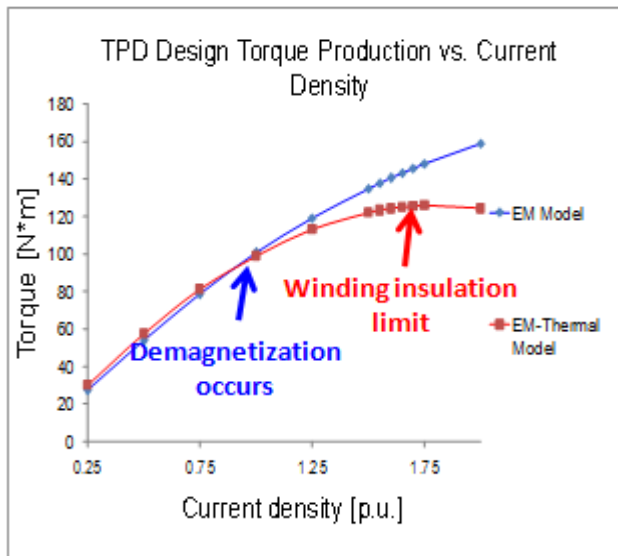


Fig. 4 - 26: TPD Design EM model and EM/Thermal model comparison

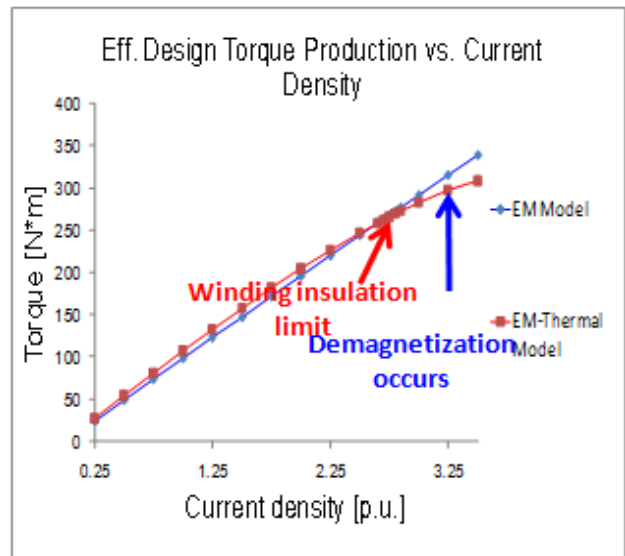


Fig. 4 - 27: Eff. Design EM model and EM/Thermal model comparison

## 4.6 Conclusions

This chapter describes the development of a coupled EM/thermal model for electric machines based on FE analysis. The electromagnetic and thermal analyses are linked via temperature-dependent material properties and machine losses. The characteristics of the coupled model have been studied by using it to analyze three 30 kW (continuous) surface PM machines under various current density conditions.

The results of these coupled model analytical tests show that two EM/thermal iterations are sufficient to achieve accurate machine performance results in the majority of the considered cases. Compared to the EM (alone) model, the coupled EM/thermal model has the advantage of being able to recognize winding insulation maximum thermal limits and the onset of irreversible magnet demagnetization during the design stage.

This work has also demonstrated that the coupled EM/thermal model can be used to efficiently determine the maximum current density the machine can sustain under steady-state operating conditions without exceeding temperature limits for the insulation or inducing irreversible magnet demagnetization. For the same cooling conditions, the maximum allowable current density varies significantly among the three different types of machine designs that were investigated. Similarly, irreversible demagnetization occurs at different magnet temperatures for the different types of machine designs.

This investigation has clearly demonstrated that: 1) adoption of a pre-determined current density as a surrogate for the imposition of a temperature limit on the winding temperature is oversimplified in most cases; and 2) avoiding demagnetization is more complicated than simply setting a maximum temperature for the rotor magnets.

## Chapter 5: Coupled Electromagnetic/Thermal Machine Design Optimization for Steady-State Operation

### 5.1 Finding the Maximum Current Density for Winding Insulation Limit

#### 5.1.1 Problem Identification

The solid blue curve in Fig. 5-1 shows the predicted TD Design maximum winding temperature from the first coupled EM/thermal model iteration as a function of the current density. The result from the first EM/thermal iteration is used because the computation cost is low and it is close to the final solution especially in the region close to the initial temperature assumption as discussed in the previous section. The most important point on the curve is the one at which the maximum winding temperature intersects with the insulation limit; 155°C. This suggests that finding the current density that corresponds to the maximum winding temperature insulation thermal limit can be considered a root-finding problem.

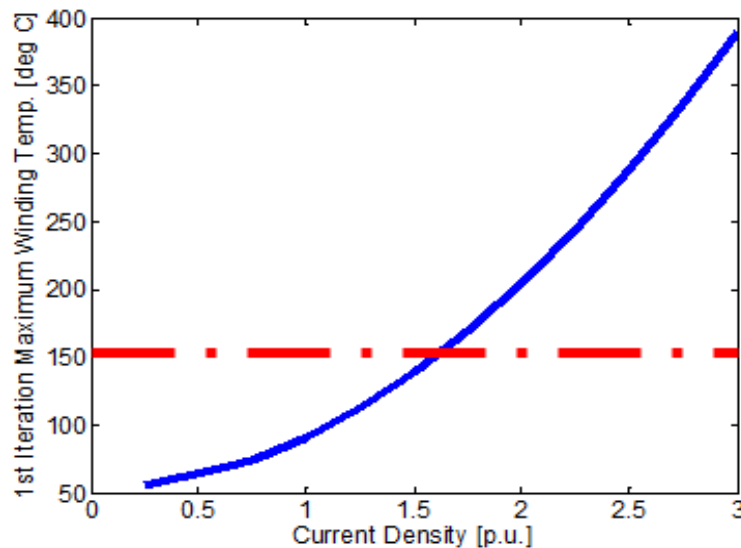


Fig. 5 - 1: TD Design maximum winding temperature from 1st EM/Thermal iteration

### 5.1.2 Finding the Maximum Current Density Using Numerical Methods

There are several algorithms widely used for solving the root-finding problems, such as the bisection method, false-position method, Newton-Raphson method, secant method, and Müller's method [120-122]. Each of these methods can be applied in this study except for the Newton-Raphson method because it requires derivative calculation of the model, and the derivative information cannot be easily extracted from the FE model used in this study.

In order to determine which of the remaining algorithms is most suitable for this FE optimization problem, all four methods have been applied sequentially to estimate the current density at which the maximum winding temperature reaches the insulation thermal limit for the three machine designs. The convergence criterion is that the maximum winding temperature must fall between 150°C and 155°C.

#### **Bisection Method**

The bisection method can be described as repeatedly bisecting an interval and then selecting a subinterval in which a root must lie for further processing. Previous experience suggests that for various machine designs the maximum winding temperature should be below 150°C at 1 p.u. current density and above 155 °C at 3 p.u. current density. In other words, the expected current density for reaching the insulation limit falls in the current density region between 1 p.u. and 3 p.u.. Therefore, the two initial points are chosen to be 1 p.u. and 3 p.u.. The maximum winding temperature at the two initial points is evaluated using one EM/thermal iteration FE analysis, and the results are listed in Table 5-1. Then the maximum winding temperature at the middle point 2 p.u. is calculated, such that the updated interval is 1 p.u. to 2 p.u. By repeating this procedure, the current density of 1.625 p.u. is found with a maximum winding temperature of 153.55°C, which

meets the convergence criterion. This operation is described in Fig. 5-2, and it requires a total number of 6 EM/thermal iterations to reach the final result.

**Table 5 - 1: Finding TD Design Max. Current Density for Insulation Limit Using Bisection Method**

	Current Density [p.u.]	Max. Winding Temp. [°C]
<b>1</b>	1.0000	91.07
<b>2</b>	3.0000	389.62
<b>3</b>	2.0000	204.67
<b>4</b>	1.5000	138.73
<b>5</b>	1.7500	169.48
<b>6</b>	1.6250	153.55

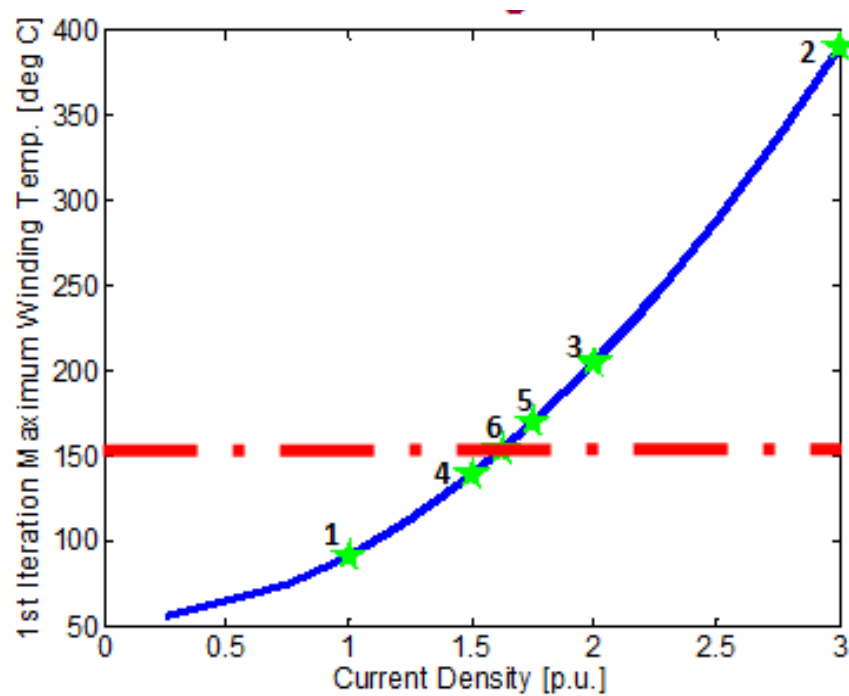


**Fig. 5 - 2: Finding TD Design max. current density for insulation limit using Bisection method**

### False-Position Method

The false-position method can be summarized as obtaining a root estimate by projecting a straight line to the x-axis through two function values, where the two function values must always bracket the root. As before, the two initial points are chosen as 1 p.u. and 3 p.u. current density. A straight line is projected using these two points, and it intercepts the 152.5°C temperature line (the average between 150°C and 155°C, according to the predefined convergence criterion) at the current density of 1.4115 p.u.. The maximum winding temperature at this current density is evaluated to be 128.96°C, as shown in Table 5-2. Since the expected 152.5°C falls between 128.96°C at 1.4115 p.u. and 389.62°C at 3 p.u., the updated line is projected via 1.4115 p.u. and 3 p.u.. By repeating this process, the current density of 1.5987 p.u. is found with a maximum winding temperature of 150.34 °C, fulfilling the convergence criterion. This procedure is described by Fig. 5-3 and requires a total number of 5 EM/thermal iterations to obtain the final result.

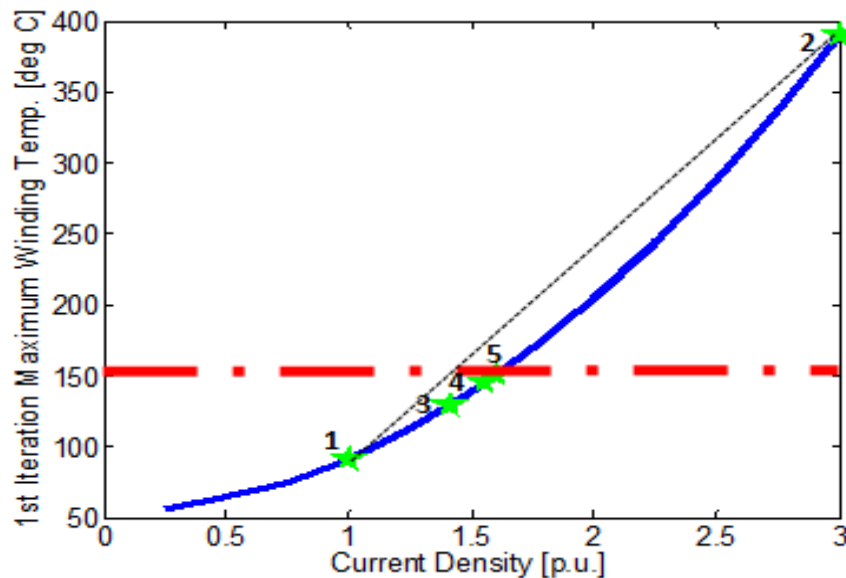


Fig. 5 - 3: Finding TD Design max. current density for insulation limit using the false-position method

**Table 5 - 2: Finding TD Design Max. Current Density for Insulation Limit Using the False-Position Method**

	Current Density [p.u.]	Max. Winding Temp. [°C]
<b>1</b>	1.0000	91.07
<b>2</b>	3.0000	389.62
<b>3</b>	1.4115	128.96
<b>4</b>	1.5550	145.10
<b>5</b>	1.5987	150.34

### Secant Method

The secant method is very similar to the false-position method, in that it also obtains a root estimate by projecting a straight line to the x-axis through two function values. The difference is that the two function value data points should be in strict sequence when using the secant method. Again, Point 1 is chosen to be at 1 p.u., and Point 2 is at 3 p.u.. The first line is projected using these two initial points, and the intercepted current density is 1.4115 p.u., which is marked as Point 3. Then the second line is projected using Point 2 and Point 3, marking the new intercept Point 4. Following this sequence, the current density of 1.6208 p.u. is found with a maximum winding temperature of 153.02°C, satisfying the convergence criterion. The results are recorded in Table 5-3, and the procedure is described by Fig. 5-4. It takes a total number of 5 EM/thermal iterations to locate the final result.

**Table 5 - 3: Finding TD Design Max. Current Density for Insulation Limit Using Secant Method**

	Current Density [p.u.]	Max. Winding Temp. [°C]
<b>1</b>	1.0000	91.07
<b>2</b>	3.0000	389.62
<b>3</b>	1.4115	128.96
<b>4</b>	1.5550	145.10
<b>5</b>	1.6208	153.02

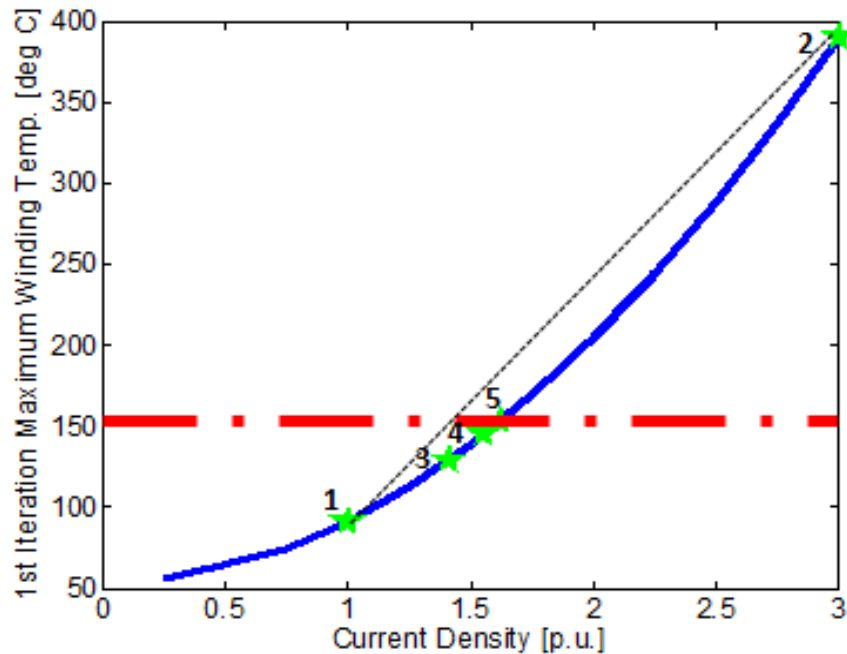


Fig. 5 - 4: Finding TD Design max. current density for insulation limit using secant method

### Müller's Method

Instead of projecting a straight line as in the false-position and secant methods, Müller's method can attain a root estimate by projecting a parabola to the x-axis through three function values. First of all, three initial guess points must be chosen randomly. Point 1 at 1 p.u., Point 2 at 2 p.u., and Point 3 at 3 p.u. are chosen as the three initial points for this case. The maximum winding temperatures at these three points are evaluated and the results are listed in Table 5-4. The coefficients of a second order polynomial can be determined using the (x, y) values at these three points, resulting in  $y = 35.675x^2 + 6.575x + 48.82$ . The parabola intercepts the 152.5°C temperature line at the current density of 1.6151 p.u., marked as Point 4. The maximum winding temperature at this point needs to be evaluated. If the resulting temperature does not fulfill the convergence criterion, the three data points closest to the root are used to update the parabola. The process will continue until the termination requirement is satisfied. In this case, the



maximum winding temperature at Point 4 is 152.33°C, which falls between 150°C and 155°C. A total number of 4 EM/thermal iterations are sufficient to find this maximum current density corresponding to the insulation limit.

Figure 5-5 illustrates the process of using Müller's method to find the expected current density for the TD Design. The blue curve is the data taken from FE analysis, while the dotted green line is a parabola whose coefficients are determined by the three initial guess points. Results show that the maximum winding temperature vs. current density curve can be well fitted by a second order polynomial. As a result, Müller's method is suitable for finding the maximum current density, at which the winding temperature reaches the insulation limit.

The four numerical methods have also been applied to the TPD Design and the Eff. Design. Table 5-5 compares the number of EM/thermal model iterations required to find the threshold current density that just reaches the maximum winding temperature using each of the numerical methods, for all three designs. These results show that Müller's method always requires the fewest EM/thermal iterations. Therefore, Müller's method has been chosen as the preferred root-finding algorithm for determining the maximum current density when the maximum winding temperature just reaches the insulation thermal limit during steady-state operation.

**Table 5 - 4: Finding TD Design Max. Current Density for Insulation Limit Using Müller's Method**

	<b>Current Density [p.u.]</b>	<b>Max. Winding Temp. [°C]</b>
<b>1</b>	1.0000	91.07
<b>2</b>	2.0000	204.67
<b>3</b>	3.0000	389.62
<b>4</b>	1.6151	152.33

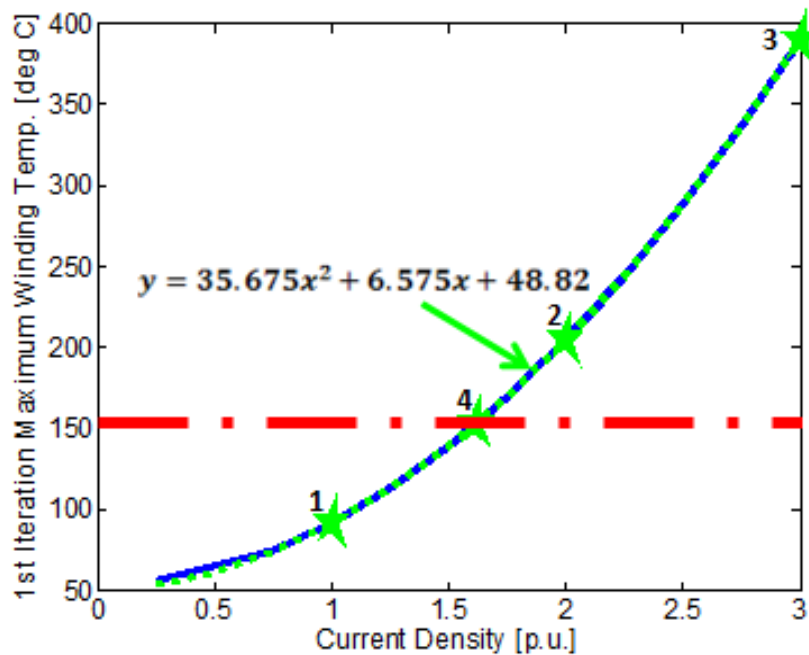


Fig. 5 - 5: Finding TD Design max. current density for insulation limit using Müller's method

Table 5 - 5: Required Iterations to Calculate Maximum Current Density for Winding Insulation Limit

	TD Design Iteration no.	TPD Design Iteration no.	Eff. Design Iteration no.
Bisection Method	6	8	5
False-Position Method	5	5	4
Secant Method	5	5	4
Müller's Method	4	5	4

## 5.2 Estimating the Maximum Current Density While Avoiding Irreversible Demagnetization

After identifying the current density at which the maximum winding insulation reaches the insulation temperature limit, an additional EM/thermal iteration is required in order to update the machine performance and determine whether the rotor magnets have suffered irreversible demagnetization. The magnet status for the TD Design and Eff. Design machines is confirmed to be healthy for the maximum current density value determined by the insulation thermal limit constraint. By contrast, the TPD Design machine suffers demagnetization in some of the magnet

material at the corresponding maximum current density value. These conclusions are supported by the results in Figs. 4-25 to 4-27 as well.

In order to find the revised maximum current density for the TPD Design machine that will meet the demagnetization constraint, further analysis is required. Fig. 5-6 shows the calculated curve for the demagnetization ratio vs. current density in the TPD Design machine. It can be observed that there is a linear relationship between the demagnetization ratio and the current density above the threshold for current density at which demagnetization begins. By evaluating two current density points with a non-zero demagnetization ratio, such as the two points identified with a green star in Fig. 5-6, the maximum current density for the TPD Design machine while avoiding demagnetization (approx. 0.95 p.u. in this case) can be readily calculated with linear extrapolation [121], and this procedure is summarized in Table 5-6.

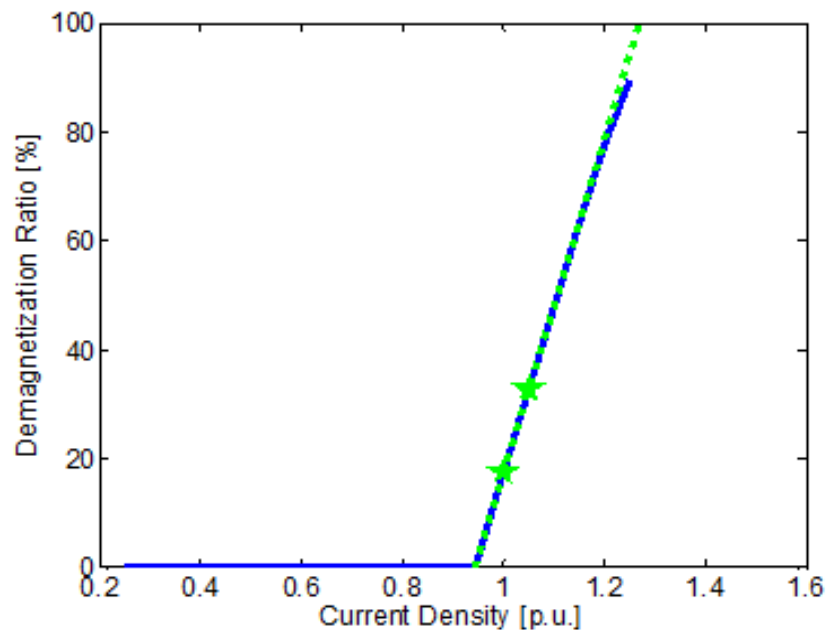


**Fig. 5 - 6: Finding TPD Design max. current density for demag. constraint using linear extrapolation method**

**Table 5 - 6: Finding TPD Design Max. Current Density for Demagnetization Constraint Using Linear Extrapolation Method**

	Current Density [p.u.]	Demag. Ratio [%]
<b>1</b>	1.0000	17.47
<b>2</b>	1.0500	32.77
<b>3</b>	0.9429	0.00

### **5.3 Procedure for Efficiently Obtaining Maximum Current Density for Steady-State Operation**

The maximum current density for a machine design is considered to be the lower of the two current density threshold values at which either 1) the maximum winding temperature reaches the insulation thermal limit; or 2) the rotor magnets are at the threshold of irreversible demagnetization. According to this definition, the procedure for efficiently determining the maximum current density for machine steady-state operation can be summarized by the flow chart in Fig. 5-7.

As indicated in the Fig. 5-7 flow chart, the current density value at which the maximum winding temperature reaches the insulation thermal limit is first identified using Müller's method, as discussed in Section 5.1. Then, an additional EM/thermal iteration is applied in order to update the machine performance and examine whether demagnetization has occurred. If there is no sign of demagnetization, then the current density value associated with the insulation thermal limit is identified as the machine's maximum current density. If demagnetization is detected, additional analysis using the coupled EM/thermal model is carried out using extrapolation (Section 5.2) to find the maximum current density at which the rotor magnet demagnetization is at its threshold of occurring.

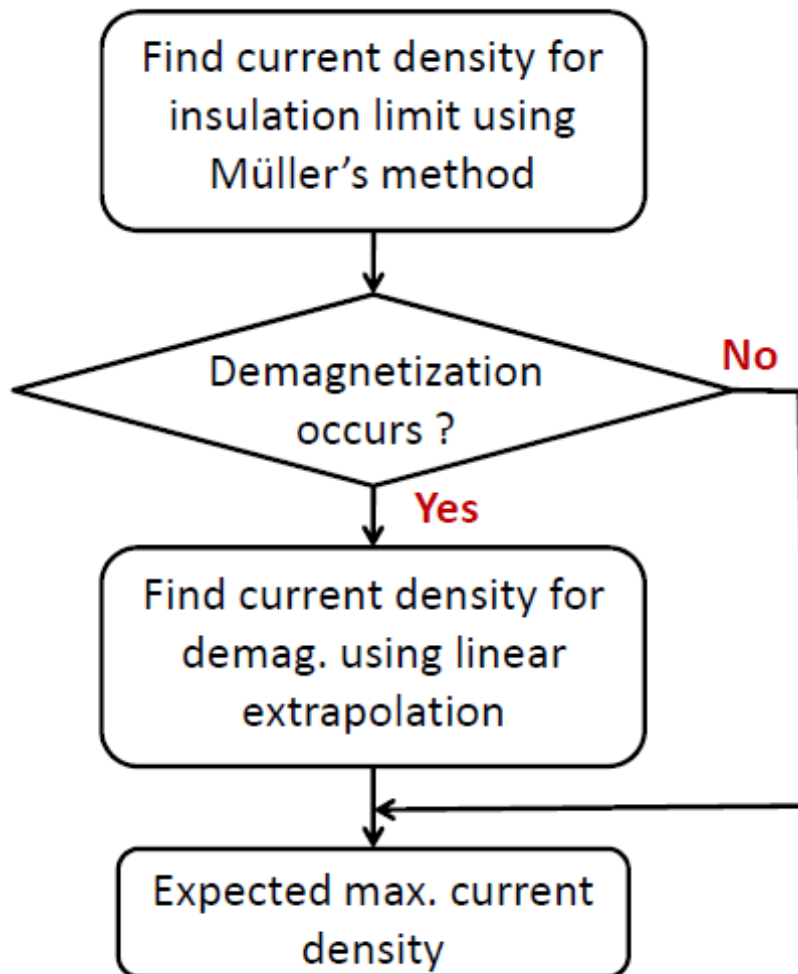


Fig. 5 - 7: Flow chart of proposed procedure for finding the maximum current density for machine steady-state operation

#### 5.4 Coupled EM/Thermal Machine Design Optimization for Steady-State Operation

Comprehensive optimization of an electrical machine design requires that its electromagnetic (EM) and thermal performance be analyzed and optimized simultaneously, since electric machines are heavily constrained by thermal limits. This section presents a coupled EM/thermal model that can efficiently identify the maximum current density for a given machine during static operation, integrated into an iterative machine design optimization program.

### 5.4.1 Implementation of Coupled EM/Thermal Machine Design Optimization

An iterative machine design optimization program was developed in Chapter 3, and its flow diagram is summarized in Fig. 3-1. The differential evolution (DE) optimization algorithm written in MATLAB provides the outer shell of the optimization program. The performance of the candidate SPM machine was significantly improved using the optimization program with the EM-only FE model in this earlier work. In order to take thermal constraints into consideration more directly, the EM-only model is replaced with the coupled EM/thermal model in this study.

Each coupled EM/thermal FE model for a candidate SPM machine can be defined by a set of parameters, both fixed and varied. The fixed parameters are defined by the machine specifications listed in Table 2-2. The six variable parameters are identified in Fig. 3-3, including the stator tooth width, stator yoke thickness, magnet span ratio, rotor yoke thickness, magnet thickness, and airgap radius. The ranges for these variables, shown in Table 3-1, are defined as ratios rather than absolute values in order to help ensure that each candidate design meets all of the geometric constraints. The range boundary values are chosen to ensure that the optimum values fall within the allowable design space. Machine specifications, the selected variable parameters, and their ranges used in this coupled EM/thermal optimization are kept equivalent to those applied in the EM-only optimization. Next, all of the parameters in the parameter set are fed into the template visual basic (VB) script for both EM and thermal FE analyses, which contain information on the machine configuration, material, cooling condition, and excitation, in order to create a specific script for each candidate design. By following the flow chart procedure in Fig. 5-7, the performance of each candidate design is evaluated at its maximum safe current density.

The coupled EM/thermal machine design optimization software has been applied in order to optimize the torque density for the FSPM-SPM machine using a desktop computer with an Intel(R) Core(TM) i7-960 processor. The candidate machine was designed for rated operating conditions, i.e.,  $n = 2800$  r/min,  $P = 30$  kW, and  $T = 102.3$  Nm, where  $n$ ,  $P$ , and  $T$  represent the rotor speed, output mechanical power, and torque, respectively. The objective function has been defined as

$$OF_{TD} = \frac{\text{Calculated Active Mass to Produce Required Torque}}{\text{Base Machine Active Mass}} \quad (25)$$

where the base machine is the one studied previously in [103] with an active mass of 27.8 kg that includes the stator and rotor electromagnetic assemblies.

Based on previous experience, the control parameters for the DE optimizer were selected as: maximum number of generations,  $GenMax = 50$ ; number of designs in each generation,  $NP = 30$ ; crossover probability,  $Cr = 0.8$ ; and scale factor,  $F = 0.8$ . Six cores out of the 8-core desktop are dedicated in this optimization, with one core running the main MATLAB code and the other five cores conducting FE analyses in parallel, which can lead to an acceleration in computation speed approx. 5 times greater than with one single core computer.

#### 5.4.2 Optimized Design

The optimization was then run and converged for the 50<sup>th</sup> generation, with a total number of 1500 designs evaluated. The best design is found to have a total active mass (stator and rotor) of 13.48 kg. It can continuously produce the required torque at its maximum current density of 9.84 A/mm<sup>2</sup>. The optimized machine using the coupled EM/thermal model (Fig. 5-9) has a mass reduction of 7.17 kg compared to the machine optimized previously using the EM-only model

(Fig. 5-8). The key parameters of these two machines are listed in Table 5-7, demonstrating a significant improvement in torque density for the machine using the coupled EM/thermal model.

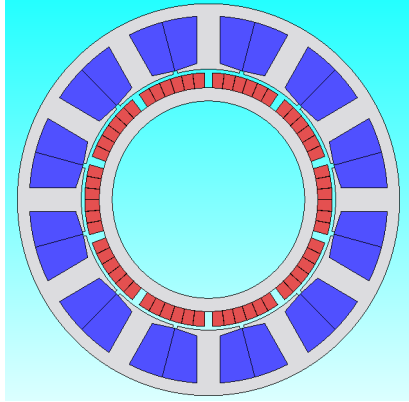


**Fig. 5 - 8: EM-only optimal machine design**

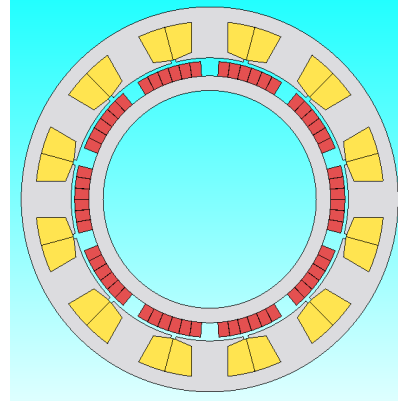


**Fig. 5 - 9: Coupled EM/thermal optimal machine design**

**Table 5 - 7: Comparison of Optimal Machines with EM-Only and Coupled EM/Thermal Models**

Parameter/Dimension	EM-Only	EM/Thermal
Airgap Diameter [mm]	181.48	200.57
Active Stack Length [mm]	57.01	40.78
Magnet Height [mm]	10.46	10.40
Magnet Span [deg. elec.]	32.14	28.31
Volume [m <sup>3</sup> ]	0.0025	0.0016
Copper Mass [kg]	10.11	5.21
Magnet Mass [kg]	2.07	1.46
Total Mass [kg]	<b>20.65</b>	<b>13.48</b>
Cont. Current Density [A/mm <sup>2</sup> ]	<b>4.6</b>	<b>9.84</b>
Torque Ripple [pk-pk/T <sub>rated</sub> ]	0.05	0.05
Power Factor	0.91	0.88
Magnet Loss [W]	59.44	74.29
Core Loss [W]	282.39	184.24
Copper Loss [W]	609.64	1430.85
Efficiency	0.97	0.95



### 5.4.3 Computational Time

The optimization went through 50 generations with a total of 1,500 evaluated designs. Each design requires 5 transient EM and 5 static thermal FE analyses to predict a candidate design's performance for most cases. As a result, the total number of analyses required to accomplish the optimization is approx. 7,500 transient EM + 7,500 static thermal FE analyses.

One transient EM analysis usually takes 10 minutes, while one static thermal analysis runs for approx. 30 seconds. Therefore the computation time for the optimization can be estimated as follows:

- Each coupled EM/thermal model:  $(10 \text{ min} + 0.5 \text{ min}) \times 5 = 52.5 \text{ min}$
- Each generation (5 compute cores in parallel):  $52.5 \text{ min} \times (30/5) = 315 \text{ min} = 5.25 \text{ hr}$
- Serial data reading time for each generation: 10 min
- Total time for the optimization:  $(315 \text{ min} + 10 \text{ min}) \times 50 = 11 \text{ days } 6 \text{ hr } 50 \text{ min}$

## 5.5 Coupled EM/Thermal Machine Design Optimization for Steady-State Operation with Application of Artificial Neural Network

The simulation time for one machine design with the coupled EM/thermal model is considerably longer than the corresponding time for the EM-only model, due to the iterative process between the EM and thermal analyses. As a result, the total time required to finish one complete coupled EM/thermal optimization, consisting of the summed execution times for each of the candidate designs, becomes prohibitively large. Using multi-core PCs helps to reduce the computation time, but the completion time for a full EM/thermal optimization is still very long. Reduction of the computation time would help make this optimization tool considerably more practical.

Differential evolution, the optimization algorithm used for this study, can narrow its search to a much smaller region in parameter space after exploring the entire design space for several generations. The designs in this smaller region share some similar attributes with one another, and this similarity extends to their maximum current densities. As a result, if the maximum current densities of some of the promising designs are found, less effort will be required to determine the maximum current densities for other similar designs.

In order to reduce the computation time, it would be highly desirable to modify the coupled EM/thermal optimization procedure to incorporate some type of learning capability, using an approach such as artificial neural networks (ANN). An ANN can be trained to learn the relationships governing the design parameters and the maximum current densities for an electrical machine from the results of designs in the first several generations. Then the trained ANN can be used to rapidly predict the maximum current density for new sets of machine design parameters. More details related to the ANN technique are discussed as follows.

### **5.5.1 Construct the Artificial Neural Network**

Artificial neural networks are defined by Swingler in [123] as

statistical models of real world systems which are built by tuning a set of parameters. These parameters, known as weights, describe a model which forms a mapping from a set of given values known as inputs to an associated set of values: the outputs. The process of tuning the weights to the correct values—training—is carried out by passing a set of examples of input-output pairs through the model and adjusting the weights in order to minimize the error between the answer the network gives and the desired output. Once the weights have been set, the model is able to produce answers for input values which were not included in the training data. The model does not refer to the training data after they have been trained; in this sense they are a functional summary of the training data.

The process of tuning the neural network is also described in Fig. 5-10.

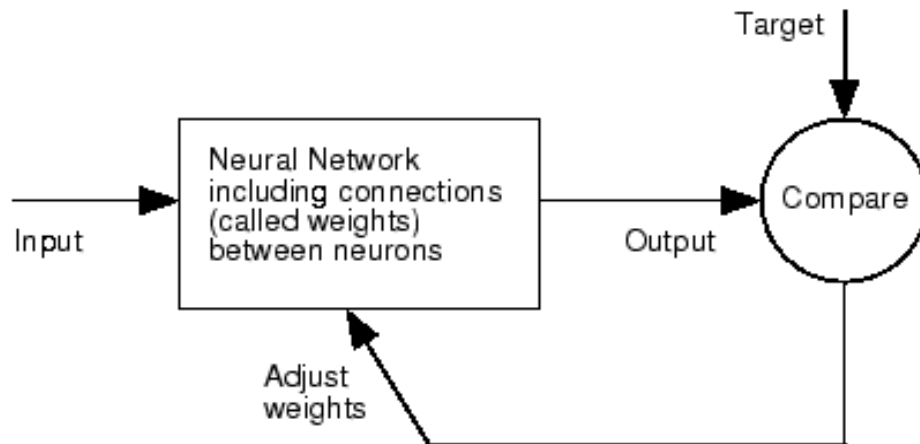


Fig. 5 - 10: Artificial neural network [124]

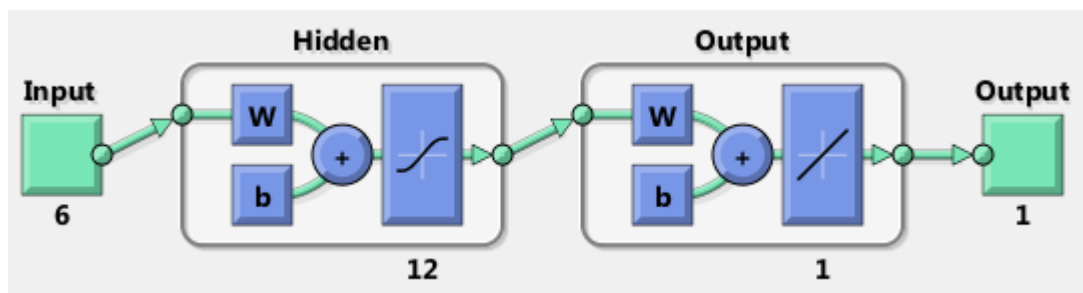


Fig. 5 - 11: Configuration of the neural network

A feedforward network with one hidden layer and one output layer is chosen for this investigation, as shown in Fig. 5-11. The configuration of this neural network is listed as follows:

- Number of neurons in the hidden layer: 12
- Dimension of the input: 6 (machine variable parameters in the optimization)
- Dimension of the output: 1 (machine maximum current density)
- Training algorithm: Levenberg-Marquardt backpropagation
- Training function for the hidden layer: hyperbolic tangent sigmoid
- Training function for the output layer: linear
- Performance function: mean square error—the average squared error between the network outputs  $\alpha$  and the target output  $t$ .

$$F = mse = \frac{1}{N} \sum_{i=1}^N (e_i)^2 = \frac{1}{N} \sum_{i=1}^N (t_i - \alpha_i)^2 \quad (26)$$

Then the results of the first 10 generations (i.e., the first 300 designs) from the optimization discussed in Section 5.4 are loaded, of which 70% are used for training, 15% are applied to validate the network's generalization and to stop training before overfitting, and the last 15% are used as a completely independent test of network generalization [124].

The training process terminates when the validation reaches its minimum value, as shown in the performance plot (Fig. 5-12). The error histogram provides an additional verification of network performance. As can be seen in Fig. 5-13, most errors fall between -0.1136 and 0.1056.

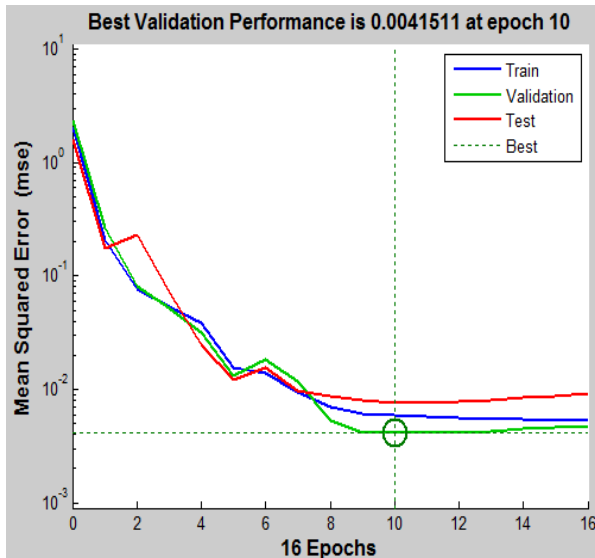


Fig. 5 - 12: Performance plot when training the neural network

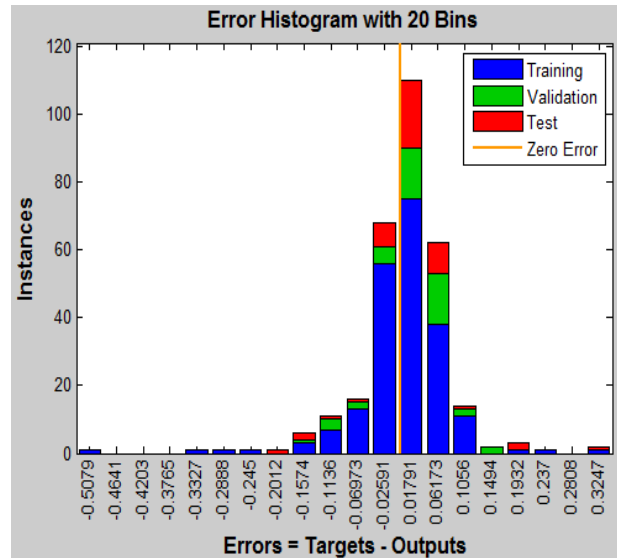
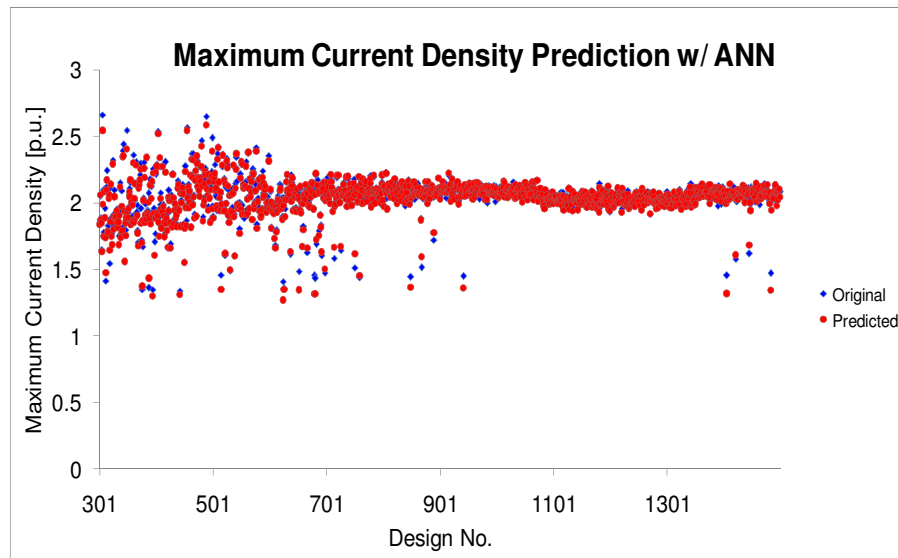


Fig. 5 - 13: Error histogram for the trained neural network

### 5.5.2 Validation of the Trained Neural Network

The six dimensional parameters of each of the remaining 1,200 designs from the optimization in Section 5.4 are fed into the trained artificial network, with which the maximum current densities of these designs are predicted and shown as red dots in Fig. 5-14. They are further compared with the original current density values (blue dots), calculated with the coupled EM/thermal analysis. It can be observed in Fig. 5-14 that there is a good agreement between the predicted results using ANN and the original data.



**Fig. 5 - 14: Max. current density found with coupled EM/thermal model (blue) and predicted by ANN (red)**

The trained network is built into the optimization program. An EM-only model, combined with the predicted maximum current densities provided by the trained ANN, is sufficient to replace the full coupled EM/thermal model for the remaining 1,200 designs. This updated optimization with an application of ANN is run, and the resulting optimal design (Fig. 5-15) is compared with the optimal design from Section 5.4 (Fig. 5-16). The key parameters of these two machines are listed in Table 5-8. The similarities between the two designs demonstrate the applicability of the ANN technique.

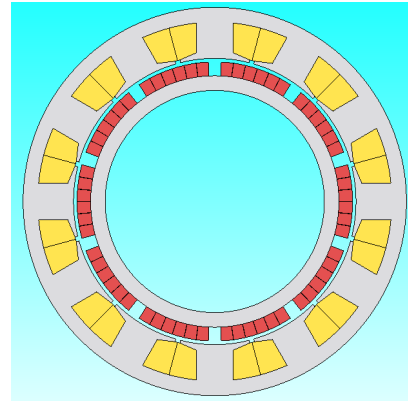
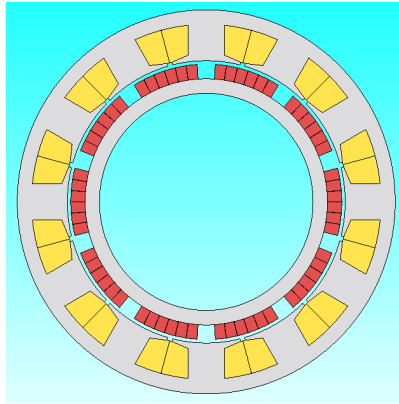


Fig. 5 - 15: Optimal machine design w/o ANN    Fig. 5 - 16: Optimal machine design w/ ANN

Table 5 - 8: Comparison of Optimal Machines w/ and w/o ANN

Parameter/Dimension	w/o ANN	w/ ANN
Airgap Diameter [mm]	200.57	201.09
Active Stack Length [mm]	40.78	41.13
Magnet Height [mm]	10.40	9.77
Magnet Span [deg. elec.]	28.31	30.61
Volume [m <sup>3</sup> ]	0.0016	0.0016
Copper Mass [kg]	5.21	5.17
Magnet Mass [kg]	1.46	1.51
Total Mass [kg]	<b>13.48</b>	<b>13.54</b>
Cont. Current Density [A/mm <sup>2</sup> ]	<b>9.84</b>	<b>9.71</b>
Torque Ripple [pk-pk/T <sub>rated</sub> ]	0.05	0.03
Power Factor	0.88	0.89
Magnet Loss [W]	74.29	87.69
Core Loss [W]	184.24	190.92
Copper Loss [W]	1430.85	1271.52
Efficiency	0.95	0.95

As discussed in 5.4.3, the total number of analyses required to accomplish the optimization without ANN is approx. 7,500 transient EM + 7,500 static thermal FE analyses. Applying the ANN technique, the machine design parameters and their associated maximum current densities found in the first 10 generations—that is, the first 300—designs, can be used to train a network. The EM-only model (one transient EM FE analysis) and the maximum current density predicted

using the trained network are sufficient to replace the original coupled EM/thermal model for the rest of the optimization. As a result, the total number of analyses is reduced to approx. 2,700 transient EM + 1,500 static thermal FE analyses. The application of ANN has contributed to a significant reduction in the required computing effort and time.

## 5.6 Conclusion

This chapter presents a procedure for using this coupled model for determining the maximum current density for PM synchronous machines considering both the stator winding insulation thermal limit and the rotor magnet demagnetization threshold. A quadratic relationship has been identified between the maximum winding temperature and the continuous current density, indicating that Müller's method is suitable for locating the maximum current density for the winding insulation limit. The linear relationship between the demagnetization ratio and the current density led to the adoption of the linear extrapolation method for finding the threshold current density for demagnetization.

The coupled EM/thermal model was integrated into the previously developed optimization program. The software has been applied in order to optimize a 30 kW (continuous) FSCW-SPM machine for high torque density using a multi-core desktop computer. Commercially - available FE analysis software was used for these calculations.

The resulting optimal design exhibits a 35% reduction in its active mass, as compared to the design using EM-only optimization. An artificial neural network has been incorporated into the optimization. The EM-only model and the maximum current density predicted using the trained network are sufficient to replace the original coupled EM/thermal model, leading to a significant reduction in computational effort and time.

## **Chapter 6: Coupled EM/Thermal Machine Design Optimization Including Transient Operation with Application of Artificial Neural Network**

For applications such as traction motors, the machine does not run at fixed operating points and is often required to deliver high torque/power for short intervals. According to U.S. DRIVE specifications for an advanced traction machine, the machine is required to deliver its peak power (55 kW) for 18 sec [105]. Determining the maximum safe current density during this transient operation is essential for optimizing the machine design. It is assumed that the machine temperatures drop to their maximum steady-state values before a peak power pulse is applied.

### **6.1 Valid Initial Current Density Region for Machine Transient Operation**

To solve the machine thermal transient problem, the first step is to identify valid initial conditions. Figs. 6-1 to 6-3 plot the steady-state torque produced by the three candidate machines as a function of the current density. The current density values that are valid for examination during the transient operation design process lie in the domain where the machine design's maximum steady-state winding temperature at rated power (30 kW) falls below the insulation limit and there is no sign of demagnetization. (It is assumed in this discussion that magnet temperature is not a limiting constraint.) According to this definition and the data in Figs. 6-1 to 6-3, the valid current density ranges for the TD Design, TPD Design, and Eff. Design machines are [0, 1.63 p.u.], [0, 0.95 p.u.], and [0, 2.78 p.u.], respectively. These ranges are adopted as the valid initial current density regions for examination during the transient operation design process described in the following sections.



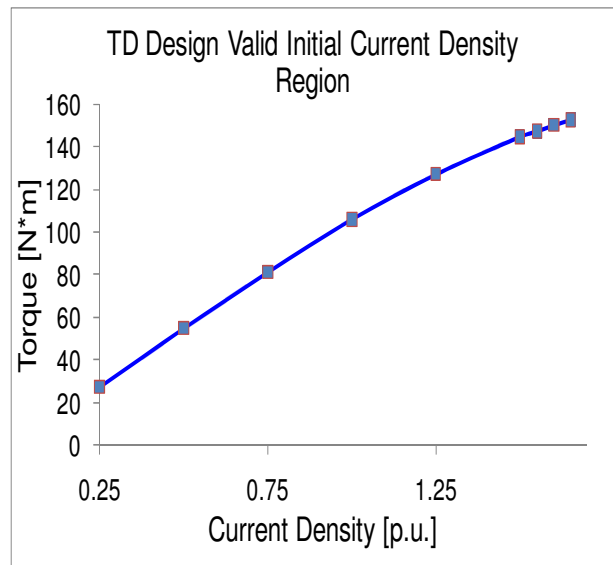


**Fig. 6 - 1: TD Design valid initial current density region**

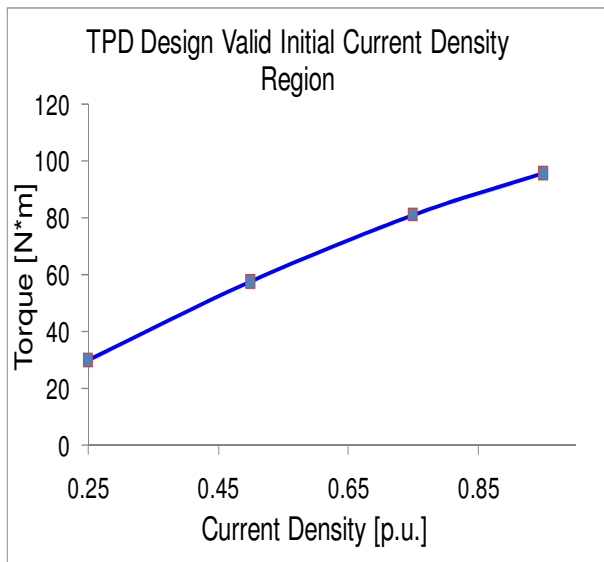


**Fig. 6 - 2: TPD Design valid initial current density region**

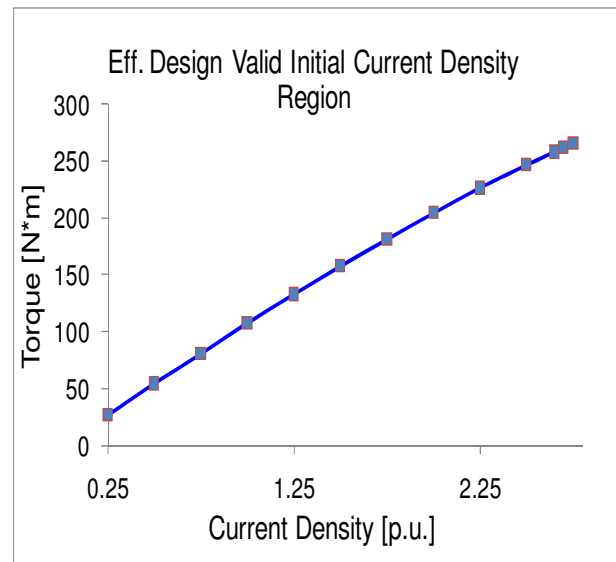


**Fig. 6 - 3: Eff. Design valid initial current density region**

## 6.2 Coupling EM and Transient Thermal FE Analysis

Next, the machine loss profile during peak transient power operation must be identified. One example case is used here to demonstrate this transient operation condition: Assume that the TD Design initially operates at steady-state rated power with a current density of  $J = 1.3$  p.u. (falling within the valid initial condition region). At  $t = 0$  sec, the current density suddenly rises to 4.3 p.u. and continues for 18 sec. It is assumed that the machine electrical time constant is much shorter than its thermal time constant. The electrical time constant (electrical period) for target machines used in this study is 4.29 msec, while the machines' thermal time constant is approx. 30 min.

### 6.2.1 Initial Loss Profile Assumption

The initial loss profile assumed for the analysis is shown by the blue lines in Fig.6-4. Before  $t = 0$  sec, the machine losses are constant, which is consistent with steady-state operation with a current density of 1.3 p.u.. It is assumed that there is a step change in every loss component at  $t = 0$  when the current density is suddenly increased to 4.3 p.u.. Initially, the thermal transient analysis is performed assuming that all of these higher loss values remain constant during the following 18 secs. The resulting component temperature rises are shown in Fig. 6-5. Table 6-1 lists the initial component temperatures at  $t=0$  sec and the elevated temperatures at  $t = 18$  sec for this first iteration.

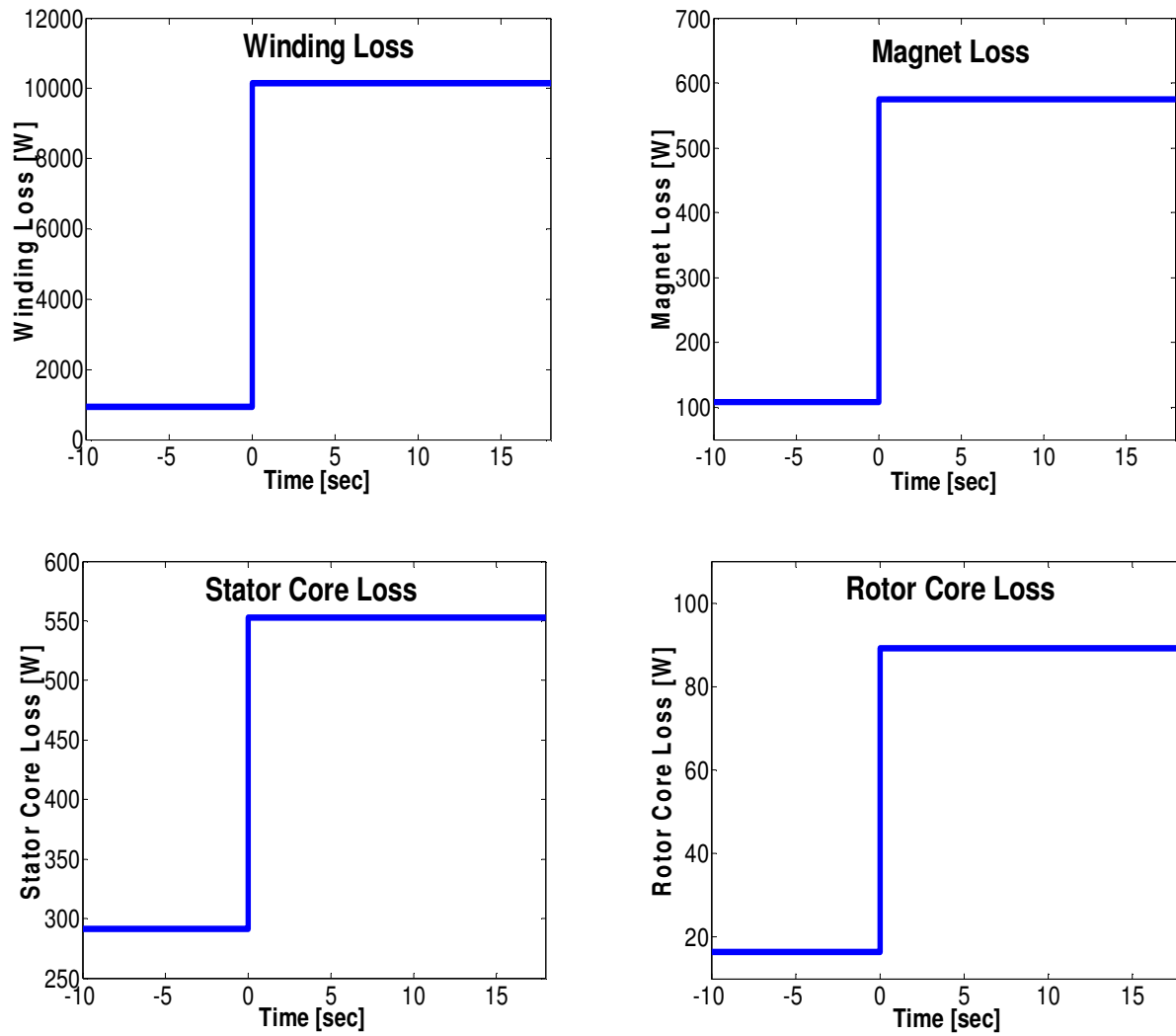


**Fig. 6 - 4: Initial Loss Profile Assumption**

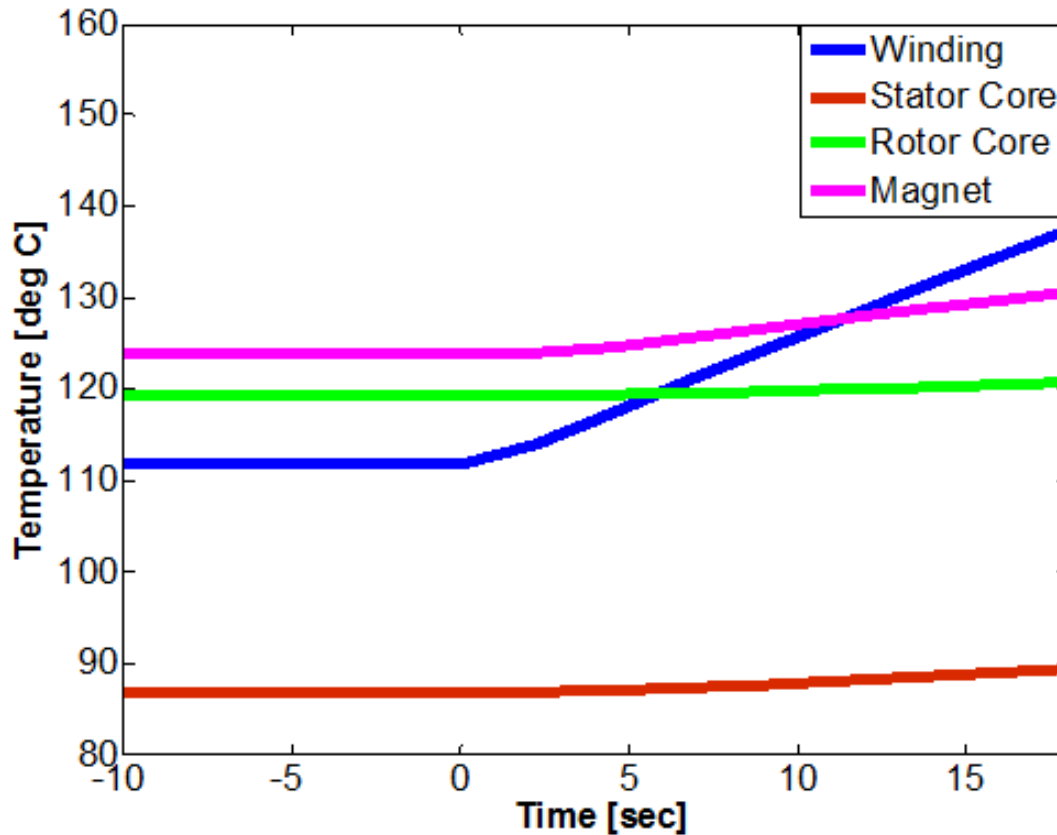


Fig. 6 - 5: Predicted temperature transient based on initial loss profile assumption

Table 6 - 1: Component Temperatures Based on Initial Loss Profile Assumption

Time [sec]	Stator Core Temp. [°C]	Rotor Core Temp. [°C]	Winding Temp. [°C]	PM Temp. [°C]	Max. Winding Temp. [°C]
0	86.67	119.37	111.69	123.96	112.33
18	89.37	120.71	137.44	130.60	138.22

### 6.2.2 Loss Profile Update

Figure 6-5 shows that the predicted component temperatures increase almost linearly as time elapses. These temperature rises cause the temperature-dependent material properties to change, leading to changes in the losses. Based on the temperatures calculated from the first iteration listed in Table 6-1, all of the material properties are updated, and the losses are re-evaluated as

shown by the red stars in Fig. 6-6. Results from the coupled EM/thermal analyses show that the key loss values increase approx. linearly with the corresponding component temperatures (Fig. 6-7). Therefore, the loss profile can be updated using a linear interpolation method—the constant loss line in Fig. 6-4 is replaced with a sloped line that connects the initial loss value at  $t = 0$  and the loss value evaluated with the predicted temperatures at  $t = 18$  sec (red line labeled 2<sup>nd</sup> iteration in Fig. 6-8). For the particular example considered here, this sloped line is clearly distinguishable from the blue 1<sup>st</sup> iteration line, which only shows the winding losses in the top plot.

The thermal transient analysis is then performed again with this new loss profile (2<sup>nd</sup> iteration), and the resulting component temperatures are listed in Table 6-2 using red numbers labeled as 18 (2<sup>nd</sup>). Repeating this process one more time (3<sup>rd</sup> iteration), the loss profile is updated with green stars and lines, as shown in Fig. 6-8. It can be observed that the green lines coincide very closely with the red lines, indicating that the first two iterations are sufficient for convergence of the results in this case.

The final predicted temperature rises are shown as dotted lines in Fig. 6-9. Here again, the dotted line is only clearly distinguishable for the windings (blue). The final maximum winding temperature is 139.4°C, found in the 18 (3<sup>rd</sup>) row in Table 6-2, which is lower than the insulation temperature limit (155°C for Class F insulation). This suggests that 4.3 p.u. is not the highest “safe” current density for the TD Design transient operation with an initial value of 1.3 p.u..

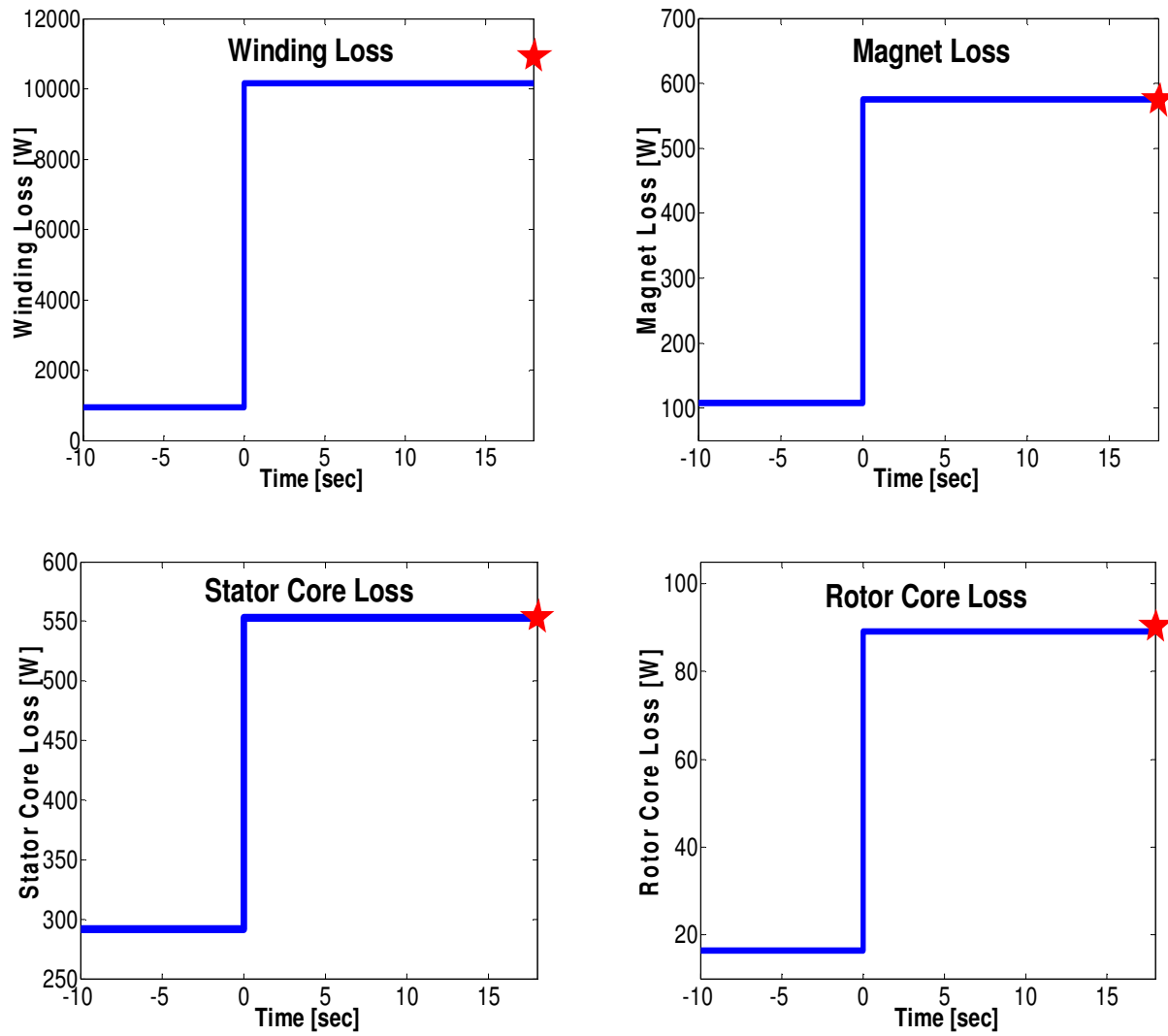
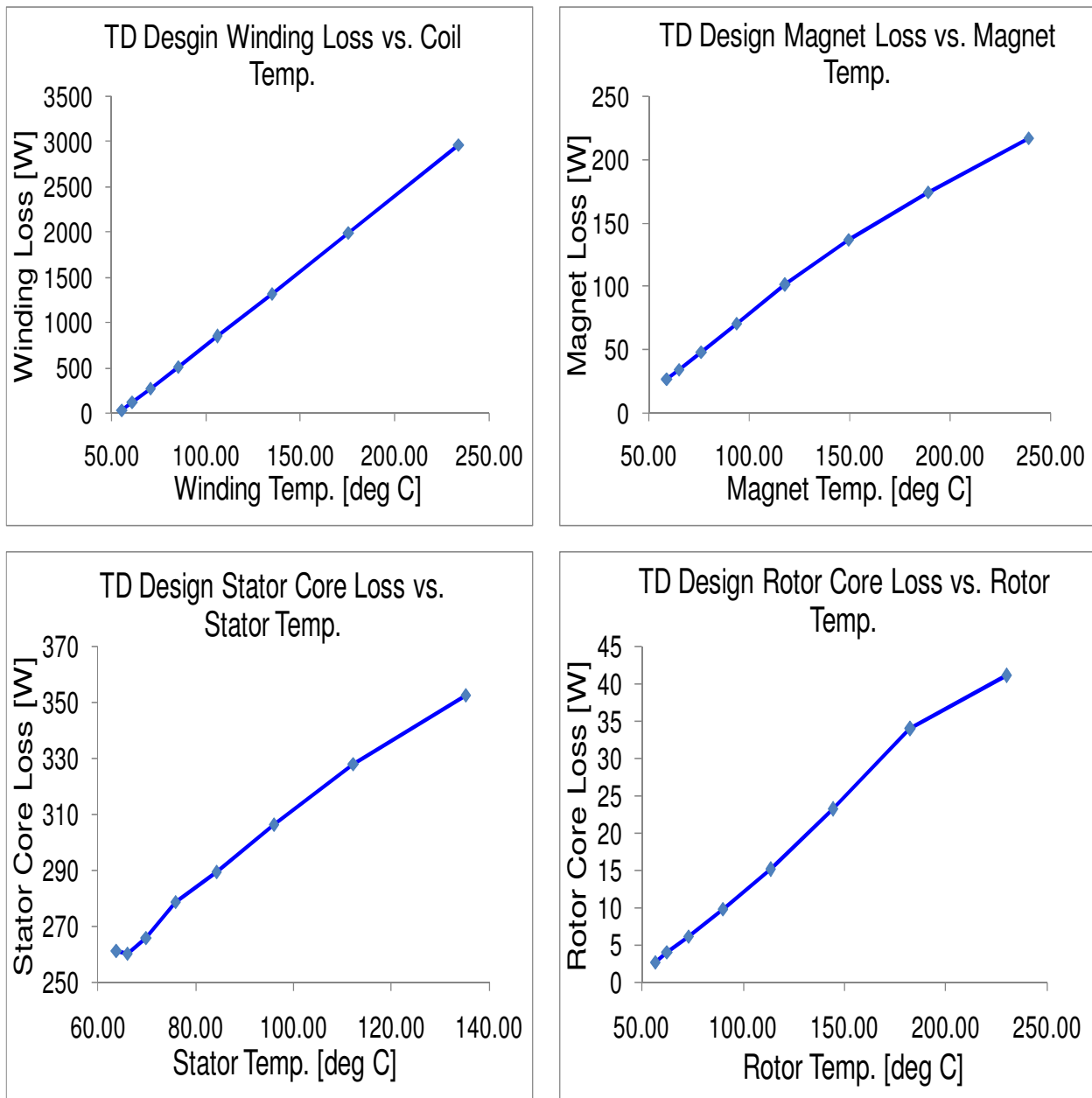


Fig. 6 - 6: Loss components estimation at time = 18 sec



**Fig. 6 - 7: Linear relationship between loss components and their corresponding temperatures**

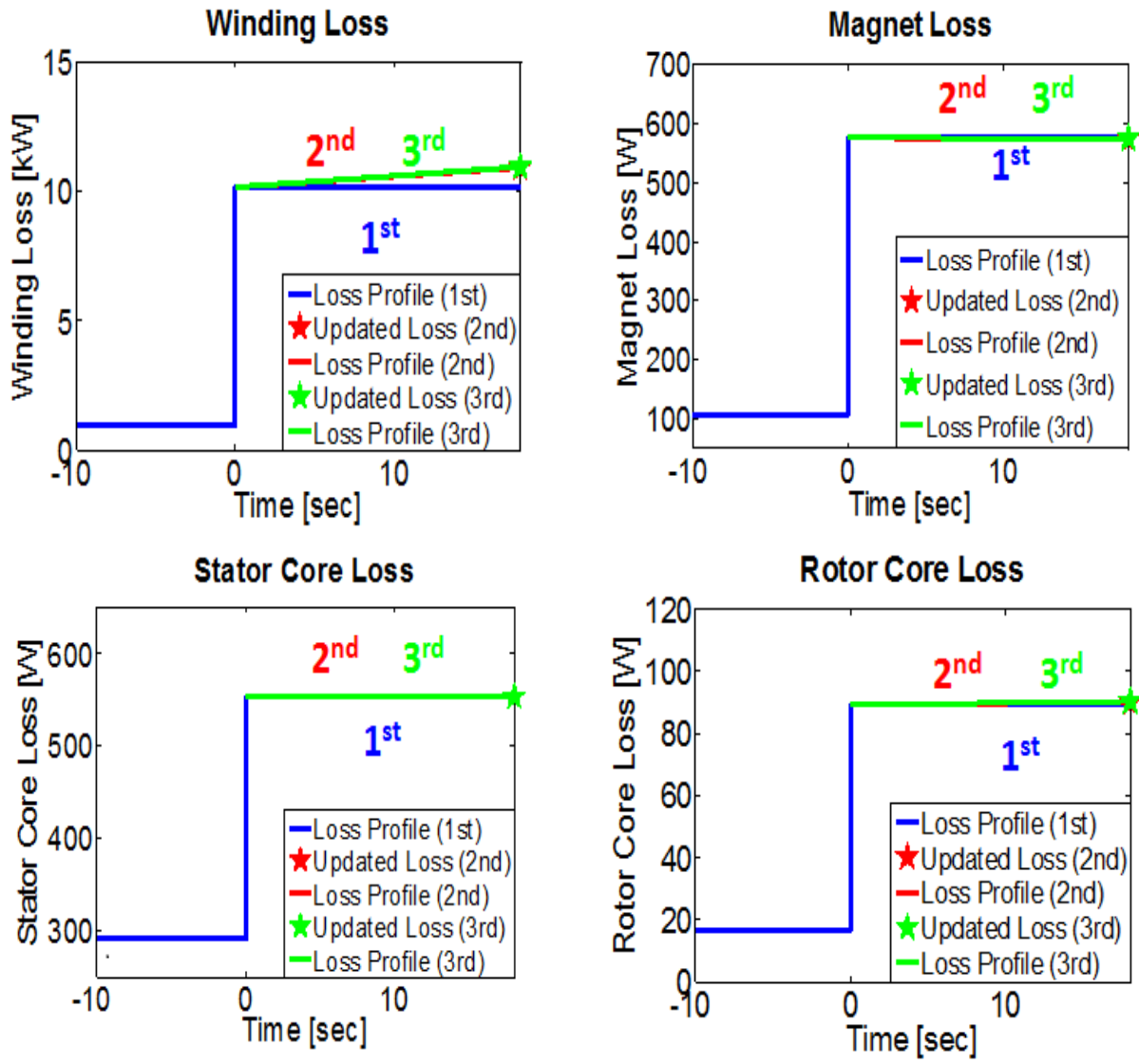


Fig. 6 - 8: Loss profile update

Table 6 - 2: Component Temperatures Based on Updated Loss Profile

Time [sec]	Stator Core Temp. [°C]	Rotor Core Temp. [°C]	Winding Temp. [°C]	PM Temp. [°C]	Max. Winding Temp. [°C]
0	86.67	119.37	111.69	123.96	112.33
18 (1 <sup>st</sup> )	89.37	120.71	137.44	130.60	138.22
18 (2 <sup>nd</sup> )	89.43	120.72	138.60	130.59	139.39
18 (3 <sup>rd</sup> )	89.44	120.72	138.65	130.59	139.44



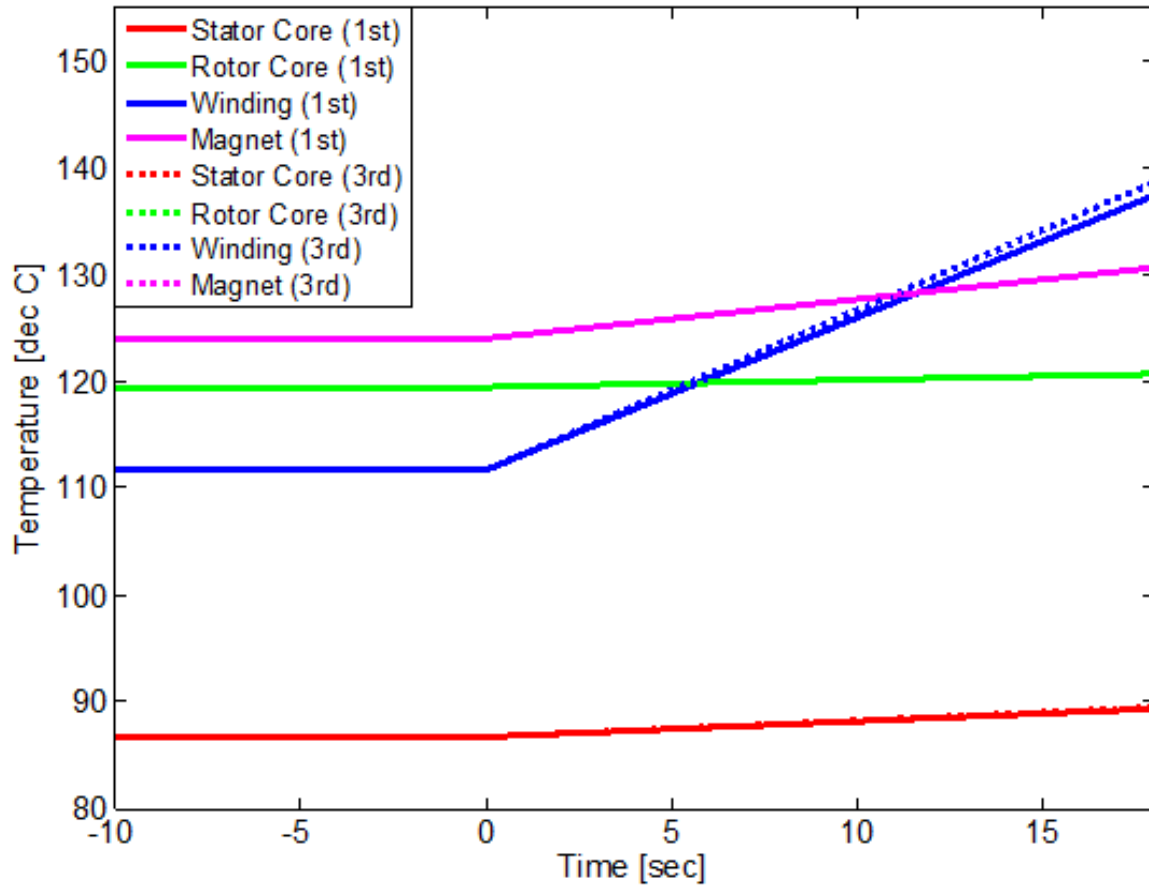


Fig. 6 - 9: Predicted temperature transient based on updated loss profile

### 6.3 Maximum Transient Current Density Identification

As with the case of machine steady-state operation, the component temperature limits and the demagnetization constraint determine the maximum safe current density for machine transient operation. An example case is used to demonstrate how the maximum winding temperature and demagnetization ratio vary as the current density changes during transient operation: Assume that the TD Design machine is initially operating at steady-state with  $J = 1.3$  p.u., as it was in Fig. 6-4. The demagnetization ratio is defined as the fraction of magnet FE cells that experience

irreversible demagnetization. At  $t = 0$ , the current density steps up to a higher value ( $J_{tr}$ ) and continues for 18 sec.

The blue curve in Fig. 6-10 shows the FE-calculated peak winding temperature as a function of the  $J_{tr}$  current density, and the values can be fit very well by a quadratic curve. As a result, Müller's method can be applied in order to rapidly identify the maximum current density for which the maximum winding temperature just reaches the insulation thermal limit during the transient power pulse [121]. The convergence criterion for this example is set as the maximum winding temperature that falls between  $150^{\circ}\text{C}$  and  $155^{\circ}\text{C}$ .

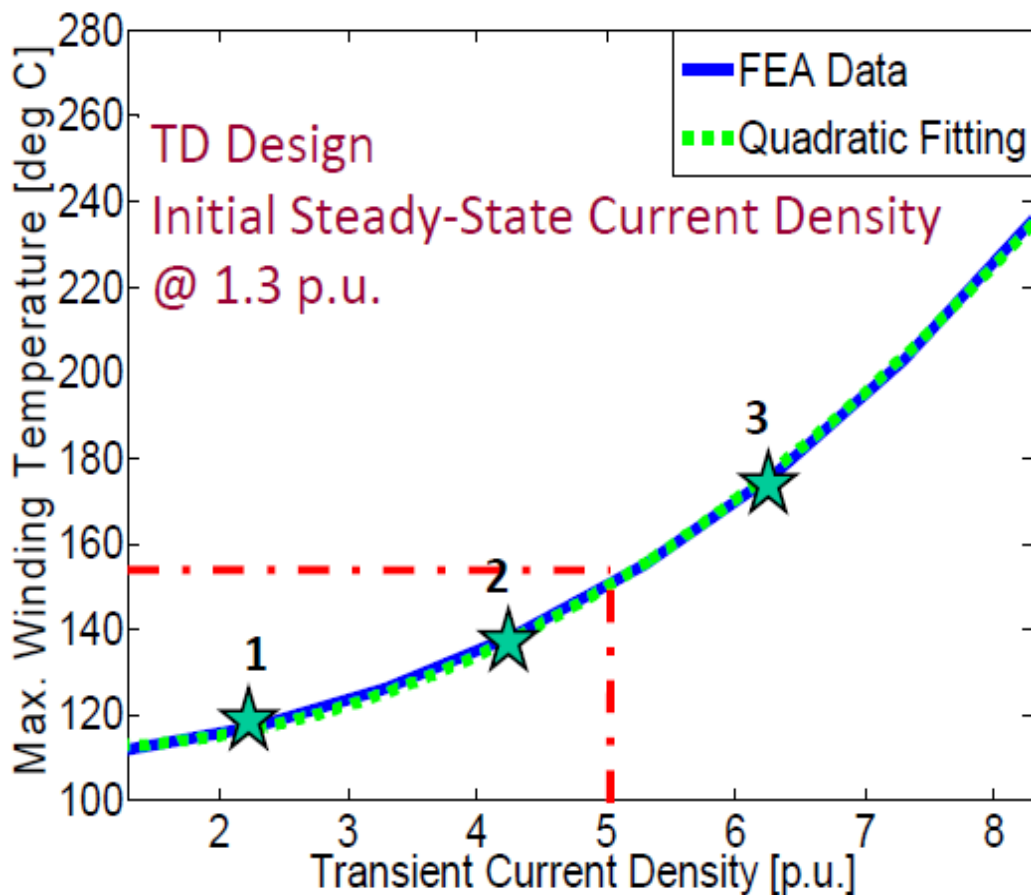


Fig. 6 - 10: Maximum winding temperature vs. current density under transient operation condition

Müller's method develops a root estimate by fitting a second-order equation, illustrated by the dotted green curve in Fig. 6-10, to the results from three function values, identified by the starred points 1, 2, and 3. This fitted parabolic equation can then be used to calculate the current density at which the winding hot spot first reaches the insulation temperature limit ( $J_{tr} = 5.14$  pu, Point 4). If the FE-calculated maximum temperature for this  $J_{tr}$  value does not meet the convergence criterion, three more data points closer to the desired root are used to update the parabola. The process continues until the convergence requirement is satisfied. In this TD Design case, the predicted maximum winding temperature at Point 4 is  $152.7^{\circ}\text{C}$ , satisfying the criterion.

The calculated demagnetization ratio curve for this same example is shown in Fig. 6-11. It can be observed that there is a linear relationship between the demagnetization ratio and current density above the threshold current density value at which demagnetization begins. By evaluating two current density points with a non-zero demagnetization ratio value, such as the two star points labeled 2 and 3 in Fig. 6-11, the maximum current density at which the TD Design machine avoids demagnetization (approx. 4.01 p.u. in this case) can be readily calculated via linear extrapolation [121].

The maximum transient current density for a machine design is considered to be the lower of the two current density threshold values at which either: 1) the maximum winding temperature just reaches the insulation thermal limit; or 2) the rotor magnets are at the threshold of experiencing irreversible demagnetization. Accordingly, the maximum transient current density for the TD Design machine with an initial steady-state current density of  $J = 1.3$  p.u. is  $J_{tr} = 4.01$  p.u., set by the demagnetization ratio.

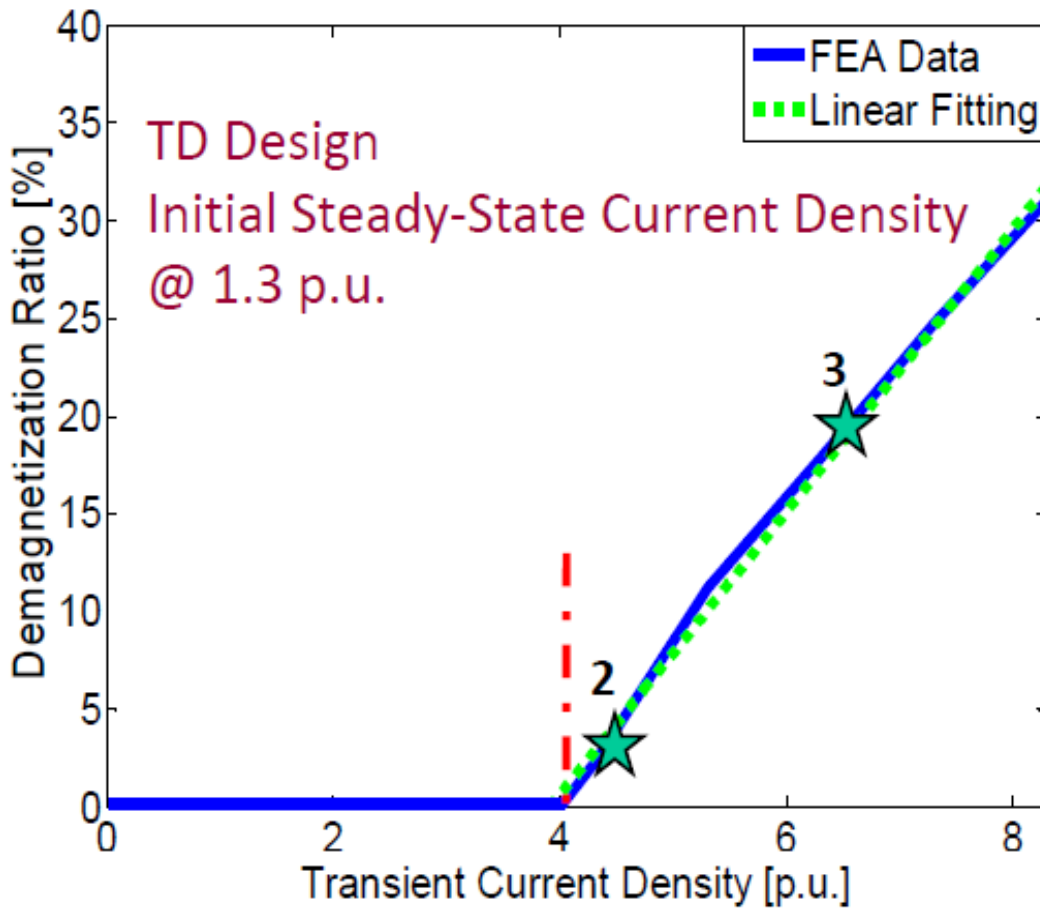


Fig. 6 - 11: Demagnetization ratio vs. current density under transient operation condition

#### 6.4 Optimization of Machine Operation with a Given Peak/Continuous Power Ratio

According to U.S. DRIVE specifications [105], the required peak/continuous power ratio for the advanced traction motor is (55/30=1.83). Finding both the maximum initial current density during steady-state operation and the maximum current density for the 18 sec peak power transient period to optimize the machine operation is a demanding task.

The maximum current density for a machine that is designed for a fixed steady-state operating point with no transient peak power requirement typically occurs when its maximum steady-state winding temperature reaches the insulation limit. This assumes that the magnet temperature or

demagnetization ratio do not limit the current density to a lower value. When the machine requirements (such as the U.S. DRIVE case) include a peak power transient, then the initial current density during steady-state operation must be lowered to provide the necessary thermal margin for transient operation.

Figures 6-12 to 6-14 show the FE-calculated initial steady-state maximum winding temperatures as a function of the peak/continuous ratio for TD Design, TPD Design, and Eff. Design machines, respectively. It can be observed that the relationship between the peak/continuous ratio and the maximum winding temperature prior to the power pulse is approx. linear. The initial maximum steady-state winding temperature for achieving a peak/continuous ratio of 1.83 is 115°C for the TD Design machine, 75°C for TPD Design, and 130°C for Eff. Design.

These results for the three machines confirm that, for a desired peak/continuous power ratio, different machine designs allow different values of maximum winding temperature prior to the high-power pulse. As a result, finding the initial steady-state current density based on a pre-defined maximum winding temperature is not the correct approach for optimizing the operation of a machine with a specified peak/continuous power ratio.

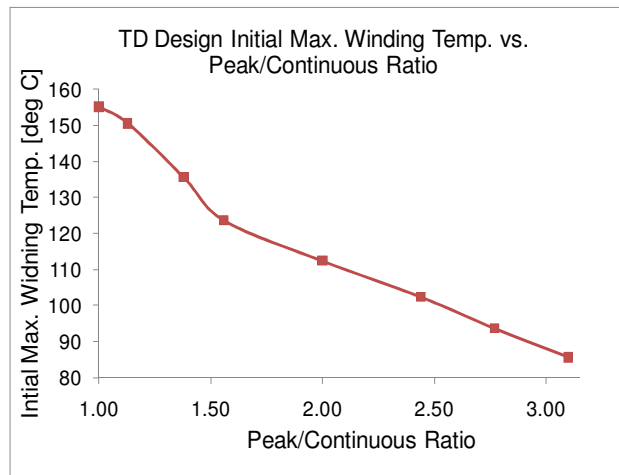


**Fig. 6 - 12: TD Design initial max. winding temperature vs. peak/continuous ratio**

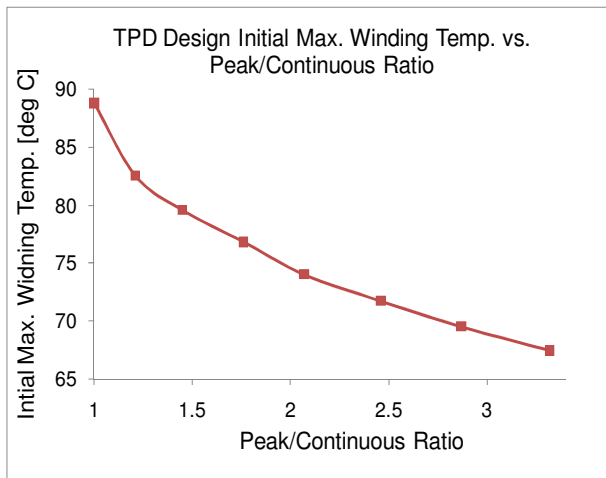


**Fig. 6 - 13: TPD Design initial max. winding temperature vs. peak/continuous ratio**

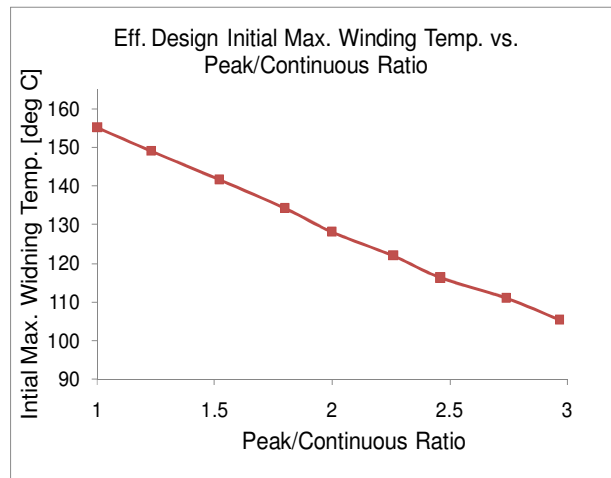


**Fig. 6 - 14: Eff. Design initial max. winding temperature vs. peak/continuous ratio**

Figures 6-15 to 6-17 show results of the EM/thermal coupled transient analyses for the three machine designs, confirming that there is a near-linear relationship between the peak/continuous power ratio and the initial current density value. Therefore, the expected initial current density for optimizing a machine design with a given peak/continuous power ratio can be determined using a linear extrapolation method. More specifically, the peak/continuous ratio for two selected initial current density values can be found first using the method discussed in Section 6.3. Then, a straight line can be fit to these two points. The initial steady-state current density can then be

easily calculated using this line for the desired peak/continuous power value, as illustrated in Fig. 6-15 for the TD machine and U.S. DRIVE specs.

The resulting proposed procedure for identifying the initial steady-state current density to optimize machine operation with a specified peak/continuous power ratio is summarized in Fig. 6-18.

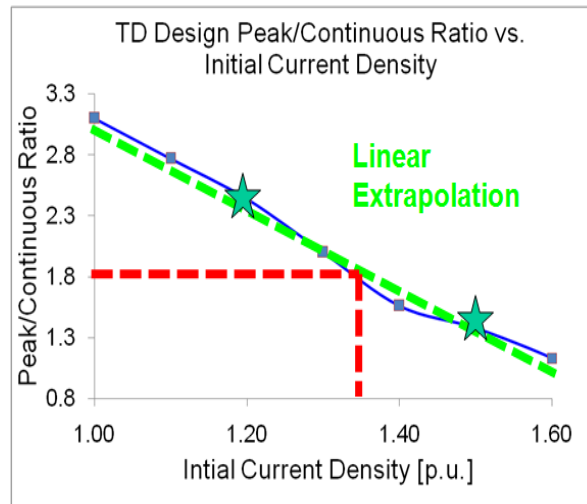


**Fig. 6 - 15: TD Design peak/continuous ratio vs. initial current density**

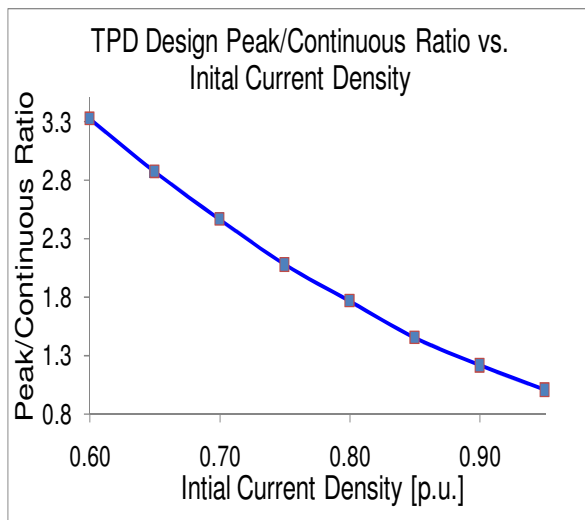


**Fig. 6 - 16: TPD Design peak/continuous ratio vs. initial current density**

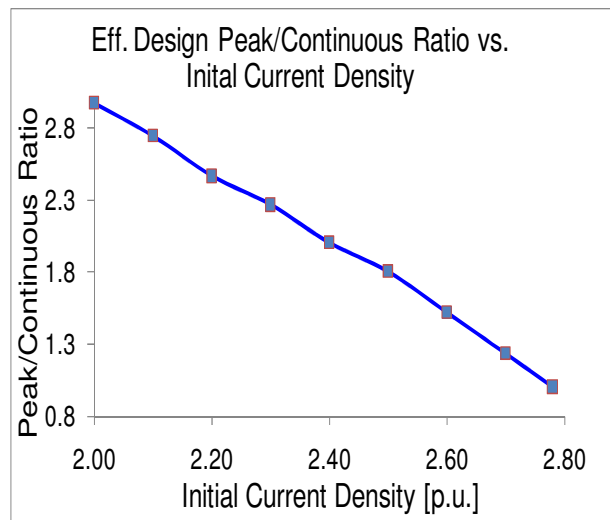


**Fig. 6 - 17: Eff. Design peak/continuous ratio vs. initial current density**

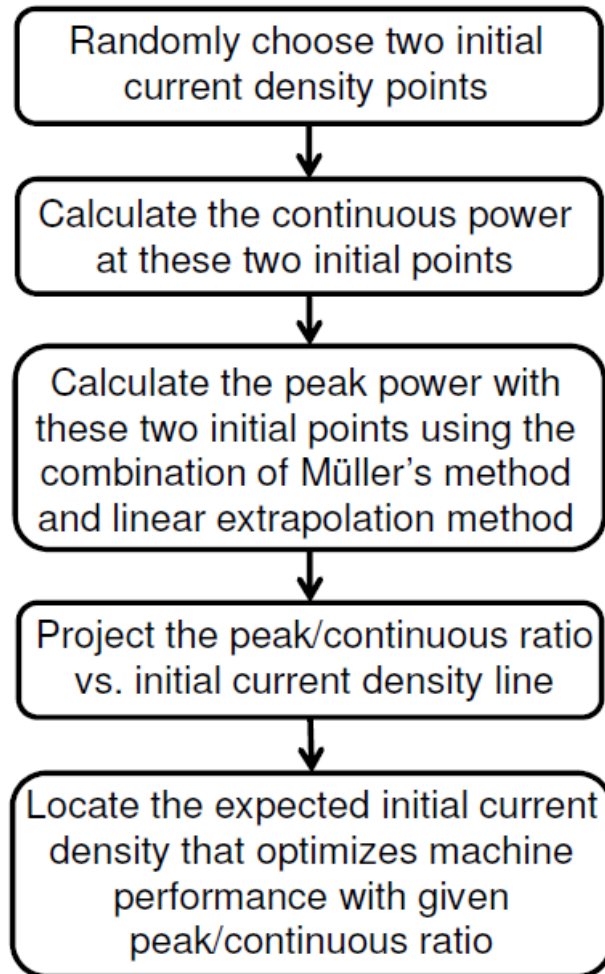


**Fig. 6 - 18: Flow chart of procedure for finding the initial current density for optimizing machine operation with a given peak/continuous power ratio**

### **6.5 Coupled EM/Thermal Machine Design Optimization for a Given Peak/Continuous Power Ratio with Application of ANN Technique**

The transient version of the coupled EM/thermal model that can efficiently determine the maximum initial steady-state current density to achieve a given peak/continuous power ratio is integrated into the previously developed optimization program. All the parameters and settings for the optimization are kept the same as those mentioned in Section 5.4.1.



The performance of each candidate design is evaluated at its maximum initial steady-state current density, by following the flow chart procedure in Fig. 6-18. The total number of analyses required to identify this maximum initial steady-state current density is displayed below:

1. Initial current density trial Point 1:
  - Calculate losses under steady-state operation: 2 transient EM + 2 static thermal FE analyses
  - Calculate maximum winding temperature for three transient current density trial points: 3 transient EM + 6 transient thermal FE analyses
  - Locate the maximum transient current density and calculate the peak/continuous power ratio: 2 transient EM + 2 transient thermal FE analyses
2. Repeat Step 1 for the initial current density trial Point 2: 7 transient EM + 2 static thermal + 8 transient thermal FE analyses
3. Locate the maximum initial steady-state current density according to the required peak/continuous power ratio and repeat Step 1 to determine the actual peak/continuous power ratio: 7 transient EM + 2 static thermal + 8 transient thermal FE analysis

In sum, 21 transient EM + 6 static thermal + 24 transient thermal FE analyses are required to evaluate each candidate design.

The optimization was first run for 10 generations, with a total of 300 designs evaluated. After completing the above-mentioned analyses, the actual peak/continuous power ratio of each evaluated design was determined —these are represented by a blue dot in Fig. 6-19. It can be observed that the peak/continuous power ratios of most designs fall in the vicinity of the required value 1.833, indicating that the developed procedure effective at predicting the maximum initial steady-state current density for a given peak/continuous power ratio.

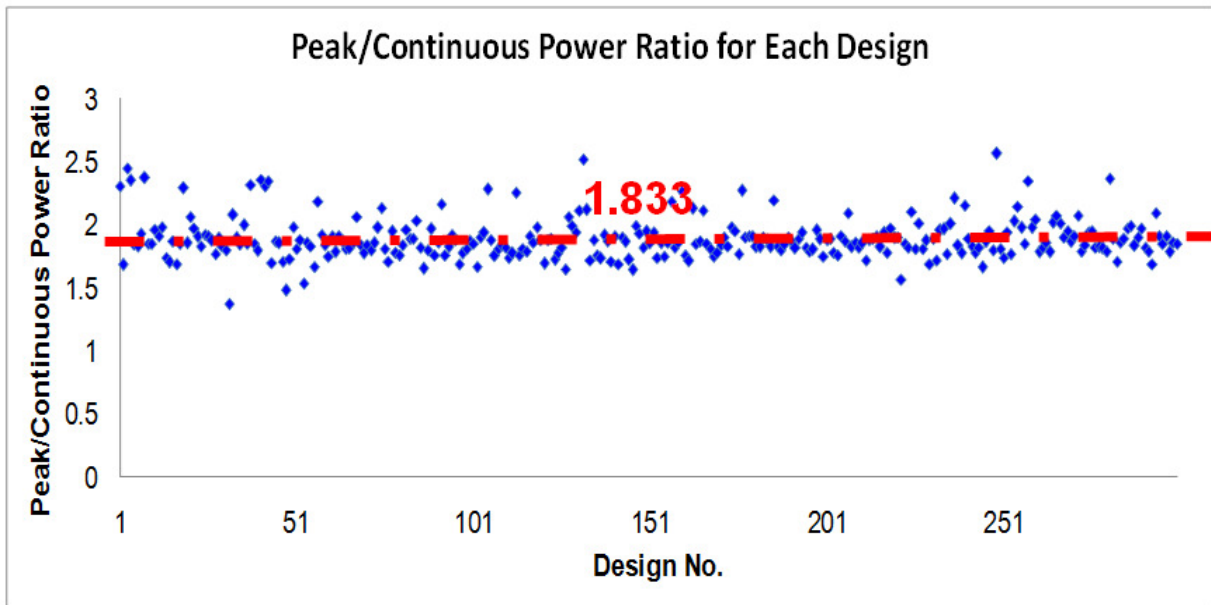


**Fig. 6 - 19: Actual peak/continuous power ratio of the first 300 evaluated designs**

The outliers, wherein the peak/continuous power ratios are away from 1.833, exist because the relationship between the peak/continuous power ratio and the initial current density is not strictly linear, as shown in Figs. 6-15 to 6-17. Replacing the linear extrapolation method with the secant method, i.e., repeating the above-mentioned Step 1 one or two more times, can help to reduce the distance between the actual peak/continuous power ratio and the desired value, but at the cost of additional computing efforts and time.

Applying the ANN technique, the machine design parameters and their associated maximum current densities found in the first 10 generations (the first 300 designs) can be used to train a network. The maximum initial steady-state (continuous) current densities for the designs of the 11<sup>th</sup> generation (Design 301 to 330) predicted using the trained network match very well with the ones found using the coupled EM/thermal model, as shown in Fig. 6-20. Therefore, the EM-only model (one transient EM FE analysis) and the maximum initial steady-state current density predicted using the trained network are sufficient to replace the original coupled EM/thermal

model during the rest of the optimization. As a result, the total number of analyses is reduced to approx. 7,500 transient EM + 1,800 static thermal + 7,200 transient thermal FE analyses, which is almost one-fifth the number required by the optimization in which every design is evaluated using the full coupled EM/thermal model.

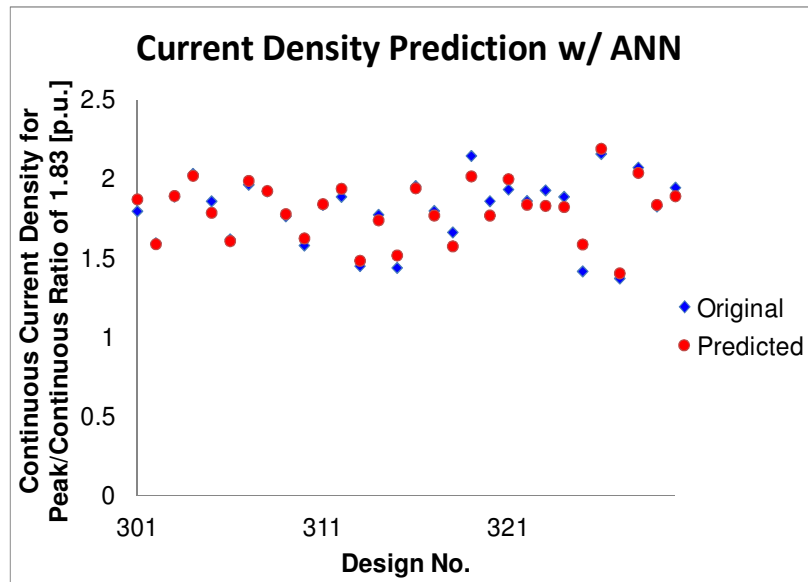


**Fig. 6 - 20: Maximum initial steady-state (continuous) current density found with coupled EM/thermal model (blue) and predicted by ANN (red)**

The best design is found to have a total active mass (stator and rotor) of 14.29 kg. It can continuously produce the required torque at its maximum initial steady-state (continuous) current density of  $8.65 \text{ A/mm}^2$  and deliver its peak power pulses without exceeding the maximum allowable winding temperature or inducing irreversible demagnetization in the rotor magnets. The optimized machine using the transient version of the coupled EM/thermal model (Fig. 6-22) has a mass increment of 0.81 kg compared to the machine optimized previously using the static version of the coupled EM/thermal model (Fig. 6-21). The key parameters of these two machines are listed in Table 6-3. The reduction in torque density for the machine using the transient version of the coupled EM/thermal model gives it the capability to withstand the required peak power pulses for short periods of time.

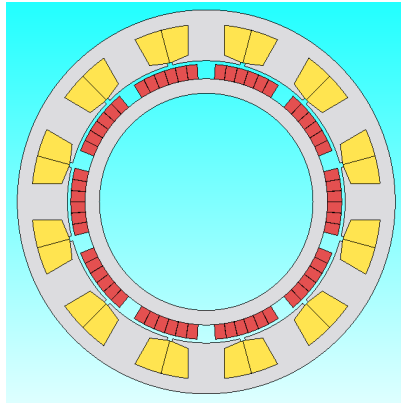


**Fig. 6 - 21: Static version of coupled EM/thermal optimal machine design**

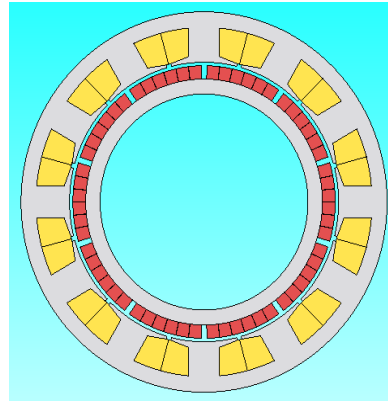


**Fig. 6 - 22: Transient version of coupled EM/thermal optimal machine design**

**Table 6 - 3: Comparison of Optimal Machines with Static and Transient Coupled EM/Thermal Models**

<b>Parameter/Dimension</b>	<b>Static EM/Thermal</b>	<b>Transient EM/Thermal</b>
Airgap Diameter [mm]	200.57	200.53
Active Stack Length [mm]	40.78	42.70
Magnet Height [mm]	10.40	9.62
Magnet Span [deg. elec.]	28.31	33.49
Volume [m <sup>3</sup> ]	0.0016	0.0017
Copper Mass [kg]	5.21	5.50
Magnet Mass [kg]	1.46	1.70
Total Mass [kg]	<b>13.48</b>	<b>14.29</b>
Cont. Current Density [A/mm <sup>2</sup> ]	<b>9.84</b>	<b>8.65</b>
Torque Ripple [pk-pk/T <sub>rated</sub> ]	0.05	0.04
Power Factor	0.88	0.92
Magnet Loss [W]	74.29	92.25
Core Loss [W]	184.24	200.99
Copper Loss [W]	1430.85	1079.09
Efficiency	0.95	0.96

## 6.6 Conclusions

This chapter presents techniques for achieving coupled EM/thermal analysis of electric machines using commercial FE software for both steady-state and transient operation. For steady-state conditions, iteration between the EM and thermal analyses is used to converge on solutions that are consistent with the temperature-dependent properties of the machine materials. The work has been extended to address the challenges imposed by applications that include transient operation at torque/power levels much higher than the steady-state conditions.

A method to couple the EM FE analysis with the transient thermal FE analysis has been developed. A linear relationship has been identified between the machine loss components and the corresponding machine temperatures, leading to the development of a technique for updating the loss profile using linear interpolation.

For a given machine design with a pre-set initial current density, a procedure has been developed to determine the winding's maximum current density for transient operation (peak power) that will avoid having the winding exceed its maximum temperature during the transient event. This was achieved using a combination of Müller's method and linear extrapolation.

For a given machine design with a specified peak/continuous power requirement, a method has been developed to determine the maximum initial steady-state current density that will allow the machine to deliver its peak power pulses without exceeding the maximum allowable winding temperature or inducing irreversible demagnetization in the rotor magnets. These techniques can be conveniently extended to cases where the temperature of the magnets or some other machine component becomes the key thermal constraint.

The transient version of the coupled EM/thermal model has been integrated into the previously developed optimization program. The resulting optimal design exhibits a 6% increase in its active mass compared to the design using the static version of coupled EM/thermal optimization, in exchange for the capability of operating at peak power conditions for short periods of time. An artificial neural network has been incorporated into the optimization, reducing the computational effort and time by a factor of 5.

## **Chapter 7: Generalization of Machine Design Optimization Techniques**

### **7.1 Interior Permanent Magnet Machine Design Optimization**

Interior permanent magnet (IPM) machines are widely used in hybrid and battery electrical vehicles, such as the Toyota Prius, Ford Fusion, and Nissan Leaf. They offer opportunities to reduce the required amount of magnet material for a required torque production by taking advantage of the reluctance torque component. It is desirable to apply design optimization techniques to this type of machine in order to achieve improved performance and higher fuel economy.

The differences between SPM and IPM machines are larger and more significant for their electromagnetic designs than for their thermal designs, largely due to the presence of the reluctance torque component in the IPM machine that was noted above. As a result, there is reason for confidence that, if the electromagnetic design of an IPM machine design can be successfully optimized, then the previously-developed coupled EM/thermal machine design optimization techniques can likely be readily extended to IPM machines. The implementation of an iterative FE-based IPM machine design optimization procedure is presented in the following sections.

#### **7.1.1 Target IPM Machine Configuration**

The target machine selected for this study is a three-phase 30 kW (continuous) 8-pole 48-slot interior PM machine configured with distributed windings, as shown in Fig. 7-1. The magnets are embedded in the rotor core in a “V” shape for harvesting the reluctance torque. This machine

configuration is similar to the one adopted by Toyota engineers for the 2007 Toyota Camry hybrid vehicle that has been thoroughly investigated by Oak Ridge National Laboratory [114].

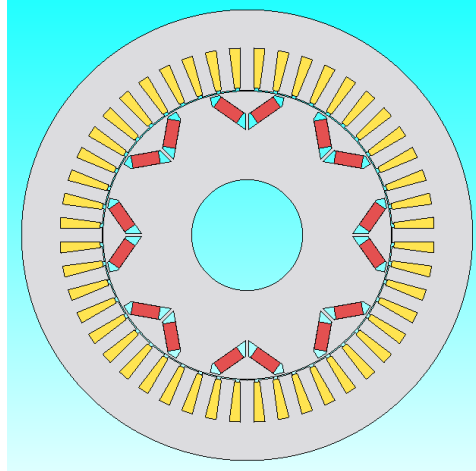


**Fig. 7 - 1: Target IPM machine configuration**

**Table 7 - 1: Target IPM Traction Machine Key Dimensions and Material Characteristics**

Parameter/Metric	Value
Continuous Power Rating [kW]	30
Rated Speed [r/min]	2800
Stator Outer Diameter [mm]	274.2
Airgap Thickness [mm]	1
Cont. Current Density [ $A/mm^2$ ]	4.6
Copper Fill Factor [%]	47%
Copper Resistivity [nOhm-m]	25 @ 150 °C
Steel Lamination Material, Packing Factor	M19, 95%
Remanent Flux Density [T]	1.1 @ 150 °C
Magnet Coercive Force [kA/m]	800
Hysteresis Loss Coeff. [ $W/m^3/Hz$ ]	256
Eddy Current Loss Coeff. [ $W/m^3/Hz^2$ ]	0.37
Copper Density [ $kg/m^3$ ]	8940
Steel Density [ $kg/m^3$ ]	7850
Magnet Density [ $kg/m^3$ ]	7450

The specifications used for designing the IPM machine are shown in Table 7-1. The differences between the specifications for the IPM machine and the specifications for the FSCW SPM machine are particularly apparent in the copper fill factor and the banding thickness. The



copper fill factor is lower for this IPM machine because it uses distributed windings, while the SPM machine is wound using concentrated windings that can be compactly wound if a segmented stator configuration is chosen. Banding is required by the SPM machine to hold the magnets in place, while the magnets are secured in cavities under the laminated steel pole pieces in the rotor core of the IPM machine. Therefore, eliminating the need for banding reduces the effective airgap thickness in the IPM machine.

### 7.1.2 Implementation of IPM Machine Design Optimization

The iterative IPM machine design optimization is organized in the same way as it was for the SPM machine, which is summarized by the flow diagram in Chapter 3, Fig. 3-1. In this case, the SPM machine model is replaced with a 2D FE model for the IPM machine. Each IPM machine FE model can be defined by a set of parameters, including both fixed and variable types. The fixed parameters are defined by the machine specifications listed in Table 7-1. The nine variable parameters for the IPM machine are identified in Fig. 7-2, consisting of:

1. The stator tooth width (**wt**)
2. The stator yoke thickness (**hsy**)
3. The magnet inner corner thickness (**hrm**)
4. The magnet span ratio (**ms**)
5. The magnet slot exterior point span ratio (**es**)
6. The magnet slot height (**hms**)
7. The magnet width (**wm**)
8. The rotor yoke thickness (**hry**)
9. The airgap radius (**Rg**)

The numerical ranges for these variables, shown in Table 7-2 for this example, are defined as ratios rather than absolute values. The idea of defining these dimensional variables in ratios is introduced by Zarko in Ref. [104]. There are 3 additional variables specified in the IPM machine design optimization than those in previous SPM machine optimization (Table 3-1), due to the complex shape of the magnet cavities in the IPM machine. The range boundary values are chosen to ensure that the optimum values will fall within the variable ranges.

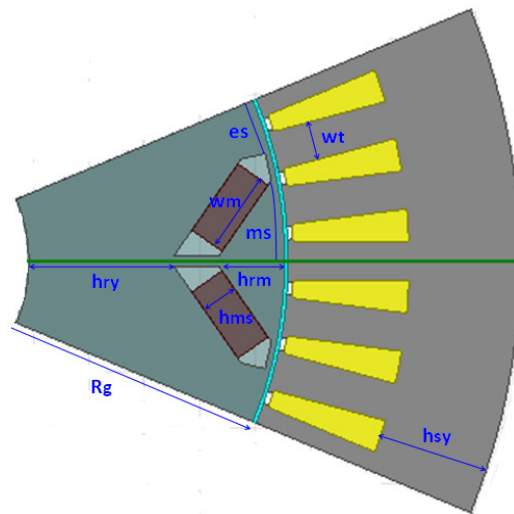


**Fig. 7 - 2: IPM machine design variables**

**Table 7 - 2: IPM Variable Definitions and Ranges**

Variable Parameters	Range
Tooth Width to Slot Pitch Ratio	[0.2, 0.8]
Stator Yoke Thickness to Its Geometric Limit Ratio	[0.1, 0.5]
Magnet Inner Corner Thickness to Inner Rotor Radius Ratio	[0.05, 0.7]
Magnet Span Ratio	[0.2, 0.95]
Magnet Slot Exterior Point Span Ratio	[0.2, 0.95]
Magnet Slot Thickness to Its Geometric Limit Ratio	[0.1, 0.7]
Magnet Width to Its Geometric Limit Ratio	[0.5, 0.98]
Rotor Yoke Thickness to Its Geometric Limit Ratio	[0.1, 0.7]
Airgap Radius to Stator Outer Radius Ratio	[0.4, 0.75]

As noted at the beginning of this chapter, IPM machines develop two distinct torque components: magnet torque and reluctance torque. Magnet torque is generated because of the interaction of the stator currents and the magnetic flux in the stator caused by the permanent magnets buried inside the rotor. Reluctance torque is generated due to the IPM machine rotor magnetic saliency created by the magnet cavities that behave as large airgaps with respect to the stator winding inductances. The placement of the cavities inside the rotor causes the stator inductance to change cyclically as the rotor angular position is varied, and the reluctance torque varies as well with this angular position. Therefore, the total torque produced by an IPM machine is a combination of magnet and reluctance torque that varies with the current angle for a fixed stator current amplitude, as shown in Fig. 7-3.

It is assumed that the maximum-torque-per-Ampere (MTPA) control method is applied on candidate IPM machines. For the particular current amplitude associated with Fig. 7-3, the current angle that develops the highest positive motoring torque is approx. 45 degree, and the value of this MTPA angle varies with the desired current and the machine.

A step search method is often used to find the current angle at which the IPM machine can produce the maximum amount of torque with a specified current amplitude. The flow diagram to implement this search algorithm is outlined in Fig. 7-4.  $T(\gamma)$  is the torque evaluated at current angle  $\gamma$ ,  $\gamma_0$  represents the initial current angle, and  $\gamma_s$  is the current angle step. It can be seen from Fig. 7.3 that the MTPA current angle for the candidate IPM machine is  $45^\circ$ , and the variation in the machine's torque production is less than  $\pm 1.5\%$  when the current angle varies  $\pm 5^\circ$  around the optimum MTPA angle. As a result, the initial current angle  $\gamma_0$  and the step current

angle  $\gamma_s$  have been selected to be  $45^\circ$  and  $5^\circ$ , respectively, for each candidate IPM machine evaluated during the optimization process.

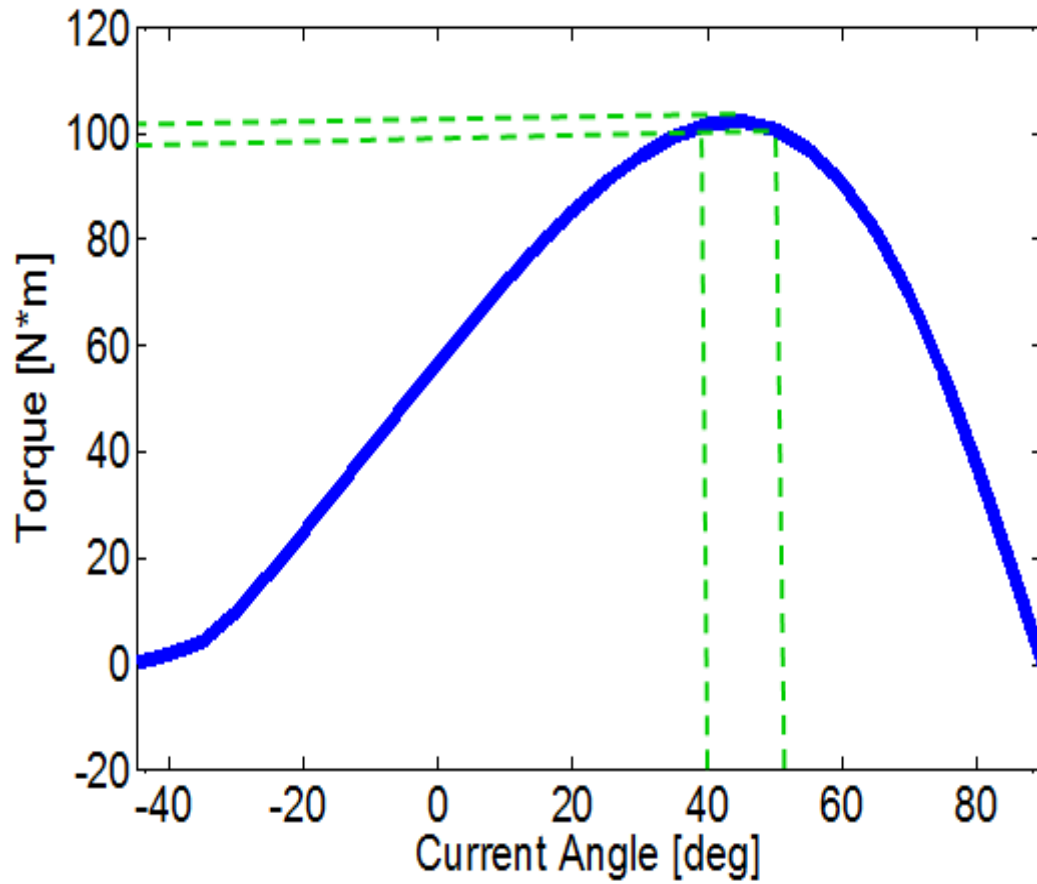
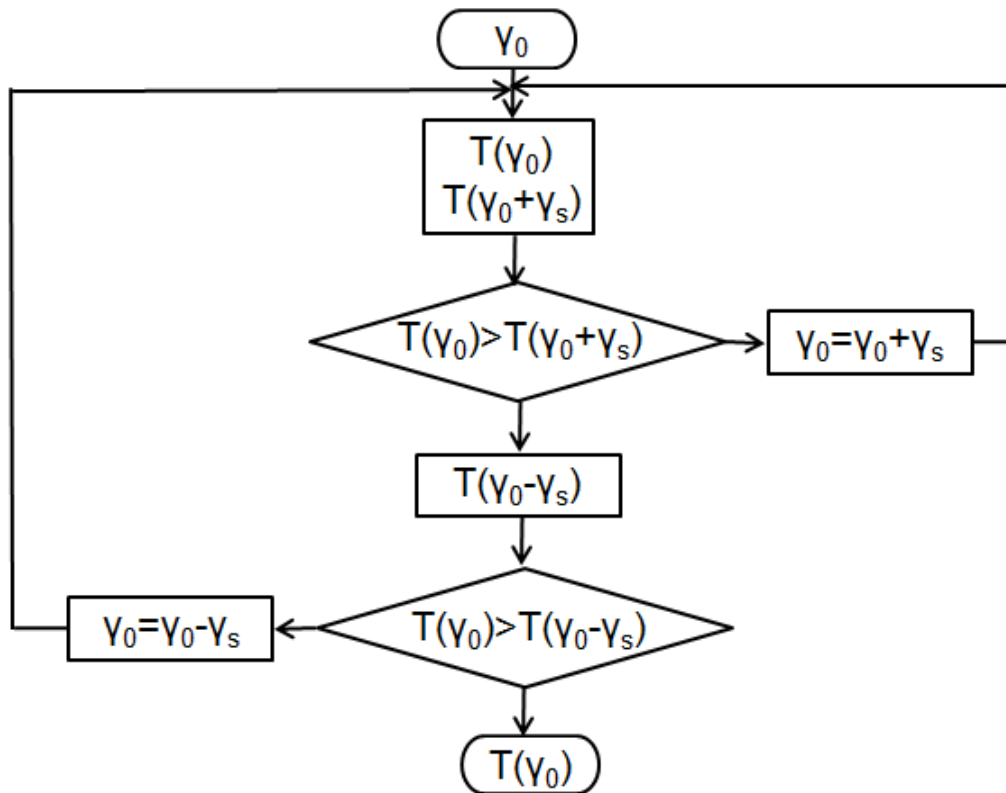


Fig. 7 - 3: Torque vs. current angle for a candidate IPM machine



**Fig. 7 - 4: Flow chart for finding the MTPA angle of the IPM machine with step search method**

Next, all of the parameters in the parameter set are fed into the template visual basic (VB) script for the EM FE analysis that contains information on the machine configuration, material, and excitation in order to create a specific script for each candidate design. By following the procedure described by the flow chart shown in Fig. 3-1, the performance of each candidate design is evaluated at its MTPA current angle.

### 7.1.3 Optimized Design

The candidate machine was designed for rated operating conditions, i.e.,  $n = 2800$  r/min,  $P = 30$  kW, and  $T = 102.3$  Nm, where  $n$ ,  $P$ , and  $T$  represent the rotor speed, output mechanical power, and torque, respectively. The material properties for the IPM machine and the key electrical constraints used for this optimization exercise are found in Table 7-1, including the slot

copper fill factor limit of 47% (compared to 50% for the SPM machine) and the winding continuous current density limit of 4.6 A/mm<sup>2</sup> (the same as for the SPM machine).

As previously discussed for the SPM machine optimization, the objective function  $OF$  for the IPM machine has been defined the same as

$$OF_{TD} = \frac{\text{Calculated Active Mass to Produce Required Torque}}{\text{Base Machine Active Mass}} \quad (27)$$

where the base machine is the one studied previously in [103] with an active mass of 27.8 kg including the stator and rotor electromagnetic components.

Based on previous experience, the control parameters for the DE optimizer were chosen to be: maximum number of generations  $GenMax = 50$ ; number of designs in each generation  $NP = 50$ ; crossover probability  $Cr = 0.8$ ; and scale factor  $F = 0.8$ . The optimization was then run. It converged after the 50<sup>th</sup> generation, with a total number of 2,500 designs evaluated. It is too difficult to control the input variable parameters listed in Table 7-2 to ensure that each candidate design meets all of the geometric constraints. Therefore, the optimization program was modified to include a function block that rejects any design with a physically infeasible geometry.

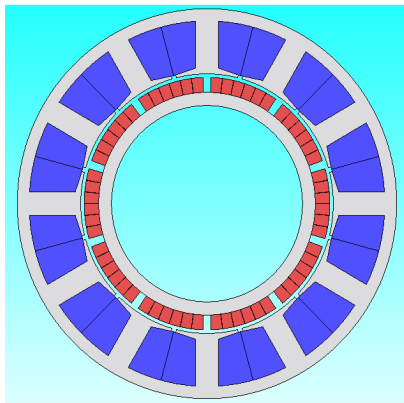


Fig. 7 - 5: Optimal SPM machine design

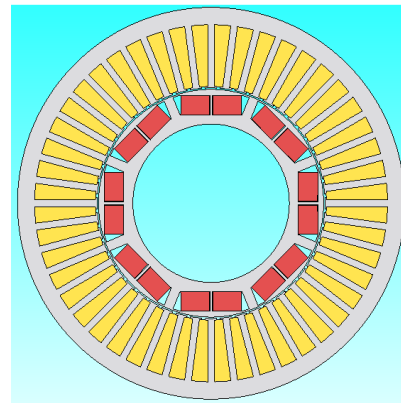


Fig. 7 - 6: Optimal IPM machine design w/  
MTPA

**Table 7 - 3: Comparison of Optimal SPM and IPM Machines**

<b>Parameter/Dimension</b>	<b>SPM</b>	<b>IPM w/ MTPA</b>
Airgap Diameter [mm]	181.48	160.44
Active Stack Length [mm]	57.01	55.39
Volume [m <sup>3</sup> ]	0.0025	0.0027
Copper Mass [kg]	10.11	10.47
Magnet Mass [kg]	2.07	1.85
Total Mass [kg]	<b>20.65</b>	<b>22.03</b>
Cont. Current Density [A/mm <sup>2</sup> ]	<b>4.6</b>	<b>4.6</b>
Current Angle [deg]	<b>0</b>	<b>35</b>
Torque Ripple [pk-pk/T <sub>rated</sub> ]	0.05	0.22
Power Factor	0.91	0.94
Magnet Loss [W]	59.44	1.49
Core Loss [W]	282.39	249.49
Copper Loss [W]	609.64	627.20
Efficiency	0.97	0.97

The best design is found to have a total active mass (stator and rotor) of 22.03 kg. It can continuously produce the required torque at the specified maximum continuous current density of 4.6 A/mm<sup>2</sup> and MTPA current angle of 35°. The optimized IPM machine (Fig. 7-6) has a mass increase of 1.38 kg compared to the FSCW SPM machine optimized previously (Fig. 7-5). The reduction in slot areas for the distributed stator winding configuration in the IPM machine is a major contributing factor to this mass penalty.

The key parameters of the optimized SPM and IPM machines are listed in Table 7-3. The deep slots adopted by the optimized IPM machine compensate for slot area loss associated with the lower slot fill factor attributable to the distributed winding configuration. The shape of the magnets in the optimized IPM machine design become “flat” rather than “V-shaped”, which helps to reduce the rotor yoke thickness and also boost the torque density. The torque ripple of the IPM machine is much higher than that of the SPM machine. Effort is needed to shape the

stator winding slots and the rotor magnet slots to smooth the flux path and thereby reduce the torque ripple.

It takes at least 3 EM FE analyses to locate the MTPA current angle for each candidate IPM machine design with the MTPA module during the optimization. There is another way to deal with the excitation current angle, which is to set it as an additional variable parameter in the optimization. In order to investigate the effectiveness of this approach, the optimization was rerun with the excitation current angle chosen from the range between  $5^\circ$  to  $65^\circ$  and the MTPA search module deactivated.

The new optimization also converged after the 50<sup>th</sup> generation, with a total number of 2,500 designs evaluated. The IPM machine optimized without the MTPA module (Fig. 7-8) looks almost identical to the one optimized with the MTPA module (Fig. 7-7). The key parameters of these two machines are listed in Table 7-4. The best design is found to have a total active mass (stator and rotor) of 22.18 kg, only 0.7% larger than the predicted IPM machine mass using the MTPA search algorithm. It can continuously produce the required torque at the current angle of  $32^\circ$ , and it has been verified that this angle corresponds to the MTPA angle for this machine design. The close similarity between the two optimal IPM machine designs indicates that setting the excitation current angle as an input variable for the optimization can be used to replace the MTPA module, leading to a reduction in computation time by a factor of 5 compared to the optimization with the activated MTPA module.



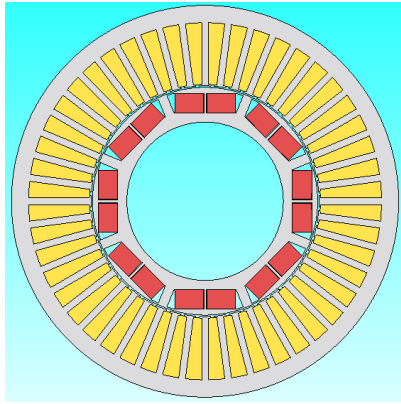


**Fig. 7 - 7: Optimal IPM machine design w/ MTPA**

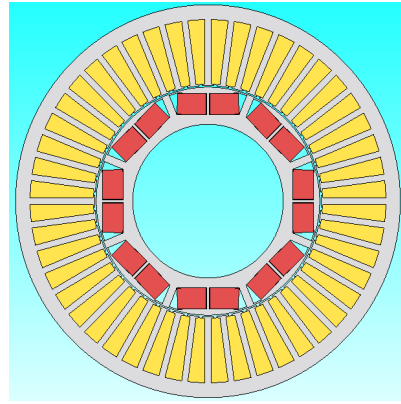


**Fig. 7 - 8: Optimal IPM machine design w/o MTPA**

**Table 7 - 4: Comparison of Optimal IPM Machines w/ and w/o MTPA**

Parameter/Dimension	IPM w/ MTPA	IPM w/o MTPA
Airgap Diameter [mm]	160.44	160.20
Active Stack Length [mm]	55.39	54.41
Volume [m <sup>3</sup> ]	0.0027	0.0027
Copper Mass [kg]	10.47	11.48
Magnet Mass [kg]	1.85	2.01
Total Mass [kg]	<b>22.03</b>	<b>22.18</b>
Cont. Current Density [A/mm <sup>2</sup> ]	<b>4.6</b>	<b>4.6</b>
Current Angle [deg]	<b>35</b>	<b>32</b>
Torque Ripple [pk-pk/T <sub>rated</sub> ]	0.22	0.28
Power Factor	0.94	0.95
Magnet Loss [W]	1.49	2.85
Core Loss [W]	249.49	223.49
Copper Loss [W]	627.20	687.77
Efficiency	0.97	0.97

## 7.2 Constrained Optimization Routine for the U.S. DRIVE Specifications

Up to this point, the investigation has been focused on optimizing machine designs for corner point operating conditions alone. In practical traction motor applications, electric machines are required to satisfy various constraints over the entire torque-speed envelope, suggesting that the

machine design challenge is considerably more complicated than optimization for a single operating point. The U.S. DRIVE advanced traction motor specifications (2020) are defined by the US Department of Energy working together with several major automotive manufacturers, providing some insight into what is expected for electric machines used in future hybrid electric vehicles. Proposing an optimization routine for the complete set of U.S. DRIVE specifications can help to explore how the optimization techniques developed during this research program can be applied for practical applications.

### **7.2.1 U.S. DRIVE (FreedomCAR) Advanced Traction Motor Specifications**

The U.S. DRIVE specifications [125] are summarized in Table 7-5, and the corresponding torque/power-speed envelope for continuous operation is presented in Chapter 2, Fig. 2-15. It can be observed that the corner speed is 2,800 rpm, and the required maximum speed is 14,000 rpm, resulting in a constant speed power ratio (CSPR) of 5:1. Three critical operating points are readily identifiable: delivering 30 kW continuously at 2,800 rpm, producing 55 kW at 2,800 rpm for 18 sec, and delivering 30 kW continuously at 14,000 rpm.

In this investigation, the operating constraints are classified into two major categories: primary constraints, and secondary constraints. The primary constraints that “must” be obeyed include the DC bus voltage, maximum phase current limits, and thermal limits (winding insulation and demagnetization constraints). Machine designs that do not meet any of the primary constraints are rejected.

In contrast, secondary constraints are challenging performance objectives that are “softer” in the sense that candidate designs are not automatically rejected if they do not meet the specified values. For this exercise, the efficiency and torque ripple specifications identified in Table 7-5

are considered to be secondary constraints. The maximum line-to-line back-EMF voltage limit (600 V<sub>peak</sub>) is considered to be a secondary constraint as well.

The nominal machine cooling conditions adopted for this initial study have been simplified to correspond to the machine cooling configuration in the WEMPEC Lab that combines a stator water jacket with forced air cooling of the stator end windings and rotor. These conditions are very similar to the final cooling conditions discussed in Section 4.2.2.

**Table 7 - 5: U.S. DRIVE (FreedomCAR) Advanced Traction Motor Specifications [125]**

Requirement	Target	Condition
Minimum Top Speed	14,000 rpm	
Peak Output Power	55 kW for 18 sec	at 20% max. speed
Continuous Output Power	30 kW	at 20~100% max. speed
Weight	≤ 35 kg	
Volume	≤ 9.7 L	
Unit Cost	≤ \$275	in quantities of 100,000
Operating DC Bus Voltage	200~450V, 325V nominal	
Maximum Phase Current	400Arms	
Characteristic Current	< max. current	
Efficiency	> 95%	at 10~100% max. speed for 20% rated torque
Line-to-Line Back-EMF	< 600V peak	at 100% speed
Torque Pulsation	< 5% peak torque	at any speed
Ambient Operating Temp.	-40~140°C	outside housing
Coolant inlet temperature	105°C	
Max. coolant flow rate	10 liters/min	
Max. coolant pressure drop	2 psi	
Max. coolant inlet pressure	20 psi	
Min. isolation impedance	1 MΩ	terminals to ground

### **7.2.2 Constrained Optimization of a Given Machine Cross-Section Design Based on U.S. DRIVE Specifications**

Although it would be desirable to combine the coupled EM/thermal model with the machine design optimization procedures in a HTC environment to design either an optimized SPM or IPM machine to meet the U.S. Drive specifications, this ambitious objective lies beyond the scope of the current research program due to a combination of technical and practical obstacles.

In its place, a constrained optimization procedure was defined that exercises only a subset of the variables in the developed machine models without changing the machine cross-sections as a precursor to the ultimate objective outlined above. More specifically, tests have been carried out on the three candidate SPM machines discussed initially in Chapter 2, i.e., the 30 kW 10-pole, 12-slot FSCW SPM machines optimized for maximum torque density (TD Design), the minimum cost machine (TPD Design), and the maximum efficiency machine (Eff. Design). These tests were conducted in order to find ways to fulfill key U.S. DRIVE specifications by adjusting a subset of the machine design variables that do not require changes to the machine lamination dimensions, or to reject the design when primary constraints are violated and no option is available without modifying its cross-section.

A procedure was developed to implement this constrained optimization based on the U.S. DRIVE specifications for a given machine cross-section as follows:

1. Evaluate the EM performance of a candidate machine design operating at 2,800 rpm with phase current of 400 Arms.
  - Adjust the machine's stack length to render it capable of delivering 55 kW, the peak transient output power requirement.
  - If the DC bus voltage  $V_{dc}$  is outside the range of 300 to 400 V (more restricted than the 200 to 450 V range defined in the specifications), adjust the number of turns to satisfy this requirement. Then modify the stack length accordingly.
  - Calculate  $J_{400}$ , i.e., the current density when the phase current is 400 Arms.

(Note: The operating point of 55 kW @ 2,800 rpm was chosen because it corresponds to the highest torque required from the machine, and its terminal voltage is usually higher

than the voltage for the top speed operating point of 30 kW @ 2,800 rpm. There is a linear relationship between a machine's torque production and its stack length, and the machine's terminal voltage is proportional to both its stack length and number of turns. Therefore, the iterative adjustments of the stack length and number of turns generally converges very rapidly.)

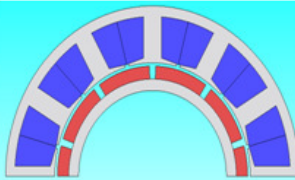
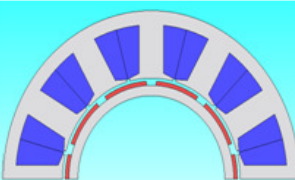
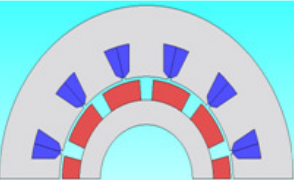
2. Build the corresponding 3D thermal FE model and run the coupled EM/thermal analysis to find the maximum transient current density  $J_{tr\_max}$  for achieving the peak/continuous power ratio of  $55/30 = 1.833$ .
  - If  $J_{400} > J_{tr\_max}$ , update the phase current based on the maximum transient current density  $J_{tr\_max}$ , and repeat Step 1.
  - If  $J_{400} < J_{tr\_max}$ , keep the winding current density as  $J_{400}$
3. Identify the characteristic current  $I_{char}$ .
  - Evaluate the winding flux linkage at two different current points that are aligned on the negative d-axis.
  - Apply the linear extrapolation method to locate  $I_{char}$ , i.e., the current point at which the winding flux linkage drops to zero.
4. Evaluate the EM performance of the candidate machine design operating at 14,000 rpm with phase current  $I = I_{char}$ . Step search for the current angle  $\gamma$  until  $P > 30$  kW and the DC bus voltage is within the range of 300-400V.
5. Feed the losses calculated in Step 4 into the thermal model, and check whether any thermal constraint is violated.

### 7.2.3 Application of the Constrained Optimization Routine to the Target Machines

The effectiveness of this constrained optimization routine has been investigated for the three 30 kW 10-pole, 12-slot FSCW surface PM machine designed presented in Chapter 2 that were optimized for maximum torque density (TD Design), minimum cost (TPD Design), and maximum efficiency (Eff. Design). The results of applying the special optimization routine procedures are summarized in Fig. 7-9 and explained as follows:

**TD Design:** The stack length of the machine is adjusted from 57.01 mm to 54.14 mm in order to make the machine capable of delivering 55 kW when excited with the maximum phase current. The number of turns is kept at the default value, since the DC bus voltage is within the specified range. After running the coupled EM/thermal analysis, the maximum transient current density is found to be  $22.08 \text{ A/mm}^2$ , higher than the current density calculated based on the phase current of 400 Arms. This result indicates that the machine can operate within its thermal constraints at 2,800 rpm. The total mass, magnet mass, and volume of the modified TD machine are updated (blue in Fig. 7-9), and the new values are slightly smaller than the original design.

The characteristic current is found to be 300 A pk, and the current angle  $\gamma$  is located by sweeping it from  $75^\circ$  with an incremental step size of  $2.5^\circ$  until both the power and voltage requirements are satisfied. The efficiency and torque ripple are evaluated at this high speed operating condition, shown in green in Fig. 7-9. It is worth noting that the magnets are assumed to be axially segmented into 26 pieces and that the magnet loss is estimated to be the magnet loss value from the 2D FE analysis divided by a factor of 5 to approximately account for the segmentation according to [106]. Then all of the loss components of the machine are specified as heat sources in the thermal model for evaluating the machine temperature distribution. The

	<i>TD Design</i>	<i>TPD Design</i>	<i>Eff. Design</i>
			
<b>400 A rms @ 2800 rpm</b>	57.01 mm -> 54.14 mm 10 turns $J_{400A} = 11.21 \text{ A/mm}^2$	82.18 mm -> 119.66 mm 10 turns -> 5 turns $J_{400A} = 6.08 \text{ A/mm}^2$	174.66 mm -> 44.63 mm 10 turns $J_{400A} = 36.95 \text{ A/mm}^2$
<b>Coupled EM/Thermal Analysis</b>	$J_{tr\_max} = 22.08 \text{ A/mm}^2$ 400 A rms 54.14 mm 10 turns $M_{total} = 20.65 \text{ kg} \rightarrow 19.73 \text{ kg}$ $M_{magnet} = 2.07 \text{ kg} \rightarrow 2.00 \text{ kg}$ $Vol = 0.0025 \text{ m}^3 \rightarrow 0.0024 \text{ m}^3$	$J_{tr\_max} = 10.35 \text{ A/mm}^2$ 400 A rms 119.66 mm 5 turns $M_{total} = 27.16 \text{ kg} \rightarrow 36.80 \text{ kg}$ $M_{magnet} = 0.83 \text{ kg} \rightarrow 1.24 \text{ kg}$ $Vol = 0.0037 \text{ m}^3 \rightarrow 0.0053 \text{ m}^3$	$J_{tr\_max} = 22.54 \text{ A/mm}^2$ 244.01 A rms 44.63 mm -> 69.45 mm 10 turns $M_{total} = 63.76 \text{ kg} \rightarrow 25.81 \text{ kg}$ $M_{magnet} = 6.56 \text{ kg} \rightarrow 2.66 \text{ kg}$ $Vol = 0.0093 \text{ m}^3 \rightarrow 0.0037 \text{ m}^3$
<b>Identify <math>I_{char}</math></b>	$I_{char} = 300 \text{ A pk}$	$I_{char} = 200 \text{ A pk}$	$I_{char} = 175 \text{ A pk}$
<b><math>I_{char}</math> @ 14000 rpm</b>	$\gamma = 77.5^\circ$ $\eta = 94.29\%$ $T_{ripple} = 18.11\%$	$\gamma = 72.5^\circ$ $\eta = 94.05\%$ $T_{ripple} = 23.16\%$	$\gamma = 75^\circ$ $\eta = 96.86\%$ $T_{ripple} = 7.23\%$
<b>Thermal Check @ 14000 rpm</b>	$T_{coils\_max} = 144.40^\circ\text{C}$ $T_{magnet} = 290.88^\circ\text{C}$	$T_{coils\_max} = 85.90^\circ\text{C}$ $T_{magnet} = 285.62^\circ\text{C}$	$T_{coils\_max} = 140.45^\circ\text{C}$ $T_{magnet} = 202.25^\circ\text{C}$

**Note:** The magnets are assumed to be axially segmented into 26 pieces, which leads to approx. 80% magnet loss reduction.

**Fig. 7 - 9: Results of applying the constrained optimization procedure to the TD Design, TPD Design, and Eff. Design machines**

magnet temperature is found to be very high ( $>290^\circ\text{C}$ ), indicating that demagnetization is inevitable. Hence, the TD Design is not qualified to meet the key U.S. DRIVE specifications under the terms of the constrained optimization.

**TPD Design:** The stack length is adjusted from 82.18 mm to 119.66 mm in order to make the machine capable of delivering 55 kW when excited with the maximum phase current of 400 Arms. The number of turns is adjusted from 10 to 5 turns in order to satisfy the DC bus voltage constraint. The machine can operate at 2,800 rpm without exceeding the maximum allowable winding temperature or inducing irreversible demagnetization, since the current density

associated with the maximum phase current is below the maximum transient current density determined from the coupled EM/thermal analysis. The updated total machine mass, magnet mass, and volume are significantly larger than those of the original design because of the increased stack length.

The machine is then excited by the characteristic current of 200 A pk with the current angle  $\gamma = 72.5^\circ$  to evaluate its EM performance at 14,000 rpm. The estimated core loss, magnet loss, and copper loss are fed into the thermal model in order to predict temperatures inside the machine. Although the winding hot spot winding temperature ( $86^\circ\text{C}$ ) is much lower than the insulation temperature constraint ( $155^\circ\text{C}$  for F Class insulation), the maximum magnet temperature ( $286^\circ\text{C}$ ) is well beyond the upper limit of the safe operating temperature range for the magnet material. Therefore, the TPD Design is also eliminated from the candidate machine list for meeting the key U.S. DRIVE specifications.

**Eff. Design:** The stack length of the machine is decreased by nearly 75% from 174.66 mm to 44.63 mm in order to make the machine capable of delivering 55 kW when excited with the maximum phase current of 400 Arms.. The DC bus voltage is within the specified range, so no change is needed in the number of turns (10). The maximum transient current density of the Eff. Design machine is found to be  $22.54 \text{ A/mm}^2$  through the coupled analysis, which is lower than the current density associated with the 400 Arms phase current excitation. Therefore, the maximum allowable phase current is reduced to 244.01 Arms in order to meet the maximum transient current density. The machine's stack length is subsequently increased to 69.45 mm in order to deliver the required torque, and the machine's total mass, magnet mass, and volume are then modified accordingly, and the updated machine design becomes much more appealing in terms of torque density than the original one that was optimized for efficiency.



The machine's EM performance is evaluated at 14,000 rpm with its characteristic current of 175 A pk and the current angle  $\gamma$  for 30 kW power delivery is found to be 75°. The updated Eff. Design machine has higher efficiency and lower torque ripple at this high-speed operating condition compared to the updated TD Design and TPD Design machines (green in Fig. 7-9). It can also deliver the required power without exceeding the maximum allowable winding temperature or inducing irreversible demagnetization in the rotor magnets. With all of the key primary constraints met, the updated Eff. Design machine is the best-qualified candidate among the three alternatives for meeting the U.S. DRIVE specifications.

There are some key observations that have been developed during the course of this constrained optimization study which include:

- The U.S. DRIVE specifications require high-efficiency machine designs that produce low rotor losses during high-speed operation.
- The cooling system can be segregated into different stages based on the machine operating conditions. For example, the baseline cooling conditions selected for this study are sufficient for corner point operation of both the TD Design and the TPD Design machines, but the cooling is insufficient for these two machines to deliver 30 kW continuous at high speeds. If some additional cooling is available during high-speed operation, both of these designs could qualify as traction machines fulfilling the key requirements of the U.S. DRIVE specifications.
- To date, the optimization routine is proposed based on a fixed cooling configuration. However, an electrical machine is heavily constrained by its thermal limits. As a result, comprehensive optimization of an electrical machine requires that its electromagnetic and thermal (cooling) design be optimized simultaneously.

### 7.3 Conclusion

The application of the iterative FE-based machine design optimization algorithm has been extended to IPM machines. The software has been applied to optimize a 30 kW (continuous) IPM machine with a distributed winding for high torque density. The torque produced by an IPM machine consists of both magnet torque and reluctance torque component, and the torque varies as a function of current amplitude and current angle.

Two approaches for finding the current angle needed by specific candidate designs to maximize the torque production are demonstrated. In one approach, the current angle for each candidate design is determined using an MTPA angle search module, while in the other method it is set as a variable in the optimization. The two optimization approaches converge to similar designs. This result suggests that setting the excitation current angle as an input variable for the optimization can be used to replace the MTPA angle search module, leading to a significant reduction in computational effort and time.

As a result of the success of implementing the EM machine design optimization algorithm for the IPM machine, there is a basis for confidence that the previously-developed coupled EM/thermal machine design optimization techniques for the SPM machine can be adopted for optimization of IPM synchronous machines as well.

A constrained optimization routine that can be used to optimize a subset of the key machine parameters for electric machine designs to meet key U.S. DRIVE specs is proposed based on the coupled EM/thermal model. The effectiveness of the constrained optimization routine is evaluated by applying it to the three candidate surface PM machine designs without changing their lamination cross-section dimensions. The results show that high efficiency machine designs

are appealing candidates for meeting the traction motor application. In addition, the constrained optimization results show that the EM and cooling design optimizations should be conducted in tandem in order to determine the optimum machine and thermal management system designs to meet demanding performance specifications, including those developed by U.S. DRIVE.

## Chapter 8: Parameter Sensitivity

The FE models' mesh size affects both the accuracy of the results and the computational time. It is challenging to precisely estimate the thermal coefficients for setting boundary conditions in the thermal FE model. Moreover, the machine dimensions vary from those specified in the model due to manufacturing tolerance. The uncertainties in all the above-mentioned parameters affect the performance of machine designs predicted using the coupled EM/thermal FE model. Therefore, it is worthwhile to perform some sensitivity analyses on these parameters in order to examine their impacts.

### 8.1 Investigation of Mesh Size of the EM FE Model

Transient EM FE analysis typically takes much more time than the thermal FE analysis when using the coupled EM/thermal model. Therefore, the EM FE model mesh size is studied here in order to better understand the trade-offs between analysis time and result accuracy.

As an example, the TD Design SPM machine has been meshed with three different sizes: coarse mesh (illustrated by Fig. 8-1), medium mesh (Fig. 8-2), and fine mesh (Fig. 8-3). Table 8-1 compares the number of total elements, model analysis time, predicted torque, core loss, and magnet loss associated with the three mesh sizes. The results suggest that the fine mesh model is the most accurate of the three models' results, so that result set is chosen as the baseline. The per-unit values of torque, core loss, and magnet losses of the three models are calculated and displayed in parentheses in Table 8-1.

It can be observed in Table 8-1 that the simulation time of the coarse mesh model is approx. 1/250 that of the fine mesh model. The difference in torque prediction is only 2%, while the discrepancies in the predicted core loss and magnet loss between the two models are quite large.

These results suggest that, if torque prediction is the main result needed from an FE analysis, then it is reasonable to use a coarse mesh in the model in order to save computation time.

The medium mesh model and the fine mesh model agree closely in terms of predicted torque, core loss, and magnet loss. . Although the computational time reduction when in moving from the fine mesh-density model to the medium mesh model is not as significant as the drop when moving from the medium mesh model to the coarse mesh model, the medium mesh has been adopted in the coupled EM/thermal model that requires accurate predictions of both the torque and machine losses.

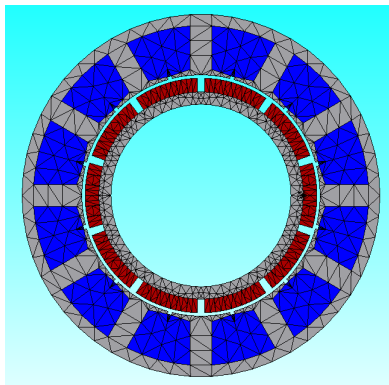


**Fig. 8 - 1: TD Design FE model with coarse mesh**

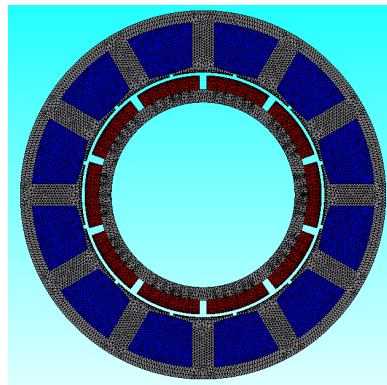


**Fig. 8 - 2: TD Design FE model with medium mesh**

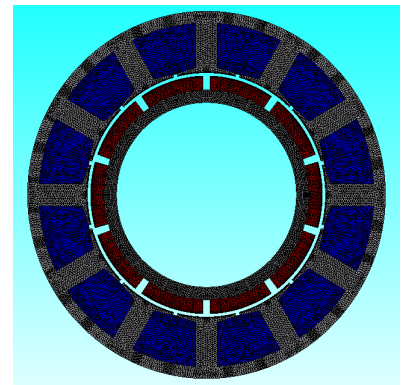


**Fig. 8 - 3: TD Design FE model with fine mesh**

**Table 8 - 1: Comparison of EM FE Models with Different Mesh Sizes**

	<b>Coarse Mesh</b>	<b>Medium Mesh</b>	<b>Fine Mesh</b>
No. of Elements	3071	36896	64914
Analysis Time	8 sec	12 min 50 sec	32 min 13 sec
Torque	100.58 N*m (0.98)	102.23 N*m (1.00)	102.22 N*m (1.00)
Core Loss	240.69 W (0.81)	271.77 W (0.91)	297.15 W (1.00)
Magnet Loss	31.67 W (0.43)	71.18 W (0.97)	73.09 W (1.00)

## 8.2 Thermal Coefficient Sensitivity for a Given Machine Design

There are four thermal coefficients used to set the boundary conditions in the FE thermal model: the water jacket coolant temperature (**Temp\_cool**), the contact resistance between the water jacket and the stator core (**Rc\_jacket**), the heat transfer coefficient in the airgap (**h\_airgap**), and the heat transfer coefficient at the machine ends (**h\_coil\_end**). Understanding the impact of each of the thermal coefficients on a machine design's thermal performance provides some insight into how to improve the cooling effectiveness.

Taking the TD Design as the example again, the variations in machine component temperatures when operating at 2800 rpm with a excitation current density of  $4.6 \text{ A/mm}^2$  are evaluated by altering these thermal coefficients around their default values (**Temp\_cool** =  $65^\circ\text{C}$ , **Rc\_jacket** =  $1.955 \times 10^{-4} \text{ K} \cdot \text{m}^2/\text{W}$ , **h\_airgap** =  $125 \text{ W}/(\text{m}^2 \cdot \text{K})$ , **h\_coil\_end** =  $53.84 \text{ W}/(\text{m}^2 \cdot \text{K})$ ), as shown in Figs. 8-4 to 8-7. It can be observed that the winding and PM temperatures are highly sensitive to coolant temperature changes and the changes in the machine ends' heat transfer coefficients. However, these end temperatures are much less sensitive to variations in water jacket contact resistance and the air gap heat transfer coefficient.

## 8.3 Sensitivity Analysis of Machine Design Parameters and Thermal Coefficients

With thousands of candidate designs evaluated in one optimization process, it is important to understand how the uncertainty in the coupled EM/thermal model's predicted machine performance can be apportioned to different sources of uncertainties in the input parameters. These input parameter uncertainties include machine dimensions and thermal coefficients, and the performance sensitivities will vary over a large range of candidate machine designs. Sensitivity analyses of the machine parameters and thermal coefficients have been conducted.

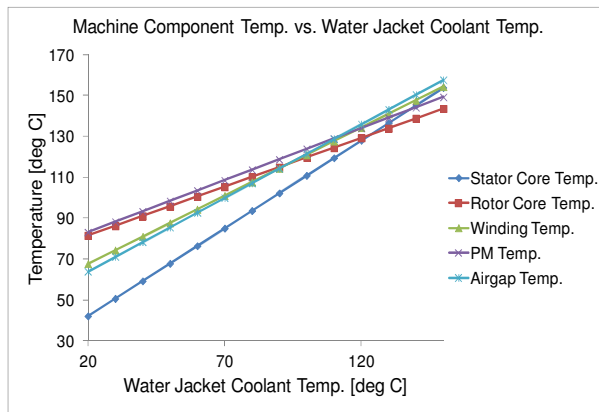


**Fig. 8 - 4: TD machine component temperatures vs. water jacket coolant temperature**

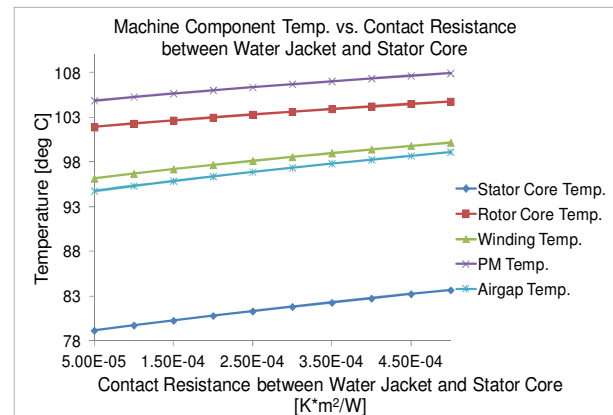


**Fig. 8 - 5: TD machine component temperatures vs. contact resistance between water jacket and stator lamination core**

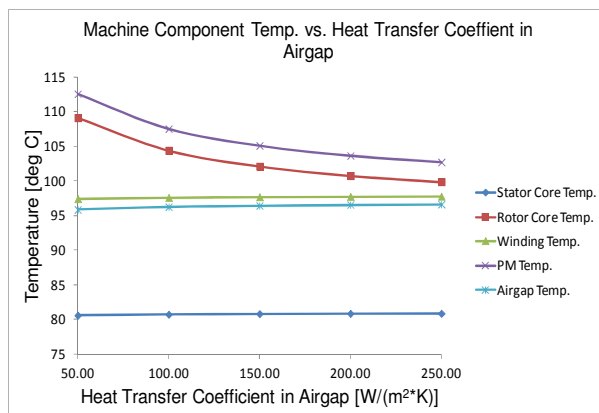


**Fig. 8 - 6: TD machine component temperatures vs. heat transfer coefficient in the airgap**

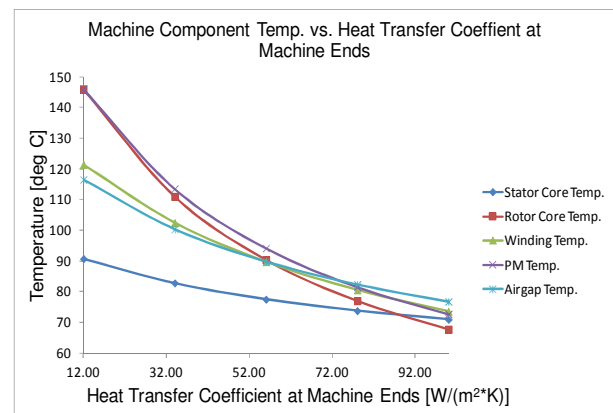


**Fig. 8 - 7: TD machine component temperatures vs. heat transfer coefficient at machine ends**

### 8.3.1 Data Collection: Parametric Study Using the Monte Carlo Method

Parametric studies focused on the impact of the machine dimensions and thermal coefficients have been performed for the TD Design machine using the Monte Carlo method in order to collect data for the sensitivity analysis. The ten input parameters for the coupled EM/thermal model are:

- The water jacket coolant temperature (**Temp\_cool**)
- Contact resistance between the water jacket and stator core (**Rc\_jacket**)

- The heat transfer coefficient in the airgap (**h\_airgap**)
- The heat transfer coefficient at machine ends (**h\_coil\_end**)
- The tooth width to slot pitch ratio (**Tau\_wt**)
- The stator yoke thickness to tooth width ratio (**Tau\_hsy**)
- The magnet span to rotor pole pitch ratio (**Alpha\_Neo**)
- The rotor yoke thickness to rotor pole pitch ratio (**Tau\_hry**)
- The magnet thickness to airgap thickness ratio (**Tau\_hm**)
- The airgap radius to stator outer radius ratio (**Rg\_Rsout**)

The ranges for these variables, shown in Table 8-2, are chosen based on practical experience and physical geometric constraints.

Next, all of the parameters in the parameter set are fed into the template visual basic (VB) script for both the EM and thermal FE analyses, which contain information on the machine configuration, material, cooling condition, and excitation, in order to create a specific script for each candidate design. By following the flow chart procedure for the static version of the coupled analysis discussed in Section 5.3, the predicted torque production values of a total

**Table 8 - 2: FSCW-SPM Variable Definitions and Ranges**

<b>Variable Parameters</b>	<b>Range</b>
Water Jacket Coolant Temperature: <b>Temp_cool</b> [°C]	[20, 150]
Contact Resistance between Water Jacket and Stator Core: <b>Rc_jacket</b> [°C-m <sup>2</sup> /W]	[5e-5, 5e-4]
Heat Transfer Coefficient in the Airgap: <b>h_airgap</b> [W/m <sup>2</sup> °C]	[50, 250]
Heat Transfer Coefficient at Machine Ends: <b>h_coil_end</b> [W/m <sup>2</sup> °C]	[12, 100]
Tooth Width to Slot Pitch Ratio: <b>Tau_wt</b>	[0.1, 0.8]
Stator Yoke Thickness to Tooth Width Ratio: <b>Tau_hsy</b>	[0.1, 0.8]
Magnet Span to Rotor Pole Pitch Ratio: <b>Alpha_Neo</b>	[0.5, 0.95]
Rotor Yoke Thickness to Rotor Pole Pitch Ratio: <b>Tau_hry</b>	[0.1, 0.6]
Magnet Thickness to Airgap Thickness Ratio: <b>Tau_hm</b>	[1, 7]
Airgap Radius to Stator Outer Radius Ratio: <b>Rg_Rsout</b>	[0.3, 0.75]



number of 600 candidate designs have been evaluated under different cooling conditions during operation at their maximum safe current densities.

### 8.3.2 Sensitivity Analysis with Scatter Plots Method

The scatter plot method is a simple but useful way to compare the output variables' response over an individual input variable's range of permissible values. The scatter plots shown from Fig. 8-8 to 8-17 were produced by randomly sampling the average torque values predicted by the coupled EM/thermal model for the 600 designs over the input parameter range specified above.

Each red dot in these scatter plots represent an individual design with its specific cooling condition, and all of the data points in every scatter plot are fitted using a straight line (blue lines shown in Figs. 8-8 to 8-17). There are 600 red dots in every scatter plot. Patterns of the scatter plots or the slope of the fitted line can help qualitatively evaluate the sensitivities of these input parameters. It can be observed in Figs. 8-8 to 8-11 that the average machine torque is more sensitive to the water jacket coolant temperature and the heat transfer coefficient at machine ends

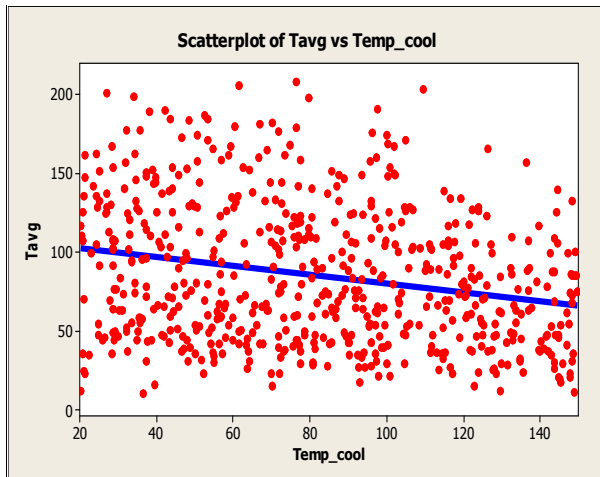


**Fig. 8 - 8:** Scatter plot (red dots) of average torque vs. water jacket coolant temperature with regression (blue line)

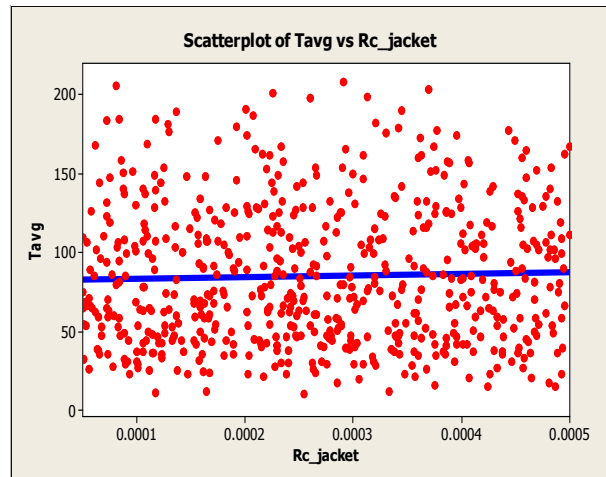


**Fig. 8 - 9:** Scatter plot (red dots) of average torque vs. contact resistance between water jacket and stator core with regression (blue line)

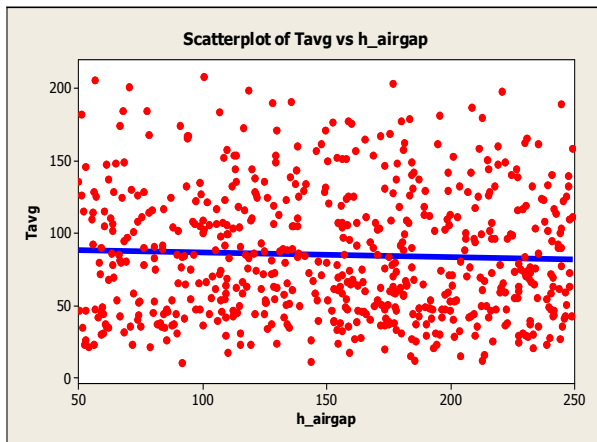


**Fig. 8 - 10:** Scatter plot (red dots) of average torque vs. heat transfer coefficient in the airgap with regression (blue line)

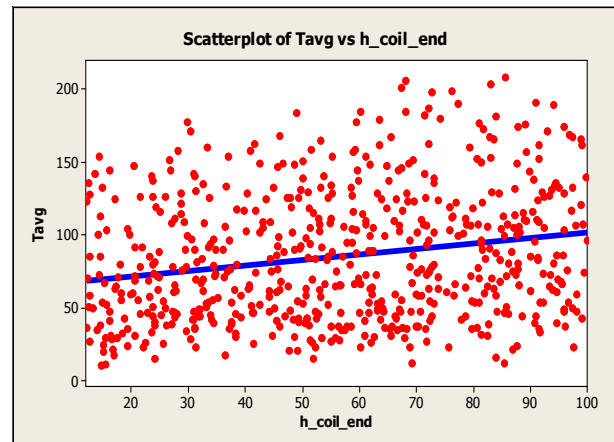


**Fig. 8 - 11:** Scatter plot (red dots) of average torque vs. heat transfer coefficient at machine ends with regression (blue line)

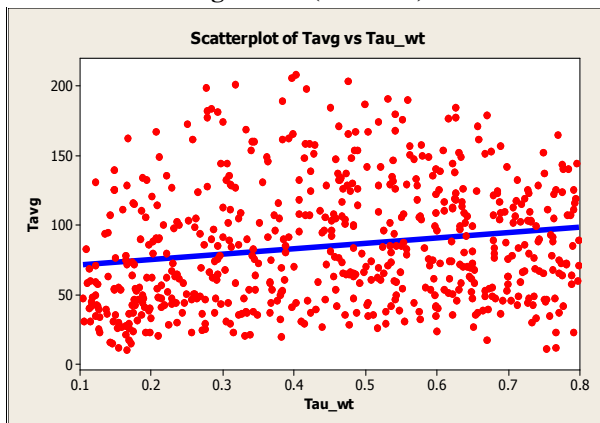


**Fig. 8 - 12:** Scatter plot (red dots) of average torque vs. tooth width to slot pitch ratio with regression (blue line)

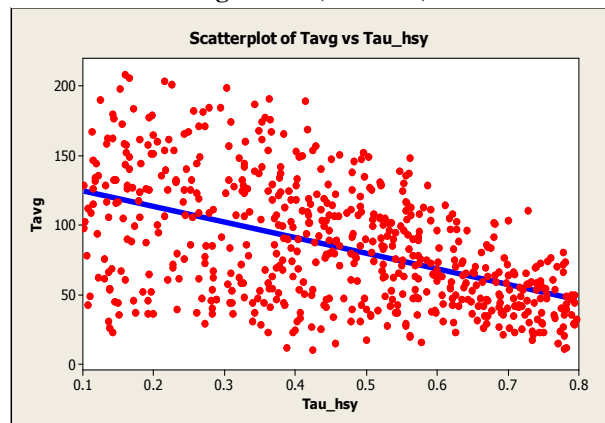


**Fig. 8 - 13:** Scatter plot (red dots) of average torque vs. stator yoke thickness to tooth width ratio with regression (blue line)

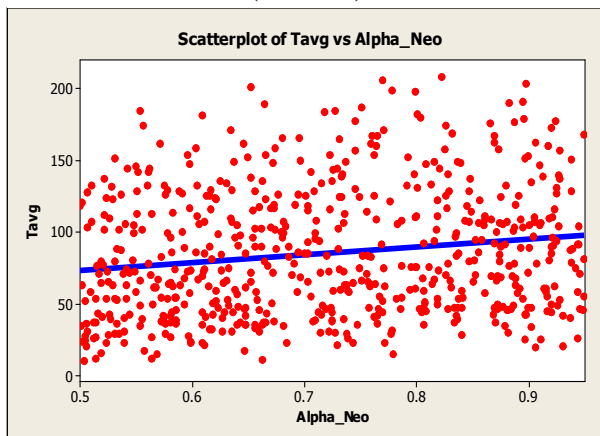


**Fig. 8 - 14:** Scatter plot (red dots) of average torque vs. magnet span to rotor pole pitch ratio with regression (blue line)

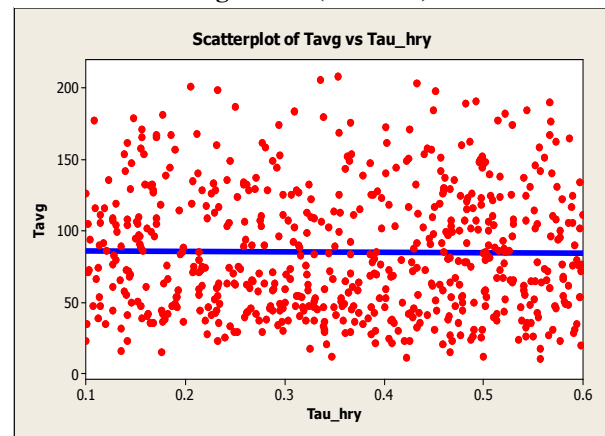


**Fig. 8 - 15:** Scatter plot (red dots) of average torque vs. rotor yoke thickness to rotor pole pitch ratio with regression (blue line)

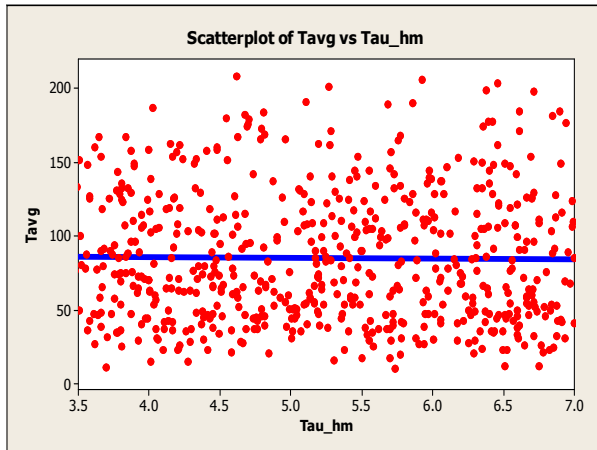


**Fig. 8 - 16: Scatter plot (red dots) of average torque vs. magnet thickness to airgap thickness ratio with regression (blue line)**

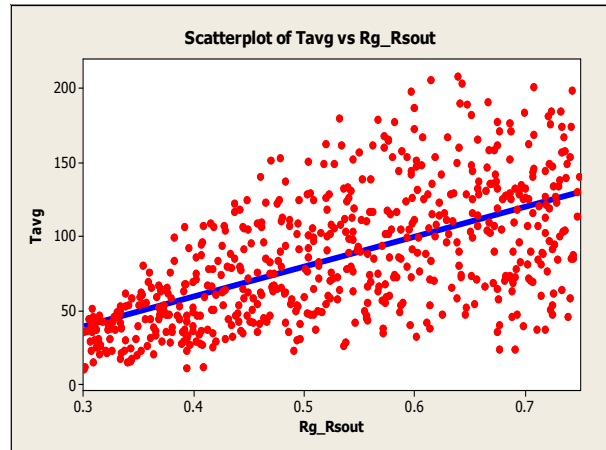


**Fig. 8 - 17: Scatter plot (red dots) of average torque vs. airgap radius to stator outer radius ratio with regression (blue line)**

compared to the other thermal coefficient. Among all of the machine geometric parameters, larger changes in average torque are caused by the variations in the ratio of stator yoke thickness to tooth width, as well as the ratio of airgap radius to stator outer radius, as shown in Figs. 8-12 to 8-17.

### 8.3.3 Evaluation of Parameter Sensitivity Using Regression Analysis

Another simple and effective tool for analyzing sensitivity is regression analysis, which is a statistical method for estimating the relationship between a dependent variable and one or more independent variables [126, 127]. The regression function is expressed in (28).

$$Y \approx f(X, \beta) \quad (28)$$

where  $Y$  is the dependent variable,  $X$  represents the independent variables, and  $\beta$  represents the unknown parameters. In this case, the average torque is the dependent variable. Since the cross-coupling effects of the input parameters are also considered in this analysis, the independent variables include all of the individual input parameters and their second-order product terms, e.g.,  $\text{Temp\_cool} * \text{Temp\_cool}$  and  $\text{h\_coil\_end} * \text{Tau\_wt}$ . The values of  $\beta$  that best fits the data

collected in Section 8.3.1 is determined from the regression analysis, which minimizes the distance between the average torques calculated by the coupled models and the predicted average torques from the regression function.

The dimensional parameters and the thermal coefficients of the 600 designs are normalized using the feature scaling method, as expressed in (29):

$$x' = \frac{x - \min(x)}{\max(x) - \min(x)} \quad (29)$$

where  $x$  is the original value,  $x'$  is the normalized value, and  $\min(x)$  and  $\max(x)$  are the lower and upper boundary of the variable's range, respectively. For instance, suppose that the coolant temperature is 65°C. The normalized coolant temperature is  $(65^\circ\text{C} - 20^\circ\text{C}) / (150^\circ\text{C} - 20^\circ\text{C}) = 0.3462$ . The upper and lower boundaries of the input parameters (thermal coefficients and design parameters) are chosen based on practical experience and machine geometric constraints.

These normalized parameters along with the evaluated average torque values collected in Section 8.3.1 are loaded into Minitab, a statistics analysis software package used in the study, to conduct the regression analysis. The results of this analysis are presented in Figs. 8-18 and 8-19, and the calculated regression function is expressed by (29), as follows:

$$\begin{aligned} T_{avg} = & -75.19 + 229.44 * Tau_{wt} + 121.19 * Tau_{hsy} + 36.33 * Alpha_{Neo} + 10.46 * Tau_{hm} \\ & + 283.34 * Rg_{Rsout} + 20.76 * h_{coil\_end} + 6.08 * Temp_{cool} - 141.94 * Tau_{wt} \\ & * Tau_{wt} - 51.1 * Tau_{wt} * Tau_{hsy} + 17.41 * Tau_{wt} * Alpha_{Neo} - 8.8 * Tau_{wt} \\ & * Tau_{hm} - 55.59 * Tau_{wt} * Rg_{Rsout} - 21.39 * Tau_{wt} * Temp_{cool} - 92.75 \\ & * Tau_{hsy} * Tau_{hsy} - 17.8 * Tau_{hsy} * Alpha_{Neo} - 123.99 * Tau_{hsy} * Rg_{Rsout} \\ & - 23.21 * Tau_{hsy} * h_{coil\_end} + 15.7 * Tau_{hsy} * Temp_{cool} - 24.28 * Alpha_{Neo} \\ & * Alpha_{Neo} + 13.27 * Alpha_{Neo} * Rg_{Rsout} + 15.18 * Alpha_{Neo} * h_{coil\_end} + 13.06 \\ & * Tau_{hm} * Rg_{Rsout} - 13.67 * Tau_{hm} * Temp_{cool} - 111.51 * Rg_{Rsout} * Rg_{Rsout} \\ & + 40.7 * Rg_{Rsout} * h_{coil\_end} - 57.16 * Rg_{Rsout} * Temp_{cool} - 19.62 * h_{coil\_end} \\ & * h_{coil\_end} + 24.29 * h_{coil\_end} * Temp_{cool} - 20.16 * Temp_{cool} * Temp_{cool} \end{aligned} \quad (30)$$

Coefficients

Term	Coef	SE Coef	T	P	95% CI
Constant	-75.187	7.0340	-10.6892	0.000	( -89.003, -61.372)
Tau_wt	229.436	9.5718	23.9700	0.000	( 210.636, 248.237)
Tau_hsy	121.194	10.1067	11.9915	0.000	( 101.343, 141.045)
Alpha_Neo	36.335	8.8215	4.1189	0.000	( 19.008, 53.661)
Tau_hm	10.455	5.2184	2.0035	0.046	( 0.206, 20.705)
Rg_Rsout	283.340	9.9462	28.4874	0.000	( 263.804, 302.875)
h_coil_end	20.757	8.8741	2.3391	0.020	( 3.327, 38.187)
Temp_cool	6.077	9.5092	0.6391	0.523	( -12.600, 24.754)
Tau_wt*Tau_wt	-141.939	6.6060	-21.4863	0.000	(-154.914, -128.963)
Tau_wt*Tau_hsy	-51.103	6.1693	-8.2834	0.000	( -63.220, -38.986)
Tau_wt*Alpha_Neo	17.406	5.6554	3.0777	0.002	( 6.297, 28.514)
Tau_wt*Tau_hm	-8.801	5.8883	-1.4946	0.136	( -20.366, 2.765)
Tau_wt*Rg_Rsout	-55.592	6.0137	-9.2443	0.000	( -67.404, -43.780)
Tau_wt*Temp_cool	-21.389	5.8374	-3.6642	0.000	( -32.855, -9.924)
Tau_hsy*Tau_hsy	-92.748	6.6167	-14.0171	0.000	(-105.744, -79.752)
Tau_hsy*Alpha_Neo	-17.801	6.1618	-2.8890	0.004	( -29.904, -5.699)
Tau_hsy*Rg_Rsout	-123.993	6.1241	-20.2466	0.000	(-136.022, -111.964)
Tau_hsy*h_coil_end	-23.206	6.2960	-3.6858	0.000	( -35.572, -10.839)
Tau_hsy*Temp_cool	15.695	5.9726	2.6279	0.009	( 3.964, 27.426)
Alpha_Neo*Alpha_Neo	-24.281	6.5707	-3.6954	0.000	( -37.187, -11.376)
Alpha_Neo*Rg_Rsout	13.270	5.7491	2.3082	0.021	( 1.978, 24.562)
Alpha_Neo*h_coil_end	15.183	5.9084	2.5698	0.010	( 3.578, 26.788)
Tau_hm*Rg_Rsout	13.062	5.8119	2.2475	0.025	( 1.647, 24.478)
Tau_hm*Temp_cool	-13.673	6.0956	-2.2431	0.025	( -25.645, -1.700)
Rg_Rsout*Rg_Rsout	-111.512	6.5459	-17.0355	0.000	(-124.369, -98.655)
Rg_Rsout*h_coil_end	40.700	5.9194	6.8756	0.000	( 29.073, 52.326)
Rg_Rsout*Temp_cool	-57.158	5.8036	-9.8487	0.000	( -68.557, -45.759)
h_coil_end*h_coil_end	-19.621	6.6656	-2.9437	0.003	( -32.713, -6.529)
h_coil_end*Temp_cool	24.293	6.0674	4.0039	0.000	( 12.376, 36.210)
Temp_cool*Temp_cool	-20.164	6.5114	-3.0967	0.002	( -32.953, -7.375)

Fig. 8 - 18: Coefficients  $\beta$  estimated with regression analysis

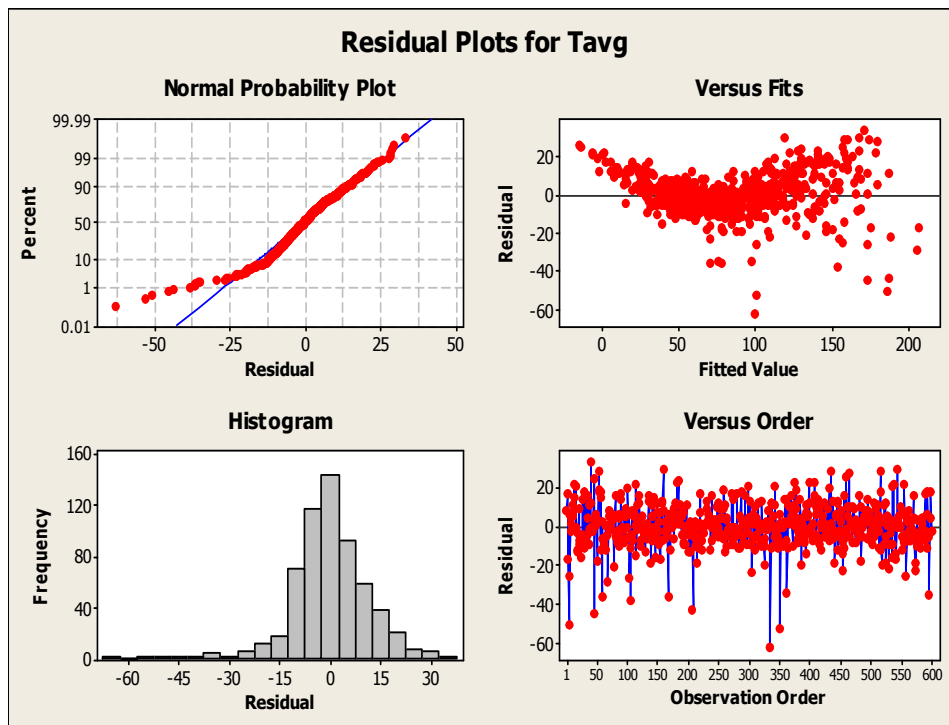


Fig. 8 - 19: Residual plots for average torque Tavg

The calculated sensitivity, as a local single-input single-output function, measures the effect of a given input on a given output. This sensitivity can be evaluated by taking the partial derivative of the output  $Y$  with respect to an input factor  $X_i$ , i.e.,  $\frac{\partial Y}{\partial X_i X^0}$ , where  $X^0$  indicates that

the derivative is evaluated at a selected local point in the space of the input parameters. This definition has been applied to find the sensitivities of the average torque calculated by the coupled EM/thermal models to the seven input parameters for the three machine designs including the TD, TPD, and Eff. Designs developed previously in Chapter 2. These sensitivities are evaluated by substituting the normalized dimensions and thermal coefficients for each of these three machines into the partial derivative equations (Eqn. (31) to (37)) that have been derived from (30), shown below:

$$\frac{\partial T_{avg}}{\partial Tau_{wt}} = 229.44 - 283.88 * Tau_{wt} - 51.1 * Tau_{hsy} + 17.41 * Alpha_{Neo} - 8.8 * Tau_{hm} - 55.59 * Rg_{Rsout} - 21.39 * Temp_{cool} \quad (31)$$

$$\frac{\partial T_{avg}}{\partial Tau_{hsy}} = 121.19 - 51.1 * Tau_{wt} - 185.5 * Tau_{hsy} - 17.8 * Alpha_{Neo} - 123.99 * Rg_{Rsout} - 23.21 * h_{coil\_end} + 15.7 * Temp_{cool} \quad (32)$$

$$\frac{\partial T_{avg}}{\partial Alpha_{Neo}} = 36.33 + 17.41 * Tau_{wt} - 17.8 * Tau_{hsy} - 48.56 * Alpha_{Neo} + 13.27 * Rg_{Rsout} + 15.18 * h_{coil\_end} \quad (33)$$

$$\frac{\partial T_{avg}}{\partial Tau_{hm}} = 10.46 - 8.8 * Tau_{wt} + 13.06 * Rg_{Rsout} - 13.67 * Temp_{cool} \quad (34)$$

$$\frac{\partial T_{avg}}{\partial Rg_{Rsout}} = 283.34 - 55.59 * Tau_{wt} - 123.99 * Tau_{hsy} + 13.27 * Alpha_{Neo} + 13.06 * Tau_{hm} - 223.02 * Rg_{Rsout} + 40.7 * h_{coil\_end} - 57.16 * Temp_{cool} \quad (35)$$

$$\frac{\partial T_{avg}}{\partial h_{coil\_end}} = 20.76 - 23.21 * Tau_{hsy} + 15.18 * Alpha_{Neo} + 40.7 * Rg_{Rsout} - 39.24 * h_{coil\_end} + 24.29 * Temp_{cool} \quad (36)$$

$$\frac{\partial T_{avg}}{\partial Temp_{cool}} = 6.08 - 21.39 * Tau_{wt} + 15.7 * Tau_{hsy} - 13.67 * Tau_{hm} - 57.16 * Rg_{Rsout} + 24.29 * h_{coil\_end} - 40.33 * Temp_{cool} \quad (37)$$

The original values of the seven key dimensions and thermal coefficients for each of the three candidate designs are summarized in Table 8-3. The torque sensitivity values for these same seven input variables are evaluated by substituting the values in Table 8-3 into Eqns. (31) to (37)

for each of the three machines. The results are presented in Fig. 8-20, along with the cross-sections of the TD, TPD, and Eff. designs. The machine design optimized for high torque density with the coupled EM/thermal model is also shown on the left side of the figure for comparison.

**Table 8 - 3: Dimensions and Thermal Coefficients of the TD, TPD, and Eff. Designs**

Parameter	TD Design	TPD Design	Eff. Design
Tau_wt	0.3488	0.5258	0.7608
Tau_hsy	0.1875	0.2089	0.5190
Alpha_Neo	0.8927	0.8151	0.7412
Tau_hm	4.1849	1.3689	6.4082
Rg_Rsout	0.6619	0.5960	0.5860
h_coil_end [W/m <sup>2</sup> °C]	53.84	53.84	53.84
Temp_cool [°C]	65	65	65

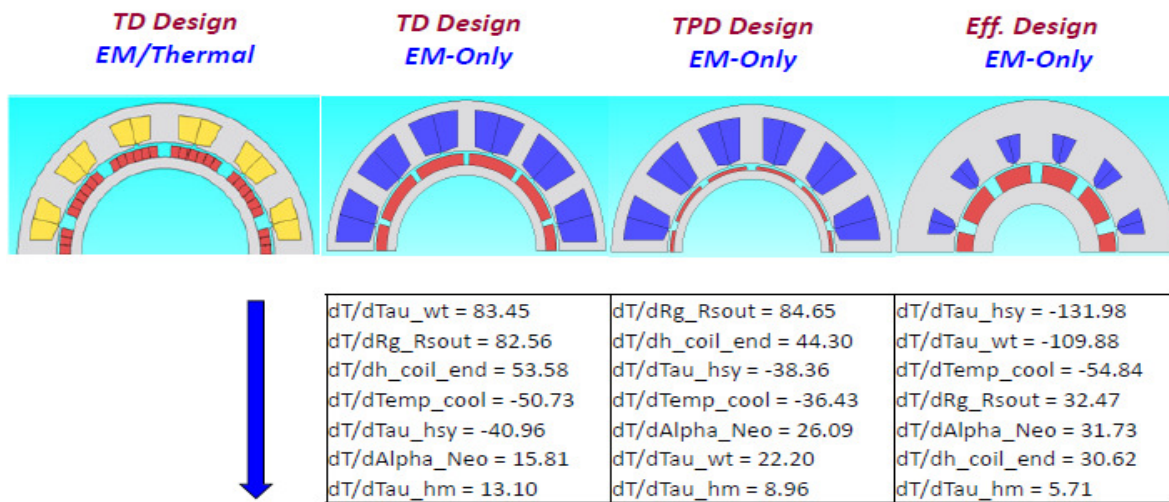


**Fig. 8 - 20: Parameter sensitivities for the TD Design, TPD Design, and Eff. Design machines, including the cross section of the optimized torque density machine using the coupled EM/thermal model (left)**

It can be observed from Fig. 8-20 that the torque density of the TD Design can be noticeably improved by increasing its tooth width and airgap radius. Similarly, the TPD Design can achieve the same goal by increasing its airgap radius and decreasing its stator yoke thickness, while the Eff. Design can do so by reducing both its stator yoke thickness and tooth width. Applying these changes to the machine designs would make them look more like the high torque density design

from the coupled EM/thermal optimization, also shown in Fig. 8-20. Hence, the results from the sensitivity analysis are quite useful in that they can provide some guidance for improving the performance of the machine designs.

#### **8.4 Experimental Thermal Coefficient Estimation**

So far, the thermal coefficients used for setting up the boundary conditions for the thermal component of the coupled EM/thermal model are defined by evaluating empirical equations found in the literature for the given cooling conditions. However, manufacturing techniques and variations can play a significant role in determining the values of these coefficients in actual machines. The accuracy of the thermal model could be improved if these coefficients are provided by manufacturers, predicted via computational fluid dynamics (CFD) analysis, or estimated from application-specific experiments.

A prototype 30 kW (continuous) 10-pole, 12-slot FSCW surface PM machine was designed and built for a traction motor application based on the U.S. DRIVE specifications discussed in Chapter 7. It has an active mass of 27.8 kg including the stator and rotor electromagnetic assemblies [103]. It is mounted in a water jacket with machine ends air-cooled by an external blower (Fig. 8-21). The average air velocity was measured close to the end windings to be 7.46 m/sec using an anemometer.



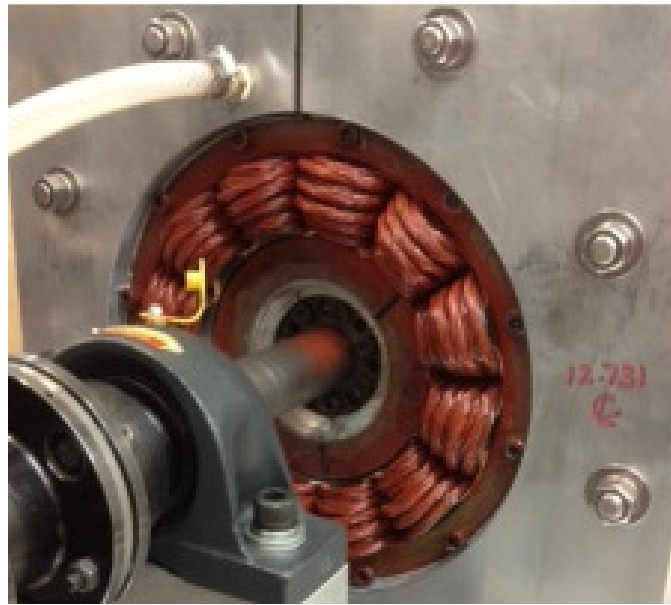


**Fig. 8 - 21: Prototype FSCW surface PM machine mounted on a water jacket**

A dc power supply has been used to heat up the stationary wye-connected machine with the phase A winding terminal connected to one end of the power supply, and the phase B and C terminals attached to the other end. The cooling pump for the water jacket and the blower are both activated. The dc power source supplies the windings with constant current, generating winding losses that cause the machine temperatures to rise.

The temperatures in different parts of the machine have been measured after steady-state thermal conditions were reached. The tests have been carried out with several current (i.e., winding loss) values, and the results are shown in Fig. 8-22. The locations of the nine thermocouples are: 1) TC1 is placed between the side of a stator tooth and winding at half the radial length of the tooth; 2) TC2 is placed between the side of a stator tooth and winding at the junction of the tooth shaft and tooth tip; 3) TC3 is placed at the interface between the windings in one slot; 4) TC4 is mounted on the outer surface of the stator yoke; 5) TC5 is mounted on the stator tooth shaft at the end of the stack, under the end winding; 6) TC6 is mounted on the outside of the end windings; 7) TC7 is mounted on the inside curvature of an end winding; 8)

TC8 is embedded inside the stator yoke by drilling a small hole axially into yoke behind one of the stator teeth; and 9) TC9 is embedded inside a stator tooth shaft by drilling a small hole axially into the stator tooth approx. halfway along the tooth shaft length.

A 3D thermal FE model has been prepared based on the dimensions of the prototype machine. The temperatures at these thermocouple locations are predicted using static thermal FE analysis for five values of winding losses, and the mean-squared error  $F$  between the FE analysis results and experimental measurements for all nine thermocouples have been evaluated as follows:

$$F = \frac{1}{5} \sum_{p=1}^5 \left( \frac{1}{9} \sum_{q=1}^9 (T_{mpq} - T_{fpq})^2 \right) \quad (38)$$

where  $p$  is the index representing each winding loss operating condition,  $q$  is the corresponding index for each thermocouple location,  $T_m$  is the temperature measured by the thermocouple, and  $T_f$  is the temperature predicted from FE analysis.

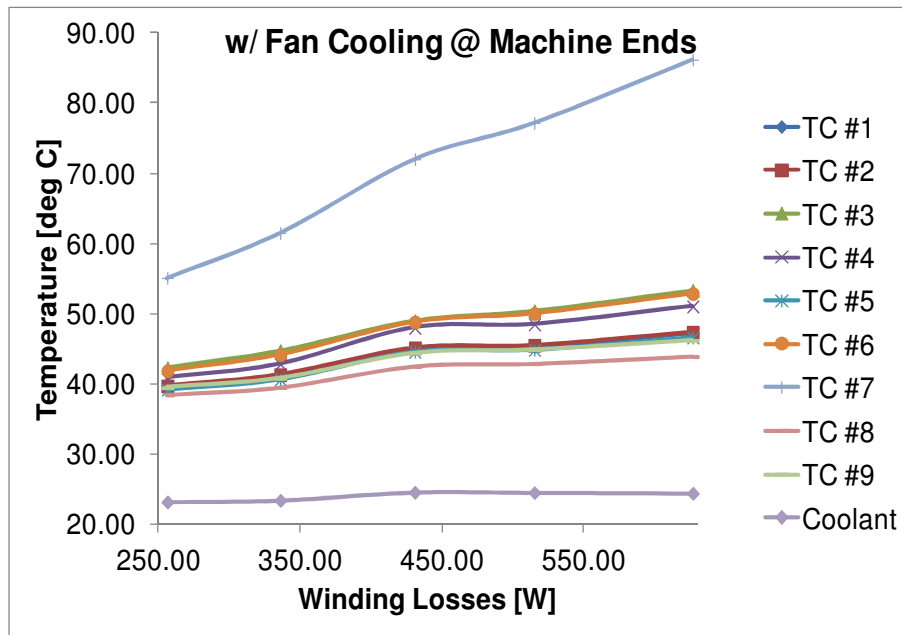


Fig. 8 - 22: Measured temperatures with fan cooling on machine ends

**Table 8 - 4: Comparison of Thermal Coefficient Predicted from Analytical Model and Experimental Test**

<b>Thermal Coefficients</b>	<b>Calculated from (14)</b>	<b>Estim. from Thermocouples</b>
Heat Transfer Coefficient of the Forced Convection Air Cooling [W/(m <sup>2</sup> C)]	87.8	109.6

The measured temperatures at the nine thermocouple locations are plotted in Fig. 8-22 as a function of the stator winding losses for operation with both the stator water jacket pump and the end winding blower activated. The heat transfer coefficient associated with the forced convection at the machine ends has been estimated by finding the value that delivers the lowest mean-squared error for the thermocouple measurements. Table 8-3 shows that this value is close to the result calculated from (14) after substituting the air velocity value noted above,  $v_1 = 7.46$  m/sec.

It was not possible to carry out this same procedure for the thermal coefficient at the interface between the stator core and the water jacket fixture because of a known problem with the experimental equipment set-up. More specifically, the outer diameter of the stator laminations is smaller than the inner bore of the water jacket fixture by 2.5 mm, making it very difficult to achieve a tight mechanical fit between the fixture and the stator, despite the split in the water jacket fixture (visible in Fig. 8-21) and available tightening bolts. The absence of a tight mechanical fit around the outer periphery of the stator core reduces the heat transfer coefficient at this interface to unacceptably low values that have very little meaningful value for this investigation.

## **8.5 Conclusion**

The issue of mesh size for the machine EM FE model has been investigated by comparing the predicted machine performances from coarse mesh, medium mesh, and fine mesh models with

the TD Design. The results indicate that the FE model with a coarse mesh is sufficient to predict the torque production of a machine, which can also lead to a reduction in computation time. However, finer mesh size is required for accurately estimating the machine's electromagnetic losses.

Scatter plots and regression analysis methods were applied to evaluate the sensitivities of the coupled EM/thermal machine design optimization to the machine's geometric parameters and thermal coefficients. Scatter plots provide a direct qualitative visual indication of the sensitivities to these studied parameters, while regression analysis provides a way to quantitatively evaluate the parameter sensitivity by calculating partial derivative values from the regression function. In addition, results from the sensitivity analysis are valuable in that they suggest design changes to improve the performance of the machines.

Experiments have been performed to estimate the forced convection heat transfer coefficient used in the thermal model. Experimental validation helps build confidence in the results of the FE thermal analysis, and it represents a meaningful first step towards providing experimental verification of the coupled EM/thermal machine model.

## **Chapter 9: Conclusions, Contributions and Future Work**

### **9.1 Conclusions**

This research program has investigated the optimization and coupled EM/thermal modeling techniques for electric machines, including EM machine design optimization in an HTC environment, a coupled EM/thermal machine model, coupled EM/thermal machine design optimization for steady-state operation, and coupled EM/thermal machine design optimization for transient operation. Key conclusions derived from this study are summarized in the following sections.

#### **9.1.1 Electromagnetic Machine Design Optimization Using High-Throughput Computing**

An iterative FE-based machine design optimization algorithm based on differential evolution was implemented in a high-throughput computing (HTC) environment. The software has been applied to optimize a 30 kW (continuous) FSCW-SPM machine for high torque density (TD Design) using both an available HTC environment (Project Condor) and a single computer of the same type used in the HTC system. Commercially-available FE analysis software was used for these calculations.

The two optimization runs converged to the same optimal design, which exhibited a mass reduction of 25.7% compared to the baseline machine design. The comparison shows that the parallel HTC environment achieves a reduction in the computational time by a factor of 28.7 compared to the single computer. This result shows that the computational time of FE-based machine design optimization problems can be significantly reduced using currently available HTC resources. Moreover, after breaking down all the time components during the optimization,

a dedicated HTC environment is estimated to be capable of raising the acceleration factor to approx. 80 for the considered case with 85 designs in each generation.

In the interest of exploring alternative formulations of the objective function, the optimization was also executed to minimize the material cost (TPD Design), and to maximize the efficiency (Eff. Design), in addition to the case of optimizing the machine torque density (TD Design) described above. Comparison results among the three optimal designs suggest that the choice of torque density as the target for the objective function was a good one, helping to enhance several other important performance metrics for the machine besides its torque density. The operating point at which the machine design is optimized was chosen to be the corner point, since it guarantees that the optimal machine will be capable of delivering the required torque/power at any other operating point along the torque-speed envelope.

Since the IPM machine configuration is widely adopted by hybrid and battery electric vehicles, the application of the iterative FE-based machine design optimization algorithm was extended to IPM machines. Two ways of dealing with the current angle are demonstrated. In one approach, the current angle for each candidate design was determined using an MTPA angle search module, while in the other method, it was set as a variable in the optimization. The comparison between the two methods indicates that setting the excitation current angle as an input variable for the optimization can be used to replace the MTPA angle search module, leading to a significant reduction in computational effort and time.

### 9.1.2 Coupled Electromagnetic/Thermal Machine Model

A coupled EM/thermal model for electric machines based on FE analysis has been developed. The electromagnetic and thermal analyses are linked via temperature-dependent material properties and machine losses. The characteristics of the coupled model have been studied by using it to analyze three 30 kW (continuous) surface PM machines under various current density conditions.

The results of these coupled model analytical tests show that two EM/thermal iterations are sufficient to converge to self-consistent machine performance results in the majority of the considered cases. Compared to the EM-only model, the coupled EM/thermal model has the advantage of being able to recognize winding insulation maximum thermal limits and the onset of irreversible magnet demagnetization during the design stage.

This work has also demonstrated that the coupled EM/thermal model can be used to efficiently determine the maximum current density that the machine can sustain under steady-state operating conditions without exceeding temperature limits for the insulation or inducing irreversible magnet demagnetization. For the same cooling conditions, the maximum allowable current density varies significantly among the three different types of machine designs that were investigated. Similarly, irreversible demagnetization occurs at different magnet temperatures for the different types of machine designs.

This investigation has clearly demonstrated that: 1) the adoption of a pre-determined current density as a surrogate for the imposition of a temperature limit on the winding temperature is oversimplified in most cases; and 2) avoiding demagnetization is more complicated than simply setting a maximum temperature for the rotor magnets.

The issue of mesh size selection for the machine EM FE model was investigated. The results indicate that forming the FE model with a coarse mesh is sufficient to predict the torque production of a machine. This is significant since adoption of a coarse mesh can lead to a reduction in FE computation time. However, a finer mesh size is required for estimating machine losses with high accuracy.

The solution sensitivities to the machine geometric parameters and thermal coefficients associated with the coupled EM/thermal machine design optimization were evaluated, and these results can provide helpful guidance for improving the performance of the resulting machine designs. In addition, experiments were performed to empirically evaluate the thermal coefficients used in the thermal model. The availability of these measured coefficients represents a meaningful first step towards providing experimental verification of the coupled EM/thermal machine model.

### **9.1.3 Coupled EM/Thermal Machine Design Optimization for Steady-State Operation**

Computationally-efficient mathematical techniques have been applied to accelerate the process of determining the maximum allowable current density for a PM synchronous machine design that respects both the stator winding insulation thermal limit and the rotor magnet demagnetization threshold. More specifically, a quadratic relationship has been identified between the maximum winding temperature and the continuous current density, indicating that Müller's method is suitable for locating the maximum current density for the winding insulation limit. In addition, the linear relationship between the demagnetization ratio and current density has led to the adoption of a linear extrapolation method for determining the threshold current density when demagnetization begins.



The coupled EM/thermal model was integrated into the previously-developed optimization program. The optimization software was applied to design a 30 kW (continuous) FSCW-SPM machine for maximum torque density using a multi-core desktop computer. The resulting optimal design exhibits a 35% reduction in its active mass compared to the design using EM-only optimization.

An artificial neural network was subsequently incorporated into the optimization. The EM-only model and the maximum current density predicted using the trained network are sufficient to replace the original coupled EM/thermal model that is used during the initial training iterations, leading to a significant reduction in computational effort and time.

#### **9.1.4 Coupled EM/Thermal Machine Design Optimization for Operation with Transient Power Pulse Intervals**

This section demonstrates techniques for achieving a coupled EM/thermal analysis of electric machines using commercial FE software for both steady-state and transient operation. For steady-state conditions, iteration between the EM and thermal analyses was used to converge on solutions that are consistent with the temperature-dependent properties of the machine materials. The work has been extended to address the challenges imposed by applications that include transient operation at torque/power levels much higher than those in steady-state conditions.

A method to couple the EM FE analysis with transient thermal FE analysis was developed. A linear relationship has been identified between the machine loss components and the corresponding machine temperatures, leading to the development of a computationally-efficient technique for updating the loss profile using linear interpolation.

For a given machine design with a pre-set initial current density, a similar technique was developed to determine the winding's maximum current density for transient operation (peak

power) that will avoid exceeding the maximum winding temperature during the transient event. This was accomplished using a combination of Müller's method and linear extrapolation.

For a given machine design with a specified peak/continuous power requirement, a method was developed to determine the maximum initial steady-state current density that will allow the machine to deliver its peak power pulses without exceeding the maximum allowable winding temperature or inducing irreversible demagnetization in the rotor magnets. These techniques can be conveniently extended to cases where the temperature of the magnets or some other machine component becomes the key thermal constraint.

The transient version of the coupled EM/thermal model was integrated into the previously developed optimization program. The resulting optimal design exhibits a 6% increase in its active mass compared to the design using the static version of the coupled EM/thermal optimization, in exchange for the capability of operating at peak power conditions for short periods of time. An artificial neural network was incorporated into the optimization, resulting in a computation time that was five times shorter than the same optimization without the ANNs.

An optimization routine that is capable of efficiently optimizing electric machine designs according to the complete set of US DRIVE specs has been proposed based on this transient version of the coupled EM/thermal machine model. The effectiveness of the optimization routine is evaluated by applying it to the three candidate surface PM machine designs: the TD Design, TPD Design, and Eff. Design.

## **9.2 Contributions**

During the course of this research program, six key technical contributions were made that are summarized in the following subsections. Each of these contributions is accompanied by some highlighted details that summarize the implementation of these contributions.

### **9.2.1 Electromagnetic Machine Design Optimization Based on FE Analysis in a High-Throughput Computing Environment**

An iterative FE-based machine design optimization algorithm based on differential evolution has been successfully implemented in the high-throughput computing (HTC) environment available at UW-Madison (Project Condor) with the assistance of the UW Condor Team and the JSOL Corporation.

- The software has been applied to optimize a 30 kW (continuous) FSCW-SPM machine for high torque density. The optimal design exhibits a mass reduction of 25.7% compared to the baseline machine design.
- Tests comparing the computational speeds achieved using the same optimization software with the HTC resources and a single computer have demonstrated a major reduction of the computational time by approx. 30:1 using the HTC approach.

### **9.2.2 Coupled Electromagnetic/ Thermal Machine Model**

A 2D electromagnetic FE model has been successfully coupled with a 3D thermal FE model using temperature-dependent material properties.

- The convergence properties for this coupled EM/thermal model have been investigated using machine design optimization tests with three different performance criteria (maximum torque density, minimum material cost, and maximum efficiency) under

various current density conditions. These tests have shown that two EM/thermal iterations are typically enough to achieve convergence of the electromagnetic and thermal solutions.

- The electromagnetic FE model alone has been compared with the coupled EM/thermal FE model in terms of achievable torque production. This investigation has shown that the EM/thermal coupled model is preferred since it can produce accurate results that take into account material limits (i.e., the winding insulation thermal limit and the demagnetization constraint).

### **9.2.3 Coupled EM/Thermal Machine Design Optimization for Steady-State Operation**

For a given machine design operating under steady-state conditions, a new computationally-efficient method has been developed for using the coupled EM/thermal model to rapidly determine the maximum current density that maintains the winding temperature within a preset maximum limit while avoiding demagnetization of the rotor magnets. This static version of the coupled EM/thermal method has been integrated into the machine design optimization program with application of artificial neural network (ANN).

- The problem of identifying the maximum current density at which the winding temperature reaches the insulation's maximum thermal limit has been formulated as a root-finding problem. Müller's method has been determined to be the most suitable alternative for minimizing the number of coupled EM/thermal solutions that are required to find this maximum current density value. This is a new contribution of this research program, representing the first time that Müller's method has been implemented in this class of problem to accelerate the convergence process for locating the maximum current density achievable within the winding insulation thermal limit.

- An investigation of the machine magnet demagnetization characteristics has revealed a linear relationship between the demagnetization ratio and the stator winding current density. This has led to the development of a linear extrapolation method that can be used to rapidly find the maximum winding current density when demagnetization first begins to occur.
- The combination of these two techniques has led to the development of an integrated procedure for finding the maximum current density in a given machine design operating under steady-state conditions—one that that will prevent the machine from exceeding its maximum winding insulation temperature and avoid irreversible demagnetization.
- The static version of the coupled EM/thermal machine model has been integrated into the previously developed optimization program. The resulting optimal design exhibits a 35% reduction in its active mass compared to the design using EM-only optimization.
- An ANN has been incorporated into the differential evolution based optimization. It is trained to learn the relationships between the machine design parameters and the maximum current densities by using the results of the coupled EM/thermal model during an initial series of machine design iterations. Then the trained ANN is used to rapidly predict the maximum current density for new parameter sets of machine design parameters, leading to a significant reduction in computational effort and time. Based on the results of the literature study, this is a new contribution representing the first time that an ANN has been applied in this type of problem to accelerate the computation time during the machine design optimization process.

### 9.2.4 Coupled EM/Thermal Machine Design Optimization for Operation with Transient Peak Power Intervals

For a machine designed to operate under demanding transient conditions that include intervals of high torque/current demand, a complementary method has been successfully developed for using the coupled EM/thermal model to rapidly determine the machine's maximum current density that will maintain the maximum winding temperature within a preset limit and avoiding demagnetization of the rotor magnets. This method takes advantage of some of the same techniques that are used in the steady-state version summarized in the preceding subsection, but incorporates key additional steps that are necessary to address the transient periods of high torque production and their resulting impact on winding temperature rise. The transient version of the coupled EM/thermal model has also been integrated into the optimization program including the application of an ANN.

- A novel method to couple the EM FE analysis with the transient thermal FE analysis has been developed to accelerate the machine thermal analysis by identifying a linear relationship between the machine loss components and the corresponding machine temperatures. The resulting linear relationship has been used for the first time to develop a new technique for updating the loss profile using linear interpolation.
- This method uses some of the same root-finding techniques based on Müller's method and a linear extrapolation technique to efficiently determine the maximum current density that will prevent the stator winding from overheating and the rotor magnets from demagnetizing, as summarized in Section 9.2.3. However, these techniques have been adapted to account for the transient nature of the torque production during short periods.

- For a given machine design with a specified peak/continuous power profile, a new method has been developed to find the maximum permissible initial current density for continuous operation that will allow the machine to deliver its peak torque pulses without exceeding the maximum allowable winding temperature or inducing irreversible demagnetization in the rotor magnets. Based on the results of the literature study, this is a new contribution representing the first time that this technique has been adopted to accelerate the process of finding the maximum current density for this type of transient thermal condition in an electric machine.
- The transient version of the coupled EM/thermal model has been integrated into the previously developed optimization program. The resulting optimal design exhibits a 6% increase in its active mass compared to the design produced with the static version of coupled EM/thermal optimization. This extra design margin is necessary in order to enable the machine to operate at peak torque conditions for short periods of time.
- Artificial neural network techniques have been incorporated into the optimization using the same approach as for the steady-state case. For the transient case, the incorporation of the ANN technique reduced the computational effort and time by a factor of 5 compared to the baseline optimization in which each candidate design is evaluated by the complete coupled EM/thermal model. As noted in Section 9.2.3, this is a significant new contribution resulting from this research program.

### **9.2.5 Generalization of Machine Design Optimization Techniques**

This research program has demonstrated that the FE-based machine design optimization techniques developed based on FSCW-SPM machines can also be applied to other machine

configurations such as the IPM machine. More complicated objective functions and performance specifications/constraints have been successfully incorporated into the analysis in order to make the coupled EM/thermal machine design optimization program more valuable for practical engineering problems.

- The application of the iterative FE-based machine design optimization algorithm has been extended to IPM machines. The software has been successfully applied to optimize the design of a 30 kW (continuous) IPM machine with distributed windings for high torque density.
- Two approaches for identifying the best current angle associated with each candidate IPM machine have been investigated and demonstrated. In one approach, the current angle for each candidate design was determined using an MTPA angle search module for each candidate design, while in the other approach, the current angle was included as an additional variable in the optimization. The results of the comparison have indicated that the latter approach based on including the current angle as an additional optimization variable requires less execution time to accomplish the same objective of identifying the optimum current angle for each candidate machine. Based on the literature review that was carried out, the implementation and comparison of these two methods for handling the choice of excitation current angle for the IPM machine design optimization is a new contribution that was carried out for the first time during this research program.
- An optimization routine capable of efficiently optimizing electric machine designs to meet the demanding U.S. DRIVE traction motor specifications has been presented, based on the coupled EM/thermal model. The effectiveness of the optimization routine has been evaluated by applying it to the three candidate surface PM machine designs, confirming



the promising features of this approach for handling challenging machine design problems that include complicated combinations of performance specifications and constraints. This is a new contribution of the research program, representing the first time that a coupled EM/thermal analysis program of this type has been used to guide the search for an optimal PM machine design in the presence of such a complicated set of machine performance requirements, operating points, and performance constraints.

### **9.2.6 Parameter Sensitivity**

The sensitivities of the machine design optimization results to mesh size, machine geometric parameters, and thermal coefficients associated with the coupled EM/thermal machine model have been investigated, yielding valuable insights into the relative importance of key machine dimensions and material characteristics for meeting the specified performance requirements.

- The mesh size of the machine EM FE model has been studied by comparing the predicted machine performance resulting from that application of coarse mesh, medium mesh, and fine mesh models to the TD Design. The results indicate that an FE model with coarse mesh is sufficient to predict the torque production of a machine, opening a path for reducing the computation time. However, a finer mesh size is required for estimating the machine losses with high accuracy. This tradeoff makes it necessary to apply engineering judgment to choose the appropriate mesh size at different stages in the optimization process.
- 600 input data sets consisting of machine geometric parameters and thermal coefficients and the same number of output data sets consisting of predicted torque from coupled EM/thermal analysis were collected using the Monte Carlo method. Scatter plots were

generated to provide a valuable visual indication of both the absolute and relative sensitivities of these studied parameters for the particular machine design problem under investigation.

- Regression analysis was also used to evaluate the parameter sensitivity quantitatively by extracting the partial derivative values from the regression function. The results from the sensitivity analysis are valuable because they provide insight into the relative effectiveness of alternative design modifications for improving the performance of the machine designs.
- Experiments have been performed using an available 30 kW FSCW-SPM machine to evaluate the thermal coefficients used in the thermal model. The availability of this empirical data increases confidence in the results of the FE thermal analysis, and it also represents a meaningful first step towards providing experimental verification of the coupled EM/thermal machine model.

### **9.3 Suggestions for Future Work**

Some suggestions for extending and expanding this machine design optimization research program are presented in this section.

#### **A. Implementation of the Coupled EM/Thermal Machine Design Optimization in High-Throughput or High-Performance Computing Environments**

The computational time will be significantly reduced by implementing the coupled EM/thermal machine design optimization program in either a high-throughput or high-performance computing (HPC) environment. This proposed effort represents a logical extension of the current work since it combines the impact of two of the major technical contributions of this research program. If successful, the accelerated computation made

possible by the HTC or HPC facilities, combined with the acceleration achieved using the ANN technique, promises to reduce the total machine design optimization time by more than two orders of magnitude ( $>100$ ) compared to what is achievable using a baseline single PC.

#### **B. Improvement of the Accuracy of the EM FE Model with Consideration for PWM Excitation and Proximity Effects**

Pure sinusoidal current excitation was assumed in the EM component of the coupled machine model. However, the impact of PWM excitation was not taken into account, which can cause errors in the loss prediction. In addition, proximity effects play an important role in estimating winding losses, especially for machines that are required to operate at high speeds with high excitation frequencies. Therefore, the accuracy of the EM FE model can be improved by incorporating the impact of PWM excitation and proximity effects into the loss calculations.

#### **C. Integration of the Thermal (Cooling) Design into the Coupled EM/Thermal Machine Design Optimization Program**

The coupled EM/thermal machine design optimization implemented in this research was based on a fixed thermal management configuration with cooling characteristics that were assumed to be constant. But an electrical machine is heavily constrained by the limitations imposed by the thermal management system. As a result, comprehensive optimization of an electrical machine requires that its electromagnetic and thermal management (cooling) design must be optimized simultaneously.

#### **D. Implementation of Multi-Physics Machine Design Optimization with the Addition of Structural Analysis**

In this study, both the rotor magnet banding thickness for the SPM machine, and the bridge and post thicknesses for the IPM machine were determined based on empirical

values. The structural integrity of these key structural dimensions not been verified. In addition, the friction and windage losses were not included as heat sources for the thermal model, leading to errors in the resulting temperature prediction. Moreover, the vibration and acoustic noise generated by the electric machines have not been evaluated. Therefore, structural analysis should be incorporated into the machine design process in order to achieve the ultimate goal of multi-physics machine design optimization. The resulting integrated optimization process must reflect the many interactions between the electromagnetic, thermal and structural design features that are known to exist but are extremely difficult to rigorously incorporate into a single integrated motor design optimization procedure.

## Bibliography

- [1] Y. Duan, R.G. Harley, T.G. Habetler, "A useful multi-objective optimization design method for PM motors considering nonlinear material properties," in Proc. of *2009 IEEE Energy Conversion Congress and Exposition (ECCE 2009)*, San Jose, pp. 187-193.
- [2] P.D. Pfister, Y. Perriard, "Very-high-speed slotless permanent-magnet motors: analytical modeling, optimization, design, and torque measurement methods," *Industrial Electronics, IEEE Transactions*, Vol.57, Issue. 1, pp. 296-303, Jan., 2010.
- [3] G. Pellegrino, F. Cupertino, "FEA-based multi-objective optimization of IPM motor design including rotor losses," in Proc. of *2010 IEEE Energy Conversion Congress and Exposition (ECCE 2010)*, Atlanta, pp. 3659-3666.
- [4] C.C. Chan, K.T. Chau, "Design of electrical machines by the finite element method using distributed computing", *Computers in Industry*, vol. 17, pp. 367-374, 1991.
- [5] <http://research.cs.wisc.edu/condor/>
- [6] K. Idir, L. Chang, H. Dai, "A neural network-based optimization approach for induction motor design," in Proc. of *1996 IEEE Canadian Conference on Electrical and Computer Engineering (CCECE 1996)*, pp. 951-954.
- [7] O.A. Mohammed, D.C. Park, F.G. Uler, "Design optimization of electromagnetic devices using artificial neural networks," in Proc. of *the Second International Forum on Application of Neural Networks to Power Systems (ANNPS ' 93)*, pp. 361-364.
- [8] M. Schoning, E. Lange, K. Hameyer, "Development and validation of a fast thermal finite element solver," in *Proc. of 2008 Intl. Conf. on Elec. Machines (ICEM ' 08)*, Vilamoura, Portugal, Sept. 2008, pp. 1-5.
- [9] M. Schoning, "Application of automated electrical machine design with differential evolution techniques," in *Proc. of 2011 IEEE International Electric Drives Production Conference (EDPC ' 11)*, Nuremberg, Germany, Sept. 2011, pp. 221-224.
- [10] W. Cao, B.C. Mecrow, G.J. Atkinson, J.W. Bennett, "Overview of electric motor technologies used for more electric aircraft," *IEEE Trans. on Indus. Electronics*, vol. 59, pp. 3523-3531, Sept. 2012.
- [11] J. Chun, J. Lim, H. Jung, J. Yoon, "Optimal design of synchronous motor with parameter correction using immune algorithm," *IEEE Trans. on Energy Conversion*, vol. 14, no.3, pp. 610-615, Sept. 1999.

- [12] R. Wrobel, J. Goss, A. Mlot, P. Mellor, "Design considerations of a brushless open-slot radial-flux PM hub motor," *Proc. 2012 IEEE Ener. Conv. Congr. & Expo (ECCE '12)*, Raleigh, Sep. 2012, pp. 3678-85.
- [13] J. Wang, D. Howe, "Design optimization of radially magnetized, iron-cored, tubular permanent-magnet machines and drive systems," *IEEE Trans.on Magnetics*, vol. 40, no.5, pp. 3262-3277, Sept. 2004.
- [14] S.A. Semidey, Y. Duan, J.R. Mayor, R.G. Harley, T.G. Habetler, "Optimal electromagnetic-thermo-mechanical integrated design candidate search and selection for surface-mount permanent-magnet machines considering load profiles," *IEEE Transactions on Industry Applications*, vol. 47, no. 6, pp. 2460-2468, Nov. 2011.
- [15] A. Sari, F. Dubas, C. Espanet, "Multi-objective design optimization of PMSM for PEM fuel cell air-circuit with PSO algorithms," in Proc. of *2009 IEEE International Electric Machines and Drives Conference (IEMDC '09)*, Miami, pp. 1360-1367.
- [16] L. Chedot, G. Friedrich, J. Biedinger, P. Macret, "Integrated starter generator: the need for an optimal design and control approach. application to a permanent magnet machine," *Industry Applications, IEEE Transactions*, Vol. 43, Issue 2, pp. 551-559, Mar., 2007.
- [17] A.H. Wijenayake, J.M. Bailey, P.J. McCleer, "Design optimization of an axial gap permanent magnet brushless DC motor for electric vehicle applications," in Proc. of *1995 IEEE Thirtieth IAS Annual Meeting (IAS '95)*, Orlando, pp. 685-692.
- [18] S. Huang, M. Aydin, T.A. Lipo, "Torque quality assessment and sizing optimization for surface mounted permanent magnet machines," in Proc. of *2001 IEEE Thirty-Sixth IAS Annual Meeting (IAS '01)*, Chicago, pp. 1603-1610.
- [19] M. Cosovic, S. Smaka, I. Salihbegovic, S. Masic, "Design optimization of 8/14 switched reluctance machine for electric vehicle," in Proc. of *2012 IEEE XXth International Conference on Electrical Machines (ICEM 2012)*, Marseille, pp. 2654-2659.
- [20] D. Hong, B. Woo, D. Koo, D. Kang, "Optimum design of transverse flux linear motor for weight reduction and improvement thrust force using response surface methodology," *Magnetics, IEEE Transactions*, Vol. 44, Issue 11, pp. 4317-4320, Nov., 2008.
- [21] F. Messine, B. Nogarede, J. Lagouanelle, "Optimal design of electromechanical actuators: a new method based on global optimization," *Magnetics, IEEE Transactions*, Vol. 34, Issue 1, pp. 299-308, Jan., 1998.
- [22] A.M. Omekanda, "Robust torque and torque-per-inertia optimization of a switched reluctance motor using the Taguchi methods," *Industrial Applications, IEEE Transactions*, Vol. 42, Issue 2, pp. 473-478, Mar., 2006.

- [23] E.B. Sulaiman, T. Kosaka, N. Matsui, "Design study and experimental analysis of wound field flux switching motor for HEV applications," in Proc. of *2012 IEEE XXth International Conference on Electrical Machines (ICEM 2012)*, Marseille, pp. 1269-1275.
- [24] J. Tapia, J. Pyrhonen, J. Puranen, S. Nyman, P. Lindh, "Optimal design of large permanent magnet synchronous generators," *Magnetics, IEEE Transactions*, Vol. PP, Issue 99, pp. 1-9, 2012.
- [25] X. Wang, P.C. Roberts, R.A. McMahon, "Optimization of BDFM stator design using an equivalent circuit model and a search method," in Proc. of *2006 IET 3rd International Conference on Power Electronics, Machines and Drives (PEMD 2006)*, Dublin, pp. 606-610.
- [26] X. Liu, W. Xu, "A global optimization approach for electrical machine designs," in Proc. of *2007 IEEE Power Engineering Society General Meeting (PES 2006)*, Tempa, pp. 1-8.
- [27] M.B.B. Sharifian, H.V. Kalankesh, M.R. Feyzi, "Multi-objective optimization of induction motor slot design using finite element method," in Proc. of *2003 IEEE 10th International Conference on Electronics, Circuits and Systems (ICECS 2003)*, Sharjah, pp. 1308-1311.
- [28] K. Idir, L. Chang, H. Dai, "Error-based global optimization approach for electric motor design," *Magnetics, IEEE Transactions*, Vol. 34, Issue 5, pp. 2861-2864, Sep., 1998.
- [29] M. Dabrowski, A. Rudenski, "Application of evolutionary algorithms for optimization of electric machines," in Proc. of *2006 6th International Conference of Computational Electromagnetics (CEM 2006)*, pp. 1-2.
- [30] D. Fodorean, L. Idoumghar, L. Szabo, "Motorization for electric scooter by using permanent magnet machines optimized based on hybrid metaheuristic algorithm," *Vehicular Technology, IEEE Transactions*. Vol. PP, Issue 99, pp. 1-11.
- [31] D. Ilea, M.M. Radulescu, F. Gillon, P. Brochet, "Multi-objective optimization of a switched reluctance motor for light electric traction applications," in Proc. of *2010 IEEE Vehicle Power and Propulsion Conference (VPPC 2010)*, Lille, pp. 1-6.
- [32] Y. Oh, T. Chuang, M. Kim, H. Jung, "Optimal design of electric machine using genetic algorithms coupled with direct method," *Magnetics, IEEE Transactions*. Vol. 35, Issue 3, pp. 1742-1745, May, 1999.
- [33] O.A. Mohammed, "GA optimization in electric machines," in Proc. of *1997 IEEE International Electric Machines and Drives Conference (IEMDC '97)*, Milwaukee, pp. TAI/2.1-TAI/2.6.
- [34] V.P. Sakhivel, S. Subramanian, "Using MPSO algorithm to optimize three-phase squirrel cage induction motor design," in Proc. of *2011 IEEE International Conference on*

*Emerging Trends in electrical and Computer Technology (ICETECT 2011)*, Nagercoil, pp. 261-267.

- [35] C. Kan, X. Wang, F. Xiong, J. Zhang, T. Wu, H. Tang, "Design optimization of tooth-harmonic brushless doubly-fed machine," in Proc. of *2008 IEEE International Conference on Electrical Machines and Systems (ICEMS 2008)*, Wuhan, pp. 4272-4276.
- [36] A. Deihimi, "Design optimization of switched reluctance machine operating under voltage PWM control strategy," in Proc. of *2009 Second International Conference on Computer and electrical Engineering (ICCEE ' 09)*, Dubai, pp. 522-526.
- [37] T.D. Nguyen, V. Lanfranchi, C. Doc, J.P. Vilain, "Comparison of optimization algorithms for the design of a brushless DC machine with travel-time minimization," in Proc. of *2009 IEEE 8th International Symposium on Advanced Electromechanical Motion Systems & Electric Drives Joint Symposium (ELECTROMOTION 2009)*, Lille, pp. 1- 6.
- [38] L. Chen, J. Wang, P. Lombard, P. Lazari, V. Leconte, "Design optimization of permanent magnet assisted synchronous reluctance machines for electric vehicle applications," in Proc. of *2012 IEEE XXth International Conference on Electrical Machines (ICEM 2012)*, Marseille, pp. 2647-2653.
- [39] Y. Duan, R.G. Harley, T.G. Habetler, "Comparison of particle swarm optimization and genetic algorithm in the design of permanent magnet motors," in Proc. of *2009 IEEE 6th International Power Electronics and Motion Control Conference (IPEMC ' 09)*, Wuhan, pp. 822-825.
- [40] O. Wen, D. Zarko, T.A. Lipo, "Permanent magnet machine design practice and optimization," in Proc. of *2006 IEEE 41st IAS Annual Meeting (IAS ' 06)*, Tampa, pp. 1905-1911.
- [41] D. Zarko, D. Ban, T.A. Lipo, "Design optimization of interior permanent magnet (IPM) motors with maximized torque output in the entire speed range," in Proc. of *2005 IEEE European Conference on Power Electronics and Applications (EPE 2005)*, Dresden, pp. P.1-P.10.
- [42] Y. Duan, D.M. Ionel, "Non-linear scaling rules for brushless PM synchronous machines based on optimal design studies for a wide range of power ratings," in Proc. of *2012 IEEE Energy Conversion Congress and Exposition (ECCE 2012)*, Raleigh, pp. 2334-2341.
- [43] Y. Duan, D.M. Ionel, "A review of recent development in electrical machine design optimization method with a permanent magnet synchronous motor benchmark study," in Proc. of *2011 IEEE Energy Conversion Congress and Exposition (ECCE 2011)*, Phoenix, pp. 3694-3701.



- [44] G.Y. Sizov, P. Zhang, D.M. Ionel, N.A.O. Demerdash, M. Rosu, "Automated bi-objective design optimization of multi-MW direct-drive PM machines using CE-FEA and differential evolution," in *Proc. of 2011 IEEE Energy Conversion Congress and Exposition (ECCE 2011)*, Phoenix, pp. 3672-3678.
- [45] G.Y. Sizov, D.M. Ionel, N.A.O. Demerdash, "Modeling and parametric design of permanent-magnet AC machines using computationally efficient finite-element analysis," *Industrial Electronics, IEEE Transactions*. Vol. 59, Issue 6. pp. 2403-2413, June, 2012.
- [46] D. Lee, S. Lee, J. Kim, C. Lee, S. Jung, "Intelligent memetic algorithm using GA and guided MADS for the optimal design of interior PM synchronous machine," *Magnetics, IEEE Transactions*. Vol. 47, Issue 5. pp. 1230-1233, May, 2011.
- [47] K. Yamazaki, H. Ishigami, A. Abe, "An adaptive finite element method for minor shape modification in optimization algorithms," *Magnetics, IEEE Transactions*. Vol. 44, Issue 6. pp. 1202-1205, June, 2008.
- [48] A. Ma, X. Jiang, "Application of RBFEM in the fast design optimization electric field," in *Proc. of 2008 IEEE International Conference on Electrical Machines and Systems (ICEMS 2008)*, Wuhan, pp. 384-386.
- [49] Y. Okamoto, Y. Tominaga, S. Sato, "Topological design for 3-D optimization using the combination of multistep genetic algorithm with design space reduction and nonconforming mesh connection," *Magnetics, IEEE Transactions*. Vol. 48, Issue 2. pp. 515-518, Feb., 2012.
- [50] J. Lahteenmaki, "Optimization of high-speed motors using a genetic algorithm," in *Proc. of 1997 IEEE Eighth International Conference on Electrical Machines and Drives*, Cambridge, pp. 26-30.
- [51] R. Bhuvaneshwar, V.P. Sakthivel, S. Subramanian, G.T. Bellarmine, "Hybrid approach using GA and PSO for alternator design," in *Proc. of 2009 IEEE Southeastcon Conference*, pp. 169-174.
- [52] K.S. Chai, C. Pollock, "Using genetic algorithms in design optimization of the flux switching motor," in *Proc. of 2002 IEEE Power Electronics, Machines and Drives Conference (PEMD 2002)*, pp. 540-545.
- [53] D. Bochnia, W. Hofmann, H. Hupe, "Design optimization of permanent magnet motors by evolution strategies and finite element analysis," in *Proc. of 1999 IEEE Ninth International Conference on Electrical Machines and Drives*, Kent, pp. 297-301.
- [54] D. Nedjar, S. Hlioui, L. Vido, M. Gabsi, Y. Amara, E. Hoang, A. Miraoui, "Permanent magnet synchronous machine design for hybrid traction applications: impact of magnetic laminations materials," in *Proc. of 2010 IEEE International Symposium on Industrial Electronics (ISIE 2010)*, Bari, pp. 1426-1431.

- [55] J. Faiz, B. Keyvani-Boroujeni, "Optimal design of internal permanent magnet motor for starter/generator of hybrid electric vehicle," in Proc. of *2006 IEEE 12th International Power Electronics and Motion Control Conference (EPE-PEMC 2006)*, Portoroz, pp. 984-990.
- [56] A. Tessarolo, F. Luise, P. Raffin, V. Venuti, "Multi-objective design optimization of a surface permanent-magnet slotless alternator for small power wind generation," in Proc. of *2011 IEEE International Conference on Clean Electrical Power (ICCEP 2011)*, Ischia, pp. 371-376.
- [57] K. Price, R. Storn, J. Lampinen, *Differential Evolution: A Practical Approach to Global Optimization*. Springer, 2005.
- [58] M. Barcaro, N. Bianchi, S. Bolognani, "Hybrid electric propulsion system using submersed SPM machine," in Proc. of *2008 IEEE 18th International Conference on Electrical Machines (ICEM 2008)*, Nanjing, pp. 1-6.
- [59] M. Hafner, M. Schoning, K. Hameyer, "Automated sizing of permanent magnet synchronous machines with respect to electromagnetic and thermal aspects," in Proc. of *2008 IEEE 18th International Conference on Electrical Machines (ICEM 2008)*, Nanjing, pp. 1-6.
- [60] R. Lateb, N. Takorabet, F. Meibody-Tabar, A. Mirzaian, J. Enon, A. Sarribouette, "Performances comparison of induction motors and surface mounted PM motor for POD marine propulsion," in Proc. of *2004 IEEE 40th IAS Annual Meeting (IAS '05)*, Hongkong, pp. 1342-1349.
- [61] K. Hruska, V. Kindl, R. Pechanek, "Concept, design and coupled electro-thermal analysis of new hybrid drive vehicle for public transport," in Proc. of *2010 IEEE 14th International Power Electronics and Motion Control Conference (EPE-PEMC 2010)*, Ohrid, pp. S4-5-S4-8.
- [62] Z. Bo, J. Zou, W. Qi "Magnetic-thermal element sequential coupling algorithm in the application of permanent magnet generator temperature analysis," in Proc. of *2010 IEEE International Conference on Electrical Machines and Systems (ICEMS 2010)*, Incheon, pp. 1804-1808.
- [63] Y. Huang, J. Zhu, Y. Guo, Q. Hu, "Core loss and thermal behavior of high-speed SMC motor based on 3-D FEA," in Proc. of *2007 IEEE International Electric Machines and Drives Conference (IEMDC '07)*, Antalya, pp. 1569-1573.
- [64] H. Ahn, B. Lee, S. Hahn, "An efficient investigation of coupled electromagnetic-thermal-fluid numerical model for temperature rise prediction of power transformer," in Proc. of *2011 IEEE International Conference on Electrical Machines and Systems (ICEMS 2011)*, Beijing, pp. 1-4.

- [65] L. Alberti, N. Bianchi, P. Baldassari, R. Wang, "Thermal assisted finite element analysis of electrical machines," in Proc. of *2008 IEEE 18th International Conference on Electrical Machines (ICEM 2008)*, Nanjing, pp. 1-4.
- [66] N. Bracikowski, D. Ilea, F. Gillon, M. Hecquet, P. Brochet, "Design of permanent magnet synchronous machine in order to reduce noise under multi-physic constraints," in Proc. of *2011 IEEE International Electric Machines and Drives Conference (IEMDC '11)*, Niagara Falls, pp. 29-34.
- [67] N. Bracikowski, M. Hecquet, P. Brochet, S.V. Shirinskii, "Multiphysics modeling of a permanent magnet synchronous machine by using lumped models," *Industrial Electronics, IEEE Transactions*. Vol. 59, Issue 6. pp. 2426-2437, June, 2012.
- [68] J. Chun, J. Lim, H. Jung, J. Yoon, "Optimal design of synchronous motor with parameter correction using immune algorithm," *Energy Conversion, IEEE Transactions*. Vol. 14, Issue 3. pp. 610-615, Sep., 1999.
- [69] J. Driesen, R. Belmans, K. Hameyer, "Coupled magneto-thermal simulation of thermally anisotropic electrical machines," in Proc. of *1999 IEEE International Electric Machines and Drives Conference (IEMDC '99)*, Seattle, pp. 469-471.
- [70] G. Traxler-Samek, R. Zickermann, A. Schwery, "Cooling airflow, losses, and temperatures in large air-cooled synchronous machines," *Industrial Electronics, IEEE Transactions*, Vol.57, Issue. 1, pp. 172-180, Jan., 2010.
- [71] X. Yan, Z. Dai, C. Yu, Y. Qi, "Research on magnetic field and temperature field of air core power reactor," in Proc. of *2011 IEEE International Conference on Electrical Machines and Systems (ICEMS 2011)*, Beijing, pp. 1-4.
- [72] J. Driesen, R.J.M. Belmans, K. Hameyer, "Methodologies for coupled transient electromagnetic-thermal finite element modeling of electrical energy transducers," *Industry Applications, IEEE Transactions*, Vol. 38, Issue 5, pp. 1244-1250, Sep., 2002.
- [73] V. Fireteanu, P. Taras, "Finite element models of the transient heating of squirrel-cage rotor during induction motors startup," in Proc. of *2012 IEEE International Symposium on Power Electronics, Electrical Drives, Automation and Motion (SPEEDAM 2012)*, Sorrento, pp.490-495.
- [74] R. Rothe, K. Hameyer, "Life expectancy calculation for electric vehicle traction motors regarding dynamic temperature and driving cycles," in Proc. of *2011 IEEE International Electric Machines and Drives Conference (IEMDC '11)*, Niagara Falls, pp. 1306-1309.
- [75] P.K. Vong, D. Rodger, P.C. Coles, H.C. Lai, "On modeling weakly coupled electromagnetic-thermal problems with prescribed nonlinear surface heat transfer," in Proc.

of 2002 *IEEE International Conference on Power Electronics, Machines and Drives*, Bath, pp. 260-264.

- [76] Z. Badics, P. Zhou, Z.J. Cendes, "Transient modeling of rotating electrical machines including motion, circuit, thermal and deformation," in Proc. of *2006 IEEE 12th Biennial Conference on Electromagnetic Field Computation*, Miami, pp. 457.
- [77] E.D. Ganey, "High-performance electric drives for aerospace more electric architectures Part I -- electric machines," in Proc. of *2007 IEEE Power Engineering Society General Meeting (PES '07)*, Tampa, pp. 1-8.
- [78] D. Zhu, W. Guo, R. Ma, "Automation and optimization for electrical design of hydro generator," in Proc. of *2009 WRI World Congress on Software Engineering (WCSE '09)*, Xiamen, pp. 176-180.
- [79] D. Cho, H. Jung, C. Lee, "Induction motor design for electric vehicle using a niching genetic algorithm," *Industry Applications, IEEE Transactions*. Vol. 37, Issue 4. pp. 994-999, Jul., 2001.
- [80] V. Debusschere, B. Multon, H. Ben Ahmed, P.E. Cavarec, "Life cycle design of a single-phase induction motor," *Electric Power Applications, IET Transactions*, Vol.4, Issue 5, pp. 348-356, 2010.
- [81] V. Debusschere, B. Multon, H. Ben Ahmed, P.E. Cavarec, "Minimization of life cycle energy cost of a single-phase induction motor," in Proc. of *2009 IEEE International Electric Machines and Drives Conference (IEMDC '09)*, Miami, pp. 1441-1448.
- [82] L. Drouen, J.F. Charpentier, E. Semail, S. Clenet, "A global approach for the design of a rim-driven marine turbine generator for sail boat," in Proc. of *2012 IEEE XXth International Conference on Electrical Machines (ICEM 2012)*, Marseille, pp. 549-555.
- [83] A.M. EL-Refaie, N.C. Harris, T.M. Jahns, K.M. Rahman, "Thermal analysis of multibarrier interior PM synchronous machine using lumped parameter model," *Energy Conversion, IEEE Transactions*. Vol. 19, Issue 2. pp. 303-309, June, 2004.
- [84] L. Encica, J.J.H. Paulides, E.A. Lomonova, A.J.A. Vandenput, "Electromagnetic and thermal design of a linear actuator using output polynomial space mapping," *Industry Applications, IEEE Transactions*. Vol. 44, Issue 2. pp. 534-542, Mar., 2008.
- [85] G.M. Gilson, T. Raminosa, S.J. Pickering, C. Gerada, D.B. Hann, "A combined electromagnetic and thermal optimization of an aerospace electric motor," in Proc. of *2010 IEEE XIXth International Conference on Electrical Machines (ICEM 2010)*, Rome, pp. 1-7.
- [86] X. Jannot, J. Vannier, C. Marchand, M. Gabsi, J. Saint-Michel, D. Sadarnac, "Multiphysic modeling of a high-speed interior permanent-magnet synchronous machine for

- a multiobjective optimal design,” *Energy Conversion, IEEE Transactions*. Vol. 26, Issue 2. pp. 457-467, June, 2011.
- [87] O. Keysan, A.S. McDonald, M. Mueller, “A direct drive permanent magnet generator design for a tidal current turbine (SeaGen),” in Proc. of *2011 IEEE International Electric Machines and Drives Conference (IEMDC ' 11)*, Niagara Falls, pp. 224-229.
- [88] R. Khliissa, S. Vivier, L.A. Ospina Vargas, G. Friedrich, “Application of output space mapping method for fast optimization using multi-physical modeling,” in Proc. of *2012 IEEE Energy Conversion Congress and Exposition (ECCE 2012)*, Raleigh, pp. 1306-1313.
- [89] J. Legranger, G. Friedrich, S. Vivier, J.C. Mipo, “Combination of finite-element and analytical models in the optimal multidomain design of machines: application to an interior permanent-magnet starter generator,” *Industry Applications, IEEE Transactions*. Vol. 46, Issue 1. pp. 232-239, Jan., 2010.
- [90] J. Legranger, G. Friedrich, S. Vivier, J.C. Mipo, “Comparison of two optimal rotary transformer designs for highly constrained applications,” in Proc. of *2007 IEEE International Electric Machines and Drives Conference (IEMDC ' 07)*, Antalya, pp. 1546-1551.
- [91] Z. Makni, M. Besbes, C. Marchand, “Multiphysics design methodology of permanent-magnet synchronous motors,” *Vehicular Technology, IEEE Transactions*. Vol. 56, Issue 4. pp. 1524-1530, Jul., 2007.
- [92] P. Ragot, M. Markovic, Y. Perriard, “Optimization of electric motor for a solar airplane application,” *Industry Applications, IEEE Transactions*. Vol. 42, Issue 4. pp. 1053-1061, Jul., 2006.
- [93] M. Rossi, M. Hecquet, V. Lanfranchi, J. Bou Saada, B. Lefebvre, “Multiphysics design rules applied to inductors or transformers for railway application,” in Proc. of *2011 IEEE International Electric Machines and Drives Conference (IEMDC ' 11)*, Niagara Falls, pp. 1225-1230.
- [94] M. Rosu, S. Stanton, J.R. Brauer, Z.J. Cendes, “Complete nonlinear magnetic-thermal-stress design of radial field multipole NdFeB permanent magnet cylinder,” in Proc. of *2005 IEEE International Electric Machines and Drives Conference (IEMDC ' 05)*, San Antonio, pp. 131-136.
- [95] D. Gerada, A. Mebarki, N.L. Brown, C. Gerada, “Optimal split ratio for high speed induction machines,” in Proc. of *2010 IEEE Energy Conversion Congress and Exposition (ECCE 2010)*, Atlanta, pp. 10-16.
- [96] N. Bianchi, S. Bolognani, F. Luise, “Analysis and design of a PM brushless motor for high-speed operations,” *Energy Conversion, IEEE Transactions*. Vol. 20, Issue 3. pp. 629-637, Sep., 2005.

- [97] F. Marquez-Fernandez, A. Reinap, M. Alakula, "Design, optimization and construction of an electric motor for an electric rear wheel drive unit application for a hybrid passenger car," in Proc. of *2010 IEEE XIXth International Conference on Electrical Machines (ICEM 2010)*, Rome, pp. 1-6.
- [98] K.J. Meesen, J.J.H. Paulides, E.A. Lomonova, "Modeling and experimental verification of a tubular actuator for 20-g acceleration in a pick-and-place application," *Industry Applications, IEEE Transactions*. Vol. 46, Issue 5. pp. 1891-1898, Sep., 2010.
- [99] M.F. Momen, I. Husain, "Optimizing the design and performance of a switched reluctance machine using lumped parameter thermal model," in Proc. of *2003 IEEE International Electric Machines and Drives Conference (IEMDC '03)*, Madison, pp. 955-961.
- [100] A. Reinap, D. Hagstedt, F. Marquez, Y. Loayza, M. Alakula, "Development of a radial flux machine design environment," in Proc. of *2008 IEEE 18th International Conference on Electrical Machines (ICEM 2008)*, Nanjing, pp. 1-4.
- [101] W. Wu, H.C. Lovatt, J.B. Dunlop, "Optimization of switched reluctance motors for hybrid electric vehicles," in Proc. of *2002 IEEE International Conference on Power Electronics, Machines and Drives*, Bath, pp. 177-182.
- [102] P.B. Reddy, "Loss in high speed fractional slot concentrated winding surface permanent magnet machines". PhD Thesis, University of Wisconsin - Madison, 2010.
- [103] P.B. Reddy, T.M. Jahns, P.J. McCleer, T.P. Bohn, "Design, analysis and fabrication of a high-performance fractional-slot concentrated winding surface PM machine," in *Proc. of 2010 IEEE Energy Conversion Congress and Exposition (ECCE 2010)*, Atlanta, pp. 1074-1081.
- [104] D. Zarko, "A systematic approach to optimized design of permanent magnet motors with reduced torque pulsations". PhD Thesis, University of Wisconsin - Madison, 2004.
- [105] US Dept. of Energy, "Development of power electronics and electric motor technology for plug-in hybrid electric vehicles, internal combustion engine hybrid vehicles and fuel cell vehicle traction drive applications", 2006, pp. 9-10.
- [106] J. Tangudu, "On modeling and design of fractional-slot concentrated-winding interior permanent magnet machines". PhD Thesis, University of Wisconsin - Madison, 2011.
- [107] T.A. Lipo, *Introduction to AC Machine Design, 2nd ed.*, Wisconsin Power Electronics Research Center of the University of Wisconsin, 2004

- [108] A. Boglietti, A. Cavagnino, D. Staton, M. Shanel, M. Mueller, C. Mejuto, "Evolution and modern approaches for thermal analysis of electrical machines," *Industrial Electronics, IEEE Transactions*. Vol. 56, Issue 3. pp. 871-882, Mar., 2009.
- [109] A. Boglietti, A. Cavagnino, D. Staton, "Determination of critical parameters in electrical machine thermal models," *Industry Applications, IEEE Transactions*. Vol. 44, Issue 4. pp. 1150-1159, Jul., 2008.
- [110] [http://jmag-international.com/catalog/18\\_IPMMotor\\_Thermal.html](http://jmag-international.com/catalog/18_IPMMotor_Thermal.html)
- [111] J. Saari, "Thermal analysis of high-speed induction machines". PhD Thesis, Helsinki University of Technology, 1998.
- [112] F.P. Incropera, D.P. DeWitt, *Fundamentals of Heat and Mass Transfer, 3rd ed.*, Wiley, 1990.
- [113] D.P. Kulkarni, G. Rupertus, E. Chen, "Experimental investigation of contact resistance for water cooled jacket for electric motors and generators," *Energy Conversion, IEEE Transactions*. Vol. 27, Issue 1. pp. 204-210, Mar., 2012.
- [114] T.A. Burress, C.L. Coomer, S.L. Campbell, L.E. Seiber, L.D. Marlino, R.H. Staunton, J.P. Cunningham, "EVALUATION OF THE 2007 TOYOTA CAMRY HYBRID SYNERGY DRIVE SYSTEM," OAK RIDGE NATIONAL LABORATORY, Jan., 2008.
- [115] D.A. Staton, A. Cavagnino, "Convection heat transfer and flow calculations suitable for electric machines thermal models," *Industrial Electronics, IEEE Transactions*. Vol. 55, Issue 10. pp. 3509-3516, Oct., 2008.
- [116] S. Ruoho, M. Haavisto, E. Takala, T. Santa-Nokki, M. Paju, "Temperature dependence of resistivity of sintered rare-earth permanent-magnet materials," *Magnetics, IEEE Transactions*. Vol. 46, Issue 1. pp. 15-20, Jan., 2010.
- [117] G. Nellis, S. Klein, *Heat Transfer*. Cambridge, 2008.
- [118] A. Aliferov, F. Dughiero, M. Forzan, "Coupled magneto-thermal FEM model of direct heating of ferromagnetic bended tubes," *Magnetics, IEEE Transactions*. Vol. 46, Issue 8. pp. 3217-3220, Aug., 2010.
- [119] H. Xuan, H. Polinder, D. Lahaye, J.A. Ferreira, "Modeling for the design of fractional slot PM machine with concentrated windings protected from demagnetization during three-phase short circuit," in *Proc. of 2012 IEEE Energy Conversion Congress and Exposition (ECCE 2012)*, Raleigh, pp. 1276-1283.
- [120] J.H. Mathews, K.D. Fink, *Numerical Methods Using MATLAB, 4th ed.*, Pearson Prentice Hall, 2004.

- [121] S.C. Chapra, R.P. Canale, *Numerical Methods for Engineers, 6th ed.*, McGraw-Hill, 2010.
- [122] S.C. Chapra, *Applied Numerical Methods with MATLAB for Engineers and Scientists*, McGraw-Hill, 2005.
- [123] K. Swingler, *Applying Neural Network*, Academic Press, 1996.
- [124] [www.mathworks.com/help/pdf\\_doc/nnet/nnet\\_ug.pdf](http://www.mathworks.com/help/pdf_doc/nnet/nnet_ug.pdf).
- [125] A. El-Refaie, J. Alexander, K. Huh, S. Galioto, P. Reddy, P. De Bock, X. Shen, "Advanced High Power-Density Interior Permanent Magnet Motor for Traction Applications," in *Proc. of 2013 IEEE Energy Conversion Congress and Exposition (ECCE 2013)*, Denver, pp. 581-590.
- [126] A. Saltelli, S. Tarantola, F. Campolongo, M. Ratto, *Sensitivity Analysis in Practice*, WILEY, 2004
- [127] A. Saltelli, M. Ratto, T. Andres, F. Campolongo, J. Cariboni, D. Gatelli, M. Saisana, S. Tarantola, *Global Sensitivity Analysis*, WILEY, 1996



# Appendix

## A.1 EM-Thermal Coupled Tests for TD Design under Static Operation

### Case TD1: 0.25\*rated current density = 1.15 A/mm<sup>2</sup>

Iteration no.	PM resistivity [microOhm-m]	Airgap HT coeff. [W/m <sup>2</sup> /deg C]	Copper loss [W]	Stator core loss [W]	Rotor core loss [W]	PM loss [W]	Coil Temp. [deg C]	Stator Temp. [deg C]	Rotor Temp. [deg C]	PM Temp. [deg C]	Airgap Temp. [deg C]	Torque [N*m]	Coil Max Temp. [deg C]
0	1.39	127.82					150.00	150.00	150.00	150.00	150.00		
1	1.31	128.59	38.10	229.55	2.20	17.74	55.14	63.20	52.53	54.71	61.59	26.35	55.62
2	1.31	128.64	28.75	261.32	2.74	26.94	55.56	63.82	56.87	59.26	62.98	27.57	56.05
3			28.79	261.26	2.70	26.44	55.54	63.81	56.66	59.04	62.95	27.51	56.04
1-Final			<b>9.31</b>	<b>-31.71</b>	<b>-0.50</b>	<b>-8.70</b>	<b>-0.40</b>	<b>-0.61</b>	<b>-4.13</b>	<b>-4.33</b>	<b>-1.36</b>	<b>-1.16</b>	<b>-0.42</b>
2-Final			<b>-0.04</b>	<b>0.06</b>	<b>0.04</b>	<b>0.50</b>	<b>0.02</b>	<b>0.01</b>	<b>0.21</b>	<b>0.22</b>	<b>0.03</b>	<b>0.06</b>	<b>0.01</b>

### Case TD2: 0.50\*rated current density = 2.3 A/mm<sup>2</sup>

Iteration no.	PM resistivity [microOhm-m]	Airgap HT coeff. [W/m <sup>2</sup> /deg C]	Copper loss [W]	Stator core loss [W]	Rotor core loss [W]	PM loss [W]	Coil Temp. [deg C]	Stator Temp. [deg C]	Rotor Temp. [deg C]	PM Temp. [deg C]	Airgap Temp. [deg C]	Torque [N*m]	Coil Max Temp. [deg C]
0	1.39	127.82					150.00	150.00	150.00	150.00	150.00		
1	1.32	128.92	152.41	235.57	3.90	26.49	64.23	67.83	71.57	71.59	70.99	52.54	64.65
2	1.32	128.79	118.58	259.72	3.98	33.55	60.94	65.95	62.36	64.94	67.17	54.58	61.35
3			117.28	260.31	3.99	34.23	60.90	65.95	62.60	65.19	67.18	54.74	61.31
1-Final			<b>35.13</b>	<b>-24.74</b>	<b>-0.09</b>	<b>-7.74</b>	<b>3.33</b>	<b>1.88</b>	<b>8.97</b>	<b>6.40</b>	<b>3.81</b>	<b>-2.20</b>	<b>3.34</b>
2-Final			<b>1.30</b>	<b>-0.59</b>	<b>-0.01</b>	<b>-0.68</b>	<b>0.04</b>	<b>0.00</b>	<b>-0.24</b>	<b>-0.25</b>	<b>-0.01</b>	<b>-0.16</b>	<b>0.04</b>

### Case TD3: 0.75\*rated current density = 3.45 A/mm<sup>2</sup>

Iteration no.	PM resistivity [microOhm-m]	Airgap HT coeff. [W/m <sup>2</sup> /deg C]	Copper loss [W]	Stator core loss [W]	Rotor core loss [W]	PM loss [W]	Coil Temp. [deg C]	Stator Temp. [deg C]	Rotor Temp. [deg C]	PM Temp. [deg C]	Airgap Temp. [deg C]	Torque [N*m]	Coil Max Temp. [deg C]
0	1.39	127.82					150.00	150.00	150.00	150.00	150.00		
1	1.33	129.08	342.92	247.49	6.34	43.06	73.99	70.92	72.78	75.74	76.82	78.11	74.39
2	1.33	129.03	275.47	266.38	6.17	48.12	70.63	69.92	73.33	76.33	75.02	81.13	71.04
3			272.49	266.07	6.17	48.07	70.45	69.85	73.23	76.21	74.88	81.11	70.86
1-Final			<b>70.43</b>	<b>-18.58</b>	<b>0.17</b>	<b>-5.01</b>	<b>3.54</b>	<b>1.07</b>	<b>-0.45</b>	<b>-0.47</b>	<b>1.94</b>	<b>-3.00</b>	<b>3.53</b>
2-Final			<b>2.98</b>	<b>0.31</b>	<b>0.00</b>	<b>0.05</b>	<b>0.18</b>	<b>0.07</b>	<b>0.10</b>	<b>0.12</b>	<b>0.14</b>	<b>0.02</b>	<b>0.18</b>

Case TD4:1.00\*rated current density = 4.6 A/mm<sup>2</sup>

Iteration no.	PM resistivity [microOhm-m]	Airgap HT coeff. [W/m <sup>2</sup> /deg C]	Copper loss [W]	Stator core loss [W]	Rotor core loss [W]	PM loss [W]	Coil Temp. [deg C]	Stator Temp. [deg C]	Rotor Temp. [deg C]	PM Temp. [deg C]	Airgap Temp. [deg C]	Torque [N*m]	Coil Max Temp. [deg C]
0	1.39	127.82					150.00	150.00	150.00	150.00	150.00		
1	1.34	129.34	609.64	262.87	10.29	68.36	90.58	77.76	91.88	95.54	90.35	102.27	91.07
2	1.34	129.29	515.90	274.89	9.78	70.63	85.46	75.98	90.30	93.91	87.01	105.59	85.92
3			507.82	278.60	9.77	70.71	85.08	75.87	90.20	93.80	86.82	105.68	85.54
1-Final			<b>101.82</b>	<b>-15.73</b>	<b>0.52</b>	<b>-2.35</b>	<b>5.50</b>	<b>1.89</b>	<b>1.68</b>	<b>1.74</b>	<b>3.53</b>	<b>-3.41</b>	<b>5.53</b>
2-Final			<b>8.08</b>	<b>-3.71</b>	<b>0.01</b>	<b>-0.08</b>	<b>0.38</b>	<b>0.11</b>	<b>0.10</b>	<b>0.11</b>	<b>0.19</b>	<b>-0.09</b>	<b>0.38</b>

Case TD5:1.25\*rated current density = 5.75 A/mm<sup>2</sup>

Iteration no.	PM resistivity [microOhm-m]	Airgap HT coeff. [W/m <sup>2</sup> /deg C]	Copper loss [W]	Stator core loss [W]	Rotor core loss [W]	PM loss [W]	Coil Temp. [deg C]	Stator Temp. [deg C]	Rotor Temp. [deg C]	PM Temp. [deg C]	Airgap Temp. [deg C]	Torque [N*m]	Coil Max Temp. [deg C]
0	1.39	127.82					150.00	150.00	150.00	150.00	150.00		
1	1.36	129.43	952.57	283.51	15.80	100.16	111.91	86.56	116.40	120.90	107.77	124.42	112.56
2	1.36	129.44	858.67	290.20	15.12	100.80	106.63	84.63	113.92	118.33	104.12	126.90	107.24
3	1.36	129.44	845.65	290.63	15.09	100.88	105.89	84.36	113.61	118.00	103.59	127.11	106.49
4			843.83	289.46	15.08	100.89	105.75	84.30	113.54	117.92	103.48	127.14	106.36
1-Final			<b>108.74</b>	<b>-5.95</b>	<b>0.72</b>	<b>-0.73</b>	<b>6.16</b>	<b>2.26</b>	<b>2.86</b>	<b>2.98</b>	<b>4.29</b>	<b>-2.72</b>	<b>6.20</b>
2-Final			<b>14.84</b>	<b>0.74</b>	<b>0.04</b>	<b>-0.09</b>	<b>0.88</b>	<b>0.33</b>	<b>0.38</b>	<b>0.41</b>	<b>0.64</b>	<b>-0.24</b>	<b>0.88</b>
3-Final			<b>1.82</b>	<b>1.17</b>	<b>0.01</b>	<b>-0.01</b>	<b>0.14</b>	<b>0.06</b>	<b>0.07</b>	<b>0.08</b>	<b>0.11</b>	<b>-0.03</b>	<b>0.13</b>

Case TD6:1.50\*rated current density = 6.9 A/mm<sup>2</sup>

Iteration no.	PM resistivity [microOhm-m]	Airgap HT coeff. [W/m <sup>2</sup> /deg C]	Copper loss [W]	Stator core loss [W]	Rotor core loss [W]	PM loss [W]	Coil Temp. [deg C]	Stator Temp. [deg C]	Rotor Temp. [deg C]	PM Temp. [deg C]	Airgap Temp. [deg C]	Torque [N*m]	Coil Max Temp. [deg C]
0	1.39	127.82					150.00	150.00	150.00	150.00	150.00		
1	1.39	129.17	1371.70	306.86	23.23	136.65	137.90	97.23	145.76	151.13	128.87	144.34	138.73
2	1.39	129.21	1328.75	306.30	23.29	136.65	135.41	96.29	144.54	149.80	127.08	144.22	136.22
3	1.39	129.22	1319.91	306.22	23.21	136.65	134.90	96.09	144.27	149.52	126.71	144.37	135.70
4			1318.10	306.47	23.21	136.65	134.80	96.06	144.23	149.47	126.64	144.40	135.60
1-Final			<b>53.60</b>	<b>0.39</b>	<b>0.02</b>	<b>0.00</b>	<b>3.10</b>	<b>1.17</b>	<b>1.53</b>	<b>1.66</b>	<b>2.23</b>	<b>-0.06</b>	<b>3.13</b>
2-Final			<b>10.65</b>	<b>-0.17</b>	<b>0.08</b>	<b>0.00</b>	<b>0.61</b>	<b>0.23</b>	<b>0.31</b>	<b>0.33</b>	<b>0.44</b>	<b>-0.18</b>	<b>0.62</b>
3-Final			<b>1.81</b>	<b>-0.25</b>	<b>0.00</b>	<b>0.00</b>	<b>0.10</b>	<b>0.03</b>	<b>0.04</b>	<b>0.05</b>	<b>0.07</b>	<b>-0.03</b>	<b>0.10</b>

Case TD7:1.55\*rated current density = 7.13 A/mm<sup>2</sup>

Iteration no.	PM resistivity [microOhm-m]	Airgap HT coeff. [W/m <sup>2</sup> /deg C]	Copper loss [W]	Stator core loss [W]	Rotor core loss [W]	PM loss [W]	Coil Temp. [deg C]	Stator Temp. [deg C]	Rotor Temp. [deg C]	PM Temp. [deg C]	Airgap Temp. [deg C]	Torque [N*m]	Coil Max Temp. [deg C]
0	1.39	127.82					150.00	150.00	150.00	150.00	150.00		
1	1.40	129.06	1464.67	310.93	24.93	144.38	143.63	99.57	152.14	157.68	133.49	148.03	144.50
2	1.40	129.09	1440.52	311.17	25.32	144.40	142.26	99.06	151.61	157.04	132.53	147.16	143.12
3			1435.33	310.52	25.29	144.40	141.94	98.94	151.44	156.86	132.29	147.23	142.80
1-Final			<b>29.34</b>	<b>0.41</b>	<b>-0.36</b>	<b>-0.02</b>	<b>1.69</b>	<b>0.63</b>	<b>0.70</b>	<b>0.82</b>	<b>1.20</b>	<b>0.80</b>	<b>1.70</b>
2-Final			<b>5.19</b>	<b>0.65</b>	<b>0.03</b>	<b>0.00</b>	<b>0.32</b>	<b>0.12</b>	<b>0.17</b>	<b>0.18</b>	<b>0.24</b>	<b>-0.07</b>	<b>0.32</b>

Case TD8:1.60\*rated current density = 7.36 A/mm<sup>2</sup>

Iteration no.	PM resistivity [microOhm-m]	Airgap HT coeff. [W/m <sup>2</sup> /deg C]	Copper loss [W]	Stator core loss [W]	Rotor core loss [W]	PM loss [W]	Coil Temp. [deg C]	Stator Temp. [deg C]	Rotor Temp. [deg C]	PM Temp. [deg C]	Airgap Temp. [deg C]	Torque [N*m]	Coil Max Temp. [deg C]
0	1.39	127.82					150.00	150.00	150.00	150.00	150.00		
1	1.40	128.93	1560.69	316.58	26.63	152.22	149.58	102.01	158.67	164.40	138.30	151.62	150.49
2			1558.99	314.68	27.29	152.31	149.46	101.96	158.84	164.47	138.22	149.91	150.38
1-Final			<b>1.70</b>	<b>1.90</b>	<b>-0.66</b>	<b>-0.09</b>	<b>0.12</b>	<b>0.05</b>	<b>-0.17</b>	<b>-0.07</b>	<b>0.08</b>	<b>1.71</b>	<b>0.11</b>

Case TD9:1.65\*rated current density = 7.59 A/mm<sup>2</sup>

Iteration no.	PM resistivity [microOhm-m]	Airgap HT coeff. [W/m <sup>2</sup> /deg C]	Copper loss [W]	Stator core loss [W]	Rotor core loss [W]	PM loss [W]	Coil Temp. [deg C]	Stator Temp. [deg C]	Rotor Temp. [deg C]	PM Temp. [deg C]	Airgap Temp. [deg C]	Torque [N*m]	Coil Max Temp. [deg C]
0	1.39	127.82					150.00	150.00	150.00	150.00	150.00		
1	1.41	128.76	1659.75	321.31	28.28	160.18	155.68	104.50	165.28	171.21	143.21	155.12	156.64
2	1.41	128.72	1684.15	320.12	29.29	160.35	157.11	105.04	166.37	172.21	144.27	152.49	158.07
3			1690.29	318.28	29.35	160.36	157.42	105.15	166.52	172.37	144.46	152.37	158.39
1-Final			<b>-30.54</b>	<b>3.03</b>	<b>-1.07</b>	<b>-0.18</b>	<b>-1.74</b>	<b>-0.65</b>	<b>-1.24</b>	<b>-1.16</b>	<b>-1.25</b>	<b>2.75</b>	<b>-1.75</b>
2-Final			<b>-6.14</b>	<b>1.84</b>	<b>-0.06</b>	<b>-0.01</b>	<b>-0.31</b>	<b>-0.11</b>	<b>-0.15</b>	<b>-0.16</b>	<b>-0.19</b>	<b>0.12</b>	<b>-0.32</b>

Case TD10:1.70\*rated current density = 7.82 A/mm<sup>2</sup>

Iteration no.	PM resistivity [microOhm-m]	Airgap HT coeff. [W/m <sup>2</sup> /deg C]	Copper loss [W]	Stator core loss [W]	Rotor core loss [W]	PM loss [W]	Coil Temp. [deg C]	Stator Temp. [deg C]	Rotor Temp. [deg C]	PM Temp. [deg C]	Airgap Temp. [deg C]	Torque [N*m]	Coil Max Temp. [deg C]
0	1.39	127.82					150.00	150.00	150.00	150.00	150.00		
1	1.42	128.17	1761.87	326.16	29.83	168.23	161.97	107.06	171.95	178.11	148.25	158.53	162.97
2	1.42	127.70	1816.45	325.59	31.28	168.53	165.16	108.29	174.18	180.26	150.61	154.89	166.19
3	1.42	127.58	1830.99	325.52	31.28	168.30	165.99	108.59	174.52	180.64	151.20	154.89	167.02
4			1834.78	325.48	31.45	168.56	166.22	108.69	174.82	180.93	151.38	154.54	167.25

1-Final	-72.91	0.68	-1.62	-0.33	-4.25	-1.63	-2.87	-2.82	-3.13	3.99	-4.28
2-Final	-18.33	0.11	-0.17	-0.03	-1.06	-0.40	-0.64	-0.67	-0.77	0.35	-1.06
3-Final	-3.79	0.04	-0.17	-0.26	-0.23	-0.10	-0.30	-0.29	-0.18	0.35	-0.23

Case TD11:1.75\*rated current density = 8.05 A/mm<sup>2</sup>

Iteration no.	PM resistivity [microOhm-m]	Airgap HT coeff. [W/m <sup>2</sup> /deg C]	Copper loss [W]	Stator core loss [W]	Rotor core loss [W]	PM loss [W]	Coil Temp. [deg C]	Stator Temp. [deg C]	Rotor Temp. [deg C]	PM Temp. [deg C]	Airgap Temp. [deg C]	Torque [N*m]	Coil Max Temp. [deg C]
0	1.39	127.82					150.00	150.00	150.00	150.00	150.00		
1	1.42	127.13	1867.03	331.18	31.30	176.38	168.43	109.69	178.70	185.10	153.43	161.85	169.48
2	1.42	126.39	1956.08	328.37	33.74	174.44	173.53	111.59	181.54	187.76	157.04	156.63	174.61
3	1.42	126.17	1980.72	328.46	33.90	174.52	174.96	112.13	182.39	188.65	158.07	156.24	176.05
4			1987.63	327.92	33.94	174.54	175.35	112.27	182.61	188.89	158.07	156.24	176.05
1-Final			-120.60	3.26	-2.64	1.84	-6.92	-2.58	-3.91	-3.79	-4.64	5.61	-6.57
2-Final			-31.55	0.45	-0.20	-0.10	-1.82	-0.68	-1.07	-1.13	-1.03	0.39	-1.44
3-Final			-6.91	0.54	-0.04	-0.02	-0.39	-0.14	-0.22	-0.24	0.00	0.00	0.00

Case TD12:2.00\*rated current density = 9.2 A/mm<sup>2</sup> (With Temperature Dependent Linear Magnet Model)

Iteration no.	PM resistivity [microOhm-m]	Airgap HT coeff. [W/m <sup>2</sup> /deg C]	Copper loss [W]	Stator core loss [W]	Rotor core loss [W]	PM loss [W]	Coil Temp. [deg C]	Stator Temp. [deg C]	Rotor Temp. [deg C]	PM Temp. [deg C]	Airgap Temp. [deg C]	Torque [N*m]	Coil Max Temp. [deg C]
0	1.39	127.82					150.00	150.00	150.00	150.00	150.00		
1	1.45	121.14	2438.57	355.87	37.08	217.89	203.37	123.81	213.13	221.07	181.15	177.19	204.67
2	1.46	117.86	2775.38	354.13	40.74	216.54	222.84	131.15	224.17	232.40	195.12	165.12	224.27
3	1.47	116.61	2898.26	355.48	40.97	216.87	229.98	133.86	228.08	236.58	200.26	163.13	231.46
4	1.47	116.16	2943.32	355.15	41.05	216.99	232.58	134.84	229.49	238.10	202.12	162.38	234.08
5	1.47	115.99	2959.72	354.51	41.09	217.02	233.52	135.18	229.99	238.63	202.78	162.12	235.02
6			2965.66	352.68	41.08	217.04	233.82	135.28	230.12	238.78	202.96	162.03	235.33
1-Final			-527.09	3.19	-4.00	0.85	-30.45	-11.47	-16.99	-17.71	-21.81	15.16	-30.66
2-Final			-190.28	1.45	-0.34	-0.50	-10.98	-4.13	-5.95	-6.38	-7.84	3.09	-11.06
3-Final			-67.40	2.80	-0.11	-0.17	-3.84	-1.42	-2.04	-2.20	-2.70	1.10	-3.87
4-Final			-22.34	2.47	-0.03	-0.05	-1.24	-0.44	-0.63	-0.68	-0.84	0.35	-1.25
5-Final			-5.94	1.83	0.01	-0.02	-0.30	-0.10	-0.13	-0.15	-0.18	0.09	-0.31

## A.2 EM-Thermal Coupled Tests for TPD Design under Static Operation

### Case TPD1: 0.25\*rated current density = 1.15 A/mm<sup>2</sup>

Iteration no.	PM resistivity [microOhm-m]	Airgap HT coeff. [W/m <sup>2</sup> /deg C]	Copper loss [W]	Stator core loss [W]	Rotor core loss [W]	PM loss [W]	Coil Temp. [deg C]	Stator Temp. [deg C]	Rotor Temp. [deg C]	PM Temp. [deg C]	Airgap Temp. [deg C]	Torque [N*m]	Coil Max Temp. [deg C]
0	1.39	123.00					150.00	150.00	150.00	150.00	150.00		
1	1.31	125.37	39.61	149.47	13.07	10.01	57.54	62.88	61.11	61.51	61.42	27.43	58.05
2	1.31	125.38	30.13	173.32	8.57	9.57	57.42	62.95	58.94	59.80	61.48	29.93	57.94
3			30.12	174.38	8.51	9.56	57.44	62.96	58.92	59.80	61.50	29.97	57.95
1-Final			<b>9.49</b>	<b>-24.91</b>	<b>4.56</b>	<b>0.45</b>	<b>0.10</b>	<b>-0.08</b>	<b>2.19</b>	<b>1.71</b>	<b>-0.08</b>	<b>-2.54</b>	<b>0.10</b>
2-Final			<b>0.01</b>	<b>-1.06</b>	<b>0.06</b>	<b>0.01</b>	<b>-0.02</b>	<b>-0.01</b>	<b>0.02</b>	<b>0.00</b>	<b>-0.02</b>	<b>-0.04</b>	<b>-0.01</b>

### Case TPD2: 0.50\*rated current density = 2.3 A/mm<sup>2</sup>

Iteration no.	PM resistivity [microOhm-m]	Airgap HT coeff. [W/m <sup>2</sup> /deg C]	Copper loss [W]	Stator core loss [W]	Rotor core loss [W]	PM loss [W]	Coil Temp. [deg C]	Stator Temp. [deg C]	Rotor Temp. [deg C]	PM Temp. [deg C]	Airgap Temp. [deg C]	Torque [N*m]	Coil Max Temp. [deg C]
0	1.39	123.00					150.00	150.00	150.00	150.00	150.00		
1	1.34	125.65	158.43	193.76	45.56	31.12	64.86	66.72	89.66	87.33	69.27	53.84	65.34
2	1.33	125.61	123.52	208.32	36.18	30.53	63.35	66.11	83.91	82.49	68.02	57.33	63.83
3			122.90	208.87	35.55	30.48	63.32	66.09	83.58	82.22	67.98	57.59	63.79
1-Final			<b>35.53</b>	<b>-15.11</b>	<b>10.01</b>	<b>0.64</b>	<b>1.54</b>	<b>0.63</b>	<b>6.08</b>	<b>5.11</b>	<b>1.29</b>	<b>-3.75</b>	<b>1.55</b>
2-Final			<b>0.62</b>	<b>-0.55</b>	<b>0.63</b>	<b>0.05</b>	<b>0.03</b>	<b>0.02</b>	<b>0.33</b>	<b>0.27</b>	<b>0.04</b>	<b>-0.26</b>	<b>0.04</b>

### Case TPD3: 0.75\*rated current density = 3.45 A/mm<sup>2</sup>

Iteration no.	PM resistivity [microOhm-m]	Airgap HT coeff. [W/m <sup>2</sup> /deg C]	Copper loss [W]	Stator core loss [W]	Rotor core loss [W]	PM loss [W]	Coil Temp. [deg C]	Stator Temp. [deg C]	Rotor Temp. [deg C]	PM Temp. [deg C]	Airgap Temp. [deg C]	Torque [N*m]	Coil Max Temp. [deg C]
0	1.39	123.00					150.00	150.00	150.00	150.00	150.00		
1	1.37	125.97	356.47	266.42	87.38	61.98	76.61	72.77	129.34	123.63	81.44	78.47	77.21
2	1.36	125.92	288.76	270.44	81.32	61.90	73.60	71.51	123.94	118.73	79.08	80.63	74.18
3	1.36	125.91	285.99	270.33	80.21	61.88	73.45	71.43	123.32	118.22	78.93	81.04	74.03
4			285.85	269.76	80.10	61.88	73.43	71.42	123.26	118.17	78.90	81.08	74.01
1-Final			<b>70.62</b>	<b>-3.34</b>	<b>7.28</b>	<b>0.10</b>	<b>3.18</b>	<b>1.35</b>	<b>6.08</b>	<b>5.46</b>	<b>2.54</b>	<b>-2.61</b>	<b>3.20</b>
2-Final			<b>2.91</b>	<b>0.68</b>	<b>1.22</b>	<b>0.02</b>	<b>0.17</b>	<b>0.09</b>	<b>0.68</b>	<b>0.56</b>	<b>0.18</b>	<b>-0.45</b>	<b>0.17</b>
3-Final			<b>0.14</b>	<b>0.57</b>	<b>0.11</b>	<b>0.00</b>	<b>0.02</b>	<b>0.01</b>	<b>0.06</b>	<b>0.05</b>	<b>0.03</b>	<b>-0.04</b>	<b>0.02</b>

**Case TPD4: 1.00\*rated current density = 4.6 A/mm<sup>2</sup>**

Iteration no.	PM resistivity [microOhm-m]	Airgap HT coeff. [W/m <sup>2</sup> /deg C]	Copper loss [W]	Stator core loss [W]	Rotor core loss [W]	PM loss [W]	Coil Temp. [deg C]	Stator Temp. [deg C]	Rotor Temp. [deg C]	PM Temp. [deg C]	Airgap Temp. [deg C]	Torque [N*m]	Coil Max Temp. [deg C]
0	1.39	123.00					150.00	150.00	150.00	150.00	150.00		
1	1.40	126.18	633.72	352.87	126.16	99.75	92.16	80.50	172.53	163.99	96.72	100.52	92.90
2	1.40	126.16	538.86	348.90	129.53	99.97	88.09	78.85	170.55	161.48	93.82	98.67	88.81
3			532.18	349.59	129.06	99.99	87.80	78.73	170.17	161.15	93.60	98.95	88.52
1-Final			<b>101.54</b>	<b>3.28</b>	<b>-2.90</b>	<b>-0.24</b>	<b>4.36</b>	<b>1.77</b>	<b>2.36</b>	<b>2.84</b>	<b>3.12</b>	<b>1.57</b>	<b>4.38</b>
2-Final			<b>6.68</b>	<b>-0.69</b>	<b>0.47</b>	<b>-0.02</b>	<b>0.29</b>	<b>0.12</b>	<b>0.38</b>	<b>0.33</b>	<b>0.22</b>	<b>-0.28</b>	<b>0.29</b>

**Case TPD5: 1.25\*rated current density = 5.75 A/mm<sup>2</sup>**

Iteration no.	PM resistivity [microOhm-m]	Airgap HT coeff. [W/m <sup>2</sup> /deg C]	Copper loss [W]	Stator core loss [W]	Rotor core loss [W]	PM loss [W]	Coil Temp. [deg C]	Stator Temp. [deg C]	Rotor Temp. [deg C]	PM Temp. [deg C]	Airgap Temp. [deg C]	Torque [N*m]	Coil Max Temp. [deg C]
0	1.39	123.00					150.00	150.00	150.00	150.00	150.00		
1	1.44	126.17	990.18	445.96	145.68	144.57	110.96	89.49	211.02	201.85	114.08	119.11	111.87
2	1.43	126.20	890.14	441.86	148.88	140.57	106.55	87.66	206.80	197.01	110.79	112.33	107.43
3			878.84	442.52	148.78	140.65	106.07	87.47	206.50	196.71	110.44	112.97	106.94
1-Final			<b>111.34</b>	<b>3.44</b>	<b>-3.10</b>	<b>3.92</b>	<b>4.89</b>	<b>2.02</b>	<b>4.52</b>	<b>5.14</b>	<b>3.64</b>	<b>6.14</b>	<b>4.93</b>
2-Final			<b>11.30</b>	<b>-0.66</b>	<b>0.10</b>	<b>-0.08</b>	<b>0.48</b>	<b>0.19</b>	<b>0.30</b>	<b>0.30</b>	<b>0.35</b>	<b>-0.64</b>	<b>0.49</b>

**Case TPD6: 1.50\*rated current density = 6.9 A/mm<sup>2</sup>**

Iteration no.	PM resistivity [microOhm-m]	Airgap HT coeff. [W/m <sup>2</sup> /deg C]	Copper loss [W]	Stator core loss [W]	Rotor core loss [W]	PM loss [W]	Coil Temp. [deg C]	Stator Temp. [deg C]	Rotor Temp. [deg C]	PM Temp. [deg C]	Airgap Temp. [deg C]	Torque [N*m]	Coil Max Temp. [deg C]
0	1.39	123.00					150.00	150.00	150.00	150.00	150.00		
1	1.47	125.84	1425.86	538.30	165.43	183.56	133.04	99.76	249.29	239.45	133.64	134.83	134.15
2	1.47	128.89	1363.28	538.72	169.31	180.17	130.37	98.69	246.56	236.09	131.74	121.45	131.46
3			1353.43	538.27	168.79	180.31	129.93	98.50	246.07	235.64	131.39	121.96	131.01
1-Final			<b>72.43</b>	<b>0.03</b>	<b>-3.36</b>	<b>3.25</b>	<b>3.11</b>	<b>1.26</b>	<b>3.22</b>	<b>3.81</b>	<b>2.25</b>	<b>12.87</b>	<b>3.14</b>
2-Final			<b>9.85</b>	<b>0.45</b>	<b>0.52</b>	<b>-0.14</b>	<b>0.44</b>	<b>0.19</b>	<b>0.49</b>	<b>0.45</b>	<b>0.35</b>	<b>-0.51</b>	<b>0.45</b>

**Case TPD7: 1.55\*rated current density = 7.13 A/mm<sup>2</sup>**

Iteration no.	PM resistivity [microOhm-m]	Airgap HT coeff. [W/m <sup>2</sup> /deg C]	Copper loss [W]	Stator core loss [W]	Rotor core loss [W]	PM loss [W]	Coil Temp. [deg C]	Stator Temp. [deg C]	Rotor Temp. [deg C]	PM Temp. [deg C]	Airgap Temp. [deg C]	Torque [N*m]	Coil Max Temp. [deg C]
0	1.39	123.00					150.00	150.00	150.00	150.00	150.00		
1	1.48	125.29	1522.50	555.56	169.90	191.81	137.87	101.99	257.60	247.59	137.88	137.62	139.02
2	1.47	125.56	1474.71	554.75	174.12	187.60	135.80	101.14	255.35	244.70	136.38	122.68	136.94

3	1.47	125.61	1466.55	554.64	173.74	187.74	135.45	101.00	254.84	244.21	136.11	123.14	136.58
4			1465.17	555.01	173.95	187.77	135.40	100.98	254.89	244.24	136.09	123.21	136.53
1-Final			<b>57.33</b>	<b>0.55</b>	<b>-4.05</b>	<b>4.04</b>	<b>2.47</b>	<b>1.01</b>	<b>2.71</b>	<b>3.35</b>	<b>1.79</b>	<b>14.41</b>	<b>2.49</b>
2-Final			<b>9.54</b>	<b>-0.26</b>	<b>0.17</b>	<b>-0.17</b>	<b>0.40</b>	<b>0.16</b>	<b>0.46</b>	<b>0.46</b>	<b>0.29</b>	<b>-0.53</b>	<b>0.41</b>
3-Final			<b>1.38</b>	<b>-0.37</b>	<b>-0.21</b>	<b>-0.03</b>	<b>0.05</b>	<b>0.02</b>	<b>-0.05</b>	<b>-0.03</b>	<b>0.02</b>	<b>-0.07</b>	<b>0.05</b>

**Case TPD8: 1.60\*rated current density = 7.36 A/mm<sup>2</sup>**

Iteration no.	PM resistivity [microOhm-m]	Airgap HT coeff. [W/m <sup>2</sup> /deg C]	Copper loss [W]	Stator core loss [W]	Rotor core loss [W]	PM loss [W]	Coil Temp. [deg C]	Stator Temp. [deg C]	Rotor Temp. [deg C]	PM Temp. [deg C]	Airgap Temp. [deg C]	Torque [N*m]	Coil Max Temp. [deg C]
0	1.39	123.00					150.00	150.00	150.00	150.00	150.00		
1	1.48	124.45	1622.31	579.66	174.94	199.99	142.98	104.37	266.38	256.16	142.42	140.31	144.17
2	1.48	124.66	1592.84	572.44	179.37	194.86	141.56	103.74	264.71	253.85	141.28	123.70	142.75
3			1586.88	572.96	179.39	194.98	141.32	103.65	264.62	253.75	141.11	124.07	142.50
1-Final			<b>35.43</b>	<b>6.70</b>	<b>-4.45</b>	<b>5.01</b>	<b>1.66</b>	<b>0.72</b>	<b>1.76</b>	<b>2.41</b>	<b>1.31</b>	<b>16.24</b>	<b>1.67</b>
2-Final			<b>5.96</b>	<b>-0.52</b>	<b>-0.02</b>	<b>-0.12</b>	<b>0.24</b>	<b>0.09</b>	<b>0.09</b>	<b>0.10</b>	<b>0.17</b>	<b>-0.37</b>	<b>0.25</b>

**Case TPD9:1.65\*rated current density = 7.59 A/mm<sup>2</sup>**

Iteration no.	PM resistivity [microOhm-m]	Airgap HT coeff. [W/m <sup>2</sup> /deg C]	Copper loss [W]	Stator core loss [W]	Rotor core loss [W]	PM loss [W]	Coil Temp. [deg C]	Stator Temp. [deg C]	Rotor Temp. [deg C]	PM Temp. [deg C]	Airgap Temp. [deg C]	Torque [N*m]	Coil Max Temp. [deg C]
0	1.39	123.00					150.00	150.00	150.00	150.00	150.00		
1	1.49	123.63	1725.29	593.55	180.32	208.10	147.99	106.61	274.23	263.90	146.73	142.92	149.19
2	1.49	123.71	1716.32	591.88	185.15	202.01	147.54	106.40	273.53	262.56	146.33	124.70	148.73
3			1714.31	591.12	185.30	202.08	147.45	106.36	273.51	262.53	146.26	124.93	148.64
1-Final			<b>10.98</b>	<b>2.43</b>	<b>-4.98</b>	<b>6.02</b>	<b>0.54</b>	<b>0.25</b>	<b>0.72</b>	<b>1.37</b>	<b>0.47</b>	<b>17.99</b>	<b>0.55</b>
2-Final			<b>2.01</b>	<b>0.76</b>	<b>-0.15</b>	<b>-0.07</b>	<b>0.09</b>	<b>0.04</b>	<b>0.02</b>	<b>0.03</b>	<b>0.07</b>	<b>-0.23</b>	<b>0.09</b>

**Case TPD10:1.70\*rated current density = 7.82 A/mm<sup>2</sup>**

Iteration no.	PM resistivity [microOhm-m]	Airgap HT coeff. [W/m <sup>2</sup> /deg C]	Copper loss [W]	Stator core loss [W]	Rotor core loss [W]	PM loss [W]	Coil Temp. [deg C]	Stator Temp. [deg C]	Rotor Temp. [deg C]	PM Temp. [deg C]	Airgap Temp. [deg C]	Torque [N*m]	Coil Max Temp. [deg C]
0	1.39	123.00					150.00	150.00	150.00	150.00	150.00		
1	1.50	122.74	1831.44	609.33	186.16	216.00	153.29	109.08	284.32	273.54	151.37	145.44	154.58
2	1.50	122.67	1847.03	608.45	191.10	208.89	153.88	109.28	284.45	273.07	151.70	125.27	155.17
3			1849.83	608.94	191.13	208.92	154.01	109.34	284.61	273.23	151.80	125.35	155.30
1-Final			<b>-18.39</b>	<b>0.39</b>	<b>-4.97</b>	<b>7.08</b>	<b>-0.72</b>	<b>-0.26</b>	<b>-0.29</b>	<b>0.31</b>	<b>-0.43</b>	<b>20.09</b>	<b>-0.72</b>
2-Final			<b>-2.80</b>	<b>-0.49</b>	<b>-0.03</b>	<b>-0.03</b>	<b>-0.13</b>	<b>-0.06</b>	<b>-0.16</b>	<b>-0.16</b>	<b>-0.10</b>	<b>-0.08</b>	<b>-0.13</b>

**Case TPD11:1.75\*rated current density = 8.05 A/mm<sup>2</sup>**

Iteration no.	PM resistivity [microOhm-m]	Airgap HT coeff. [W/m <sup>2</sup> /deg C]	Copper loss [W]	Stator core loss [W]	Rotor core loss [W]	PM loss [W]	Coil Temp. [deg C]	Stator Temp. [deg C]	Rotor Temp. [deg C]	PM Temp. [deg C]	Airgap Temp. [deg C]	Torque [N*m]	Coil Max Temp. [deg C]
0	1.39	123.00					150.00	150.00	150.00	150.00	150.00		
1	1.51	121.78	1940.76	624.47	191.97	224.14	158.77	111.60	295.06	284.06	156.24	147.87	160.10
2	1.51	121.58	1984.80	626.42	197.44	215.56	160.50	112.24	294.84	283.16	157.25	125.55	161.85
3			1993.49	626.14	197.41	215.62	160.87	112.39	295.21	283.56	157.52	125.71	162.22
1-Final			<b>-52.73</b>	<b>-1.67</b>	<b>-5.44</b>	<b>8.52</b>	<b>-2.10</b>	<b>-0.79</b>	<b>-0.15</b>	<b>0.50</b>	<b>-1.28</b>	<b>22.16</b>	<b>-2.12</b>
2-Final			<b>-8.69</b>	<b>0.28</b>	<b>0.03</b>	<b>-0.06</b>	<b>-0.37</b>	<b>-0.15</b>	<b>-0.37</b>	<b>-0.40</b>	<b>-0.27</b>	<b>-0.16</b>	<b>-0.37</b>

**Case TPD12:2.00\*rated current density = 9.2 A/mm<sup>2</sup>**

Iteration no.	PM resistivity [microOhm-m]	Airgap HT coeff. [W/m <sup>2</sup> /deg C]	Copper loss [W]	Stator core loss [W]	Rotor core loss [W]	PM loss [W]	Coil Temp. [deg C]	Stator Temp. [deg C]	Rotor Temp. [deg C]	PM Temp. [deg C]	Airgap Temp. [deg C]	Torque [N*m]	Coil Max Temp. [deg C]
0	1.39	123.00					150.00	150.00	150.00	150.00	150.00		
1	1.55	116.63	2534.86	704.80	223.75	162.99	187.64	124.58	340.25	327.66	180.86	158.88	189.16
2	1.56	114.99	2781.78	710.33	232.02	247.26	198.15	128.79	349.98	336.89	188.24	126.69	199.73
3	1.56	114.51	2850.73	709.78	232.74	246.40	201.10	129.98	353.21	340.19	190.36	124.97	202.70
4	1.56	114.37	2870.08	710.35	232.82	246.09	201.94	130.31	354.05	341.07	190.96	124.36	203.54
5			2875.59	709.81	232.92	246.01	202.17	130.40	354.32	341.35	191.12	124.19	203.77
1-Final			<b>-340.73</b>	<b>-5.01</b>	<b>-9.17</b>	<b>-83.02</b>	<b>-14.53</b>	<b>-5.82</b>	<b>-14.07</b>	<b>-13.69</b>	<b>-10.26</b>	<b>34.69</b>	<b>-14.61</b>
2-Final			<b>-93.81</b>	<b>0.52</b>	<b>-0.90</b>	<b>1.25</b>	<b>-4.02</b>	<b>-1.61</b>	<b>-4.34</b>	<b>-4.46</b>	<b>-2.88</b>	<b>2.50</b>	<b>-4.04</b>
3-Final			<b>-24.86</b>	<b>-0.03</b>	<b>-0.18</b>	<b>0.39</b>	<b>-1.07</b>	<b>-0.42</b>	<b>-1.11</b>	<b>-1.16</b>	<b>-0.76</b>	<b>0.78</b>	<b>-1.07</b>
4-Final			<b>-5.51</b>	<b>0.54</b>	<b>-0.10</b>	<b>0.08</b>	<b>-0.23</b>	<b>-0.09</b>	<b>-0.27</b>	<b>-0.28</b>	<b>-0.16</b>	<b>0.17</b>	<b>-0.23</b>

### A.3 EM-Thermal Coupled Tests for Eff. Design under Static Operation

**Case Eff1: 0.25\*rated current density = 1.15 A/mm<sup>2</sup>**

Iteration no.	PM resistivity [microOhm-m]	Airgap HT coeff. [W/m <sup>2</sup> /deg C]	Copper loss [W]	Stator core loss [W]	Rotor core loss [W]	PM loss [W]	Coil Temp. [deg C]	Stator Temp. [deg C]	Rotor Temp. [deg C]	PM Temp. [deg C]	Airgap Temp. [deg C]	Torque [N*m]	Coil Max Temp. [deg C]
0	1.39	122.24					150.00	150.00	150.00	150.00	150.00		
1	1.31	124.99	20.98	240.83	0.23	6.68	62.29	64.98	54.12	56.28	64.86	24.65	63.36
2	1.31	125.00	16.21	278.62	0.25	7.85	62.45	65.17	54.69	56.88	65.18	27.30	63.53
3			16.22	278.57	0.27	7.84	62.45	65.17	54.70	56.88	65.18	27.28	63.53
1-Final			<b>4.76</b>	<b>-37.74</b>	<b>-0.04</b>	<b>-1.16</b>	<b>-0.16</b>	<b>-0.19</b>	<b>-0.58</b>	<b>-0.60</b>	<b>-0.32</b>	<b>-2.63</b>	<b>-0.17</b>
2-Final			-0.01	0.05	-0.02	0.01	0.00	0.00	-0.01	0.00	0.00	0.02	0.00



Case Eff2: 0.50\*rated current density = 2.3 A/mm<sup>2</sup>

Iteration no.	PM resistivity [microOhm-m]	Airgap HT coeff. [W/m <sup>2</sup> /deg C]	Copper loss [W]	Stator core loss [W]	Rotor core loss [W]	PM loss [W]	Coil Temp. [deg C]	Stator Temp. [deg C]	Rotor Temp. [deg C]	PM Temp. [deg C]	Airgap Temp. [deg C]	Torque [N*m]	Coil Max Temp. [deg C]
0	1.39	122.24					150.00	150.00	150.00	150.00	150.00		
1	1.31	125.03	83.90	246.55	0.81	16.94	64.56	65.61	57.11	59.36	66.07	49.30	65.61
2			65.35	276.50	0.85	18.52	64.21	65.65	57.52	59.77	66.12	54.40	65.27
1-Final			<b>18.55</b>	<b>-29.95</b>	<b>-0.04</b>	<b>-1.58</b>	<b>0.35</b>	<b>-0.04</b>	<b>-0.41</b>	<b>-0.41</b>	<b>-0.05</b>	<b>-5.10</b>	<b>0.34</b>

Case Eff3: 0.75\*rated current density = 3.45 A/mm<sup>2</sup>

Iteration no.	PM resistivity [microOhm-m]	Airgap HT coeff. [W/m <sup>2</sup> /deg C]	Copper loss [W]	Stator core loss [W]	Rotor core loss [W]	PM loss [W]	Coil Temp. [deg C]	Stator Temp. [deg C]	Rotor Temp. [deg C]	PM Temp. [deg C]	Airgap Temp. [deg C]	Torque [N*m]	Coil Max Temp. [deg C]
0	1.39	122.24					150.00	150.00	150.00	150.00	150.00		
1	1.31	125.09	188.78	245.24	1.78	33.74	68.26	66.59	61.96	64.33	67.98	73.91	69.32
2	1.32	125.09	148.84	283.63	1.83	35.65	67.27	66.51	62.18	64.55	67.81	81.14	68.33
3			148.36	286.73	1.84	35.65	67.28	66.52	62.20	64.57	67.83	81.12	68.34
1-Final			<b>40.42</b>	<b>-41.49</b>	<b>-0.06</b>	<b>-1.91</b>	<b>0.98</b>	<b>0.07</b>	<b>-0.24</b>	<b>-0.24</b>	<b>0.15</b>	<b>-7.21</b>	<b>0.98</b>
2-Final			<b>0.48</b>	<b>-3.10</b>	<b>-0.01</b>	<b>0.00</b>	<b>-0.01</b>	<b>-0.01</b>	<b>-0.02</b>	<b>-0.02</b>	<b>-0.02</b>	<b>0.02</b>	<b>-0.01</b>

Case Eff4:1.00\*rated current density = 4.6 A/mm<sup>2</sup>

Iteration no.	PM resistivity [microOhm-m]	Airgap HT coeff. [W/m <sup>2</sup> /deg C]	Copper loss [W]	Stator core loss [W]	Rotor core loss [W]	PM loss [W]	Coil Temp. [deg C]	Stator Temp. [deg C]	Rotor Temp. [deg C]	PM Temp. [deg C]	Airgap Temp. [deg C]	Torque [N*m]	Coil Max Temp. [deg C]
0	1.39	122.24					150.00	150.00	150.00	150.00	150.00		
1	1.32	125.18	335.60	253.90	3.11	56.39	73.51	68.02	68.63	71.19	70.75	98.48	74.59
2	1.32	125.16	269.17	291.03	3.22	58.55	71.64	67.72	68.53	71.06	70.17	107.33	72.72
3			267.55	293.22	3.21	58.56	71.60	67.72	68.52	71.05	70.17	107.34	72.68
1-Final			<b>68.05</b>	<b>-39.32</b>	<b>-0.10</b>	<b>-2.17</b>	<b>1.91</b>	<b>0.30</b>	<b>0.11</b>	<b>0.14</b>	<b>0.58</b>	<b>-8.86</b>	<b>1.91</b>
2-Final			1.62	-2.19	0.01	-0.01	0.04	0.00	0.01	0.01	0.00	-0.01	0.04

Case Eff5:1.25\*rated current density = 5.75 A/mm<sup>2</sup>

Iteration no.	PM resistivity [microOhm-m]	Airgap HT coeff. [W/m <sup>2</sup> /deg C]	Copper loss [W]	Stator core loss [W]	Rotor core loss [W]	PM loss [W]	Coil Temp. [deg C]	Stator Temp. [deg C]	Rotor Temp. [deg C]	PM Temp. [deg C]	Airgap Temp. [deg C]	Torque [N*m]	Coil Max Temp. [deg C]
0	1.39	122.24					150.00	150.00	150.00	150.00	150.00		
1	1.33	125.28	524.38	274.12	4.87	84.12	80.32	69.90	77.02	79.81	74.36	122.99	81.43
2	1.33	125.25	429.82	304.60	5.01	85.97	77.46	69.33	76.39	79.12	73.30	132.82	78.57
3			425.94	303.86	5.00	86.00	77.33	69.29	76.34	79.06	73.23	132.92	78.43

1-Final	98.44	-29.74	-0.13	-1.88	2.99	0.61	0.68	0.75	1.13	-9.93	3.00
2-Final	3.88	0.74	0.01	-0.03	0.13	0.04	0.05	0.06	0.07	-0.10	0.14

Case Eff6:1.50\*rated current density = 6.9 A/mm<sup>2</sup>

Iteration no.	PM resistivity [microOhm-m]	Airgap HT coeff. [W/m <sup>2</sup> /deg C]	Copper loss [W]	Stator core loss [W]	Rotor core loss [W]	PM loss [W]	Coil Temp. [deg C]	Stator Temp. [deg C]	Rotor Temp. [deg C]	PM Temp. [deg C]	Airgap Temp. [deg C]	Torque [N*m]	Coil Max Temp. [deg C]
0	1.39	122.24					150.00	150.00	150.00	150.00	150.00		
1	1.34	125.39	755.11	279.24	7.07	115.63	88.46	72.07	86.68	89.71	78.54	147.42	89.59
2	1.34	125.35	634.85	314.99	7.19	117.12	84.78	71.31	85.60	88.54	77.14	157.54	85.92
3			627.66	311.93	7.18	117.15	84.52	71.24	85.49	88.43	77.00	157.73	85.65
1-Final			127.45	-32.69	-0.11	-1.52	3.94	0.83	1.19	1.28	1.54	-10.31	3.94
2-Final			7.19	3.06	0.01	-0.03	0.26	0.07	0.11	0.11	0.14	-0.19	0.27

Case Eff7:1.75\*rated current density = 8.05 A/mm<sup>2</sup>

Iteration no.	PM resistivity [microOhm-m]	Airgap HT coeff. [W/m <sup>2</sup> /deg C]	Copper loss [W]	Stator core loss [W]	Rotor core loss [W]	PM loss [W]	Coil Temp. [deg C]	Stator Temp. [deg C]	Rotor Temp. [deg C]	PM Temp. [deg C]	Airgap Temp. [deg C]	Torque [N*m]	Coil Max Temp. [deg C]
0	1.39	122.24					150.00	150.00	150.00	150.00	150.00		
1	1.35	125.49	1027.79	289.15	9.58	150.71	98.07	74.63	97.66	100.98	83.46	171.76	99.25
2	1.35	125.46	889.66	309.26	9.69	152.13	93.68	73.64	96.13	99.33	81.65	181.35	94.85
3			877.98	310.56	9.70	152.18	93.30	73.56	96.01	99.20	81.49	181.67	94.47
1-Final			149.81	-21.41	-0.12	-1.47	4.77	1.07	1.65	1.78	1.97	-9.91	4.78
2-Final			11.68	-1.30	-0.01	-0.05	0.38	0.08	0.12	0.13	0.16	-0.32	0.38

Case Eff8:2.00\*rated current density = 9.2 A/mm<sup>2</sup>

Iteration no.	PM resistivity [microOhm-m]	Airgap HT coeff. [W/m <sup>2</sup> /deg C]	Copper loss [W]	Stator core loss [W]	Rotor core loss [W]	PM loss [W]	Coil Temp. [deg C]	Stator Temp. [deg C]	Rotor Temp. [deg C]	PM Temp. [deg C]	Airgap Temp. [deg C]	Torque [N*m]	Coil Max Temp. [deg C]
0	1.39	122.24					150.00	150.00	150.00	150.00	150.00		
1	1.36	125.58	1342.41	303.29	12.40	189.61	109.17	77.59	110.03	113.67	89.14	195.99	110.38
2	1.36	125.56	1200.57	318.81	12.52	190.89	104.61	76.55	108.26	111.76	87.23	204.08	105.82
3	1.36	125.55	118.73	319.92	12.51	190.95	104.09	76.43	108.08	111.58	87.00	204.50	105.31
4			1182.92	319.78	12.51	190.96	104.03	76.41	108.06	111.56	86.98	204.54	105.24
1-Final			159.49	-16.49	-0.11	-1.35	5.14	1.18	1.97	2.11	2.16	-8.55	5.14
2-Final			17.65	-0.97	0.01	-0.07	0.58	0.14	0.20	0.20	0.25	-0.46	0.58
3-Final			-1064.19	0.14	0.00	-0.01	0.06	0.02	0.02	0.02	0.02	-0.04	0.07

Case Eff9:2.25\*rated current density = 10.35 A/mm<sup>2</sup>

Iteration no.	PM resistivity [microOhm-m]	Airgap HT coeff. [W/m <sup>2</sup> /deg C]	Copper loss [W]	Stator core loss [W]	Rotor core loss [W]	PM loss [W]	Coil Temp. [deg C]	Stator Temp. [deg C]	Rotor Temp. [deg C]	PM Temp. [deg C]	Airgap Temp. [deg C]	Torque [N*m]	Coil Max Temp. [deg C]
0	1.39	122.24					150.00	150.00	150.00	150.00	150.00		
1	1.37	125.66	1698.99	319.99	15.58	232.15	121.73	80.94	123.73	127.73	95.55	220.12	122.99
2	1.37	125.64	1574.69	331.29	15.65	233.10	117.72	80.01	121.92	125.79	93.85	225.66	118.98
3	1.37	125.64	1557.06	333.97	15.66	233.18	117.15	79.89	121.75	125.61	93.62	226.14	118.41
4			1554.56	332.56	15.66	233.19	117.06	79.86	121.71	125.56	93.57	226.19	118.32
1-Final			<b>144.43</b>	<b>-12.57</b>	<b>-0.08</b>	<b>-1.04</b>	<b>4.67</b>	<b>1.08</b>	<b>2.02</b>	<b>2.17</b>	<b>1.98</b>	<b>-6.07</b>	<b>4.67</b>
2-Final			<b>20.13</b>	<b>-1.27</b>	<b>-0.01</b>	<b>-0.09</b>	<b>0.66</b>	<b>0.15</b>	<b>0.21</b>	<b>0.23</b>	<b>0.28</b>	<b>-0.53</b>	<b>0.66</b>
3-Final			<b>2.50</b>	<b>1.41</b>	<b>0.00</b>	<b>-0.01</b>	<b>0.09</b>	<b>0.03</b>	<b>0.04</b>	<b>0.05</b>	<b>0.05</b>	<b>-0.05</b>	<b>0.09</b>

Case Eff10:2.50\*rated current density = 11.5 A/mm<sup>2</sup>

Iteration no.	PM resistivity [microOhm-m]	Airgap HT coeff. [W/m <sup>2</sup> /deg C]	Copper loss [W]	Stator core loss [W]	Rotor core loss [W]	PM loss [W]	Coil Temp. [deg C]	Stator Temp. [deg C]	Rotor Temp. [deg C]	PM Temp. [deg C]	Airgap Temp. [deg C]	Torque [N*m]	Coil Max Temp. [deg C]
0	1.39	122.24					150.00	150.00	150.00	150.00	150.00		
1	1.38	125.69	2097.52	339.45	19.08	278.15	135.75	84.68	138.74	143.14	102.69	244.13	137.07
2	1.38	125.69	2020.17	342.84	19.10	278.51	133.23	84.08	137.16	141.45	101.61	246.00	134.54
3			2006.49	342.66	19.12	278.60	132.77	83.97	137.02	141.29	101.40	246.46	134.09
1-Final			<b>91.03</b>	<b>-3.21</b>	<b>-0.04</b>	<b>-0.45</b>	<b>2.98</b>	<b>0.71</b>	<b>1.72</b>	<b>1.85</b>	<b>1.29</b>	<b>-2.33</b>	<b>2.98</b>
2-Final			<b>13.68</b>	<b>0.18</b>	<b>-0.02</b>	<b>-0.09</b>	<b>0.46</b>	<b>0.11</b>	<b>0.14</b>	<b>0.16</b>	<b>0.21</b>	<b>-0.46</b>	<b>0.45</b>

Case Eff11:2.65\*rated current density = 12.19 A/mm<sup>2</sup>

Iteration no.	PM resistivity [microOhm-m]	Airgap HT coeff. [W/m <sup>2</sup> /deg C]	Copper loss [W]	Stator core loss [W]	Rotor core loss [W]	PM loss [W]	Coil Temp. [deg C]	Stator Temp. [deg C]	Rotor Temp. [deg C]	PM Temp. [deg C]	Airgap Temp. [deg C]	Torque [N*m]	Coil Max Temp. [deg C]
0	1.39	122.24					150.00	150.00	150.00	150.00	150.00		
1	1.39	125.69	2356.78	352.61	21.32	307.40	144.87	87.11	148.37	153.01	107.32	258.49	146.22
2	1.39	125.69	2325.49	350.31	21.30	307.22	143.82	86.85	147.10	151.66	106.86	257.62	145.17
3			2319.08	350.65	21.32	307.30	143.61	86.80	147.04	151.60	106.77	258.01	144.97
1-Final			<b>37.70</b>	<b>1.96</b>	<b>0.00</b>	<b>0.10</b>	<b>1.26</b>	<b>0.31</b>	<b>1.33</b>	<b>1.41</b>	<b>0.55</b>	<b>0.48</b>	<b>1.25</b>
2-Final			<b>6.41</b>	<b>-0.34</b>	<b>-0.02</b>	<b>-0.08</b>	<b>0.21</b>	<b>0.05</b>	<b>0.06</b>	<b>0.06</b>	<b>0.09</b>	<b>-0.39</b>	<b>0.20</b>

Case Eff12:2.70\*rated current density = 12.42 A/mm<sup>2</sup>

Iteration no.	PM resistivity [microOhm-m]	Airgap HT coeff. [W/m <sup>2</sup> /deg C]	Copper loss [W]	Stator core loss [W]	Rotor core loss [W]	PM loss [W]	Coil Temp. [deg C]	Stator Temp. [deg C]	Rotor Temp. [deg C]	PM Temp. [deg C]	Airgap Temp. [deg C]	Torque [N*m]	Coil Max Temp. [deg C]
0	1.39	122.24					150.00	150.00	150.00	150.00	150.00		
1	1.40	125.69	2446.55	354.30	22.09	317.43	148.00	87.93	151.66	156.39	108.89	263.26	149.37
2	1.40	125.69	2433.89	352.64	22.08	317.06	147.58	87.82	150.55	155.21	108.71	261.38	148.94
3			2431.23	353.34	22.07	317.12	147.49	87.81	150.53	155.20	108.68	261.73	148.86
1-Final			<b>15.32</b>	<b>0.96</b>	<b>0.02</b>	<b>0.31</b>	<b>0.51</b>	<b>0.12</b>	<b>1.13</b>	<b>1.19</b>	<b>0.21</b>	<b>1.53</b>	<b>0.51</b>
2-Final			<b>2.66</b>	<b>-0.70</b>	<b>0.01</b>	<b>-0.06</b>	<b>0.09</b>	<b>0.01</b>	<b>0.02</b>	<b>0.01</b>	<b>0.03</b>	<b>-0.35</b>	<b>0.08</b>

Case Eff13:2.75\*rated current density = 12.65 A/mm<sup>2</sup>

Iteration no.	PM resistivity [microOhm-m]	Airgap HT coeff. [W/m <sup>2</sup> /deg C]	Copper loss [W]	Stator core loss [W]	Rotor core loss [W]	PM loss [W]	Coil Temp. [deg C]	Stator Temp. [deg C]	Rotor Temp. [deg C]	PM Temp. [deg C]	Airgap Temp. [deg C]	Torque [N*m]	Coil Max Temp. [deg C]
0	1.39	122.24					150.00	150.00	150.00	150.00	150.00		
1	1.40	125.68	2538.00	358.76	22.86	327.61	151.21	88.78	155.02	159.84	110.52	268.03	152.59
2	1.40	125.68	2545.95	355.40	22.83	326.98	151.46	88.83	154.07	158.83	110.63	265.09	152.84
3			2547.59	355.56	22.83	327.05	151.51	88.85	154.10	158.87	110.66	265.39	152.89
1-Final			<b>-9.59</b>	<b>3.20</b>	<b>0.03</b>	<b>0.56</b>	<b>-0.30</b>	<b>-0.07</b>	<b>0.92</b>	<b>0.97</b>	<b>-0.14</b>	<b>2.64</b>	<b>-0.30</b>
2-Final			<b>-1.64</b>	<b>-0.16</b>	<b>0.00</b>	<b>-0.07</b>	<b>-0.05</b>	<b>-0.02</b>	<b>-0.03</b>	<b>-0.04</b>	<b>-0.03</b>	<b>-0.30</b>	<b>-0.05</b>

Case Eff14:2.80\*rated current density = 12.88 A/mm<sup>2</sup>

Iteration no.	PM resistivity [microOhm-m]	Airgap HT coeff. [W/m <sup>2</sup> /deg C]	Copper loss [W]	Stator core loss [W]	Rotor core loss [W]	PM loss [W]	Coil Temp. [deg C]	Stator Temp. [deg C]	Rotor Temp. [deg C]	PM Temp. [deg C]	Airgap Temp. [deg C]	Torque [N*m]	Coil Max Temp. [deg C]
0	1.39	122.24					150.00	150.00	150.00	150.00	150.00		
1	1.40	125.67	2631.13	362.15	23.67	337.93	154.47	89.64	158.43	163.34	112.17	272.80	155.86
2	1.40	125.67	2661.57	356.65	23.58	337.04	155.44	89.86	157.64	162.51	112.59	268.74	156.84
3			2668.17	357.97	23.59	337.09	155.67	89.93	157.74	162.62	112.70	268.99	157.07
1-Final			<b>-37.04</b>	<b>4.18</b>	<b>0.08</b>	<b>0.84</b>	<b>-1.20</b>	<b>-0.29</b>	<b>0.69</b>	<b>0.72</b>	<b>-0.53</b>	<b>3.81</b>	<b>-1.21</b>
2-Final			<b>-6.60</b>	<b>-1.32</b>	<b>-0.01</b>	<b>-0.05</b>	<b>-0.23</b>	<b>-0.07</b>	<b>-0.10</b>	<b>-0.11</b>	<b>-0.11</b>	<b>-0.25</b>	<b>-0.23</b>

Case Eff15:2.85\*rated current density = 13.11 A/mm<sup>2</sup>

Iteration no.	PM resistivity [microOhm-m]	Airgap HT coeff. [W/m <sup>2</sup> /deg C]	Copper loss [W]	Stator core loss [W]	Rotor core loss [W]	PM loss [W]	Coil Temp. [deg C]	Stator Temp. [deg C]	Rotor Temp. [deg C]	PM Temp. [deg C]	Airgap Temp. [deg C]	Torque [N*m]	Coil Max Temp. [deg C]
0	1.39	122.24					150.00	150.00	150.00	150.00	150.00		
1	1.41	125.66	2725.94	367.32	24.47	348.39	157.81	90.53	161.90	166.90	113.86	277.56	159.21
2	1.41	125.65	2781.04	360.51	24.37	347.23	159.58	90.94	161.31	166.29	114.63	272.33	160.99
3			2793.52	361.70	24.36	347.27	160.01	91.05	161.48	166.47	114.83	272.51	161.41

1-Final	-67.58	5.62	0.11	1.12	-2.20	-0.52	0.42	0.43	-0.97	5.05	-2.20
2-Final	-12.48	-1.19	0.01	-0.04	-0.43	-0.11	-0.17	-0.18	-0.20	-0.18	-0.42

Case Eff16:3.00\*rated current density = 13.8 A/mm<sup>2</sup>

Iteration no.	PM resistivity [microOhm-m]	Airgap HT coeff. [W/m <sup>2</sup> /deg C]	Copper loss [W]	Stator core loss [W]	Rotor core loss [W]	PM loss [W]	Coil Temp. [deg C]	Stator Temp. [deg C]	Rotor Temp. [deg C]	PM Temp. [deg C]	Airgap Temp. [deg C]	Torque [N*m]	Coil Max Temp. [deg C]
0	1.39	122.24					150.00	150.00	150.00	150.00	150.00		
1	1.42	125.61	3020.43	378.47	26.95	380.65	168.12	93.26	172.60	177.88	119.07	291.81	169.56
2	1.42	125.58	3162.07	369.04	26.81	378.49	172.73	94.35	172.75	178.07	121.08	282.74	174.18
3	1.42	125.57	3198.10	369.49	26.81	378.46	173.93	94.65	173.20	178.55	121.61	282.68	175.39
4			3207.48	368.19	26.80	378.43	174.23	94.71	173.29	178.65	121.74	282.52	175.69
1-Final			-187.05	10.28	0.15	2.22	-6.11	-1.45	-0.69	-0.77	-2.67	9.29	-6.13
2-Final			-45.41	0.85	0.01	0.06	-1.50	-0.36	-0.54	-0.58	-0.66	0.22	-1.51
3-Final			-9.38	1.30	0.01	0.03	-0.30	-0.06	-0.09	-0.10	-0.13	0.16	-0.30

Case Eff17:3.25\*rated current density = 14.95 A/mm<sup>2</sup>

Iteration no.	PM resistivity [microOhm-m]	Airgap HT coeff. [W/m <sup>2</sup> /deg C]	Copper loss [W]	Stator core loss [W]	Rotor core loss [W]	PM loss [W]	Coil Temp. [deg C]	Stator Temp. [deg C]	Rotor Temp. [deg C]	PM Temp. [deg C]	Airgap Temp. [deg C]	Torque [N*m]	Coil Max Temp. [deg C]
0	1.39	122.24					150.00	150.00	150.00	150.00	150.00		
1	1.43	125.45	3544.81	400.16	31.32	437.30	186.49	98.12	191.48	197.27	128.34	315.48	188.00
2	1.43	125.34	3879.56	383.34	31.03	432.84	197.42	100.72	193.33	199.29	133.10	298.85	198.95
3	1.44	125.30	3979.83	382.42	31.05	432.63	200.74	101.53	194.54	200.58	134.57	298.13	202.28
4	1.44	125.29	4010.29	383.67	31.03	432.51	201.76	101.78	194.91	200.97	135.04	297.66	203.30
5			4019.64	382.39	31.02	432.44	202.06	101.85	195.00	201.07	135.16	297.52	203.60
1-Final			-474.83	17.77	0.30	4.86	-15.57	-3.73	-3.52	-3.80	-6.82	17.96	-15.60
2-Final			-140.08	0.95	0.01	0.40	-4.64	-1.13	-1.67	-1.78	-2.06	1.33	-4.65
3-Final			-39.81	0.03	0.03	0.19	-1.32	-0.32	-0.46	-0.49	-0.59	0.61	-1.32
4-Final			-9.35	1.28	0.01	0.07	-0.30	-0.07	-0.09	-0.10	-0.12	0.14	-0.30

Case Eff18:3.50\*rated current density = 16.1 A/mm<sup>2</sup>

Iteration no.	PM resistivity [microOhm-m]	Airgap HT coeff. [W/m <sup>2</sup> /deg C]	Copper loss [W]	Stator core loss [W]	Rotor core loss [W]	PM loss [W]	Coil Temp. [deg C]	Stator Temp. [deg C]	Rotor Temp. [deg C]	PM Temp. [deg C]	Airgap Temp. [deg C]	Torque [N*m]	Coil Max Temp. [deg C]
0	1.39	122.24					150.00	150.00	150.00	150.00	150.00		
1	1.45	124.43	4111.14	422.59	35.97	497.45	206.30	103.35	211.66	217.99	138.31	339.03	207.88
2	1.45	122.91	4710.14	395.00	35.74	472.19	225.65	107.88	212.82	219.38	146.46	310.83	227.26
3	1.45	122.33	4916.01	395.01	35.74	472.07	232.47	109.55	215.87	222.63	149.50	310.27	234.10
4	1.46	122.13	4988.57	393.81	35.72	471.75	234.86	110.13	216.89	223.73	150.55	308.97	236.50

5	1.46	122.06	5014.00	393.40	35.71	471.63	235.70	110.33	217.25	224.11	150.92	308.54	237.34
6			5022.93	393.49	35.70	471.61	236.00	110.40	217.38	224.25	151.05	308.38	237.64
1-Final			-911.79	29.10	0.27	25.84	-29.70	-7.05	-5.72	-6.26	-12.74	30.65	-29.76
2-Final			-312.79	1.51	0.04	0.58	-10.35	-2.52	-4.56	-4.87	-4.59	2.45	-10.38
3-Final			-106.92	1.52	0.04	0.46	-3.53	-0.85	-1.51	-1.62	-1.55	1.89	-3.54
4-Final			-34.36	0.32	0.02	0.14	-1.14	-0.27	-0.49	-0.52	-0.50	0.59	-1.14
5-Final			-8.93	-0.09	0.01	0.02	-0.30	-0.07	-0.13	-0.14	-0.13	0.16	-0.30

## A.4 EM-Thermal Coupled Tests for TD Design under Transient Operation

### Case TD1: 1.60 p.u. to 1.91 p.u.

Time [sec]	PM resistivity [microOhm-m]	Airgap HT coeff. [W/m <sup>2</sup> /deg C]	Copper loss [W]	Stator core loss [W]	Rotor core loss [W]	PM loss [W]	Coil Temp. [deg C]	Stator Temp. [deg C]	Rotor Temp. [deg C]	PM Temp. [deg C]	Airgap Temp. [deg C]	Torque [N*m]	Coil Max Temp. [deg C]
Initial Steady State	1.40	128.93	1558.99	314.68	27.29	152.31	149.46	101.96	158.84	164.47	138.22	149.91	150.38
0	1.40	128.93	2216.28	345.56	35.55	202.62	149.46	101.96	158.84	164.47	138.22	169.71	150.38
18	1.40	128.93	2226.91	345.81	35.54	202.62	151.33	102.35	158.53	164.06	138.36	169.77	152.28
											Ratio =	1.13	

### Case TD2: 1.50 p.u. to 2.44 p.u.

Time [sec]	PM resistivity [microOhm-m]	Airgap HT coeff. [W/m <sup>2</sup> /deg C]	Copper loss [W]	Stator core loss [W]	Rotor core loss [W]	PM loss [W]	Coil Temp. [deg C]	Stator Temp. [deg C]	Rotor Temp. [deg C]	PM Temp. [deg C]	Airgap Temp. [deg C]	Torque [N*m]	Coil Max Temp. [deg C]
Initial Steady State	1.39	129.22	1318.10	306.47	23.21	136.65	134.80	96.06	144.23	149.47	126.64	144.40	135.60
0	1.39	129.22	3476.23	397.98	45.38	290.44	134.80	96.06	144.23	149.47	126.64	199.70	135.60
18	1.39	129.22	3532.51	398.55	45.48	290.41	140.90	96.87	144.30	150.82	127.15	199.46	141.67
											Ratio =	1.38	

### Case TD3: 1.40 p.u. to 2.75 p.u.

Time [sec]	PM resistivity [microOhm-m]	Airgap HT coeff. [W/m <sup>2</sup> /deg C]	Copper loss [W]	Stator core loss [W]	Rotor core loss [W]	PM loss [W]	Coil Temp. [deg C]	Stator Temp. [deg C]	Rotor Temp. [deg C]	PM Temp. [deg C]	Airgap Temp. [deg C]	Torque [N*m]	Coil Max Temp. [deg C]
Initial Steady State	1.38	129.33	1123.65	299.07	19.65	121.69	122.87	91.22	131.40	136.31	117.09	137.82	123.59
0	1.38	129.37	4287.67	426.20	50.21	341.78	122.87	91.22	131.40	136.31	117.09	215.93	123.59
18	1.38	129.36	4392.68	426.48	50.37	341.69	131.96	92.30	131.71	138.80	117.82	215.43	132.74
											Ratio =	1.56	

### Case TD4: 1.30 p.u. to 4.01 p.u.

Time [sec]	PM resistivity [microOhm-m]	Airgap HT coeff. [W/m <sup>2</sup> /deg C]	Copper loss [W]	Stator core loss [W]	Rotor core loss [W]	PM loss [W]	Coil Temp. [deg C]	Stator Temp. [deg C]	Rotor Temp. [deg C]	PM Temp. [deg C]	Airgap Temp. [deg C]	Torque [N*m]	Coil Max Temp. [deg C]
Initial Steady State	1.37	129.42	941.67	291.61	16.41	107.53	111.69	86.67	119.37	123.96	108.14	130.71	112.33
0	1.37	129.43	8824.61	531.94	83.03	534.27	111.69	86.67	119.37	123.96	108.14	261.84	112.33
18	1.37	129.43	9382.83	532.58	83.75	533.39	134.57	89.07	120.56	129.92	110.04	260.33	135.33
											Ratio =	2.00	

Case TD5: 1.20 p.u. to 5.50 p.u.

Time [sec]	PM resistivity [microOhm-m]	Airgap HT coeff. [W/m^2/deg C]	Copper loss [W]	Stator core loss [W]	Rotor core loss [W]	PM loss [W]	Coil Temp. [deg C]	Stator Temp. [deg C]	Rotor Temp. [deg C]	PM Temp. [deg C]	Airgap Temp. [deg C]	Torque [N*m]	Coil Max Temp. [deg C]
Initial Steady State	1.36	129.44	780.79	284.28	13.90	94.29	101.78	82.63	108.63	112.86	100.16	122.93	102.35
0	1.36	129.43	16140.38	630.02	106.28	734.51	101.78	82.63	108.63	112.86	100.16	301.67	102.35
18	1.36	129.44	18191.16	629.96	107.05	731.48	147.93	86.99	110.53	122.39	103.66	298.82	148.78
											Ratio =	2.44	

Case TD6: 1.10 p.u. to 6.18 p.u.

Time [sec]	PM resistivity [microOhm-m]	Airgap HT coeff. [W/m^2/deg C]	Copper loss [W]	Stator core loss [W]	Rotor core loss [W]	PM loss [W]	Coil Temp. [deg C]	Stator Temp. [deg C]	Rotor Temp. [deg C]	PM Temp. [deg C]	Airgap Temp. [deg C]	Torque [N*m]	Coil Max Temp. [deg C]
Initial Steady State	1.35	129.41	639.49	280.23	11.82	81.96	93.11	79.11	99.05	102.94	93.21	114.54	93.62
0	1.35	129.38	19860.90	667.67	111.26	820.45	93.11	79.11	99.05	102.94	93.21	319.01	93.62
18	1.36	129.41	23403.09	667.75	112.02	816.21	152.35	84.47	101.20	114.14	97.45	315.48	153.25
												Ratio =	2.77

Case TD7: 1.00 p.u. to 6.57 p.u.

Time [sec]	PM resistivity [microOhm-m]	Airgap HT coeff. [W/m^2/deg C]	Copper loss [W]	Stator core loss [W]	Rotor core loss [W]	PM loss [W]	Coil Temp. [deg C]	Stator Temp. [deg C]	Rotor Temp. [deg C]	PM Temp. [deg C]	Airgap Temp. [deg C]	Torque [N*m]	Coil Max Temp. [deg C]
Initial Steady State	1.34	129.29	507.82	278.60	9.77	70.71	85.08	75.87	90.20	93.80	86.82	105.68	85.54
0	1.34	129.29	21902.71	686.44	113.00	869.97	85.08	75.87	90.20	93.80	86.82	329.72	85.54
18	1.35	129.35	26408.06	687.35	113.76	864.90	151.87	81.78	92.50	106.04	91.43	325.81	152.78
												Ratio =	3.10

## A.5 EM-Thermal Coupled Tests for TPD Design under Transient Operation

Case TPD1: 0.90 p.u. to 1.34 p.u.

Time [sec]	PM resistivity [microOhm-m]	Airgap HT coeff. [W/m^2/deg C]	Copper loss [W]	Stator core loss [W]	Rotor core loss [W]	PM loss [W]	Coil Temp. [deg C]	Stator Temp. [deg C]	Rotor Temp. [deg C]	PM Temp. [deg C]	Airgap Temp. [deg C]	Torque [N*m]	Coil Max Temp. [deg C]
Initial Steady State	1.39	126.12	427.71	316.90	112.57	84.06	81.85	75.75	152.68	144.86	87.66	92.21	82.52
0	1.39	126.08	676.19	405.65	137.47	122.45	81.85	75.75	152.68	144.86	87.66	111.99	82.52
18	1.39	126.08	676.19	405.65	137.47	122.45	81.89	75.46	150.06	142.35	86.64	111.99	82.54
												Ratio =	1.21

Case TPD2: 0.85 p.u. to 1.36 p.u.

Time [sec]	PM resistivity [microOhm-m]	Airgap HT coeff. [W/m^2/deg C]	Copper loss [W]	Stator core loss [W]	Rotor core loss [W]	PM loss [W]	Coil Temp. [deg C]	Stator Temp. [deg C]	Rotor Temp. [deg C]	PM Temp. [deg C]	Airgap Temp. [deg C]	Torque [N*m]	Coil Max Temp. [deg C]
Initial Steady State	1.38	126.07	377.78	300.80	102.52	76.50	78.93	74.26	142.98	136.01	84.67	88.55	79.57
0	1.38	126.03	960.20	498.32	152.45	160.44	78.93	74.26	142.98	136.01	84.67	128.75	79.57
18	1.38	126.03	960.20	498.32	152.45	160.44	79.83	74.25	141.04	133.83	84.00	128.75	80.44
												Ratio =	1.45

Case TPD3: 0.80 p.u. to 1.69 p.u.

Time [sec]	PM resistivity [microOhm-m]	Airgap HT coeff. [W/m <sup>2</sup> /deg C]	Copper loss [W]	Stator core loss [W]	Rotor core loss [W]	PM loss [W]	Coil Temp. [deg C]	Stator Temp. [deg C]	Rotor Temp. [deg C]	PM Temp. [deg C]	Airgap Temp. [deg C]	Torque [N*m]	Coil Max Temp. [deg C]
Initial Steady State	1.37	126.02	331.52	285.46	91.80	69.09	76.18	72.85	133.32	127.24	81.80	84.69	76.79
0	1.37	125.97	1459.51	604.51	182.83	214.80	76.18	72.85	133.32	127.24	81.80	148.65	76.79
18	1.37	125.97	1459.51	604.51	182.83	214.80	78.47	73.18	132.27	125.43	81.55	148.65	79.03
											Ratio =	1.76	

Case TPD4: 0.75 p.u. to 2.08 p.u.

Time [sec]	PM resistivity [microOhm-m]	Airgap HT coeff. [W/m <sup>2</sup> /deg C]	Copper loss [W]	Stator core loss [W]	Rotor core loss [W]	PM loss [W]	Coil Temp. [deg C]	Stator Temp. [deg C]	Rotor Temp. [deg C]	PM Temp. [deg C]	Airgap Temp. [deg C]	Torque [N*m]	Coil Max Temp. [deg C]
Initial Steady State	1.36	125.91	285.85	269.76	80.10	61.88	73.43	71.42	123.26	118.17	78.90	81.08	74.01
0	1.36	125.91	2204.55	727.78	233.43	277.54	73.43	71.42	123.26	118.17	78.90	168.02	74.01
18	1.36	125.91	2234.94	727.78	233.43	277.54	77.74	72.18	123.43	116.81	79.14	168.02	78.26
											Ratio =	2.07	

Case TPD5: 0.70 p.u. to 2.66 p.u.

Time [sec]	PM resistivity [microOhm-m]	Airgap HT coeff. [W/m <sup>2</sup> /deg C]	Copper loss [W]	Stator core loss [W]	Rotor core loss [W]	PM loss [W]	Coil Temp. [deg C]	Stator Temp. [deg C]	Rotor Temp. [deg C]	PM Temp. [deg C]	Airgap Temp. [deg C]	Torque [N*m]	Coil Max Temp. [deg C]
Initial Steady State	1.36	125.91	249.38	255.64	71.30	54.97	71.19	70.25	114.98	110.61	76.51	76.38	71.74
0	1.36	125.85	3576.66	874.55	315.03	358.74	71.19	70.25	114.98	110.61	76.51	187.94	71.74
18	1.36	125.85	3666.89	874.55	315.03	358.74	79.08	71.57	116.68	109.70	77.34	187.94	79.56
											Ratio =	2.46	

Case TPD6: 0.65 p.u. to 3.43 p.u.

Time [sec]	PM resistivity [microOhm-m]	Airgap HT coeff. [W/m <sup>2</sup> /deg C]	Copper loss [W]	Stator core loss [W]	Rotor core loss [W]	PM loss [W]	Coil Temp. [deg C]	Stator Temp. [deg C]	Rotor Temp. [deg C]	PM Temp. [deg C]	Airgap Temp. [deg C]	Torque [N*m]	Coil Max Temp. [deg C]
Initial Steady State	1.35	125.84	213.28	242.31	61.55	48.31	68.97	69.08	106.38	102.83	74.12	71.91	69.49
0	1.35	125.79	5879.47	1027.06	394.18	450.93	68.97	69.08	106.38	102.83	74.12	206.71	69.49
18	1.35	125.79	6139.96	1027.06	394.18	450.93	82.85	71.12	109.62	102.40	75.65	206.71	83.32
											Ratio =	2.87	

Case TPD7: 0.60 p.u. to 4.27 p.u.

Time [sec]	PM resistivity [microOhm-m]	Airgap HT coeff. [W/m <sup>2</sup> /deg C]	Copper loss [W]	Stator core loss [W]	Rotor core loss [W]	PM loss [W]	Coil Temp. [deg C]	Stator Temp. [deg C]	Rotor Temp. [deg C]	PM Temp. [deg C]	Airgap Temp. [deg C]	Torque [N*m]	Coil Max Temp. [deg C]
Initial Steady State	1.35	125.78	180.36	229.15	52.46	41.99	66.90	67.99	98.31	95.52	71.89	67.24	67.41
0	1.34	125.73	9087.89	1169.25	477.92	542.46	66.90	67.99	98.31	95.52	71.89	223.04	67.41
18	1.34	125.73	9731.79	1169.25	477.92	542.46	89.26	70.88	103.12	95.57	74.17	223.04	89.76
											Ratio =	3.32	



## A.6 EM-Thermal Coupled Tests for Eff. Design under Transient Operation

### Case Eff1: 2.70 p.u. to 3.35 p.u.

Time [sec]	PM resistivity [microOhm-m]	Airgap HT coeff. [W/m^2/deg C]	Copper loss [W]	Stator core loss [W]	Rotor core loss [W]	PM loss [W]	Coil Temp. [deg C]	Stator Temp. [deg C]	Rotor Temp. [deg C]	PM Temp. [deg C]	Airgap Temp. [deg C]	Torque [N*m]	Coil Max Temp. [deg C]
Initial Steady State	1.40	125.69	2431.23	353.34	22.07	317.12	147.49	87.81	150.53	155.20	108.68	261.73	148.86
0	1.40	125.69	3741.85	405.35	33.12	460.42	147.49	87.81	150.53	155.20	108.68	323.03	148.86
18	1.40	125.69	3797.21	406.00	33.10	460.24	153.30	88.93	152.29	156.88	108.60	322.43	155.04
												Ratio =	1.23

### Case Eff2: 2.60 p.u. to 4.00 p.u.

Time [sec]	PM resistivity [microOhm-m]	Airgap HT coeff. [W/m^2/deg C]	Copper loss [W]	Stator core loss [W]	Rotor core loss [W]	PM loss [W]	Coil Temp. [deg C]	Stator Temp. [deg C]	Rotor Temp. [deg C]	PM Temp. [deg C]	Airgap Temp. [deg C]	Torque [N*m]	Coil Max Temp. [deg C]
Initial Steady State	1.39	125.69	2220.36	347.77	20.56	297.53	140.18	85.89	143.72	148.19	105.06	253.80	141.52
0	1.39	125.69	5233.20	473.15	46.14	627.74	140.18	85.89	143.72	148.19	105.06	386.53	141.52
18	1.39	125.69	5413.99	472.37	46.12	627.35	153.63	87.20	145.49	150.80	105.18	385.41	155.33
												Ratio =	1.52

### Case Eff3: 2.50 p.u. to 4.60 p.u.

Time [sec]	PM resistivity [microOhm-m]	Airgap HT coeff. [W/m^2/deg C]	Copper loss [W]	Stator core loss [W]	Rotor core loss [W]	PM loss [W]	Coil Temp. [deg C]	Stator Temp. [deg C]	Rotor Temp. [deg C]	PM Temp. [deg C]	Airgap Temp. [deg C]	Torque [N*m]	Coil Max Temp. [deg C]
Initial Steady State	1.38	125.69	2006.49	342.66	19.12	278.60	132.77	83.97	137.02	141.29	101.40	246.46	134.09
0	1.38	125.69	6784.72	545.04	59.81	800.65	132.77	83.97	137.02	141.29	101.40	445.31	134.09
18	1.39	125.69	7162.57	546.53	59.79	799.97	154.24	85.39	138.79	144.83	101.65	443.38	155.88
												Ratio =	1.80

### Case Eff4: 2.40 p.u. to 4.90 p.u.

Time [sec]	PM resistivity [microOhm-m]	Airgap HT coeff. [W/m^2/deg C]	Copper loss [W]	Stator core loss [W]	Rotor core loss [W]	PM loss [W]	Coil Temp. [deg C]	Stator Temp. [deg C]	Rotor Temp. [deg C]	PM Temp. [deg C]	Airgap Temp. [deg C]	Torque [N*m]	Coil Max Temp. [deg C]
Initial Steady State	1.38	125.68	1832.92	338.13	17.69	259.96	126.72	82.38	130.87	134.98	98.36	238.01	128.01
0	1.38	125.68	7572.38	841.76	67.09	893.08	126.72	82.38	130.87	134.98	98.36	476.12	128.01
18	1.38	125.68	8113.73	645.20	67.09	892.19	152.75	83.98	132.63	139.06	98.85	473.98	154.35
												Ratio =	2.00

### Case Eff5: 2.30 p.u. to 5.35 p.u.

Time [sec]	PM resistivity [microOhm-m]	Airgap HT coeff. [W/m^2/deg C]	Copper loss [W]	Stator core loss [W]	Rotor core loss [W]	PM loss [W]	Coil Temp. [deg C]	Stator Temp. [deg C]	Rotor Temp. [deg C]	PM Temp. [deg C]	Airgap Temp. [deg C]	Torque [N*m]	Coil Max Temp. [deg C]
Initial Steady State	1.37	125.67	1657.86	332.82	16.34	241.92	120.61	80.77	124.84	128.79	95.30	229.82	121.88
0	1.37	125.65	8875.20	792.35	78.58	1036.52	120.61	80.77	124.84	128.79	95.30	520.59	121.88
18	1.38	125.66	9694.31	1422.22	78.47	1035.23	153.67	82.75	126.61	133.66	96.20	517.82	155.23
												Ratio =	2.26

Case Eff6: 2.20 p.u. to 5.60 p.u.

Time [sec]	PM resistivity [microOhm-m]	Airgap HT coeff. [W/m^2/deg C]	Copper loss [W]	Stator core loss [W]	Rotor core loss [W]	PM loss [W]	Coil Temp. [deg C]	Stator Temp. [deg C]	Rotor Temp. [deg C]	PM Temp. [deg C]	Airgap Temp. [deg C]	Torque [N*m]	Coil Max Temp. [deg C]
Initial Steady State	1.37	125.64	1494.43	329.91	15.02	224.40	114.92	79.28	119.08	122.87	92.45	221.43	116.17
0	1.37	125.63	9569.06	683.31	85.21	1119.18	114.92	79.28	119.08	122.87	92.45	546.58	116.17
18	1.37	125.63	10576.82	688.27	85.13	1117.61	152.07	80.96	120.83	128.21	93.04	543.43	153.59
											<b>Ratio =</b>	<b>2.46</b>	

Case Eff7: 2.10 p.u. to 6.00 p.u.

Time [sec]	PM resistivity [microOhm-m]	Airgap HT coeff. [W/m^2/deg C]	Copper loss [W]	Stator core loss [W]	Rotor core loss [W]	PM loss [W]	Coil Temp. [deg C]	Stator Temp. [deg C]	Rotor Temp. [deg C]	PM Temp. [deg C]	Airgap Temp. [deg C]	Torque [N*m]	Coil Max Temp. [deg C]
Initial Steady State	1.36	125.62	1342.20	324.25	13.73	207.37	109.58	77.87	113.54	117.19	89.75	212.85	110.82
0	1.36	125.59	10817.93	744.73	96.18	1252.83	109.58	77.87	113.54	117.19	89.75	585.74	110.82
18	1.37	125.60	12187.72	743.47	96.09	1250.72	153.62	79.68	115.30	123.28	90.47	581.93	155.11
											<b>Ratio =</b>	<b>2.74</b>	

Case Eff8: 2.00 p.u. to 6.23 p.u.

Time [sec]	PM resistivity [microOhm-m]	Airgap HT coeff. [W/m^2/deg C]	Copper loss [W]	Stator core loss [W]	Rotor core loss [W]	PM loss [W]	Coil Temp. [deg C]	Stator Temp. [deg C]	Rotor Temp. [deg C]	PM Temp. [deg C]	Airgap Temp. [deg C]	Torque [N*m]	Coil Max Temp. [deg C]
Initial Steady State	1.36	125.55	1182.92	319.78	12.51	190.96	104.03	76.41	108.06	111.56	86.98	204.54	105.24
0	1.36	125.55	11470.22	779.46	102.59	1331.36	104.03	76.41	108.06	111.56	86.98	609.50	105.24
18	1.36	125.56	13080.71	777.57	102.56	1328.90	152.13	78.27	109.80	118.10	87.77	605.28	153.58
											<b>Ratio =</b>	<b>2.97</b>	